Ionic Liquid Ion Source Emitter Arrays Fabricated on Bulk Porous Substrates for Spacecraft Propulsion

by

Daniel George Courtney

BSc.Eng., Engineering Physics, Queen's University (2006)
S.M., Aeronautics and Astronautics, Massachusetts Institute of Technology (2008)

Submitted to the Department of Aeronautics and Astronautics
in partial fulfillment of the requirements for the degree of

Doctor of Philosophy

at the

MASSACHUSETTS INSTITUTE OF TECHNOLOGY

June 2011

Author .....
Department of Aeronautics and Astronautics
June 3, 2011

Certified by .....
Paulo Lozano
H.N. Slater Associate Professor of Aeronautics and Astronautics
Thesis Supervisor

Certified by .....
Manuel Martínez-Sánchez
Professor of Aeronautics and Astronautics

Certified by .....
Brian L. Wardle
Associate Professor of Aeronautics and Astronautics

Certified by .....
Jeffrey H. Lang
Professor of Electrical Engineering

Accepted by .....
Eytan H. Modiano
Associate Professor
Chair, Graduate Program Committee

Ionic Liquid Ion Source Emitter Arrays Fabricated on Bulk Porous Substrates for Spacecraft Propulsion

by

Daniel George Courtney

Submitted to the Department of Aeronautics and Astronautics
on June 3, 2011, in partial fulfillment of the
requirements for the degree of
Doctor of Philosophy

Abstract

Ionic Liquid Ion Sources (ILIS) are a subset of electrospray capable of producing bipolar beams of pure ions from ionic liquids. Ionic liquids are room temperature molten salts, characterized by negligible vapor pressures, relative high conductivities and surface tensions lower than water. Compared with the colloid form of electrospray, renowned for its applications to spectroscopy, ILIS yield highly monoenergetic beams composed entirely of ions. In this respect they are similar to Liquid Metal Ions Sources, but offer the ability to emit both positive and negative ions from a benign propellant that remains in the liquid state over a wide range of temperatures.

When applied to spacecraft propulsion these sources are very power efficient and yield high specific impulses. Furthermore, the low flow rates and negligible vapor pressures of ionic liquids allow for passive feeding systems which can remain exposed to the vacuum of space. This configuration would remove the need for pressurized propellant tanks or valves, both of which are difficult to miniaturize for small satellites. However; the thrust produced from each emitter is very low, less than 0.1 μN. As a result, compact arrays of active ILIS have been sought since their discovery. If arrays of modest packing density (~ 5 emitters/mm^2) could be achieved, ILIS as thrusters would offer a scalable form of propulsion capable of providing useful thrust levels to small satellites with performance comparable to established, but difficult to miniaturize, plasma based ion engines.

This research has sought a technique for creating arrays of ILIS from bulk porous substrates as part of an overall process for microfabricating complete thrusters. The thesis includes a survey of potential fabrication methods considering both suitability for forming arrays of ILIS and the ability to integrate each technique within a thruster packaging process. Electrochemical etching is highly selective and can proceed at rates which are limited by mass transport conditions. In this thesis we show how this etching regime can be exploited to smoothly remove material from the surface of a bulk porous metal substrate without damaging the internal pore structure. Dry film photoresists have been identified as a suitable alternative to spin on techniques for porous materials and have been applied within an electrochemical etching process.

A two step process for forming arrays of ILIS has been motivated using numerical simulations of the etching process to predict emitter profiles and investigate the impacts of non-uniform etching conditions. These concepts have been applied experimentally using a custom built, automated, etching station capable of repeatedly producing arrays of 480 emitters spaced 500 μm apart on a 1 x 1 cm porous nickel substrate pre-mounted, and aligned,

within a silicon thruster package. The emitters are typically 165 μm tall with rounded tips suitable for operation as ILIS. Pulsed voltage conditions were found to significantly enhance wafer level uniformity enabling fabrication of functional emitters within a few hundred μm of the substrate boundary. The structures have been smoothed and rounded, making them suitable for use as ILIS, during a secondary etch process using electrolytes doped with nickel chloride to suppress transient effects. These doped solutions enabled a few μm of material to be removed selectively from the porous surface while maintaining smooth features.

These arrays have been mounted and aligned with electrostatic grids to demonstrate their emission capabilities. Propellant has been fed to the emitters by capillarity within the porous bulk and then extracted at potentials as low as 850 V. Beam currents exceeding several 100 μA at both positive and negative polarities have been measured using both EMI-Im and EMI-BF_4 ionic liquid propellant. Two complete devices were tested yielding large beam currents and very high transmission fractions ($\sim$ 88-100 %) from both attempts. We estimate that these devices can supply 10's of μN of thrust at modest operating potentials, $\sim$ 1.5 kV, with a specific impulse of roughly 2000-3000 s. When completely packaged, the thrusters measure 1.2 x 1.2 x 0.2 cm, weigh less than 1 g and require less than 0.65 W of operating power. These characteristics would be ideal for a small satellites where volume, mass and power are all at a premium, while the thrust levels would be sufficient to enable a variety of orbit variation and attitude control maneuvers. For example, applied to a CubeSat, this type of thruster system, including PPU, would occupy roughly 10 % of the spacecraft volume and mass while enabling de-orbiting from an 800 km altitude in roughly 100 days, compared with many years when left to decay naturally.

Thesis Supervisor: Paulo Lozano
Title: H.N. Slater Associate Professor of Aeronautics and Astronautics

Committee Member: Manuel Martínez-Sánchez
Title: Professor of Aeronautics and Astronautics

Committee Member: Brian L. Wardle
Title: Associate Professor of Aeronautics and Astronautics

Committee Member: Jeffrey H. Lang
Title: Professor of Electrical Engineering

Acknowledgments

For as long as I can remember I have wanted to work on, and help develop, spacecraft hardware. I would like to thank my advisor, Professor Paulo Lozano for providing me with the opportunity to realize my ambition and pursue my Ph.D. in this exciting field. I will forever be indebted to Prof. Martínez-Sánchez for all of his insight/genious and the many discussions we have had throughout my graduate career. I would like to thank my thesis committee members, Profs. Jeffrey Lang and Brian Wardle, and thesis readers, Dr. Hanqing Li and Dr. William Hargus, for their patience and guidance throughout the process of forming this document.

This research has been made possible through funds provided by the Natural Sciences and Engineering Research Council of Canada (NSERC), the US Air Force Office of Scientific Research (AFOSR), the US National Reconnaissance Office (NRO) and the Busek Company.

I am very much indebted to all of the staff from both the Aero/Astro department and MIT Microsystems Technology Laboratories (MTL) for all of their help throughout my my time at MIT. In particular, the experimental work presented here would not have been possible without the valuable insight of Todd Billings, the Aero/Astro department technical instructor, and Kurt Broderick of MTL.

I would like to thank Dr. Hanqing Li of MTL for his guidance and brilliant contributions to this project, without which many of the results presented would not have been possible.

Throughout my time at MIT I am very fortunate to have made many great friends, for too many to list them all here. I will certainly miss our daily (or more) coffee breaks, playing hockey at every opportunity and general tomfoolery.

I would never have been able to complete this work if it was not for the constant support from my family. My Mum and Dad have been there for me through all of the ups and downs of graduate school. Even when all else seems to have failed they are always there to cheer me up and put things in perspective. They have also, very generously and tirelessly, proof read my entire thesis and have made many contributions both stylistic and technical to this final document. My sister, Dr. Tiz Dennis, has been a great inspiration for me as I have pursued this degree, I am very excited that we can finally call each other Doctor. Finally, despite being a country apart for many years, my girlfriend Ashley has always been ready and willing to support me and help me make the most of myself.

Contents

Chapter 1

Introduction

Very small satellites are an exciting and emerging field, not just as thesis topics, but as realistic platforms for performing useful missions in space. Their low development and launch costs are equivalent to a new access to space which can be exploited by academia, research groups and government agencies.

To be successful, a small satellite must have a very simple design. For one of the smallest satellite types, CubeSats, this has resulted in satellites built to achieve a goal without any form of active propulsion. Developing a simple propulsion system suitable for small satellites would enable a wide variety of missions. Achieving this with existing propulsion technologies is very difficult. Currently, established propulsion technologies which have been developed for larger spacecraft with an emphasis on reliability, performance and versatility are often discarded in favor of inefficient but small, simple propulsion systems (or none at all) simply because the former are difficult to scale down.

The intention of this research has been to fabricate and then test planar electrospray thrusters using porous substrate material. Specifically arrays of porous emitters intended to serve as Ionic Liquid Ion Sources (ILIS) have been fabricated electrochemically using a custom made processing tool. The work has been divided between fabrication of the emitter arrays and subsequent experimental tests demonstrating their capabilities. Detailed reviews and introductions of both electrospray sources and the fabrication challenges inherent in attempting to create arrays of porous ILIS suitable for propulsion are given in Chapters 2 and 3 respectively.

In this introduction we focus on motivating the niche these thrusters could fill by demon-

strating their applicability to CubeSats. Relevant propulsion metrics and key features inherent in porous ILIS thrusters will be introduced as part of the discussion. Finally, this chapter concludes with a summary of the contributions this research has made to both microfabrication and electrospray sources.

1.1 CubeSats : A Type of Nano-Satellite

CubeSats are very small satellites which emerged in the last decade as an attractive option for educational and research satellites due to their low launch and development costs. Beginning in 2003, at least 26 CubeSats have been launched[1]. A single unit (or 1U) CubeSat measures 10 cm x 10 cm x 10 cm, has a mass not exceeding 1 kg and has at most a few Watts of onboard power available through solar panels[2, 3, 4]. Several U's can be combined to form a larger satellite. The satellites are typically launched as secondary payloads and are deployed from the launch vehicle using a simple spring mechanism once on orbit[4]. At the time of writing no CubeSat has been launched with active onboard propulsion[3]. Useful missions may be completed without active propulsion, for example using tethers or gravity booms for stabilization[2], but introducing propulsion could expand mission capabilities.

As a baseline for what level of thrust could be useful for a CubeSat we can estimate the atmospheric drag at the orbit altitude. If we are concerned with a CubeSat in a circular orbit, the drag can be estimated with equations 1.1 and 1.2. Here, F_{drag} is the drag force, C_d is the drag coefficient (roughly 2[5]), A_{sat} is the satellite projected area ($\sim$0.01 m^2 here), ρ is the atmospheric density, v is the spacecraft velocity, a is the satellite altitude from the center of the earth and μ is a constant equal to the mass of the earth multiplied by the gravitational constat G (6.6743 x 10^{-11} m^3/kgs^2). Typical CubeSats orbit at an altitude of $\sim$ 600-700 km above the earth's surface[1]. The maximum predicted atmospheric drag at 650 km is roughly 0.15 μN using tabulated atmospheric density data[6], while at 300 km that value increases to $\sim$ 23 μN.

$$F_{drag} = \frac{1}{2} C_d A_{sat} \rho v^2 \tag{1.1}$$

$$v = \sqrt{\frac{\mu}{a}} \tag{1.2}$$

Given these estimates, a suitable propulsion system might be one which provides thrust levels of at least a few 10's of μN such that missions can be performed over a range of altitudes without losing control over the orbital decay. Although, a tiny amount of force to someone on the surface of the earth, we will see below that thrusts of this order are indeed useful.

In addition to simply providing enough thrust, when applied to a CubeSat, the limited size, mass and power are all significant constraints on the propulsion system. Determining if a propulsion system can fit within these constrains involves understanding both the performance of the thruster and its physical design constraints. For example, typical CubeSats use solar panels capable of generating the $\sim$ 1W of power cited above. However this requires the sides of the CubeSat to be relatively free from other components to accommodate the panels. Hence any propulsion system which relies on electrical power from solar panels should have a small frontal area or risk a reduction in available power.

1.2 Propulsion Metrics

Before discussing some potential thruster options, it is useful to introduce some common metrics and relations for describing spacecraft propulsion systems. Further details on these concepts are available in the references[7, 8, 9]. The thrust, F, from an in-space propulsion system is given by equation 1.3. Here $\dot{m}_p$ is the portion of propellant mass flow contributing to thrust and $\bar{c}$ is the average exhaust velocity.

$$F = \dot{m}_p \bar{c} \tag{1.3}$$

The efficiency of an electric spacecraft propulsion system, η_p measures the ability to convert input electrical power, P_{in} (the product of the net current I and the voltage V), into useful thrust power and is given by equation 1.4,.

$$\eta_p = \frac{1/2\dot{m}_p \bar{c}^2}{P_{in}} \tag{1.4}$$

The specific impulse, I_{sp} (s), is a measure of propellant economy for propulsion systems and is defined in equation 1.5 as the ratio of thrust, F, to net mass flow rate, $\dot{m}_{net}$ divided by the acceleration due to gravity at sea level, g. The simplification to the right of the

equation results when the net propellant flow rate and that contributing to propulsion are equal, as seen by substituting the thrust, F from equation 1.3 into equation 1.5 and setting $\dot{m}_p = \dot{m}_{net}$. In chemical rockets, where chemical energy is converted to thermal motion prior to expansion through a nozzle, the specific impulse is typically less than $\sim$ 450 s[10]. However; if the propellant is ionized and can be electrostatically accelerated as in this research, the specific impulse can soar to many thousands of seconds[10]. For example the NEXT grided ion engine developed by NASA JPL can operate with a specific impulse of up to 4100 s[11].

$$I_{sp} = \frac{F}{\dot{m}_{net} g} \sim \frac{\bar{c}}{g} \tag{1.5}$$

The benefit of a large specific impulse is a reduction in propellant mass required to execute a manoeuver. Propulsive missions can be described in terms of their ΔV, equivalent to the change in velocity in a force free environment (units m/s). For a constant specific impulse system, equation 1.6 for the ΔV results by integrating Newton's second law[12] from the beginning to the end of a propulsive maneuver. Here Δm_p is the propellant mass consumed and m_0 is the initial spacecraft mass.

$$\Delta m_p = m_0 \left(1 - e^{\frac{-\Delta V}{I_{sp} g}}\right) \tag{1.6}$$

Hence lower propellant masses are required to perform the same ΔV missions using systems with higher specific impulse. However; high specific impulse is not always beneficial. As an example, consider a propulsion system constrained to operate efficiently within a range of specific impulses and employed in a power limited system. The system thrust, as a function of power, specific impulse and efficiency results by combining equations 1.3 through 1.4 leaving equation 1.7. We see that, for a constrained power application, a system designed to operate at a very high specific impulse could be limited in terms of thrust. Consider a CubeSat with 1 W of onboard power using a propulsion system designed to operate optimally at a specific impulse of 10,000 s with an efficiency, including power delivery, of 50 %. For example some forms of grided ion engines (see the description below and[9, 10]), or electrospray thrusters with high post extraction accelerations (see Chapter 2) could fit this description. Using equation 1.7, the maximum thrust from such a device would be power limited to only 10 μN.

$$F = \frac{2P_{in}\eta_p}{gI_{sp}} \tag{1.7}$$

1.3 Challenges for CubeSat Propulsion Candidates

Candidate propulsion systems for CubeSats are very limited, and as mentioned above, no active system has been employed to date. Recently, Mueller, Hofer and Ziemer[3] compiled an extensive review of state of the art propulsion systems and their applicability to CubeSats. In lieu of a detailed review, here we can consider as an example the challenges inherent in applying grided ion engines, an electrostatic propulsion system with relatively significant flight heritage[9], to a CubeSat.

In the discussion above, we have established that a suitable propulsion system need only deliver a few 10's of μN of thrust to dominate over drag forces but that they must do so within the tight mass, volume and area constraints of a CubeSat. Typical components comprising a grided ion engine system are shown schematically in Figure 1-1. These thrusters are similar to the porous ILIS thrusters developed here in that they accelerate a beam of charged ions electrostatically through electrostatic grids. The NEXT device mentioned above, a large kW level thruster, can operate at high efficiencies, up to $\sim$ 70%, at high specific impulse levels, from a few $1000s$ up to $4100s$, and yield thrust levels per unit area up to $\sim 1.5\ N/m^2$. These specific performance metrics would be well suited for a CubeSat application. The high power efficiency and specific impulse are beneficial given the mass and power constraints, while for a fully scalable device only a tiny amount of area would be required to supply 10's of μN of thrust. Of course, the problem is that these devices are difficult to scale, and can not maintain such high specific performance within a small package and at low power levels. Current miniaturized thrusters of this type require at least 10 W of power, have electrical efficiencies lower than $\sim$ 50 %[3] and, without any other components, are several hundred grams in mass. This level of power would require complicated deployed solar arrays, and as discussed below, the required ancillary components comprising such a thruster are substantial.

The problem of miniaturization does not only involve reductions in specific metrics (like I_{sp} and thrust per unit area) but also challenges with miniaturizing the other components which comprise the thruster system. Consider the general components for a grided ion en-

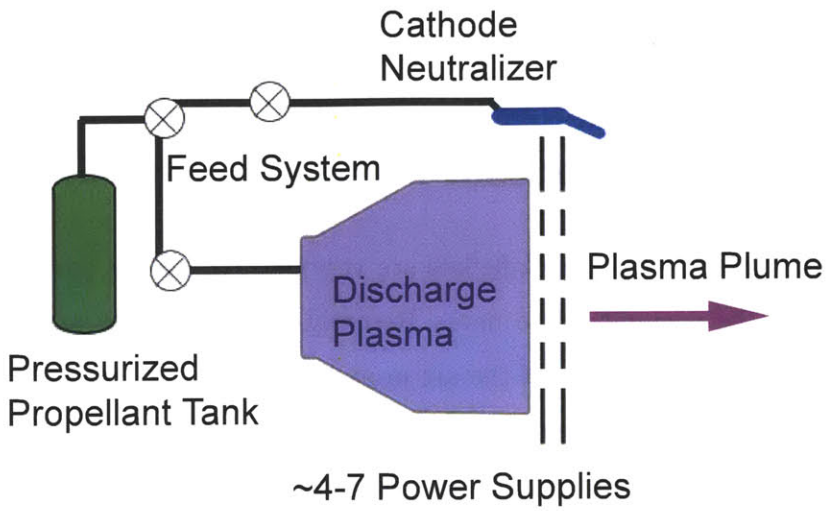

Figure 1-1: Schematic of the components required for an electrostatic grided ion engine. The discharge chamber includes either an internal cathode or a RF antenna to ionize the gas, both require at least one dedicated power supply. The external neutralizer requires its on propellant feed and additonal power supplies. Finally beam acceleration occurs through at least two grids.

gine shown in Figure 1-1. The xenon propellant is stored in a pressurize vessel then fed to the thruster through a series of valves and tubes, all of which are difficult to miniaturize[3]. Ionization then takes place in a discharge chamber, consuming volume, power and mass converting the neutral propellant into useful positive ions. Ionization could be achieved in one of two ways. In electron bombardment designs, an additional cathode is required within the discharge chamber which passes electrons through the gas to induce ionization[13][7]. In this case an increasingly strong magnetic field would be required to maintain high efficiencies at small sizes[14]. Alternatively, radio frequency signals could be used to induce ionization and form a plasma[3], again this becomes challenging for small satellites in that the required RF supply and coils may be difficult to scale. Finally, regardless of the ionization mechanism, an external cathode is required to neutralize the positive ion beam and prevent spacecraft charging. In summary, although a reasonably efficient and compact thruster head may be possible, the complete system requires a number of other components which are difficult to miniaturize and could consume a significant amount of electrical power.

These types of scaling problems are not limited to electrostatic thrusters, for example

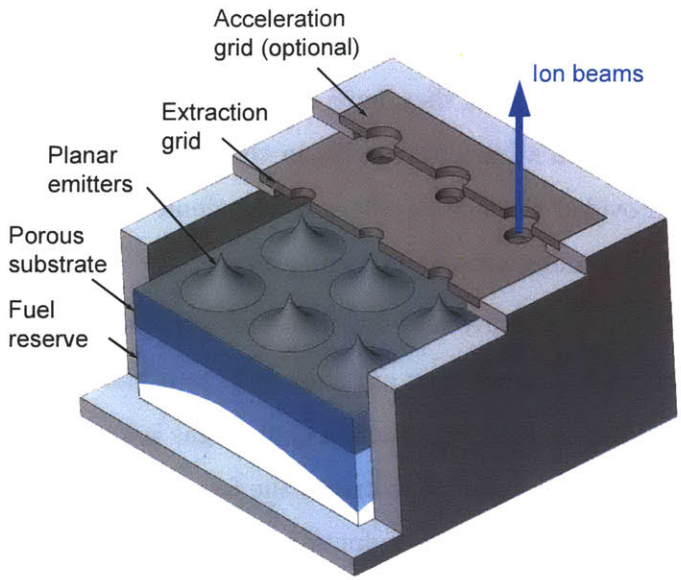

Figure 1-2: The porous ILIS thruster concept uses no moving parts for propellant supply, relying on capillarity to feed ionic liquid propellant to emitter tips. Ions are evaporated directly from the liquid with only a small percent of total power consumed in extracting them.

cold gas or chemical rockets require similar pressurized feeding mechanisms. Cold gas thrusters have very low specific impulses, $\sim$<70 s[3], but are attractive for small satellites in that they are very simple, with thrust generated by releasing a gas, through a nozzle from a tank. However; as noted in the cited reference, the valves alone require several, if not 10's, of W of onboard power. Ultimately, selection and sizing of a propulsion system will depend on the specific mission requirements, however; any approach aimed at scaling down an existing design could be susceptible to constraints on both the thruster and its required systems. In this thesis, and introduced below, an alternative approach has been taken. Starting from an efficient, simple and small device and scaling it up.

1.4 The Porous Ionic Liquid Ion Source Thruster Solution

In this thesis preliminary examples of microfabricated ionic liquid ion source thrusters have been fabricated and tested. These thrusters take the form of Figure 1-2 and offer methods for overcoming many of the constraints preventing successful CubeSat propulsion which were briefly discussed above.

Here, room temperature ionic liquids are passively fed, through a porous medium to the tips of small features on a porous metal substrate. These liquids, referred to hereafter as ionic liquids, are remarkable in that they have negligible vapor pressures. The passive feeding mechanism, is similar to a burning candle, in that as ions are evaporated, a fresh supply of propellant is provided through capillary forces alone. This feature removes any need for a heavy, power consuming propellant feed system.

Ionic liquids consist only of positive and negative ions, without a solvent, ready to be extracted for propulsion. In this sense they are analogous to a plasma in a bottle. Unlike the the grided ion engine described above, where a neutral gas is ionized on orbit, by using ionic liquids the work and energy required to create the ion source is done in a laboratory on the ground. This represents a valuable reduction in the energy required for achieving electrostatic thrust in space.

Furthermore, unlike plasmas which only emit positive ions and use an additional electron source to achieve neutralization, ionic liquids are known to support emission of both positive and negative ions directly from the liquid. This bipolar emission capability can be exploited to prevent spacecraft charging by always operating two thruster packages simultaneously but at oppositive polarities (one positive, one negative). Spacecraft charging can therefore be achieved without any power, mass or volume wasted on an external cathode neutralizer. When pure ions are removed directly from an ionic liquid in this manner, the emission is referred to as an Ionic Liquid Ion Source. Details on the basic properties of ionic liquids and operating principles for emission from ILIS are reviewed in Chapter 2.

However; each emitter shown in Fig. 1-2 is expected to yield less than 0.1 μN of thrust. This research has tailored a particular form of electrochemical etching to create arrays of 480 functional emitters on a single 1 cm x 1 cm array. These arrays have been fabricated as part of a complete thruster packaging process which includes a reliable method for aligning the emitters and electrostatic grids. The overall package measures only 12.2 mm x 12.2 mm x 2 mm, has a mass of roughly 0.7 g, and could, for example, be distributed to the corners of a CubeSat as shown on a satellite mockup in Figure 1-3. Direct thrust measurements have not been made but estimated performance levels based on measured beam emission supports the capability to achieve $\sim$ 10's of μN of thrust at specific impulse levels from $\sim$ 2000 to 3000 s while consuming less than 0.6 W (at peak thrust/specific impulse) with these devices.

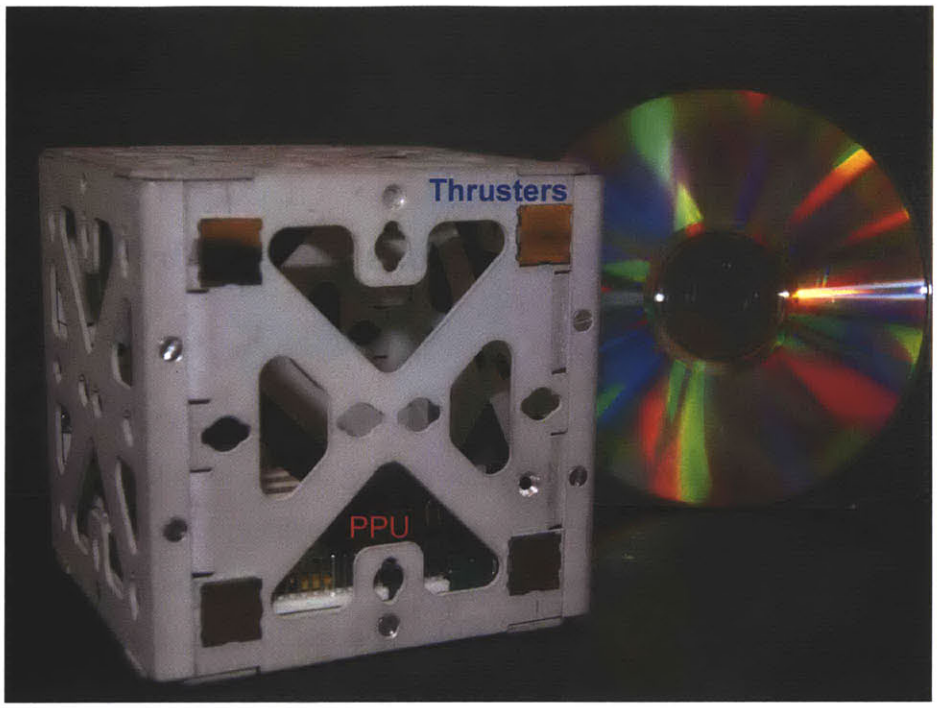

Figure 1-3: Mockup of a CubeSat showing 4 thruster modules in the package used for this research and a small PPU occupying less than 10 % of the total CubeSat volume.

As with the other forms of propulsion described above, a porous ILIS thruster module would require some ancillary components in the form of a propellant reservoir and a PPU (power processing unit). However; the passive feeding system allows for distributed thruster packages with independent porous propellant reservoirs, negating most benefits for a centralized propellant tank. The tanks themselves would only serve to confine the propellant from leaking and provide a coupled path to the emission site. They could, for example, be constructed from a relatively high porosity material (relative to the emitters) and mounted directly behind each thruster package.

Similarly, because these thrusters operate in a bipolar configuration, a single power supply can be used to power the active thrusters (see section 2.2.1 for a schematic of this configuration). Recall that for a grided ion thruster, 4 or more, power systems could be typical. For porous ILIS a simple PPU could, for example, be constructed using existing off the shelf components. For example, a PPU concept developed by colleagues within the MIT Space Propulsion Laboratory, based on off the shelf EMCO[15] voltage converters can be seen in Fig. 1-3 at the base of the satellite. The entire PPU occupies less than 10 % of the satellite internal volume and has a mass of roughly 100 g.

The mission samples below demonstrate how this type of thruster could provide both attitude control and orbit maneuverability on 1U CubeSat while leaving ample room for a payload.

1.5 Examples of CubeSat Missions Enabled by Porous ILIS Thrusters

This section presents a short example of how thrusters using the results of this thesis could be used as both attitude control and orbit maneuvering devices for a CubeSat in low earth orbit. In this example we assume the de-centralized propellant delivery and scalability of these devices have been exploited such that multiple thruster packages are configured at the corners of CubeSat, as in Fig. 1-3 but controlled by a single PPU. Each thruster could have an independent propellant tank which we will see below would require only a small amount of propellent. Using the PPU described above we stipulate that at least 2 (to maintain charge neutrality) but no more than 4 thruster packages are used at any one time such that the combined thrust and total power are held to $\sim$ 35 μN and $\sim$ 0.6 W respectively. In this example, a conservative estimate for the specific impulse, 2000s, has been used. When combined, these estimated performance metrics are analogous to assuming an efficiency of roughly 57 %. For a satellite capable of supplying 1 W of onboard power, these mission would be possible with a, reasonable, 60 % PPU efficiency[15].

1.5.1 CubeSat Spin Down and Slew Maneuvers

First, we can consider using these thrusters to apply a torque on the spacecraft, as shown in Figure 1-4(left). In this configuration, we activate two thrusters on either side of the CubeSat, such that the total torque is $T = Fa/2$, where a is, roughly, the side length of a CubeSat, 10 cm. The change in rotational speed as a function of time is then given by equation 1.8 assuming the CubeSat mass, m_{cube} to be constant.

$$\Delta\dot{\theta} = \frac{3Ft}{m_{cube}a} \tag{1.8}$$

Suppose, for example, the CubeSat is released into orbit rotating at 1 or 2 Hz about its central axis. We can estimate the time required to de-spin the spacecraft with our thruster

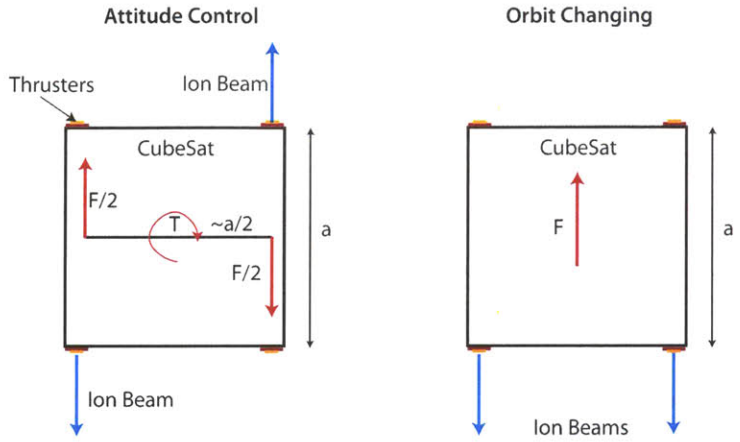

Figure 1-4: With porous ILIS thrusters distributed at the corners of a CubeSat, different missions can be performed by selecting which thrusters are active at a given time.

using this equation. For a 1 kg CubeSat and the propulsion system used here, the rotation could be stopped after $\sim$ 3.3 hours starting from 2 Hz, or 1.7 hours beginning at 1 Hz. On the scale of a typical CubeSat mission lasting several weeks (see for example[2]), this is a relatively short period of time. Referring to equation 1.5, for a thruster operating at constant thrust and specific impulse the mass flow rate would also be constant. The mass expelled during a given operating time is therefore proportional to the maneuver time. For our ILIS thruster, only 10.6 mg and 21.3 mg would be required during these 1 Hz or 2 Hz de-spin maneuvers respectively. Hence the assumption of roughly constant mass is justified.

Once stopped, we may have interest in slewing the thruster through given angles, such that it points at different targets on the ground, or in space. The time required to slew the spacecraft through a given angle, $\Delta\theta$ is given by equation 1.9. Here we would use 8 thrusters in total. First, 4 thrusters firing as above could be used for half the time, at which point we will have slewed through $\Delta\theta/2$ and be rotating at a rate given by equation 1.8. Subsequently, two opposite pairs of thrusters could be used to reduce the rotation rate while the thruster completes its rotation until, at the time given in equation 1.9, the net angle reaches $\Delta\theta$ and the rotation rate is returned to zero.

$$t_{slew} \sim \sqrt{\frac{4m_{cube}a\Delta\theta}{3F}} \tag{1.9}$$

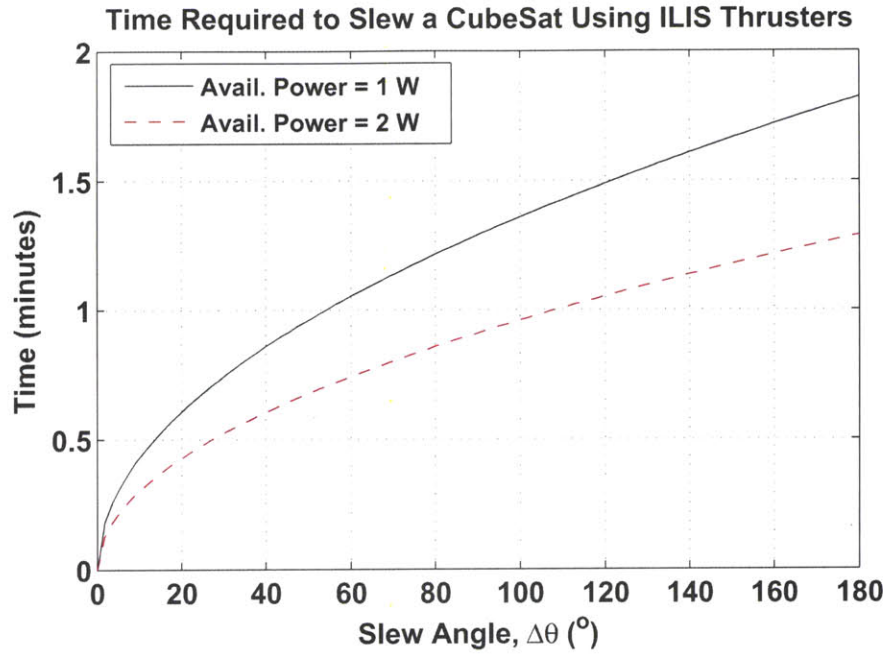

Figure 1-5: Time required to slew a cubesat, using the described propulsion system, through the indicated degrees.

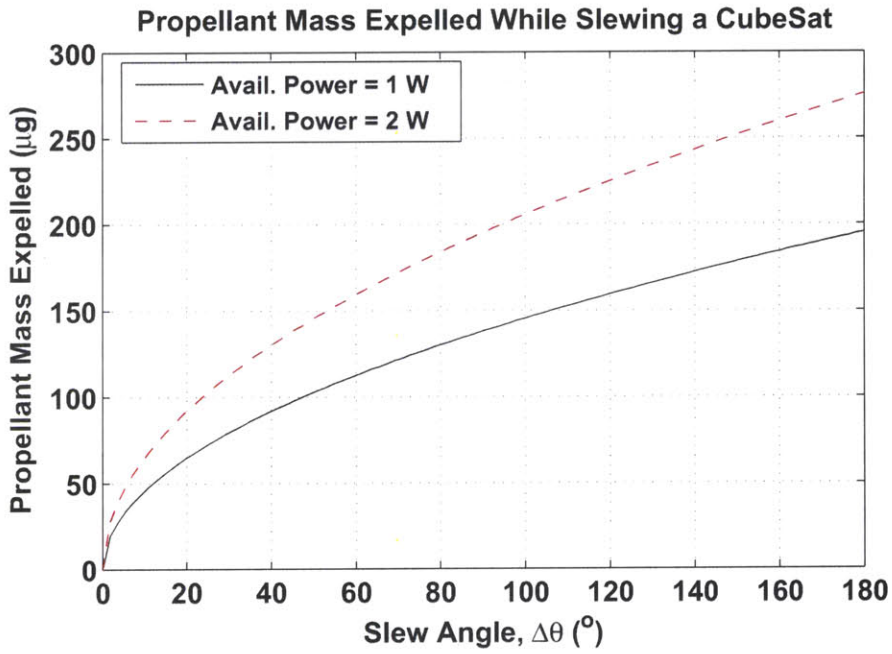

Figure 1-6: Mass required to slew a CubeSat, using the described propulsion system, through the indicated degrees.

The slew time for using an ILIS thruster system has been plotted in Figure 1-5. The mass of the CubeSat has again been taken as constant here, a valid assumption given the propellant mass required, plotted in Figure 1-6. The plots also demonstrate the benefits (in time) and costs (in terms of propellant mass) which would be incurred if twice as much power were available to the propulsion system. Specifically, the plots demonstrate the time and mass required if 2 W were available and could be applied to the thruster system, again using a 60 % efficient PPU, such that the thrust was doubled while maintaining a constant specific impulse.

These examples demonstrate that realistic attitude control maneuvers could be accomplished using ILIS thrusters within reasonable time scales. For example, with these thrusters, a CubeSat beginning in a 2 Hz spin, spun down to a rest and then slewed through 180^o angles 100 times would required only $\sim$ 40 mg of propellant.

1.5.2 CubeSat De-Orbiting

Alternatively, all 4 thrusters on a single side of the CubeSat could be aligned and fired simultaneously to alter the CubeSat orbit altitude. This mode is shown on the right side of Fig. 1-4. Take for example the time required to de-orbit a CubeSat. De-orbiting, refers to a maneuver intended to reduce the CubeSat orbit sufficiently such that it will soon disintegrate within the earths atmosphere. This could, for example, be desirable to prevent CubeSats from contributing to existing space debris, a hazard for other spacecraft.

For this type of maneuver, we can use the ΔV metric introduced earlier. Specifically, for an approximately circular orbit, the ΔV required to change the altitude from a high to low altitude using a low thrust spiral maneuver is given by equation 1.10[10]. That is, the ΔV is the difference between the final and initial orbital velocities, each given by equation 1.2. For a spiral climb, the same equation is valid but we interchange the orbital velocity subscripts.

$$\Delta V = v_{final} - v_{initial} \tag{1.10}$$

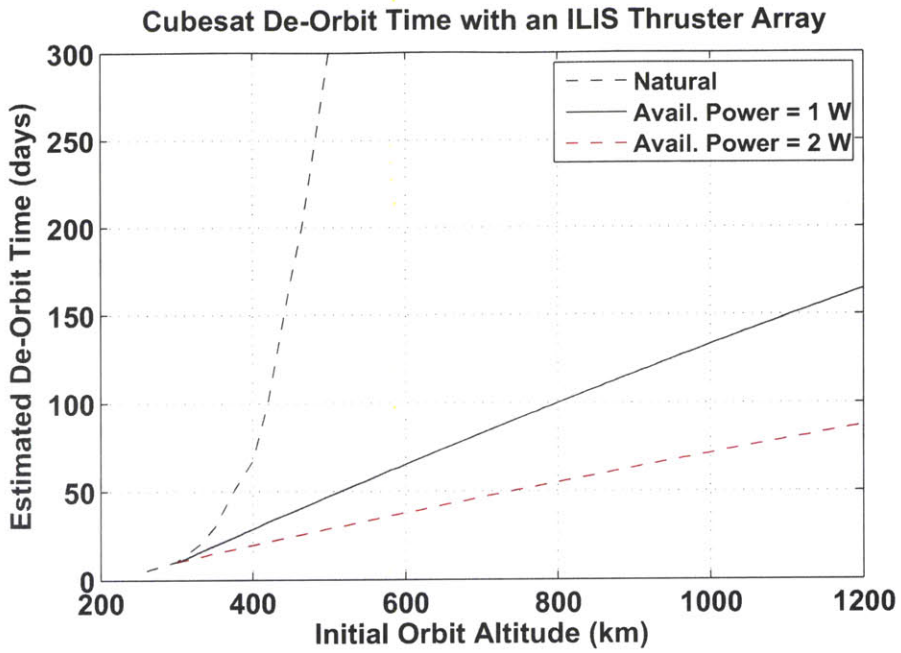

Figure 1-7: Time required to de-orbit a CubeSat either naturally or using a porous ILIS thruster.

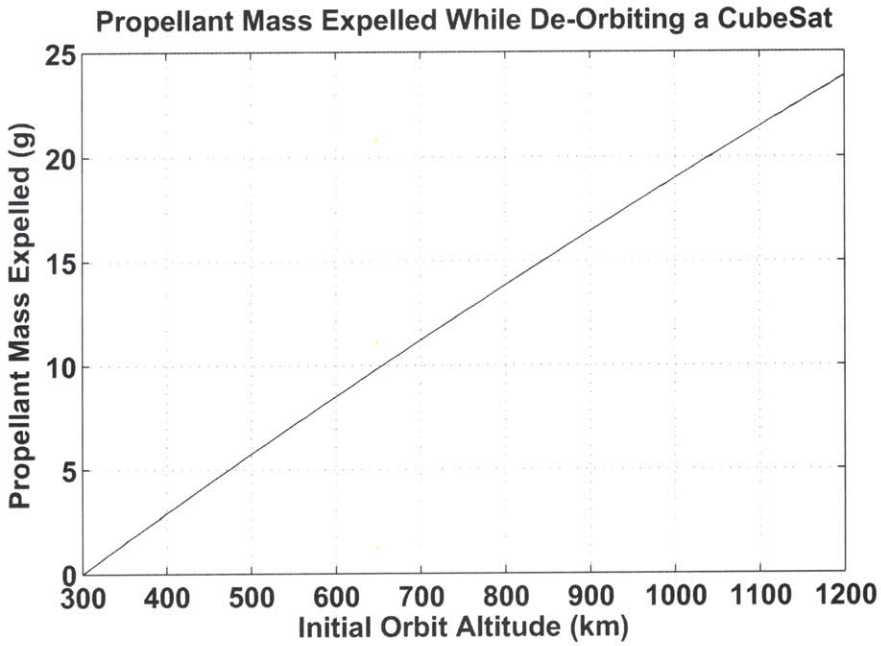

Figure 1-8: Mass required to de-orbit a CubeSat using a porous ILIS thruster with a 2000s specific impulse.

The propellant mass is then given, for our fixed specific impulse device, by equation 1.6. The time required to execute the maneuver can be estimated with equation 1.11, where the simplification is valid for small ΔV to specific impulse ratios.

$$t = \frac{m_{cube} g I_{sp}}{F} \left[1 - e^{-\frac{\Delta V}{g I_{sp}}} \right] \sim \frac{m_{cube} \Delta V}{F} \tag{1.11}$$

The de-orbit time due to atmospheric drag alone can be estimated using tabulated data in the literature[5]. Above $\sim$ 500 km, this natural de-orbit time would tend towards many years. However, at say 300 km, where above we calculated drag forces beginning to approach the roughly 35 μN available from these thrusters, the natural de-orbit time would be only 10 days. Given this we can estimate the time required to de-orbit the spacecraft assuming a spiral orbit transfer from a given altitude to a 300 km orbit before allowing the atmosphere to take over. The time required to de-orbit our CubeSat in this manner, using the 1 W porous ILIS thruster system, has been plotted in Figure 1-7 using equation 1.11, again a 2 W curve has also been plotted.

The propellant mass required to de-orbit has been plotted in Figure 1-8 for the same range of initial altitudes. We see that using this propulsion system, de-orbiting times of a few weeks or months can be achieved while requiring relatively little amounts of propellant. For example, a CubeSat initially at an altitude of 800 km could be removed from orbit in roughly 100 days consuming only $\sim$ 14 g of propellant using these thrusters with 1 W of onboard power.

1.6 Thesis Contributions

The preceding introduction has been intended to demonstrate how the work performed in this thesis may one day be applied to useful devices. Using a CubeSat as an example, we see that these thrusters could be an enabling technology for this type of satellite by providing a means for both attitude control and orbital maneuvers within a small package. Although only simple maneuvers have been described, the distributed propulsion system could provide mission designers and engineers with exciting new capabilities on such a small platform.

Realizing these thrusters, however, is not a trivial task. This thesis is largely dedicated to identifying and developing a reliable technique for fabricating functional porous ILIS arrays

in a manner suitable for packaging within a complete thruster module. The key contributions this work has made to the field of microfabrication, particularly applied to spacecraft propulsion, are summarized here. These results, and those of previous researchers, have been applied to make contributions to the development of electrospray sources made from porous emitters. Those contributions are summarized below.

Contributions to Microfabrication :

- **Smooth Electrochemical Etching on Bulk Porous Media :** This research has demonstrated that under mass transport control an electrochemical etching tool can smoothly etch bulk porous materials with little, or no, damage to the internal pore structure.

- **Microfabrication on Porous Media using Electrochemical Etching :** A process for fabricating structures, from bulk porous materials masked with dry film resists has been demonstrated. This process uses pulsed voltage electrochemical etching and enforced cathodic agitation to achieve both a reasonably high degree of uniformity across an entire sample and good batch yields. The demonstrations performed here, using porous nickel, have produced similar features across a 1 x 1 cm sample including up to within a few hundred μm of the sample edge.

- **Etching Simulations :** An axi-symmetric moving boundary model was developed and shown to be applicable to porous media. Results of these simulations were applied to formulate a two step etch process which accounts for small non-uniformities, such that useful emitters can be created without an accurately defined etch stop.

- **Secondary Etching Using Doped Electrolytes on Porous Media :** We have shown that transient effects, which would otherwise etch the internal pore structure of a substrate, can be suppressed using electrolytes doped with salts containing the etch products. Using this technique, short etches to remove only a few μm have been performed on porous nickel to transform flat topped structures into emitters suitable for use as ILIS.

- **Fabrication of Complete Porous ILIS Thrusters :** Two dimensional arrays of porous emitters have been aligned to and fabricated within a silicon mount. An

electrostatic grid was then aligned with the mount and bonded to create complete thruster packages where the grids and emitters are aligned within a few 10's of μm.

Contributions to Electrospray Sources :

- **Pure Ion Emission from a Porous Planar Emitter :** For the first time, a porous emitter fabricated on a planar substrate was shown to yield purely ionic emission with current levels on par with previous geometries and at operating potentials useful for spacecraft propulsion.

- **High Current Emission from an Array of Porous Emitters :** Arrays of 480 porous nickel emitters have been used to obtain emission currents up to roughly 0.5 μA per emitter. No evidence of a limiting mechanism preventing high current levels was observed and high, $\sim$ 1 $\mu A/V$, current voltage slopes were typical for the range of potentials tested here.

- **High Beam Transmission :** We have demonstrated that arrays with hundreds of porous nickel emitters can yield nearly complete transmission of the emitted beams when aligned with a corresponding microfabricated extractor grid and fabricated using a two step etch mechanism to tailor the emitter tips.

- **Porous Feeding for Arrays of Emitters :** Electrospray emission has been achieved after applying ionic liquid to the rear of a 1 mm thick porous substrate containing emitters. Propellant delivery to the emission sites has been driven by internal capillary forces alone. This technique removes any requirement for an active propellant feed system.

- **Multiple Emission Sites on Porous ILIS :** We have demonstrated that porous emitters can support emission from multiple locations on a single tip. Using simple ablation tests, we showed that emitters with relatively large tip radii and flat topped plateaus are more likely support emission from multiple points compared with relatively sharp emitters. Simultaneous operation of these sites has not been confirmed.

Chapter 2

Porous Ionic Liquid Ion Sources : A Form of Electrospray

This review begins with an overview of electrospray sources focused on identifying the niche for purely ionic electrospray emission from non metals as ion sources for spacecraft propulsion. Subsequently, in the next section, previous and ongoing electrospray thruster array efforts will be reviewed and compared with the research proposed here.

2.1 Electrospray Principles

The term electrospray generally applies to any form of charged particle emission induced by applying an electrostatic field to a conducting liquid. The phenomenon has been observed since the early 1900's. For example Zeleny[16, 17] observed and photographed cone-jet formations of ethyl alcohol and glycerol from a pressure fed capillary tube when several thousands volts were applied between the tube and a counter electrode. Some important contributions leading to the particular focus of this research, sources of pure ion beams using ionic liquids, are discussed in what follows.

2.1.1 Taylor Cones

In 1964 G.I. Taylor[18] demonstrated mathematically that the static conical meniscus observed when a strong electric field is present on a liquid surface can be explained by enforcing equipotentiality on the meniscus along with a balance between the liquid surface tension and applied electric traction. This assumes that the liquid internal pressure, P_c is negligible,

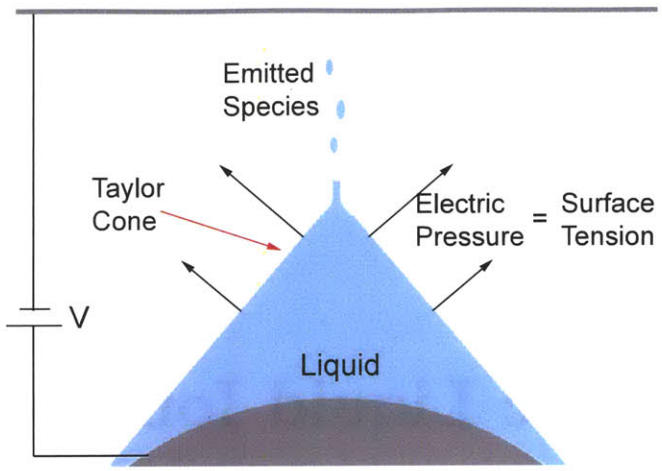

Figure 2-1: Schematic of a Taylor cone formed formed at the tip of an emitter. At the cone apex, strong fields can induce charged species emission.

as in the right side of equation 2.1. Here E_n is the normal component of the electric field, γ is the liquid surface tension and R is the radius of curvature at each point on the meniscus.

$$\frac{1}{2}\epsilon_0 E_n^2 = 2\frac{\gamma}{R} - P_c \approx 2\frac{\gamma}{R} \tag{2.1}$$

Enforcing equation 2.1 along with equipotentiality, leads to a conical solution with a half angle of 49.3^o, shown schematically in Figure 2-1. By removing the approximation of negligible internal pressure, de la Mora[19] demonstrated analytically that, far from the apex, the internal pressure can lead to a, stable, curved profile. Regardless of the corrections due to pressure, these shapes are commonly referred to as Taylor cones.

The field required to form a Taylor cone has been considered by several authors[20, 8, 19]. To within an order of magnitude these analyses all demonstrate that the instability will be induced when the electric traction due to an applied field exceeds forces due to surface tension for a spherical meniscus with radius of curvature equal to the capillary, or outlet, diameter. See Khayms[21] and Lozano[22] for comparison of these analyses. In the cited derivations it is typical to approximate the electric field as a function of applied voltage given a simplified geometrical representation where the emitter tip is the dominant length scale. This leads to the notion of a startup potential. For example, equation 2.2 assumes a capillary of radius R is positioned a distance d from an electrode with potential V[8]. The

applicability of this equation to porous emitters is discussed at the end of this chapter.

$$V_{start} = \sqrt{\frac{\gamma R}{\epsilon_0}} ln\left(\frac{4d}{R}\right) \tag{2.2}$$

2.1.2 Charged Particle Emission

At the apex of a Taylor cone, where the electric field would approach a singularity as R$\sim$ 0 in equation 2.1, the static balance between electric traction and surface tension must break down. The emitted species can be charged droplets, composed of a variable mass of liquid, pure ions, or a mixture of both. The physical structure supporting an emitting Taylor cone is referred to here as 'the emitter' and can take many forms (such as a capillary or a porous tip).

Droplet emission, also referred to as colloidal electrospray, is typically induced with a capillary where a fixed flow rate is enforced by an applied pressure upstream. Under these conditions the Taylor cone shape transforms to a jet of droplets at a critical radius which can be approximated by the radial distance at which charge convection by the fluid motion begins to dominate over electrical conduction within the fluid, as detailed by de la Mora[23] (see [22, 21, 8] for similar discussions). Dissolved salts, for example NaCl in formamide[22], are typically used in this application. When these sources are operated at low flow rates and high conductivity liquids are used, the strong fields near the cone to jet transition point, and on the drops themselves, can induce ion emission in addition to droplets. In the 1960's Perel observed this phenomenon using sulfuric acid[24], however little development was reported until the theoretical and experimental works of Loscertales, for emission from droplets[25], and Gamero-Gastano, for emission from the liquid meniscus[26]. Those studies showed that ion emission was due to field evaporation in a manner previously described by Iribarne and Thomson[27].

Purely ionic emission has been observed using liquid metals, such as cesium[24, 28], gallium[29] or indium[30], since the 1960's (eg. Perel[24], Swatik[29]). These sources are referred to as Liquid Metal Ion Sources (LMIS). They are typically achieved using a passive feeding system where capillarity alone brings new liquid to the emission site as ions evaporate[31]. The high surface tensions of some liquid metals can require high voltages to form a Taylor cone, equation 2.2. Meanwhile, the extremely high conductivities lead to ion evaporation without forming a cone jet or droplets at the cone apex where strong (~

15 V/nm) fields result[32]. These sources typically require potentials of at least 3.5 kV to start, have $\sim$10 kV operating potentials, and produce strong currents up to several 100 μA[31, 33]. When applied to propulsion these sources are often referred to as Field Emission Electric Propulsion (FEEP). The sources can only emit positive ions, requiring an external cathode neutralizer when used in propulsion.

Using non-metals, purely ionic emission remained elusive until 2003 when Romero-Sanz et. al[34] identified the ionic liquid 1-ethyl-3 methyl imidazolium tetrafluroborate (EMI-BF_4) as a candidate liquid for purely ionic emission. Ionic liquids are molten salts which are liquid at room temperature, they typically have negligible vapor pressures, relatively high conductivities and surface tensions lower than water. See Welton[35] for a concise summary of room temperature ionic liquid general properties and synthesis. Romero-Sanz used pressure fed capillary tubes and noted that purely ionic emission occurred only at low flow rates, a phenomenon confirmed by Lozano[22]. Subsequently, Lozano[36, 37] demonstrated that the negligible vapor pressures of ionic liquids could be exploited and applied to a simple passive feeding system. Here, an ionic liquid drop is applied to the exterior of a roughened tungsten needle such that sufficiently low flows can be induced passively by a balance between capillary forces and the meniscus pressure as ions evaporate from the tip of the needle. These sources, using passive feeding and ionic liquids to produce pure ion beams, are referred to as Ionic Liquid Ion Sources (ILIS). Numerous studies have followed using ILIS with a variety of ionic liquids. Table 2.1 lists properties for all ionic liquids known to the author to have been successfully applied as ILIS (see the indicated references) with independent references for the measured material properties. Since these sources emit ions through field emission, applied to propulsion they are strictly speaking a form of FEEP, however that term is traditionally reserved for LMIS. Typically these sources can emit from 10's of nA up to a μA (see references listed in table 2.1). The maximum current has been stipulated to be due to liquid starvation as the flow rate increases[36, 38]. The specific current voltage relationship will depend on the liquid conductivity, surface tension and volatility along with the hydraulics and electrostatics governed by the emitter geometry.

Table 2.1: Ionic liquids used in ILIS

Liquid	K (S/m)	ρ (g/cm^3)	γ (dyn/cm)	M^+ (amu)	M^- (amu)	ILIS	Properties
EMI-$GaCl_4$	2.2	1.53	48.6	111.2	211.5	[39]	[40] [41]
EMI-$N(CN)_2$	2.7	1.08	42.6	111.2	66.0	[39]	[41, 42]
EMI-$C(CN)_3$	1.8	1.11	47.9	111.2	90.1	[39, 38]	[41, 42]
EMI-Im	0.88	1.52	35.8	111.2	280.2	[38, 43]	[40]
EMI-BF_4	1.36	1.24	45.2	111.2	86.8	[38, 36]	[40]
EMI-Beti	0.34	1.6	28.7	111.2	380.2	[44]	[40]
EMI-$F(HF)_{2.3}$	10	1.14	-	111.2	65[a]	[45]	[46]
BMI-$FeBr_4$	0.55	1.98	47.8	139.2	375.5	[39]	[47, 40]
BMI-I	0.069	1.44	54.7	139.2	126.9	[48]	[48, 42]
C_6MI-$FeBr_4$	0.28	1.86	42.0	165.2	375.5	[39]	[47, 40]
C_6MI-$FeCl_4$	0.47	1.33	39.4	165.2	197.7	[39]	[47, 40]
PMI-$(C_2F_5)_3PF_3$	0.166	1.59	30.3	153.2	445.0	[44]	[40]

[a]Average for $F(HF)_k$, with k=2.3.

2.2 Applications of Electrospray Sources

Electrosprays can be applied to a variety of practical problems. Fenn famously applied the colloidal mode as a form of spectroscopy for heavy biological molecules by evaporating the solvent component of emitted droplets such that only ions remain[49]. In 2002, Fenn earned a Nobel in Chemistry prize for that work. Other applications of the colloidal mode include printing, electrospinning of fibers, combustion and many more (see Gassend[50] for a list of applications). The purely ionic regime can also be applied to spectroscopy by extracting ions dissolved in a liquid directly from the meniscus and detecting them downstream. Early efforts in this respect have been limited to solutes suitable for liquid metals[31] however, as ionic liquids can be employed as solvents[35, 51, 52], ILIS could have applications in spectroscopy of non-metals.

ILIS as focused ion beams[53], where emitted ions are focused to produce a highly localized beam aimed at a material of interest can be applied, for example, to microfabrication[54]. Here physical ablation, possibly enhanced by a chemical reaction, can selectively etch a masked material.

2.2.1 Electrosprays for Spacecraft Propulsion

The ability to extract and accelerate a liquid propellant to a high velocity by electrospray, often using a device at room temperature, has been exploited since the 1960's for spacecraft propulsion(a review of those efforts appears later). In chapter 1, two performance metrics

commonly used when discussing propulsion systems were introduced, the specific impulse and the thrust power efficiency, equations 1.5 and 1.4 respectively.

Recall that the specific impulse, I_{sp} (s), is a measure of propellant economy for propulsion systems relating the ratio of thrust, F, to net propellant mass flow, $\dot{m_{net}}$. Ideally, for a thruster where all propellant mass flow is used for propulsion, the thrust is proportional to the propellant mass flow, $F = \dot{m}_p \bar{c}$ (eqn. 1.3), where $\bar{c}$ is the beam velocity. Hence the specific impulse is analogous to a measure of the beam velocity. In the introduction we noted that the specific impulse can range from a few tens or hundreds seconds for chemical rockets up to many thousands of seconds for electric propulsion systems[10, 8].

For an electrospray thruster emitting discrete species, equation 2.3 approximates the beam velocity c_i when the charge to mass ratio is q_i/m_i and the particle is accelerated through the complete extracting potential V_e. The average velocity $\bar{c}$ is then given by averaging, over charge to mass ratio, the velocity for each species i. For a fixed potential and current, species with high charge to mass ratios, like ions, will have high beam velocities, and therefore specific impulse.

$$c_i = \sqrt{\frac{2q_i V_e}{m_i}} \tag{2.3}$$

Colloidal thrusters, spraying droplets, typically operate at specific impulse levels at or below 1000 s[55, 56] depending on the accelerating electric potential and emitted species. However; ILIS can achieve a much larger specific impulse for the same applied potential due to the much larger charge to mass ratio of pure ions compared with droplets.

Recall that the efficiency of a spacecraft propulsion system, equation 1.4, measures the ability to convert input electrical power, the product of the net current I and the voltage V, into useful thrust power. As shown in a detailed review of the postulated efficiency for a thruster using ILIS by Lozano[57], equation 1.4 can be broken down into the product of several efficiencies. The energy efficiency is the ratio of the average beam energy to the maximum obtainable energy at a given accelerating potential. Measurements of the energy distribution from ILIS have found highly monoenergetic beams, typically with energy deficits and spreads less than a few percent[57, 43, 48, 44]. Since ionic liquids have negligible vapor pressures, ion evaporation is the only form of mass flow from ILIS. Therefore the ionization efficiency which measures the fraction of emitted flow which is ionized is close

to one. However; there remains one source for neutrals from ILIS, downstream fragmentation of solvated ions after emission. Fedkiw studied this phenomenon for the ionic liquid BMI-I[58], postulating its effects on the polydispersive efficiency. The polydispersive efficiency quantifies the inefficiencies inherent in accelerating species of varying charge to mass ratios[21, 22, 8, 58]. See the cited references for derivations of this quantity. Low polydispersive efficiencies are common with droplet or mixed ion/droplet colloidal thrusters[22, 21]; however in ILIS Fedkiw experimentally motivated that polydispersive efficiencies greater than 85 %[58] could be expected, depending on the degree of beam fragmentation. The transmission efficiency, which quantifies the current intercepted by an electrostatic grid will depend on the degree to which ion optics have been considered in a particular design. During an early phase of this research an array of 20-80 porous emitters demonstrated negligible grid interception, or close to 100% transmission efficiency, using microfabricated silicon extraction grids. A summary of this work has been included in Appendix A. Finally, the angular spreading of ILIS was measured by Lozano[36], where the beam was found to be contained within a roughly a 20^o half angle. When combined, total power efficiencies close to 80% appear to be within reach using ILIS.

As with with ILIS, LMIS with high specific impulses and efficiencies can also be developed. However ILIS have several practical advantages over LMIS. ILIS can be operated at spacecraft bus temperatures and do not require a dedicated heater to melt the propellant. LMIS must often be heated to remain in the liquid state, the required dedicated heater adds mass and additional power draw, reducing the overall thruster power efficiency[59, 60]. ILIS can emit both positive and negative ions, negating the need for an external cathode neutralizer which would be required in LMIS. Metal contamination on spacecraft surfaces can lead to serious damage[59, 60]. Even if droplet emission and beam impingement could be avoided with an LMIS thruster design, heated liquid metals can evaporate from the surface of the Taylor cone[60]. The higher potentials required for LMIS would lead to larger, and more massive, insulation and power supplies over ILIS, which could be difficult to miniaturize[59].

One concern which must be addressed when operating ILIS for spacecraft propulsion, where long term (1000's of hours) operation can be expected, is the possibility for electrochemical breakdowns between the ionic liquid and emitter substrate material. Lozano and Martínez-Sánchez identified this issue early in the development of ILIS[37] and moti-

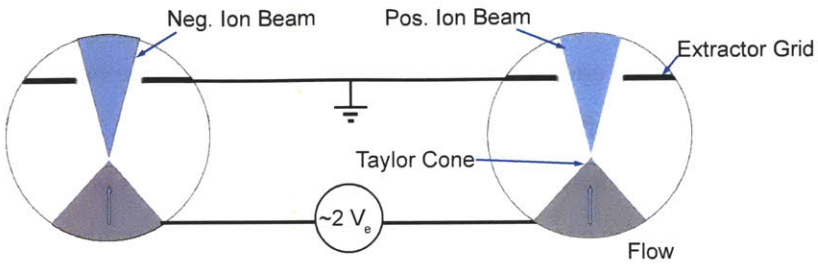

Figure 2-2: Simultaneous bi-polar emission from two ILIS such that no net current is emitted. Polarity alternation can also be used to suppress electrochemical reactions.

vated, experimentally and theoretically, that by alternating the emitter polarity at roughly 1 Hz, stable emission could be sustained without exceeding the electrochemical window of the substrate (tungsten) and ionic liquid (EMI-BF_4) system. Here, capacitive charging of the electrochemical double layer is presumed to be interrupted, and the polarity reversed, prior to significant electron transfer across the interface. However; more recent results of Castro[38] suggest that this solution could be restricted to ionic liquids, such as EMI-BF_4 which operate with nearly identical beam currents in both positive and negative modes. Any Faradic current will be detrimental to ILIS operating as thrusters regardless of if the dominant effects are propellant loss by contamination with reaction products (as observed by Lozano[37]) or alternations in performance due to changes to the interface structure. A more targeted approach to understanding this issue can be achieved using a potential probe to measure the transient potential between the ionic liquid and metal while the emission occurs. A preliminary approach at using this technique has been applied during this research comparing the response for tungsten and nickel substrates[61]. The ability to emit both positive and negative ions allows for this electrochemical requirement to be met using a configuration as in Figure 2-2, where the applied potential can be varied periodically. This configuration also prevents spacecraft charging by implicitly operating with a net neutral beam.

The metrics above paint ILIS as thrusters in a excellent light, however; both the specific impulse and efficiency are relative measures. The most important thing a spacecraft thruster must do is provide thrust. Typical ILIS can emit no more than 1 μA at potentials around 2 kV, the resultant thrust would be very small ~ 0.1 μN. Direct thrust measurements have also been made for both colloidal and LMIS thrusters yielding somewhat larger thrusts, for

example up to $\sim 50\mu N$ and $35\mu N$ per emitter have been measured for colloidal[56] and LMIS thrusters[62] respectively. Although these levels of thrust may be suitable for highly specialized scientific missions, for example an upcoming ESA mission[63, 55, 30], obtaining significantly larger thrusts from ILIS requires a closer look at the practical aspects inherent in the devices.

2.2.2 Motivation for Arrays and Porous Feeding

One option for increasing the thrust from ILIS would be to simply increase the voltage using a single emitter, an attractive option promising both increased thrust and specific impulse. For example Cohen[64] suggested a colloidal thruster with an ambitious 100 kV of total accelerating potential. However; this technique would inevitably lead to electrical insulation problems, power limitations or both.

Instead, research has been largely focused on creating arrays of emitters simultaneously firing in a uniform manner. From an array implementation standpoint, ILIS offer a number of advantages compared with both colloid and LMIS thrusters. Ionic liquids, with zero vapor pressure, can be stored as liquids without any heavy pressure tanks and fed passively to an emission site while exposed to the vacuum of space the entire time. The benefits of this configuration were discussed in the context of a CubeSat in Chapter 1. Liquid containment is then restricted to a matter of electrical isolation[50].

When multiplexed in arrays, the net thrust is expected to scale with the number of active emitters baring any space charge or hydraulic interactions. The effects of space charge on emission from non metals have been considered at an order of magnitude level by Higuera[65]and more rigorously by Lozano[22]. While Higuera found that space charge effects should be negligible for emission from a single Taylor cone, Lozano identified that space charge interactions can be expected for arrays when Taylor cone spacings are small ($<\sim 10\mu m$). However, spacings of that magnitude are not required for useful arrays of ILIS as thrusters. With thrusts on the order of 0.1 μN per emitter, an array of emitters modestly spaced 350 μm apart would produce roughly 1 N/m^2 of thrust density, already comparable to existing grided ion thrusters[11]. In terms of actual thrust, a pair of 1 cm^2 thruster models (two are required to maintain neutrality) could then produce roughly 200 μN of total thrust. As discussed in the introduction, for a small CubeSat or nano-satellite, this amount of thrust far exceeds drag in typical LEO orbits allowing for useful propulsive

manoevers[66].

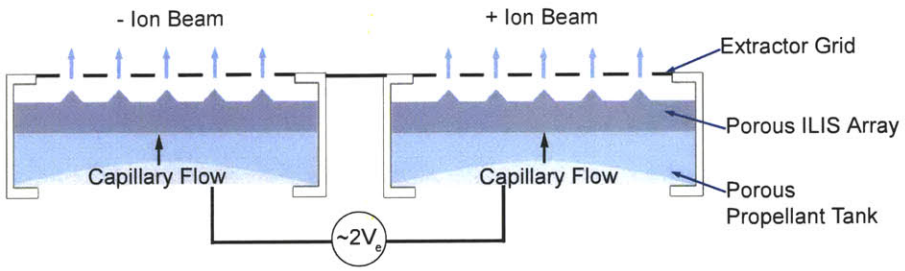

Figure 2-3: A complete thruster system will employ two emitter array modules, firing at opposite polarities. Each module could have an independent passive propellant supply.

Traditional, externally wetted, ILIS can be difficult to operate uniformly and continuously when applied to high density arrays[50, 67]. Another option would be to use porous materials to supply liquid to the emission site. The concept is analogous to a candle where, as wax is burnt away at the flame, a fresh supply is provided by the wick at a rate dictated by capillary forces alone. If a propellant is applied to a porous electrospray substrate, it will eventually saturate the material[68]. Legge first demonstrated that porous emitters could support purely ionic emission when saturated with ionic liquids[69]. Here sufficiently low propellant feed rates were achieved passively by the balance between internal capillary pressures and the meniscus pressure sustained by an applied electric field. These sources are hereafter referred to as porous ILIS.

Using bulk porous substrates, a thruster system using porous ILIS would resemble the configuration shown schematically in Figure 2-3. In this thesis, we develop and implement a technique for fabricating arrays emitters for porous ILIS in a scalable and repeatable manner such that they can be operated as in the figure.

2.2.3 Previous Porous Ionic Liquid Ion Sources

The works of Legge[70, 72, 69], and more recent results by this author (included in Chapter 7 and reported in[73, 71]), have demonstrated that 30 % porosity bulk porous tungsten emitters are characterized by wide ranges of stable ion currents compared with externally wetted ILIS. Specifically, currents from 100's of nA up to 10 μA per tip have been observed from porous emitters, with tip radii measuring roughly 10-30 μm, beginning at startup potentials around 1.5 kV. This can be compared with a limit of $\sim$ 1 μA from externally

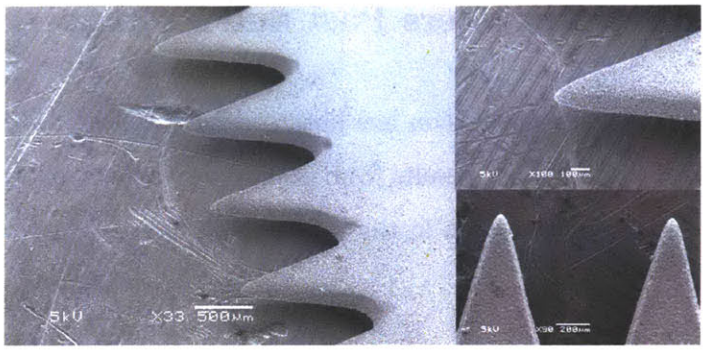

Figure 2-4: Examples of flat emitters, similar to those of Legge[70], fabricated as part of this research[71].

wetted emitters (see for example[38]). This distinction has primarily been attributed to a reduced total flow impedance in porous emitters[38, 70]. De-stabilization of externally wetted ILIS, presumably due to liquid starvation where the pressure drop due to flow impedance becomes comparable to available electric traction, has not been observed with porous emitters. Instead the maximum beam current has been limited by the device design (eg. electrical insulation) or available equipment. Prior to this research, successfully fired porous ILIS arrays have been fabricated from porous tungsten using a flat arrangement, as in Figure 2-4, originally developed by Legge[69, 72, 70] and tested further during this research[71]. Using a flat porous array, Legge directly measured thrust levels up to 0.1 μN per emitter[70]. In that research ILIS were achieved using EMI-BF_4, EMI-Im, EMI-Beti and PMI-$(C_2F_5)_3PF_3$ wetting porous tungsten, with only the purely ionic regime observed using time of flight spectroscopy during all cases.

Section 2.4 introduces the operating principles of the planar porous ionic liquid ion sources developed in this research.

2.3 Electrospray Thrusters Past and Present

Using electrospray sources for propulsion has been seriously considered since, at least, the 1960's. Presented here are some key results from preliminary arrays followed by an overview of the more recent or ongoing research in the field.

2.3.1 Early Emitter Arrays

The use of colloid emitters for electric propulsion saw a period of development and interest from ~1960 to ~1975, with little development occurring thereafter until the mid to late 1990's (see below). Clark[74] provides an overview of the state of the art technologies emerging towards the end of this initial phase of electrospray propulsion. The thrusters of this time typically employed high extraction potentials (5-15 kV) to achieve 100's of μA and up to 4400 μN of total thrust[74, 75].

Examples of the technology include Cohen and Huberman[64] who investigated using 10's of capillary tubes in the early to mid 1960's, with 100's of μN thrust levels achieved at modest specific impulse values (<800 s) at extraction potentials <7 kV. In order to increase the specific impulse those researchers made a series of trials with an extremely ambitious post extraction acceleration potential set to 100,000 V. That research identified time of flight spectrometry as a useful tool in estimating thrust by providing a break down of specific charges within the beam.

Perel et. al experimented with both 10's of pressure fed capillary needles[24] and annular colloid thrusters[76] where a continuous thin annular meniscus was investigated as an alternative means of increasing thrust density but avoiding alignment of numerous capillary tubes. That group also performed experiments with simultaneous emission of both positive and negative emitters (using different propellants) to achieve beam neutralization[24]. The annular thruster of Bailey et. al[77], was similar in design (but slightly larger) than that of the Perel group but was novel in that propellant was semi-passively fed. In order to measure thrusts directly without propellant lines (which may have interfered with the measurement), that group dropped propellant from an externally controlled overhead dispenser into an intermediate reservoir from which propellant was fed by capillarity and gravity to the downward orientated emission site (an annulus).

2.3.2 Recent and Ongoing Efforts for Microfabricated Electrospray Thrusters

Colloid (droplet)and Mixed Regime (ion/droplet) Thruster Arrays

Recently, Busek Co. of Natick, MA has completed development of a flight qualified colloid thruster designed for the Space Technology (ST7) mission, part of the ESA LISA (Laser Interferometer Space Antenna) Pathfinder spacecraft[55, 78, 63, 60]. This thruster was designed primarily to achieve and demonstrate high resolution thrusts and low thrust noise levels, rather than attributes such as power efficiency or specific impulse. Thrust levels from 5 to 30 μN with 0.1 μN resolution and 0.1 $\mu N/Hz$ noise levels were required[55]. The final thruster modules employ 9 capillary type emitters actively fed from a precise feeding mechanism using upstream pressure to drive the flow rate. Positive emission of droplets is neutralized by an external, field emission, cathode neutralizer[55]. The thruster was characterized directly, using the method described by Gamero-Gastano for a 6 emitter iteration of the thruster, using a torsional balance[78].

Krpoun and Shea[79] have developed fully integrated bipolar thrusters using arrays of silicon capillaries filled with ceramic micro-beads designed to emit in both the mixed droplet/ion and purely ionic regimes using ionic liquid propellants. This design uses a pressurized feed system to drive a prescribed flow of ionic liquid, with the micro-beads serving to increase hydraulic resistance and obtain the low flow rates required for ion emission. This example demonstrates an alternative application of porous structures than that proposed here in that the flow rate is actively controlled, not relying on capillary action to govern the flow. The beads cease below the tip of the capillary which is presumed to support a single Taylor cone. Recently, Lenguito[80], characterized emission from a similar design. Here, a 7 emitter array fabricated using the procedure of Gomez and Deng[81] was tested. These arrays have employed various solutions of ionic liquids dissolved in ethylene glycol, and formamide. Those experiments confirmed that at low flow rates, purely ionic emission could be achieved; however operation in this regime was dismissed as higher thrusts were desired from the low density array[80].

Purely Ionic Thruster Arrays from Non-Metal Propellants

Velasquez[82, 67, 83] created planar arrays of externally wetted emitters using silicon. The emitters, up to 1024 spread over a 0.64 cm^2 area, were fabricated by plasma etching on

silicon. In this design, propellant was pooled amongst protruding tall emitters with feeding achieved by external wetting. Ablative emission tests (with no extractor grid) were performed and confirmed emission could be achieved. Emission levels on par with individual externally wetted emitters were observed (100's of nA). Based on the performance of that design, Velasquez[83] suggested developing a porous planar emitter array similar to that developed here. However; as with the 'porous' colloidal thrusters above, Velasquez suggested a pressure fed design, rather than a passive, capillary driven system.

More recently Gassend[50, 84] developed planer emitter arrays similar to those of Velasquez but incorporating aligned electrostatic grids. The array supported purely ionic emission from over 500 emitters with up to 1 μA of emission per emitter[84]. This design was prone to inconsistencies in the emitted current over time which were attributed to the non uniform wetting characteristics to be expected from an externally wetted configuration. Again, the thruster propellant supply was limited to a drop/pool spread over the array surface. That author suggested passive feeding with porous materials as a solution for achieving constant and stable operation[50].

Using porous emitters, Legge demonstrated a flat (as in Fig. 2-4) 49 emitter array with measurable thrust levels on the order of $0.1\mu N$ per emitter while operating in the purely ionic regime at specific impulses around 3000 s[70, 72]. More recently, as part of this research, a demonstration thruster using 80 flat porous emitters spread over 8 arrays with 10 emitters per array has been tested, see appendix A. This low density array had an effective packing density of ~ 0.7 tips per mm^2. The laboratory thruster was specifically developed to confirm that two microfabricated silicon grids could simultaneously control both ion current and beam energy by a downstream variation in beam potential.

While successful in principle, these Legge type emitter arrays are subject to numerous inaccuracies and practical challenges inherent in assembling numerous sheets of flat emitters while maintaining complete accuracy in position, with respect to the extraction grids, across the entire thruster. Furthermore, maintaining coupled, uniform flow to the emitters requires a unified propellant supply, the most natural being a porous support for the arrays themselves. Both of these practical accounts contributed to desire in this research to use planar arrays, like those developed by Gassend and Velasquez but fabricated from a bulk porous material capable of supplying constant, and spatially uniform flow from a rear fuel supply to an array of emitters with high positional accuracy.

Liquid Metal Ion Source Thrusters

Recently two LMIS thruster designs have seen significant development in bids to provide propulsion for the ESA LISA mission[63]. Tajmar et. al[85, 62, 30] have been developing FEEP thrusters using liquid indium propellants. Meanwhile, Biagioni et. al.[86] have developed liquid cesium thrusters at Alta, Italy.

The most recent iteration of the Tajmar group design[30] is particularly relevant to this research in that they have developed a method for fabricating rings of porous tungsten emitters using a sintering process. This design exploits the low (but not negligible) vapor pressure of liquid indium[60]. A 28 emitter thruster has been fired achieving thrusts from ~ 1 to $\sim 450\ \mu N$, or $\sim 16\ \mu N$ per emitter at currents up to $100\ \mu A$ per emitter. High potentials, between 5 and 16 kV were reportedly required to sustain the emission. That thruster was successfully fired for 500 hours, during which time adjustments to the voltage were able to sustain steady emission, excellent thrust resolution and low thrust noise throughout the test.

The Alta, cesium thruster has been reported to achieve between 0.1 and 200 μN, with a specific impulse up to 8000 s[86]. The thruster employs a "surface tension" propellant tank which may be similar to the passive, capillary fed, systems desired in this research. These thrusters have been fired for continuously for over 1000 horus without significant performance degradation.

2.4 Planar Porous Ionic Liquid Ion Source Operation

In this research, planar emitter arrays, similar to the silicon arrays of Gassend[50] and Velasquez[83] have been fabricated from porous metals. As motivated above a successful result would yield both the promising emission characteristics observed by Legge from flat porous tungsten and allow for a compact device using planar arrays which support continuous propellant flow.

These porous ILIS are intended to be operated beginning with saturated porous media while a reservoir of additional propellant, if necessary, is placed far from the emitters and coupled through the porous medium. Without an active feeding mechanism, the applied electric traction must serve two purposes. First it must overcome the meniscus surface tension and internal liquid pressure to form a Taylor cone, as in equation 2.1, and second, sustain a pressure difference between the meniscus and the porous bulk such that $\Delta P = ZQ$. Where ΔP is the sustained pressure difference, Z the hydraulic impedance of the arrangement and Q the flow rate driven by ion evaporation. The static pressure, which influences the first requirement, can typically be written as in equation 2.4 where r_p is a length scale for the flow channels within a porous structure and α depends on both the wetting characteristics (contact angle) and pore structure.

$$P_c \sim -\alpha\gamma/r_p \tag{2.4}$$

Numerous approximations for the the term α can be found in the literature (for example Mason[87] or Lago[88]). For liquids which wet materials with small contact angles ($<\sim 45^o$) those estimates typically predict $\alpha \sim O(1)$ with little dependence on contact angle.

2.4.1 Taylor Cone Formation on Porous Emitters

Although it has previously been assumed that porous ILIS support a single Taylor cone on each emitter[70], this has not been confirmed through direct measurements. Conversely, physical evidence gathered during this research (see sections 7.6 and 7.6.3), suggests that multiple Taylor cones, or at least emission sites, could be sustained on each emitter. Considering equations 2.1 and 2.4, if α is order unity and r_p is much smaller than the emitter length scale (the tip radius), P_c will no longer be negligible throughout the meniscus. Rather, when the meniscus radius grows beyond the scale r_p, the term due to the meniscus curvature,

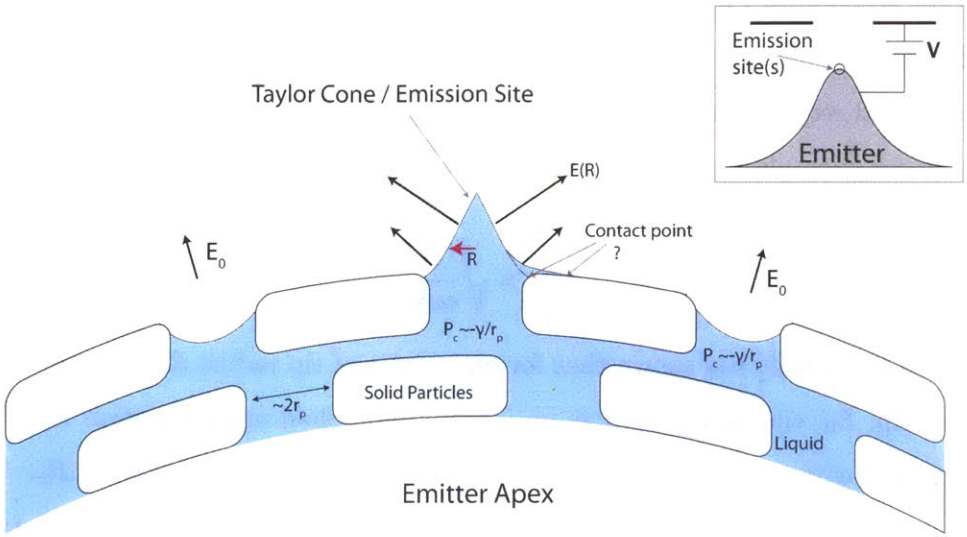

Figure 2-5: A possible schematic showing Taylor cones/emission sites localized to the the pores at the apex of a porous emitter. The force balance at the surface of the meniscus may have a significant contribution from the internal pressure. The description of the meniscus surface, for a example the contact/anchor point on the solid particles, is not completely understood.

γ/R no longer dominates. This suggests that at a length scale on the order of r_p the meniscus would deviate from that expected for an idealized, 49.3^o Taylor cone. Taylor cones with considerable, negative, internal pressures have been considered in more detail by de la Mora[19] who showed the solution to be convex, becoming perpendicular to the far field as the internal pressure begins to dominate. Thus a single Taylor spanning multiples of r_p may be unlikely. Instead multiple cones could form wherever the local field is sufficient to destabilize the meniscus and form a Taylor cone. This scenario has been illustrated in Figure 2-5. The exact size and distribution of these sites could depend on the combined effects of, for example, fluid hydraulics, space charge and electrostatics. Multiple emission sites may help explain why theoretical estimates for the emission current from the meniscus of ILIS made by Higuera[65] (10's of nA) are far less than those observed. If many sites could be supported on each emitter, the measured net current would increase accordingly.

In section 2.1, the minimum potential for forming a Taylor cone was given by equation 2.2. This relation can be modified for a porous emitter. Equation 2.2 can be derived by considering a meniscus just prior to forming a Taylor cone to be spherical with a characteristic radius R_0. The instability then takes the form of equation 2.5 and states that the applied

electrostatic stress must exceed that due to surface tension. Here E_0 is the applied field, and R_0 is a length scale for the meniscus size. A similar expression can be derived by considering the electric field required to induce a dynamic instability on a stressed unsupported liquid surface, see for example Khayms[21] for details.

$$E_0 > \sqrt{\frac{4\gamma}{\epsilon_0 R_0}} \tag{2.5}$$

Martinez-Sanchez[8] has shown that for an emitter of tip radius R_c, the electric field at an emitter tip, E_0, can be modeled as an infinite paraboloid using equation 2.6. Here the emitter is approximated by an infinite paraboloid with radius of curvature R_c. Hence it does not account for the tip height and depends only on the applied potential V, tip radius R_c, and, weakly, on the tip to extractor spacing L. The estimate is simplified further in that it does not account for modifications to the field due to an extractor aperture located directly above each emitter.

$$E_0 = \frac{2V/R_c}{ln\left(\frac{4L}{R_c}\right)} \tag{2.6}$$

If, as is the case for a capillary type emitter, the tip radius and meniscus length scale are roughly equal, $R = R_c = R_0$, combining equations 2.6 and 2.5 recovers the starting potential condition of equation 2.2. However; if the emission is localized to the pores, the length scale for the meniscus goes like $R_0 = r_p$, the pore length scale, while the electrostatic field remains scaled by R_c. Again combining equations 2.6 and 2.5, equation 2.7 now results. We see that the starting potential is similar to equation 2.2 but modified by a factor of $\sqrt{R_c/r_p}$.

$$V_{start} = \sqrt{\frac{\pi\gamma R_c}{4\epsilon_0}}\sqrt{\frac{R_c}{r_p}}ln\left(\frac{4L}{R_c}\right) \tag{2.7}$$

Legge achieved emission from porous emitters roughly 5-15 μm in radius with EMI-BF_4 propellant using porous tungsten with typical pores $\sim$ 0.5-2 μm in size. The emitter to extractor distance was stated to be small, but not measured directly, while relatively large extractor orifices (1.5 mm[72]) were used. Referring to table 2.1 and using equation 2.7, the estimated starting potentials are roughly 0.9 to 2.7 kV over this range of tip radii for a logarithmic correction factor of 3 (for $4L/R_c \sim 20$). Experimentally, Legge observed starting potentials between roughly 1 and 1.5 kV, indicating that equation 2.7 could generally be

an overestimate for the required potential. Without the correction factor for porous media, equation 2.2 yields starting potentials between $\sim$ 0.4 and 0.8 kV. It should be stressed that since both the porosity correction factor ($\sqrt{R_c/r_p}$) and logarithmic correction for the emitter to extractor spacing are often of comparable magnitude it may be difficult to discern the effects.

For ILIS intended to operate with a specific impulse in the 3000 s range, operating potentials on the order of 1-2 kV are desirable. Equation 2.7 suggests that for a given porous material, operation at these potentials will require emitters with tip radii varying as the root of the pore dimensions. Specifically, if the logarithmic factor can be taken constant at $\sim$ 3, and a typical value for γ is assumed, solving for the emitter radius yields $R_c \sim$ 0.8-1x10$^{-2}\sqrt{r_p}$, or to first approximation $R_c \sim 10\sqrt{r_p}$ when both lengths are in μm. Assuming the logarithmic factor remains constant may be reasonable as it is akin to assuming the extractor geometry is scaled proportionally to the radius R_c. In the next chapter, several possible fabrication schemes will be discussed which yield porous structures of varying degree. For some techniques, 10's of nm scale pore features result which, according to this argument would require tip radii on the order of 1 μm. At this scale, hydraulic impedance (see below), could begin to limit the emission current range or stability. It can be argued that for such small length scales, direct ion evaporation could occur from the liquid menisucs[22]. However; the strong fields predicted by equation 2.6, $\sim$ 1 V/nm, could also begin to yield unwanted electron emission from the substrate, as suspected by Gassend using externally wetted silicon emitters[50].

2.4.2 Electrostatics for Emission and Field Enhancement from Planar Emitters

From an electrostatic point of view the emitters serve two purposes. First they must support strong electric fields such that one or more Taylor cones will be induced. and second they are required to provide sufficient field enhancement to localize all emission at the emitter tip. This second requirement is necessary to prevent unguided emission from occurring from points other than the emitter tip. In this research, high density arrays of microfabricated emitters which emulate previous, per emitter, results are desired. From a packaging and alignment perspective, planar arrays are the natural geometry for this goal. However; rather than simply targeting a tip radius (eg. $\sim$ 15 μm for μm scale pores), the complete

geometry must be considered in more detail and could impact the choice of fabrication scheme. In particular, the height of the emitter, the distance from the apex to the supporting substrate, could be small and have adverse effects on the field. For very tall emitters, like externally wetted emitters or the porous emitters developed by Legge, equation 2.6 provides a reasonable estimate for the electric field strength at the emitter tip.

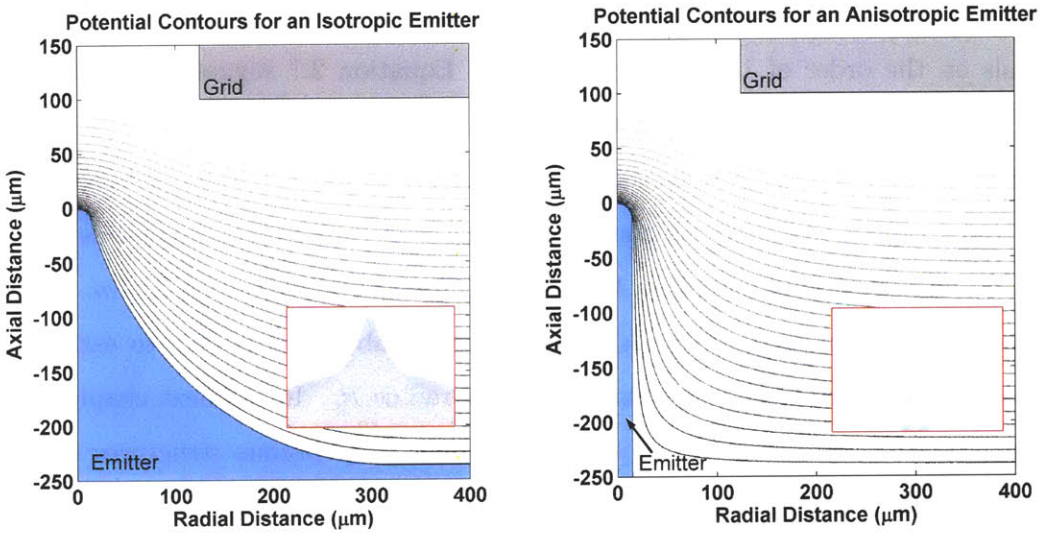

(a) Contours for an emitter geometry described by an isotropic profile terminated, tangentially, by a 15 μm diameter spherical tip.

(b) Contours for an emitter geometry described by an anisotropic (vertical) profile terminated, tangentially, by a 15 μm diameter spherical tip.

Figure 2-6: Numerically simulated contours of constant electric potential for a sample case where the emitter heights (from tip to base) are 250 μm.

To explore the impact of the geometry, the electric potential distribution has been calculated numerically for two emitter profiles. First, as in Figure 2-6(a), an isotropic profile, and second, Figure 2-6(b), an anisotropic (vertical) profile both terminated tangentially at a 15 μm spherical tip. For this demonstration a 200 μm diameter grid was positioned 100 μm from the apex of the tip. The electric field at the apex of the profile, normalized by equation 2.6, was then calculated for varying emitter heights and plotted in Figure 2-7(a). For emitters over $\sim$ 150 μm tall, the calculated fields exceed E_0 and become relatively steady. For tall emitters, the fields exceed E_0 by 10-20 %. This discrepancy arises because these emitters have assumed spherical tips, whereas equation 2.6 describes the field for an infinite paraboloid.

The second requirement for emitters, to ensure the emission is localized at the emitter apex, can also be a dominant factor influencing the design. As a metric for this requirement,

consider the ratio of the electric field at an emitter apex compared with that far from the emitter, where the geometry is roughly planar and the electric field approaches a minimum equal to $V/(d_{sg}+h)$, where $d_{sg}+h$ is the net electrode spacing. This ratio has been plotted, again as a function of emitter height, in Figure 2-7(b). The figure illustrates that good localization, for example an order of magnitude, requires emitters to be, again, over ~ 150 μm tall.

These solutions have been derived using Laplace's equation, ignoring any space charge. The relations are therefore linear and can be extended to any geometry if all values are scaled together. Scaling the grid geometry would be reasonable as a typical design is based on beam angles rather than absolute distances. Hence a more general result can be extrapolated from this example. Specifically, emitter heights more than 10 times the tip radius are required to achieve strong fields and good field enhancement compared with the field between emitters.

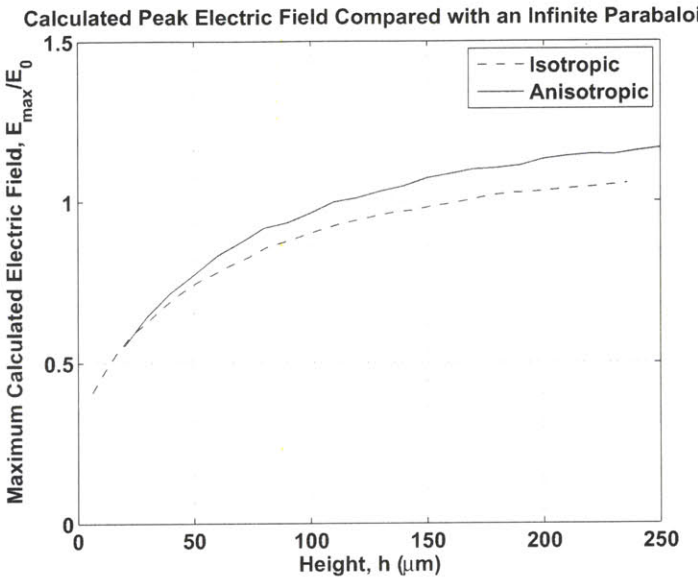

(a) Ratio of the numerically calculated electric field at the emitter apex, E_{max}, to that from equation 2.6, E_0, for for two simple geometries.

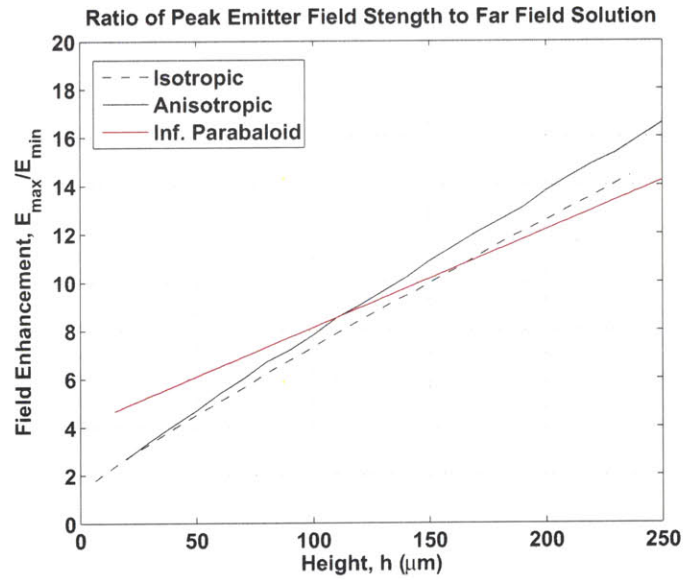

(b) Ratio of the electric field at the emitter apex, E_{max} to equation that far from the emitter, E_{min}, where a planar geometry has been assumed valid.

Figure 2-7: Variation of electrostatic parameters depending on emitter height. Tall emitters are required to both establish suitable electric fields and ensure field enhancement, necessary to prevent unwanted emission.

2.4.3 Propellant Flow

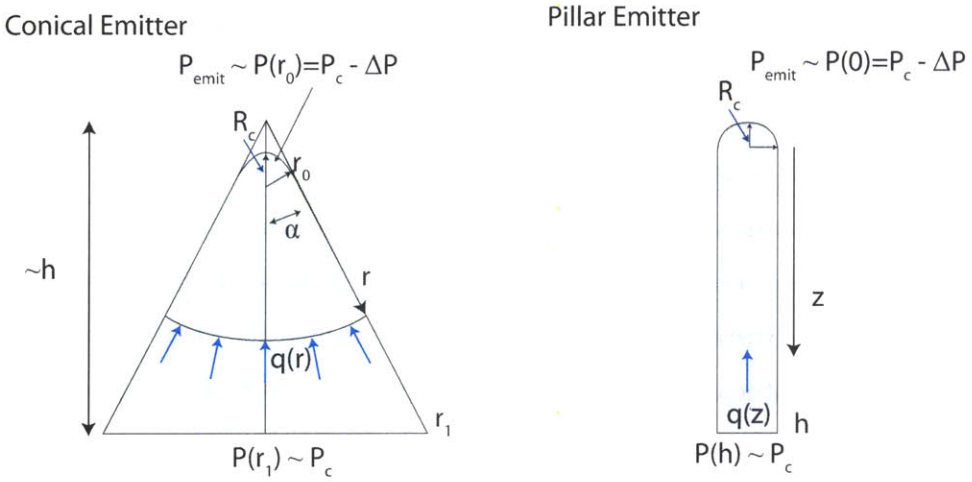

Figure 2-8: Geometries used to estimate the pressure drop, between the base of the emitter and near the emission site(s) for conical and pillar type porous emitters .

Porous ILIS emitters are passively fed, relying on the applied electrostatic field to induce a current and sustain it by maintaining the electrified meniscus while the internal pressure at the emission site is reduced due to the flow. The pressure drop, between the porous bulk and the emission site, can be approximated using Darcy's law, equation 2.8. Here, $\vec{q_s}$ is the volume flow rate per unit surface area (m/s), κ is the material permeability, μ is the fluid viscosity and ∇P is the pressure gradient.

$$\vec{q_s} = -\frac{\kappa}{\mu}\nabla P \tag{2.8}$$

$$q_s(r) = -\frac{Q}{2\pi r^2(1-cos\alpha)} \tag{2.9}$$

$$\begin{aligned}
\Delta P &= -\frac{\mu}{\kappa}\int_{r_0}^{r_1}\frac{-Q}{2\pi r^2(1-cos\alpha)}dr \\
\Delta P &= \frac{\mu}{2\pi\kappa}\frac{Q}{1-cos\alpha}\left[\frac{1}{r_o}-\frac{1}{r_1}\right] \\
\Delta P &= \frac{\mu}{2\pi\kappa}\frac{Q}{1-cos\alpha}\left[\frac{tan\alpha}{R_c}-\frac{cos\alpha}{h}\right]
\end{aligned} \tag{2.10}$$

For a porous conical emitter the pressure drop between the bulk media and emission site has been estimated in equation 2.10. Here the pressure drop from a point r_1 up to a point r_0 has been calculated for an emitter height h and half angle α. The scenario is shown schematically in Fig. 2-8. The flow distribution has been estimated by assuming uniform radial flow through a spherical cap, such that equation 2.10a) approximates $q_s(r)$. As shown in the figure r_1 is the radial coordinate at the base of the emitter, equal to $h/cos\alpha$. Here the bulk pressure is assumed to be P_c, a reasonable approximation so long as $h >> R_c$. The pressure drop has been terminated at a point r_0, equal to $R_c/tan\alpha$, the point where the conical formation transitions to a spherical tip of radius R_c. The calculated pressure drop ΔP is thus an estimate of the difference between the internal fluid pressure near the emission sites and that in the bulk.

Similarly for a tall pillar, of height h and radius R_c, as in right side of Fig. 2-8, the pressure drop between the emitter base and spherical cap is approximated in equation 2.11.

$$\Delta P = \frac{\mu}{\pi\kappa}\frac{Qh}{R_c^2} \tag{2.11}$$

The pressure in the bulk, P_c, can be estimated by equation 2.4, above. For a porous medium, the permeability can be approximated using, for example, the Kozeny-Carman Formula[89, 90], equation 2.12. The effect of contact angle is again considered to be small for wetting fluids[91]. In this equation, D_{eff} and ϕ_p are the effective particle diameter and porosity for a porous medium. The porosity is the ratio of open space, or void, volume to total volume for a porous material. For sintered metals using small initial particles, like the tungsten used previously for porous ILIS, pore dimensions and porosities of $D_{\text{eff}} \sim$ 1-5 μm and $\phi_p \sim$ 20-50 % respectively are typical. These values correspond to a wide range of permeabilities from $\sim$ 1x10$^{-16} m^2$ to $\sim$ 1x10$^{-13} m^2$. For example, in the porous nickel used to fabricate arrays in this research (see section 5.4), the typical particle sizes were $\sim$ 5-10 μm and the measured porosity was 45 %, corresponding to a permeability of around 0.5-1.5x10^{-12} m^2. The porous tungsten used by Legge consisted of particles a few μm in size with a 30 % porosity yielding an estimated permeability of $\sim$ 0.3-5x10^{-15} m^2.

$$\kappa = \frac{D_{\text{eff}}^2}{180}\frac{\phi_p^3}{(1-\phi_p)^2} \tag{2.12}$$

The relationship between effective particle size D_{eff} and the pore scale r_p is not trivial.

However; as reviewed and considered analytically by Glover[92], in so far as roughly spherical particles can be assumed, the approximation in equation 2.13 can be applied.

$$\begin{aligned} D_{\text{eff}} &\sim 2\Theta r_p \\ \Theta &= 0.87\phi_p^{-3/2} \end{aligned} \tag{2.13}$$

The emitters fabricated in this research are intended to operate at emission currents on the order of 1 μA per emitter. For typical ionic liquids (eg. EMI-BF_4), assuming an even distribution of monomer and dimer species, the equivalent net flow rate can be approximated from the parameters in table 2.1 to be $\sim$ 1.7 pL/s. Representative viscosities and densities for ionic liquids are $\sim$ 50 cP and $\sim$ 1.2 g/cm^3 respectively. Typical Reynolds numbers for 100's of nm to 10's of μm length scales and this flow rate are low, 10^{-3} - 10^{-7}, justifying use of Darcy's law.

These relationships can help determine if a selected porous material and emitter geometry may be impacted by fluid viscosity. In section 2.4.1, it was motivated that following $R_c \approx 10\sqrt{r_p}$ (all in μm) would yield emitters with starting potentials around 1-2 kV. In the following section, it was motivated that for emitters with $h \approx 10R_c$, sufficient field enhancement and strengths on par with equation 2.6 can be achieved.

Consider a material with $r_p \sim 2.2$ μm such that $R_c = 15$ μm and $h = 150$ μm are reasonable target geometries for an emitter. The pressure drops through conical and pillar emitters for 1 μA of total current have been calculated using equations 2.10 and 2.11 respectively in Figure 2-9. A half angle of $\alpha = 25^o$ was used in the calculation. In addition, an estimate for P_c as a function of permeability has been plotted using equations 2.12 and 2.13 to correlate between permeability and pore scale, r_p, for porosities, ϕ, between 20 and 50 %. The finite thickness in the plot represents this range of porosities.

The particular geometry used to generate Fig. 2-9 was selected based on a pore dimension such that emission can be expected at 1-2 kV. Specifically, we chose $r_p \sim 2.2$ μm. For this scale, the material permeability can be estimated for a range of porosities using equations 2.13 and 2.12. For porosities from 20-50 %, typical of media considered in this research, the estimated permeability ranges from 1-4x10^{-13} m^2, as reflected by the dark grey vertical bar in the figure.

Recall that these scaling criteria have been based on achieving Taylor cone formation at

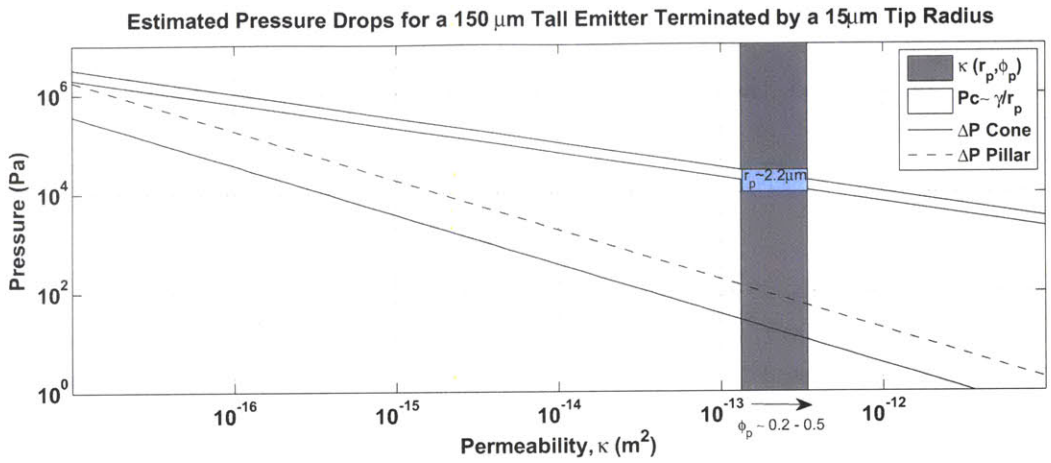

Figure 2-9: Estimated pressure drops required to sustain 1 μA of emission from an emitter 150 μm tall with a 15 μm tip as a function of the material permeability. P_c is an estimate for the internal pressure at a given permeability for porosities between 20 and 50 %. The emitter height and radius were selected based on a 2.2 μm characteristic pore scale. The range of permeabilities expected for a 2.2 μm pore scale over the same porosity range have been highlighted.

a point when electrostatic stress just exceeds $P_c \sim \gamma/r_p$. Hence, a reasonable condition for avoiding hydraulic limitations would be viscous pressure drops, ΔP, much less than P_c at a given operating condition. We see that for this specific case the predicted pressure drops at the selected operating pore dimension are much less than P_c. This emitter should not be starved, or limited by viscous losses through the structure.

As an alternative, consider a material process which yields $r_p \sim 22\ nm$. Here the same scaling relations used above lead to small emitters 15 μm tall with 1.5 μm tip radii in order to achieved starting potentials at 1-2kV. The permeability range for this pore scale and a 20-50% porosity range has again been plotted along with the calculated pressure drops to sustain 1 μA of emission in Figure 2-10. Here we see that the expected pressure loss and P_c are of similar order. For this material, the emission could be unstable or limited by hydraulics.

Cross Talk Between Emission Sites

The discussion above has only considered flow from a porous bulk, through an emitter to a point near the emission site. For a bulk porous material, much thicker than the emitter height and radius, the hydraulic impedance between emitters will be small relative to that

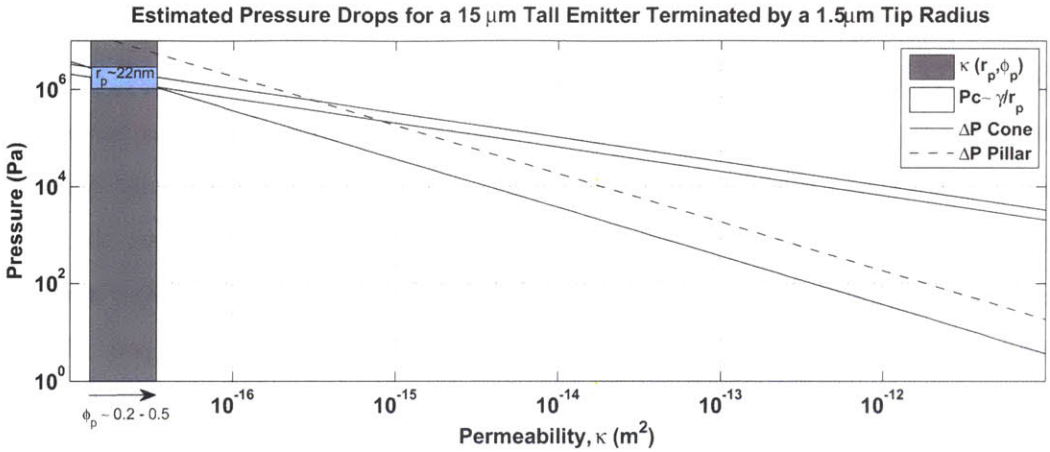

Figure 2-10: Estimated pressure drops required to sustain 1 μA of emission from an emitter 15 μm tall with a 1.5 μm tip as a function of the material permeability. P_c is an estimate for the internal pressure at a given permeability for porosities between 20 and 50 %. The emitter height and radius were selected based on a 22 nm characteristic pore scale. The range of permeabilities expected for a 22 nm pore scale over the same porosity range have been highlighted.

through the emitters themselves. As a result, activation or operation of one emitter will have little effect on the performance of another.

However; if multiple emission sites can be supported on a single emitter, hydraulic interactions between these sites may become significant. Referring to Fig. 2-5, both the process of forming and then sustaining emission from a Taylor cone at one pore could influence the behavior at adjacent pores. For example, to sustain emission at a given pore, the internal pressure within the meniscus and nearby pores would drop below the bulk value P_c. If significant, this could influence the effective minimum field required to form and stabilize cones at these adjacent pores. A more detailed understanding of the emission sites, including the coupled relationship between the hydraulics and electrical properties, would be required to determine if emission site interactions are important.

2.4.4 Space Charge Interactions

Emitted particles can have effects on the emission characteristics and surface electrostatics. For LMIS, where high currents from each emission site are typical these effects can be significant and are known to alter the electrostatics of the electrified meniscus[93]. It has previously been argued that for ILIS, space charge effects should not limit emission in the

purely ionic regime[65].

On porous ILIS with multiple emission sites, space charge interactions between the resultant beams could lead to, for example, enhanced beam spreading. Space-charge effects of this form have been considered by Lozano[22], who found that for relatively large emitter spacings, $\sim$ 10's of μm, these effects should not be significant. However; that analysis assumed a single Taylor cone per emitter. As discussed above, porous emitters may support multiple emission sites on the surface of an emitter tip measuring only a few μm. No analysis of these effects has been made here but the condition should be noted as it may, for example, play a roll in determining the density of emission sites on a single emitter.

2.4.5 Planar Porous Ionic Liquid Ion Source Conclusions and Discussion

This section has discussed the operation of porous ionic liquid ion sources within the context of this research. Specifically, the goal here is to fabricate porous emitter arrays where each emitter achieves performance levels comparable to previous efforts. That is, the ability to efficiently, and stably, extract $\sim$ 1 μA per emitter with potentials around 1-2 kV. The current, 1 μA, has been based on the results of Legge[70] and initial experiments performed here, section 7.2, which identified this order of emission as stable and relatively easy to achieve. The targeted potential range would allow for a reasonably large specific impulse while operating at voltages which, while challenging, are not too unreasonable for implementation within a MEMS package. Together, this type of performance would allow for useful thrusters like those discussed in section 1.5.

The simple scaling criteria established here are useful in assessing the suitability of porous media and fabrication schemes but should not be viewed as anything like a complete exploration of electrospray physics. We have focused on achieving emission at 1-2 kV and then assumed we can emit at $\sim$ 1 μA per emitter, but in the absence of viscous effects it is unclear what limits, or controls, the emission current. The simple and most obvious answer is that the voltage controls the current, this is true in practice but for a Taylor cone where the field becomes very large near the tip, and with the size of the Taylor cone apparently restricted by the length scale for the pores, the underlying mechanism is unclear. There are several options (eg. conductivity, space charge...) and some discussion, but not a definitive answer, has been made at end of the emission results section in Chapter 7.

As an example of why a better understanding of the emission limits would be useful, a

very reasonable counter argument to the hydraulic limitations mentioned above would be that for small emitters, many more of them could be packaged together. They could then be operated at lower currents, or equivalently flow rates, such that, per unit area, emission comparable to an array of larger 1 μA emitters is maintained. However; the current-voltage slopes for these devices tends to be very steep and can yield μA changes for relatively small (a few 100's of V) potential changes after startup. Since the arguments above have always assumed emission ultimately occurs at the tip of a Taylor cone, this I-V behavior may not change for a smaller emitter if all other geometries are scaled in turn. For a fabrication scheme which yields some, even very little, variability in emitter size, it may be difficult to build a device which ensures all emitters are operating at low currents due to the variable field strengths across emitters. Hence, operation at low currents per emitter may be challenging and may reduce the range of allowable potentials (specific impulse) for stable operation.

Chapter 3

Microfabrication Techniques for Porous Emitter Arrays

The aim of the previous chapter was to motivate that porous ionic liquid ion source arrays would constitute a contribution to the field of electric propulsion and establish some estimates for suitable geometries. The following four chapters are dedicated to fabricating porous emitter arrays in a manner conducive for future development as useful thrusters. In this chapter we review the requirements for a suitable fabrication scheme and discuss an assortment of possible techniques in this context.

3.1 Summary of Requirements and Basic Techniques

A successful fabrication technique must achieve a result which encompasses all of the following:

- An uninterrupted and uniform porous path from a propellant feed point to an array of porous emitters, whereby the material porosity must be either uniform or have a minimum at the emission site.
- Emitters which are uniform in height and radius across the device such that electrospray emission can be sustained at all emitters.
- No surface features/protrusions with radii of curvature $<\sim 100\ nm$ to prevent electron emission[50].

- Porosity, at the emission site, with pores much smaller than the desired tip radii, such that a clear tip profile can be defined which dictates the electrostatic distribution. To maintain consistency with previous devices, the range of achievable permeabilities should not be limited to values significantly smaller than used in previously tested porous ILIS ($\sim$0.3-8x10^{-15} m^2).

- Emitters with a geometry that induces sufficient field enhancement for moderate startup voltages ($\sim$1-2 kV). Specifically, tip radii satisfying $R_c \sim 10\sqrt{r_p}$ in μm and heights h of $\sim$ 10 R_c as motivated in sections 2.4.1 and 2.4.2.

- The capability to fabricate emitter arrays with a few emitters per mm^2 over dies on the order of 1 cm^2, to establish thrust densities which approach $\sim$ 1 N/m^2.

- The process must integrate with an overall packaging procedure ensuring electrical isolation and alignment with a matching array of apertures (the electrostatic extraction grids).

- A path, or connection point, for coupling the device to an external fuel tank of variable size.

- A clear and repeatable method for making electrical contacts with the device.

- A conductive substrate material.*

*This requirement is not absolute, in fact paper has been used as a combined wick and emitter substrate material for colloid electrospray[94], however, its applicability for use as ILIS has not been explored.

In general the available methods can be categorized as follows:

- Surface micromachining: Material is removed (etched) from a masked substrate with resulting emitters.

- Forming: Growing or depositing emitters such that the emitters are formed on a compatible substrate.

Meanwhile the porosity requirements can be achieved by methods that are either:

- Implicitly porous such that maintaining an uninterrupted and interconnected porous path between the backside of a substrate and the emitters results immediately.
  OR

- Compatible with existing techniques to introduce porosity within the material and complete a porous path from the feeding point to the emitters.

3.2 Previous Fabrication Techniques for Ionic Liquid Ion Source Arrays

Arrays of ILIS have been previously fabricated for both externally wetted and porous feeding. The general emission properties from these devices were discussed in section 2.3.2. Here we focus on the fabrication methods and their applicability to planar porous emitter arrays.

3.2.1 Externally Wetted Silicon Arrays

This method, including developments by Velasquez[67], Gassend[50] and Garza[95], exploited the significant heritage in using silicon for microfabricated systems (see for example Senturia[96]), primarily derived from the electronics industry. Emitters were fabricated using both roughly isotropic RIE (Reactive Ion Etching) and anisotropic DRIE (Deep Reactive Ion Etching). The arrays were then roughened by creating a 'black silicon' coating. The black silicon treatment resulted in primarily micron scale features along the emitter structures. Similar to a porous coating, these emitters relied on passive wetting to feed the emission site. However; as mentioned in the previous chapter, the resultant arrays were prone to inconsistent operation due to variations in the wetting characteristics as the propellant supply pool drained. Another issue, mentioned by Gassend[50], was the occasional tendency for unwanted electron emission from the silicon surfaces. This was confirmed to be field emission (through comparison with the Fowler-Nordheim equation) and may have been a result of the extremely sharp (100's of nm) features formed on the black silicon surfaces. Despite these concerns, this approach demonstrated that the use of established fabrication techniques can be beneficial in that many arrays of emitters were created, with high yields, without reaching the limitations of available techniques.

3.2.2 Electrochemical Etching of Porous Tungsten

Legge[70] created various 'flat' porous arrays from porous tungsten (70% dense made from particles $\sim$ 0.5-2 μm in size) using electrochemical etching. Here, bulk porous tungsten was patterned with a polyimide masking technique described in section 3.3. The selection of both tungsten and electrochemical etching stemmed from the success of that combination when applied to externally wetted needles by Lozano[36]. During Legge's etching process, which was similar to that of Lozano, the samples were immersed in a 1 N sodium hydroxide solution with an applied potential of 6 V for roughly 45 minutes. Legge identified that mass transport could influence the etch properties and experimented with a flow channel but did not observe benefits compared with a static solution[70]. Legge successfully applied the method for relatively low density linear arrays, like those shown in Fig. 2-4. However; in that work he noted that masking issues were a significant detriment to the process yields. Specifically contamination due to a tendency for photoresist and/or polyimide to penetrate into the porous layer during masking. Finally, even with a successful mask, uniformity was limited when applied to higher density arrays with non uniformities becoming significant as the emitter spacings approached $\sim$ 500 μm.

Legge attempted to apply this technique to planar arrays similar to those proposed in this research. Some promissing emitters on a few trial wafers were created but Legge noted significant wafer level non-uniformities and polyimide contamination[70]. Ion emission from those arrays was not attempted.

3.3 Masking Techniques

Many of the processes to be summarized below require a mask to either locally prevent etching (a positive mask) or allow forming (a negative mask), for growth processes. However; when applied to bulk porous materials, the standard practice of spin coating a liquid resist onto the metal wafer generally cannot be used as the resist would wick into the porous wafer rather than remain on the surface, as shown in Figure 3-1(a). This issue was identified by Legge[70] who proposed using a polyimide mask spun onto a wafer pre-saturated with photoresist. The photoresist could then be removed after curing and patterning the polyimide layer. This technique was successful but, as described above, typically had low yields and resulted in contamination of the surface to a depth of several pore diameters[70]. Alter-

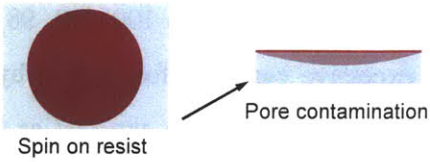

(a) Liquid, spin on, resists soak into porous materials causing contamination and poor surface coatings.

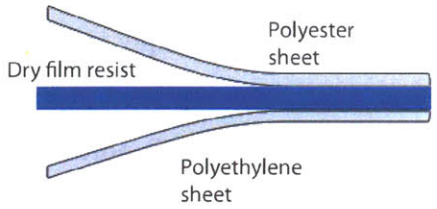

(b) Dry film resists are stored between polyethylene and polyester sheets before being laminated onto a surface

Figure 3-1: Masking porous materials must be achieved using techniques which limit contamination of the porous bulk, such as dry film resists.

natively dry film photo resists, Fig. 3-1(b), can be applied. Here, a polymer based resist is laminated onto samples using a combination of heat and pressure. The resist can then be patterned by photolithography and developed using relatively benign chemistries (typically $\sim 1\%$ sodium carbonate). Resists capable of withstanding both acidic (MacDermid Aquamer, Dupont Riston) and basic solutions (Dupont Vacrel) are available commercially, although with somewhat limited thicknesses and resolutions (15 μm for Riston FX515). A Vacrel mask was applied in the early stages of this research to create arrays similar to Legge with increased yields and reduced processing times[71].

3.4 Techniques Considered for Forming Porous Emitter Arrays

A number of fabrication techniques for the emitter array have been considered in conjunction with the requirements listed at the beginning of this section. The following descriptions are not intended to be definitive arguments against their successful implementation but rather to identify challenges in the context of the requirements for this project.

Porous Silicon

Here a post process technique could be employed whereby emitters which were previously formed in a manner similar to the successes of Gassend[50], Velasquez[67] and Garza[95] are treated to become porous. Porous silicon can be formed by electrochemical etching within an HF electrolyte[97, 98, 99]. See Smith[100] for a particularly detailed review of

the mechanisms involved. This technique could be effective, particularly as silicon wafers would integrate relatively simply into a complete thruster package. However; some potential concerns exist. The reported pores range from less than 1[97] to 100's[99, 98] of nm in size. These relatively small pores may lead to excessive capillary forces and hydraulic impedances or even electron emission if pore features at this scale are exposed at the surface. Electron emission from porous silicon has been previously reported[101]. Meanwhile larger pores may limit the allowable device thickness to $\sim 100 \mu m$[99] to prevent cracking. Therefore, for a coupled porous flow path from the wafer backside through to the emission site, mechanical issues may arise. Finally, ensuring homogeneity of the porous substrate as the total (emitter plus substrate) thickness approaches several hundred μm may complicate the process. Nevertheless, although not selected for this research, further investigation of porous silicon ionic liquid ion sources should not be completely discounted.

Reactive Ion Etching on Bulk Porous Substrates

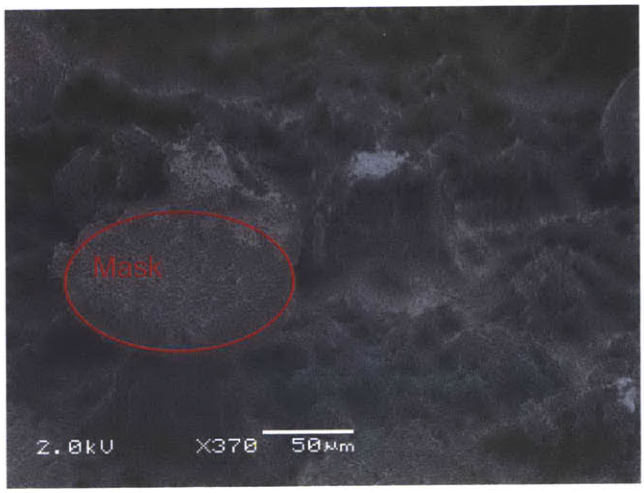

Figure 3-2: SEM image of a masked, porous tungsten sample etched using reactive ion etching in a SF_6 and O_2 plasma. The results are disconcerting, yielding irregular etching and a poorly defined feature under the mask.

A variation of the process used by Velasquez[67] and others, described above, could be applied to a masked bulk porous metal. Benefits of this technique include the selective nature of the etch, the dry conditions and the established tools available for use in processing. This method was explored as part of this project using bulk porous tungsten patterned with dry film photo resist (see below). The result shown in Figure 3-2 was disconcerting.

The tungsten sample was etched in a SF_6 and O_2 plasma following conditions reported by Tang and Hess[102] and Williams[103]. While the resist withstood the etch conditions, the etched surfaced was extremely rough and did not yield recognizable shapes. One possibility for this behavior could be the tendency for plasma based etching techniques to favor the crystal structure of the substrate, in this case a collection of randomly orientated sintered particles. These observations suggest that RIE etching of porous metals may not be feasible; however, investing in a larger study of the behavior over a range of conditions would be required before completely discounting this technique.

Micro-Powder Injection Molding

Injection molding of microparticles has been demonstrated as an effective technique by Tajmar et. al[30] in developing low density annular arrays of porous LMIS emitters. In this technique, fine particles (sub μm in size) are mixed with a binder and subjected to high pressures and temperatures. Finally the material is sintered and the binder removed through a combination of thermal and chemical processes[104]. Applied to this research, this technique could be employed to simultaneously fabricate a substrate and the emitter tips by injection moulding into a prefabricated mould. This method would be similar to the approach taken by Fu et al.[105] who developed porous cylindrical columns together with a porous substrate material. That group has noted a variability in porosity levels between the substrate and emitters[104] which would need to be well understood if applied to this research. As in the work of Tajmar, the completed emitters would likely require a postprocessing electrochemical etching step in order to create sharp emitters from the dull columns. Thus, although promising, this technique would still require an understanding and characterization of electrochemical etching and could benefit from the research undertaken here. Finally, a method for implementing this technique into an aligned, integrated grid package is not implicit and would add to the complexities involved in maturing the technique.

Electrochemical Growth

Here columns of porous material could be electrochemically grown by localized electrochemical deposition. Specifically, a relatively sharp counter electrode is positioned a short distance above the substrate material so as to localize the potential distribution and hence

the deposition. Yeo et. al[106] have demonstrated this technique by depositing nickel onto a copper surface. There columns up to ~120 μm in diameter and 100's of μm tall, were created with bulk porosity levels up to 42 %. No details concerning the uniformity of the porosity were provided. Similarly Jansson et. al[107] applied the technique to create nickel structures with very small $\sim$ 5 μm base diameters on a nickel substrate. The distribution of features sizes between those works suggests this method could be suitable for the range of length scales of interest here. A benefit of this technique is the ability to create features without a mask since the position is fixed by a locally high field strength due to the sharp counter electrode. For this research, in creating arrays, significant development would be required in both:

i)Identifying a method for creating multiple emitters, for example by using an inverted solid array as the counter electrode, or accurately positioning a single counter electrode repeatedly over the substrate and,

ii)Applying the technique to a porous surface such that a connected porous path can be established between the bulk and the emission site.

Physical Deposition

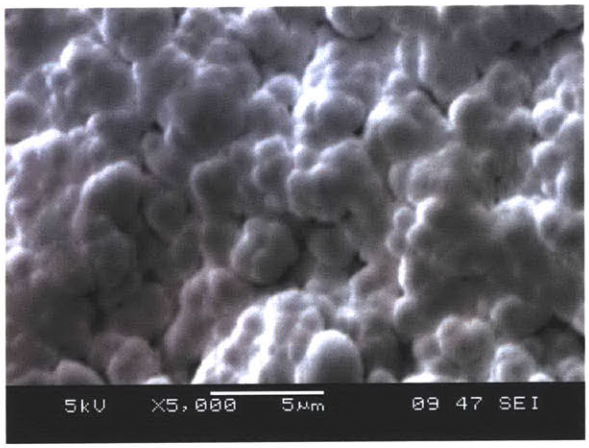

Figure 3-3: SEM image showing tungsten sputtered onto an initially porous substrate leaving a sub-micron pore structure.

Physical deposition, either through RF sputtering or thermal evaporation and Chemical Vapour Deposition (CVD) could be used to create structures by a lift-off technique, whereby a negative mask exposes only the desired emitter locations on a porous substrate. After deposition the mask is removed leaving localized deposition. For example, Spindt[108] used

thermal evaporation by electron beam heating to deposit molybdenum through a narrow aperture covering a small cavity to create very sharp emitters a few μm tall, suitable for electron emission. The techniques are typically applied to thin (several μm) fims[96] and may not inherently be suited for application to bulk porous wafers.

During this research, tungsten was deposited on porous tungsten substrates using RF sputtering. The experiment was initially performed as a means for exploring the suitability of these techniques for creating a thin solid surface suitable for a spin on masking technique. Figure 3-3 demonstrates the interesting result that rather than seal the surface, the deposited material appears porous. This indicates that such a technique could be used in growing porous structures when the initial substrate is porous. However; further investigation of this method was abandoned due to the high costs inherent with depositing the required 10's to 100's of μm necessary to create arrays of ILIS.

In the context of porous emitters, an interesting approach would be to perform 'co-sputtering' whereby two materials are simultaneously deposited on the wafer to form a structure. As a final step, one of the materials is removed leaving empty cavities which could serve as pores. However; this procedure would not alleviate the concerns addressed above for forming the initial, tall, structures.

Vertically Aligned Carbon Nanotube Columns

Figure 3-4: SEM image demonstrating wetting of a column of vertically aligned carbon nano-tubes with ionic liquid.

Columns of aligned Carbon Nano-Tubes (CNTs) can be grown on a substrate material, using, for example, the technique of Hart[109]. The fabricated columns, which can be 100's

of μm tall and with 10's of μm diameters, are composed of individual nanotubes ~1-10 nm in diameter. The interspacing between CNTs, or small groups of CNTs, roughly 10's to 100's of nm, would then be used as a porous material for supplying liquid to the tip of the column. These structures have previously been wet in material science applications, see for example Garcia[110], and have been wetted with ionic liquids while exploring techniques during this research, as shown in Figure 3-4. Preliminary experiments with these columns as ionic liquid ion sources have shown a high propensity for electron emission at negative polarities, presumably due to the inherently small length scales (nm's) of the CNTs which may protrude from the liquid meniscus even after wetting. These observations are consistent with the body of work devoted to employing similar designs as field emission electron sources, see for example de Heer[111]. Furthermore, although the fabrication technique for the columns is well established, a technique for growing the structures on a bulk porous substrate while maintaining a continuous, capillary fed, flow path from a liquid reservoir to the emission sites is not clear. Such columns can be grown on thin layers of porous silicon with nano-sized pores at the surface[112], but recent efforts to create similar structures on bulk porous metals with ~μm sized pores performed at MIT have been unsuccessful[113].

Aerogels and Metallic Foams

Aerogels are a form of porous material created by removing the liquid component, typically water, of a gel through drying under supercritical conditions[114]. The resultant materials are characterized by high porosity levels and correspondingly low densities. Silicon dioxide (silica) based aerogels are well developed and are typically composed of structures on the nm scale separated by 10's of nm. Although conducting aerogels can be formed, see below, metal oxides, or semiconductors, are more common. Examples of applications within microfabrication include Yokokawa[115] et. al who formed thin (~1 μm) aerogel cantilevers of silica, alumina (aluminum oxide) and titania (titanium oxide) supported by a silicon wafer.

Tappan et. al[116] have developed a technique for creating metal foams by combustion of a high density pellet composed of a synthesized metal compound. Upon combustion the pellet grew into a monolith of porous material approximately 5 times larger. Specifically, that work described foams of iron, cobalt, copper and silver. The process typically produced materials with large ~10 μm voids between porous structures which were themselves porous with pores ranging from 10's of nm to a few μm.

Referring to the desired requirements for this research, although aerogels and foams are an interesting material, no examples in the literature could be found to suggest that conducting arrays of these materials could be formed at the length scales required and as part of an integrated, aligned, package. Furthermore, the small length scales of the internal structures (nm's), are similar to those found in CNT columns and could be prone to similar difficulties in achieving ion beams without dominant electron evaporation.

De-alloying of a Solid Emitter Array

This method would be used to achieve a porous structure from a preformed alloy fabricated with the desired geometry for arrays of ILIS. The shaped alloy could be formed, for example, by co-sputtering or a form of surface micromachining beginning from a flat wafer. The de-alloying procedure could be chemical[117] or electrochemical[118] in nature. The resultant porous layers are typically characterized by pores from 10 nm[117] to 1 μm[118] in diameter and are limited in thickness to only a few μm in order to prevent structural failure due to the differing material properties between the solid and porous layers[117]. For porous ILIS arrays, the small pores and relatively thin porous layers expected with this method could result in significant hydraulic impedances similar to those observed with externally wetted ILIS where surface roughing can be described as a very thin porous layer[50]. Furthermore, thin porous layers are disadvantageous when considering the propellant feed mechanism. Unlike bulk porous materials, these layers would require a transverse feeding mechanism which could reduce flow uniformity.

Electrochemical Etching

Electrochemical etching has significant heritage for both ILIS and LMIS, as has been described in the sections above. Applied to tungsten this method suffered from mask incompatibilities. However, the research presented in the next section motivates that applied to many metals, a specific regime of electrochemical etching in resist compatible electrolytes can be used for fabricating bulk porous ILIS. Specifically, by operating in a diffusion controlled (also known as transport limited) regime it will be shown that smooth, surface micromachining of bulk porous materials, over a wide range of porosity, can be achieved. Due to its inherent selectivity (electrical) this form of processing can be performed on materials already mounted within a partial package.

This method is advantageous in that, if understood, it could be applied to a range of metals and porosities. This could be beneficial if, for example, a particular material is found to be incompatible with a desired ionic liquid propellant. The ability to etch a range of porosities would allow for studies concerning the impact of parameter on ion emission while maintaining constant emitter geometries. This ability will be demonstrated in Chapter 6 where very similar structures have been fabricated using both solid and a relatively high porosity nickel.

3.5 Conclusions

We have identified a variety of fabrication schemes which could be applied to creating arrays of porous ILIS. Electrochemical etching under mass transport conditions has been selected in this research. This technique will be discussed in larger detail in the next chapter. A key feature motivating this selection is the ability to, in theory, etch a range of materials. This feature offers greater applicability to future developments of porous emitter arrays beyond the examples, using nickel, which have been fabricated in this research. Furthermore, it will be shown in Chapter 5 that this etching technique integrates well with a complete thruster packaging process, including alignment with the electrostatic grids.

This review has also identified a number of other techniques which could be applied independently, or in addition to electrochemical etch steps, in the future. For example, in this research sintered porous nickel has been used as substrate material. Efforts to customize a sintering process could allow for materials specifically tailored to arrays of porous ILIS, such as sintered porous columns which are rounded electrochemically post process. Other methods, such as de-alloying or porous silicon, could be applicable but would benefit from a better understanding of the emission physics such that the relatively small pore dimensions and porous substrate thicknesses are properly accounted for in the design.

Chapter 4

Electrochemical Micromachining on Porous Metals

Transport limited electrochemical etching has been selected as a method for fabricating bulk porous ionic liquid ion source arrays. This chapter reviews the method with the intention of identifying the key parameters influencing etching characteristics and uniformity for porous metals. The review includes a summary of available literature where similar methods were applied. At the end of the chapter a numerical simulation model is presented and used to motivate a two step etching process for creating arrays of porous ILIS.

4.1 Review of Electrochemical Etching under Mass Transport Control

We begin with a review of electrochemical etching, and in particular its applications to microfabrication. The applicability of this method to porous electrodes is addressed in the following section.

4.1.1 Electrochemical Etching: Anodic Dissolution

The fundamental relation describing the kinetics of an electrochemical reaction at an electrolyte-electrode interface is the Butler-Volmer relation, expressed as an electrical current density

in equation 4.1. See Bockris[119] for a more complete description.

$$i = i_0 \left[e^{(1-\beta)\frac{\eta F}{R^0 T}} - e^{-\beta \frac{\eta F}{R^0 T}} \right] \tag{4.1}$$

In equation 4.1, i_0 is the exchange current density, a constant for a given reaction which depends, in part, on the solvation energy of the reacting species. The overpotential, η, is the difference between the enforced potential difference at the interface and that at equilibrium. The term β is a factor, between 0 and 1, which describes the symmetry between oxidation and reduction for a given reaction. Finally, F is Faraday's constant, T is the local temperature and R^0 is the universal gas constant (the product the Boltzmann constant and the Avagadro constant). When considered in the context of electrochemical etching, the electrode in question is the metal substrate to be etched, M, and the governing reaction takes the form of equation 4.2 at a rate governed by equation 4.1.

$$M \leftrightarrow M^{z+} + ze^- \tag{4.2}$$

Equation 4.2 assumes a single step reaction with valence, z. In practice the dissolution process may have multiple steps and/or occur in parallel with other reactions (notably oxygen evolution) resulting in the use of an empirical effective valence[120, 121] in equation 4.2. When etching, the flux of material removed from the metal is related to the interfacial current by Faraday's law, equation 4.3. Here M is the molar mass, ρ is the material density and $\vec{n}$ is the unit normal vector.

$$\vec{\nu} = \frac{M}{zF\rho} i\vec{n} \tag{4.3}$$

4.1.2 Operating Regimes

For ideal, planar, geometries with a constant potential distribution and negligible transport effects, the description above would be sufficient. However; in general the reaction rate varies across the material surface and depends on both the potential distribution and concentration gradients. As described in the reviews of Datta[122, 121] and Landolt[120], in regions where transport effects can be ignored the current distribution is said to be either a primary or secondary distribution depending on the Wagner number,

$$W_a = \frac{d\eta/di}{\rho_e L}. \tag{4.4}$$

Here ρ_e is the electrolyte resistivity, L is a characteristic length and $d\eta/di$ is the differential resistance of the interface, equal to the kinetic resistance for unit area. The Wagner number is a measure of the proportion of potential drop which occurs near the material surface, compared with that within the electrolyte. For small Wagner numbers, the primary distribution, the potential across the electrochemical double layer does not change significantly for a change in current. Here the majority of the potential drop between the active electrode and a counter electrode occurs within the electrolyte and the reaction proceeds at a rate proportional to the electric field as dictated by Ohm's law. For large Wagner numbers, the secondary distribution, the potential drop occurs primarily at the interface relegating the dependence on the electric potential distribution in the electrolyte to be secondary.

At increasing overpotentials, and hence currents, mass transport effects begin to influence the reaction rate[119] and must be considered in addition to the electrical distribution described above. Specifically, the transport of a species with concentration c from the surface of the metal due to diffusion can be estimated by the normal component of Fick's law to be,

$$\vec{\Gamma} = D\nabla_n c \approx D\frac{\Delta c}{\delta}\vec{n}. \tag{4.5}$$

Here D is the species diffusivity, and Δc is the difference in concentration between the metal surface and electrolyte bulk assuming a Nernst diffusion layer of thickness δ. A Nernst diffusion layer is equivalent to assuming diffusion effects are restricted to within a layer extending from the surface to a thickness δ in the electrolyte[119]. As transport effects become significant both the reaction kinetics and transport contribute to calculating the total current[119, 121].

At still higher overpotentials (and hence current densities), mass transport effects begin to completely dominate the reaction rate[119, 121, 122, 120] and a plateau within the current versus overpotential relationship can be reached. This, transport limited, scenario has been drawn schematically in Figure 4-1. Once limited, the surface can effectively become highly polarized since the reaction rate will be independent of potential. Outside the diffusion layer the Wagner number will then be large and the electrical distribution between the counter electrode and diffusion layer boundary will be of the secondary kind. Both the rate of reactants reaching the surface, where they maintain the electrochemical double layer, or the transport of reaction products away from the metal could limit the rate[122]. The later

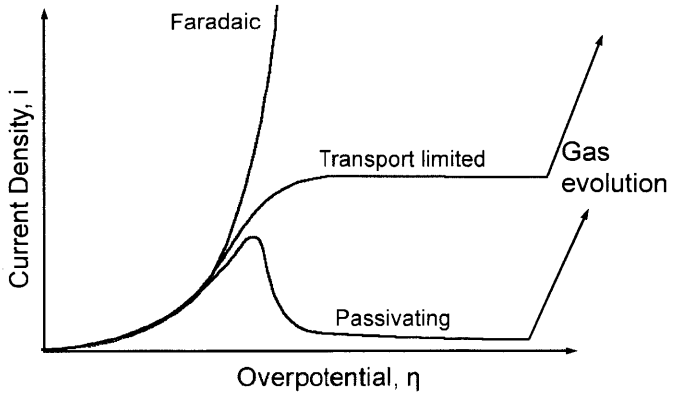

Figure 4-1: A sketch of the typical polarization curves seen in this research using potentiostatic scans on anodic electrodes. The Faradaic curve corresponds to that predicted by the Butler-Volmer relation, equation 4.1. Simple transport limited reactions are characterized by a plateau controlled by mass transport properties.

is more common within dissolution of metals[122, 120], where a resistive film of porous, saturated[123], or possibly super-saturated[124], salt forms at the surface. This surface layer has been estimated to be on the order of 10 nm thick[123]. Once established, it is the dissolution of this salt layer through the diffusion layer, δ, which limits the reaction rate.

4.1.3 Composition and Control of the Diffusion Layer

Depending on the characteristics of the reaction, the salt film may lead to anodic oxidation of the metal and passivate the surface[122, 121], as in the lower curve of Fig. 4-1. Although further increases in the electrode potential can lead to a breakdown of the passive layer, efficient etching requires that this take place prior to any additional reactions evolving, most notably oxygen evolution. Once the salt film is established the reaction will, for a point on a non uniform geometry, continue at a rate given by Fick's law, such that the surface current density will be,

$$\vec{i} = \frac{DzF}{\theta}\nabla_n c. \tag{4.6}$$

Here θ is the current efficiency which accounts for current wasted on other reactions (for example oxygen evolution)[125]. The concentration profile under quasi-steady conditions is

given by the convective diffusion equation,

$$D\nabla^2 c - \vec{v_l} \cdot \nabla c = 0, \tag{4.7}$$

where v_l is the convective velocity. A common approximation is to ignore the convective term in equation 4.7 and instead assume a stagnant diffusion layer with a thickness δ varying with the hydrodynamic conditions[121, 126]. Measurements of the diffusion layer thickness for anodic dissolution[120, 121], with various forms of forced convection, range from a few to hundreds of μm, decreasing with enhanced fluid flow. In the absence of forced convection, free convection limits the diffusion layer growth to a few hundred μm[119]. Estimates of the thickness can be made from equation 4.8 where the Sherwood number, Sh, is a dimensionless representation of the transport rate and d_e is the hydraulic diameter. Numerous correlations for the Sherwood number are available in the literature and have been extensively compiled by Selman[126] and Isaacson[127] depending on the hydrodynamic conditions (eg. cell geometry, flow rates, fluid properties).

$$\delta = \frac{d_e}{Sh} \tag{4.8}$$

For example, using the tabulated correlations of Selman, for laminar flow in a rectangular duct of width w with electrodes on the upper and lower surfaces separated by a height h, equation 4.9 can be employed. This relation applies to cells with a hydraulic diameter, d_e, more than 1.85 times larger than the electrode separation, h.

$$\begin{aligned} Sh &= 1.85 \left(R_e S_c \frac{d_e}{L} \right)^{1/3} \\ \text{for } 75 &< R_e < 7000 \\ 600 &< S_c < 12000 \\ 0.05 &< d_e/L < 20 \end{aligned} \tag{4.9}$$

In equation 4.9, L is the active electrode length and the Schmidt and Reynolds numbers, S_c and R_e respectively, are given in equation 4.10. For rectangular channel Selman sets

$d_e = 2h$.

$$\begin{aligned} R_e &= \frac{v_l d_e}{\nu} \\ S_c &= \frac{\nu}{D} \end{aligned} \tag{4.10}$$

In equation 4.10, v is the electrolyte velocity, ν is the electrolyte viscosity and D is the diffusivity. Note that in equation 4.9 the viscosity cancels between the Reynolds and Schmidt numbers (leaving the Peclet number $v_l d_e/D$) while in equation 4.11 a small dependance on viscosity remains.

For small electrode separations ($h/w \sim 0.16$), this relation is modified, according to the reference, to equation 4.11.

$$\begin{aligned} Sh &= 2.54 \left(R_e \frac{d_e}{L} \right)^{1/3} S_c^{0.29} \\ \text{for } 200 &< R_e < 2000 \\ 1000 &< S_c < 3500 \\ 0.025 &< d_e/L < 1 \end{aligned} \tag{4.11}$$

It is useful to consider some typical cases which will occur in this research. For example for nickel, Ni^{2+}, and titanium, Ti^{4+}, the diffusivity at infinite dissolution and 25^oC can be estimated using available correlations[128, 89] to be $\sim$ 6.6x10^{-6} cm^2/s and $\sim$ 1.2x10^{-6} cm^2/s respectively. These values are in good agreement with those used by other authors for nickel[129, 130] and titanium[131]. Consider a cell with an equivalent diameter of 5 mm and 10 mm long electrodes. At an electrolyte velocity of 100 cm/s ($R_e \sim 5000$ for $\nu \sim$ 1x10^{-2} cm^2/s), as used by Datta[129], equation 4.9 predicts a diffusion layer 17 μm thick. For a much slower rate of electrolyte flow, 5 cm/s for example, the calculated diffusion layer thickness increases to roughly 46 μm.

For nickel dissolution in 1 M aqueous HCl, Strehblow[130], lists a nickel saturation concentration of 4.8 M/L. Using equation 4.6, and the estimates for D and δ above, current densities between 3.6 and 1.3 A/cm^2 would be expected from a planar electrode for 17 and 46 μm diffusion layer thicknesses respectively.

4.1.4 Choice of Electrolyte

The description above has assumed simple reactions such that a well defined plateau of mass transport control exists within the cell polarization curve (Figure 4-1). As reviewed by, amongst others, Datta[122], the ability to achieve wide, clearly defined limiting current plateaus depends on the specific electrochemical cell. This includes the anode and cathode materials, the electrolyte and the hydraulic configuration.

In a review of these techniques by Landolt[120], that author notes that favorable, transport limited, conditions are typically achieved using acidic solutions. However; numerous chemistries exist for electrochemical etching of metals using acidic, basic or neutral salt solutions, see for example Datta[121]. Figure 4-1, above, schematically illustrates some typical potentiostatic sweeps, or polarization curves, for anodic dissolution depending on the electrochemical cell. In order to maintain diffusion controlled reactions throughout the activated region of a substrate, a wide limiting current plateau is desirable. The passivating case in the figure (for example sulphuric or nitric acid in nickel dissolution), was mentioned earlier. In this case, at increasing potentials, current may begin to flow again (transpassive) but often quickly becomes dominated by oxygen evolution and the limiting current plateaus are very narrow. However; using other electrolytes a large limiting current plateau can be observed (for example hydrochloric acid for nickel as identified in Chapter 6) .

An appropriate tool, as described below, should be capable of controlling the magnitude of the limiting current plateau through both electrical and hydrodynamic conditions. However; as performed by, for example, Grimm[123] and Strehblow[130], doping the bulk electrolyte with the etch products can provide additional control over the transport properties. With increased concentration of the dissolving metal ion, the difference between the saturation and bulk concentrations, and hence the etch rate, are reduced (equation 4.6). This would also reduce the amount of dissolved material required before a saturated salt layer precipitates, possibly reducing the impact of transient behavior. Adding salts can therefore provide additional control with minimal changes to the cell hydrodynamics which dictate the size and uniformity of the diffusion boundary layer. Applied to microfabrication it will be demonstrated in section 6.5 that by slowing the reaction without disturbing the highly sensitive hydraulic conditions, this method is particularly useful for achieving short duration etches on porous materials.

Non aqueous solutions can also be used. Madore[131] found that by employing sulfuric acid in pure methanol, steady diffusion controlled etching of titanium could be achieved and applied to fabricating cavities much smoother and more uniform than chemical etching or electrochemical etching in water based sodium bromide solutions.

4.2 Transport Limited Electrochemical Micromachining

Through mask electrochemical micromachining of solid metals is typically performed under transport limited conditions (see for example refs. [122, 120, 121, 131, 132, 133]). This has primarily been attributed to the ability to achieve micron scale smooth etching under these conditions. Datta and Landolt[122, 120, 121] note that outside the transport limit, etching tends to favor the crystallographic structure of the material leaving a surface which is often rough and pitted at the micron scale depending on the initial crystal structure. Applied to porous materials, where the crystallographic structure is highly randomized, this could be highly detrimental as was observed using RIE etching (section 3.4). Figure 4-3(a) in the next section demonstrates this phenomenon for porous nickel.

Achieving, predicting and controlling electrochemical microfabrication under mass transport conditions requires a precision tool to control and parameterize inputs, accept an appropriate selection of electrolytes and provide feedback to monitor the etch progression. The following paragraphs review literature addressing these concerns.

4.2.1 Existing Tools for Electrochemical Mirofabrication

Many of the cited examples of electrochemical microfabrication have been applied to forming cavities or holes through sheets of solid material. Here the bulk of the material is masked with a relatively small region exposed. At the scale of the ion emitters required here, also know as the feature scale, the appropriate tool should provide consistent hydrodynamic and electrical conditions facilitating comparisons with numerical models or empirical correlations. If known, such correlations could be fed back into the tool control system to provide a means for adjusting etch profiles in a predictable manner. At the wafer, or pattern, scale the tool should yield uniform results for all features, regardless of their position on the wafer. For emitter arrays used as ILIS, this translates to uniform emitter heights and tip geometries.

Rotating disk electrodes are well established for electrochemistry experiments specifically for their ability to isolate kinetic and mass transport effects in a defined manner[119, 126]. They are well suited for geometries that are mostly planar, or reactions where very high transport limited currents(low diffusion layer thickness) are desired. Applied to microfabrication, Madore[131] successfully used a rotating disc configuration when etching masked titanium samples.

A number of other tools which have been developed for both anodic dissolution and electrochemical deposition processes have been reviewed by Datta[122]. That author notes that, other than rotation, agitation is generally applied through some combination of a moving paddle or a flow channel with the surface either immersed in electrolyte or sprayed with impinging jets[134]. The paddle may be either electrically neutral or double as the cathodic electrode for the reaction[135, 136, 137].

One benefit of the latter configuration, using the agitator as the cathode, is evident considering the high currents required to sustain diffusion control, often exceeding 1 A/cm^2. At these currents, close electrode spacings are required to counteract Ohmic losses in the electrolyte[122]. Furthermore, the high net currents could induce significant and non uniform Joule heating within the sample itself[120] causing localized alterations to both the electrolyte and interface behavior. Unlike flow cells where the entire sample is activated, cathodic paddle agitators can be designed to provide localized dissolution[135, 132] with only the region directly below the paddle active at any given time. Finally, these paddle cells provide a means for simple reversal of the flow direction[122], alleviating, to some extent, directional non-uniformities across the wafer as would be expected in simple flow cells[138].

When applied to this research, large exposed areas are expected leading to high current magnitudes suggesting localized etching through either a closely spaced paddle or nozzle head could be optimal. However; a jet impingement design may not be suitable for fabricating sharp porous emitters where strong undercutting of the photoresist mask is desirable. The jet could cause unpredictable disruptions to the mask by physically damaging it. Therefore a cathodic paddle agitator has been applied in this research. The specific configuration is described further in Chapter 6.

4.3 Electrochemical Etching on Porous Electrodes

The subject of electrochemical reactions within porous electrodes has been well developed, particularly for their benefits as battery electrodes where a maximum activated surface area is desirable. The review of Hampson[139] includes both a general description of the important physics and summarizes efforts for a number of materials. Using simplified models for a porous structure, the penetration depth, equation 4.12, can be derived[139]. As explained in the cited reference, the penetration depth approximates the distance into the pores where the electrical resistance of the fluid matches the kinetic resistance of the surface within the pore. Here R_k is the kinetic resistance *for* unit pore length and R_Ω is the Ohmic resistance *per* unit pore length. Specifically, R_k has units $\Omega - m$ and decreases with increasing depth, while R_Ω has units Ω/m and increases with increasing depth.

$$\lambda = \left(\frac{R_k}{R_\Omega}\right)^{1/2} = \left(\frac{d\eta/di\frac{1}{\pi D_p}}{\rho_e \frac{1}{\pi D_p^2}}\right)^{1/2} \tag{4.12}$$

Comparing the right side of equation 4.12, where $D_p = 2r_p$ is a characteristic pore diameter, and equation 4.4, it is clear that the square of the penetration depth is proportional to the Wagner number. In section 4.1.2 for simple electrodes, when the Wagner number was high, the potential drop through the electrolyte became secondary leading to uniform reaction rates regardless of the physical configuration. In porous electrodes, this translates to a large penetration depth, etching will occur deep within the material. Conversely at low Wagner numbers, where the potential drop occurs primarily through the electrolyte, the electric field would be greatly reduced within pores compared with the surface.

In the context of batteries large penetration depths are desirable to maximize the reacting area. In this application etching within the pores could have several detrimental impacts when attempting to operate porous ILIS by: i)developing an adverse porosity gradient to that desired, ii)inhibiting wetting near the tip, particularly as the penetration depth approaches the target tip radius and, iii) increasing the complexity inherent in predicting etch times by introducing variations in the active area. Thus minimizing the penetration depth is desirable. As the penetration depth approaches zero (or at least a single pore diameter), etching within the pores will cease, leaving the pore structure intact.

Hampson incorporated transport effects (but not necessarily enforcing a transport lim-

ited surface) along with the penetration depth concept to show that at high reaction rates, the penetration depth will be reduced and the net current from a single pore decays to a value equivalent to that expected from solid material with the projected surface area of the pore[139]. This finding has been echoed by the macro models of Newman[140] and Alkire[141] where averages over the porous structure were used as opposed to simplified individual pore geometries. In those studies, which also included internal mass transport effects, the authors showed theoretically that as the applied potential was increased the reaction shifts to the surface with decreasing reactions occurring in the bulk. Again, this finding was deemed undesirable for batteries but can be highly advantageous for etching arrays of porous ILIS.

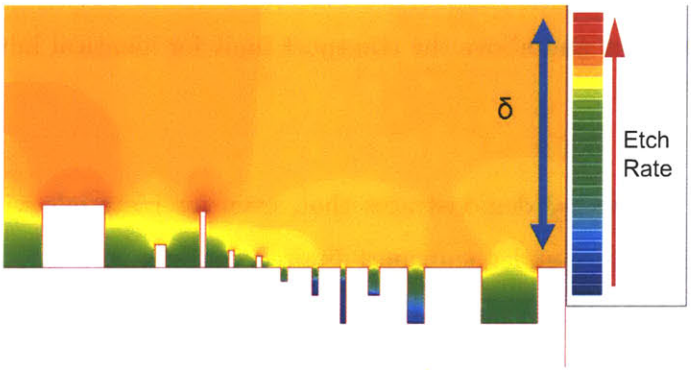

Figure 4-2: Under transport limited conditions sharp features will etch quickly due to strong concentration gradients while recesses, like pores, will be shielded.

For the case of complete mass transport control, where equations 4.5 and 4.7 govern the etch rates within a diffusion layer thickness δ, much larger than the pores, the entire surface could therefore be smoothly etched at a rate approaching that of a solid material. This concept has been illustrated in Figure 4-2 which shows the intensity of the normalized concentration gradient, proportional to the local etch rate on the surface, for a simplified 2D geometry. The figure demonstrates that, within small features similar to pores, little etching would be expected. Thus while transport limited etching has previously been applied to smoothing materials, as evident by the enhanced rates on protrusions in the figure, in this research we exploit the same mechanism to shield the internal pore structure.

Developing a consistent method for achieving this type of etching on porous materials has been a primary goal of this research. As a precursor to the results presented in the

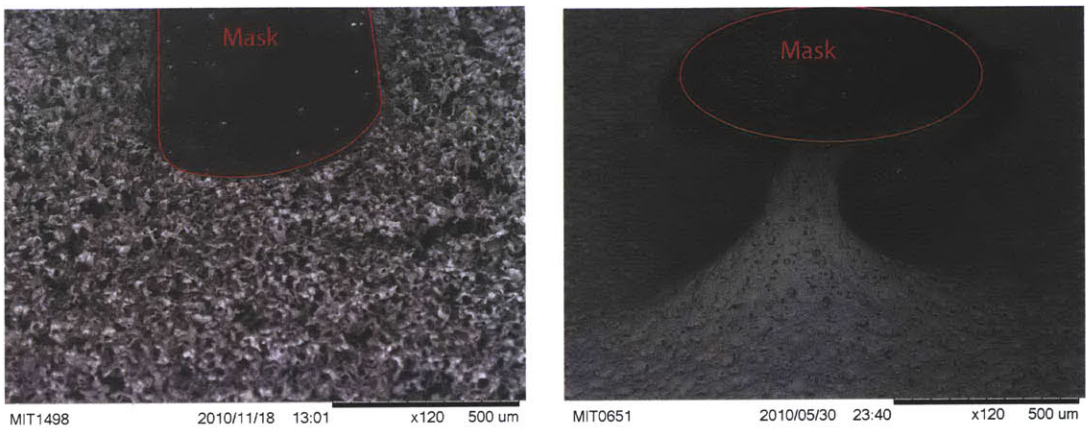

(a) Sample image after etching well below the transport limit with a high penetration depth. Note the sharp features caused by the reaction favoring crystal planes.

(b) Sample image after etching under transport limited conditions. Smooth features and strong undercutting have been achieved.

Figure 4-3: Etching below and above the transport limit for identical initial bulk materials ($>10\mu m$ pore nickel).

following chapters, Figure 4-3 demonstrates that, even for materials with relatively large pores (10's of μm), etching under transport limited conditions, Fig. 4-3(b), can lead to surface micromachining under a mask. In Figure 4-3(a), the identical material was etched at a rate well below the transport limit. The pore structure is clearly being etched and no clear shape is being formed under the mask.

4.4 A 1-D Model for Transient Behavior

The time scales for diffusion layer growth and decay are often significant when applying transport controlled etching to porous substrates. To consider this analytically we extend the assumption of an enforced stagnant region to assuming that the convective transport of etching products always maintains no additional (above the bulk concentration) etch products beyond a distance $\sim \delta$ from the material surface. The time dependent diffusion equation can then be solved analytically for a 1-D spatial problem. This type of analysis can be found in numerous texts, such as Bockris[142, 119], for treating a variety of transport problems. In the analysis shown here, the reaction has been treated as entirely transport controlled and hence all kinetics at the surface are ignored. As explained in Bockris[119] this assumption must satisfy two requirements. First the electrochemical double layer is presumed to charge/discharge at a time scale much smaller than the pulse, this time scale is typically on the order of μs[119, 143, 144]. Second, the kinetic, or Faradaic, current which would be incurred in the absence of diffusion effects, must be much larger than the transport limited current. Referring to the idealized polarization curve of Fig. 4-1, the assumption of a very large Faradaic current may be valid for potentials far to the right on the limiting current plateau. In this model, this assumption has been extended to enforcing a saturated electrode surface instantly, thereby neglecting both the capacitive charge time and the time required to form the thin ($\sim nm$, see section 4.1.3) saturated salt layer.

The problem can be treated in a general way using the following non dimensional parameters. Here, c_{sat} and δ are the salt film saturation concentration and diffusion layer thickness respectively. The time constant for diffusion, τ, and limiting current density, i_L, complete the normalization.

$$\begin{aligned} c^* &= \frac{c}{c_{sat}} \\ x^* &= \frac{x}{\delta} \\ t^* &= \frac{t}{\tau} \\ i^* &= \frac{i}{i_L} \end{aligned} \tag{4.13}$$

$$\begin{aligned} \tau &= \frac{\delta^2}{D} \\ i_L &= \frac{zFDC_{sat}}{\delta} \end{aligned} \tag{4.14}$$

Using equations 4.13 and 4.14 for a 1-D diffusion layer undergoing forced convection, the problem reduces to equation 4.15. When etching is active ($t^* = t^*_{\mathsf{on}}$), the assumption that surface saturation occurs during a negligible period of time is equivalent to enforcing $c^* = 1$ at the material surface. This assumption may be significantly detrimental in that, as will be revealed below, it leads to a singularity in the expected current for short times. Computationally this can be avoided by introducing a threshold time many orders of magnitude smaller than τ where stable solutions can be sustained. When not etching ($t^* = t^*_{\mathsf{off}}$), no material leaves the surface itself and the gradient (proportional to flux) of the concentration there is zero. As described above, forced convection is approximated by an enforced boundary condition at $x^* = 1$ where the concentration is forced to zero at all times.

$$\begin{aligned} \frac{\partial c^*}{\partial t^*} - \frac{\partial^2 c^*}{\partial x^{*2}} &= 0 \\ c^*_{x^*=0} &= 1 \text{ for } t^* = t^*_{\mathsf{on}} \\ \frac{\partial c^*}{\partial x^*}_{x^*=0} &= 0 \text{ for } t^* = t^*_{\mathsf{off}} \\ c^*_{x^*=1} &= 0 \text{ for all } t^* \end{aligned} \tag{4.15}$$

We are predominantly interested with the case when etching is occurring. Here a solution to equations 4.15 is given by equation 4.16. This solution was generated using separation of variables and applying the boundary conditions in equations 4.15. Here t^* is taken as the time after etching began, with an initial arbitrary concentration field $c^*_0(x^*)$ prescribed. For conditions where the initial boundary layer is free of etch products, such that $c^*_0 = 0$, solutions using Laplace transforms can be found[142]. However; the more general series solution has been preferred for its applicability to pulsed etching, discussed in the next section.

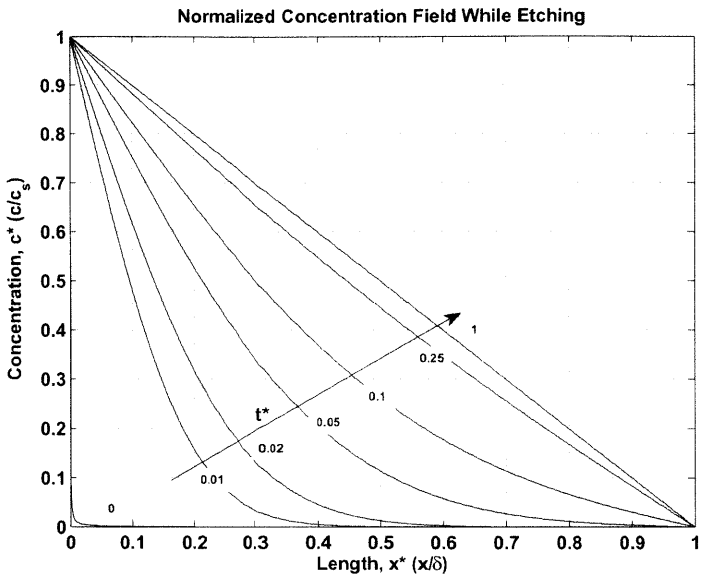

Figure 4-4: The concentration field is built up over time after beginning to etch at $t^* = 0$.

$$c^*_{\text{on}}(x^*, t^*) = 1 - x^* + \sum_{n=1}^{\infty} A^*_n \sin(n\pi x^*) e^{-\pi^2 n^2 t^*}$$
$$A^*_n = \int_0^2 (c^*_0 - 1 + x^*) \sin(n\pi x^*) dx^* \tag{4.16}$$

Equation 4.16 has been plotted in Figure 4-4 for the indicated values of t^* for the case where the concentration in the electrolyte is initially zero, $c^*_0(x^*) = 0$. In practice for this research, the concentration profile itself will not be measured, but rather the current can be observed when a fixed voltage is applied (referred to as a potentiostatic measurement).

As stated in equation 4.17, the current is proportional to the material flux and hence the negative of the concentration gradient at the material interface. Equation 4.17 gives a proportional estimate for the current evolution in time for this 1-D simplified model.

$$i^* = -\frac{\partial c^*_{\text{on}}}{\partial x^*}_{x^*=0} = 1 - \sum_{n=1}^{\infty} A^*_n n\pi e^{-\pi^2 n^2 t^*} \tag{4.17}$$

Equation 4.17 has been plotted in Figure 4-5 as a function of time, again for the case where the initial field is empty. From a practical standpoint, Figure 4-5 demonstrates how potentiostatic measurements could be used to estimate the diffusion layer thickness to, possibly, a higher degree of certainty than simply measuring the limiting current plateau.

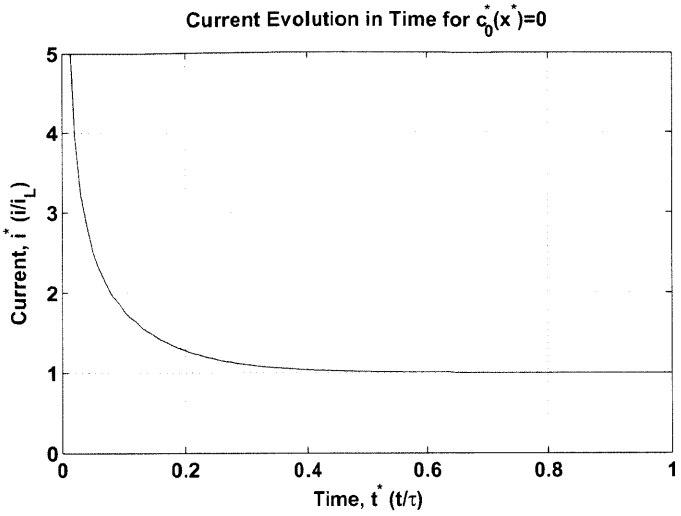

Figure 4-5: Non dimensional current versus time beginning with an initially empty concentration layer, $c_0^*(x^*) = 0$.

Referring to equation 4.14, the measured limiting current in an experiment depends on the active area, effective valence, diffusivity and diffusion layer thickness. Depending on the electrode arrangement, the active area may be difficult to measure in practice as will be evident in the configuration used in this research. However; referring to equation 4.17, under potentiostatic conditions, the current, normalized by the observed limiting current, yields a curve dependant only on t^*. A fit to the data as a function of time can then give an area independent estimate for τ, and therefore a measure of δ, if the diffusivity is known. Of course, this method is limited by the assumptions inherent in this 1-D model, including the bold assumption that while etching the active area remains constant.

Applied to etching porous materials, it is useful to consider the inverse of the value plotted in Figure 4-5. This value represents a length scale for concentration changes during the transient period while the concentration layer develops. It was previously postulated that smooth surface etching of porous materials would be possible under mass transport limited conditions so long as the diffusion layer thickness was much larger than the pores themselves. In this respect, the length scale for concentration changes of Figure 4-6 can be regarded as an effective diffusion layer thickness, δ_{eff}^*, over which the majority of the concentration drop occurs. The figure shows that initially this effective thickness will be small and could prevent pore level smoothing. The degree to which this may impact etching depends on the time scale τ, or more specifically the total etch time relative to τ.

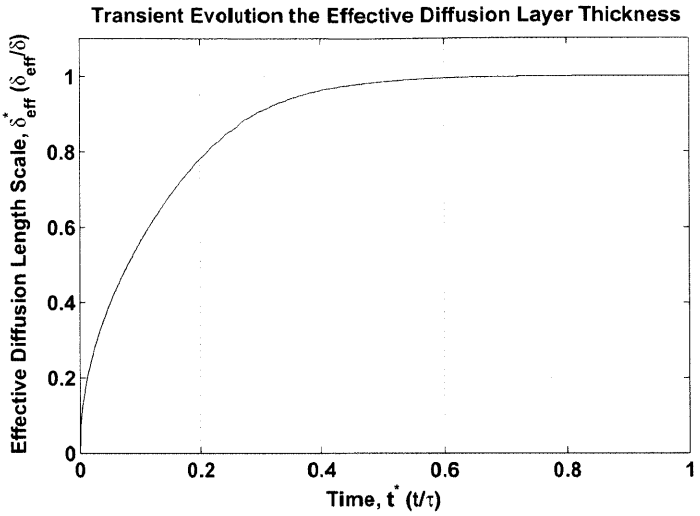

Figure 4-6: Effective diffusion layer thickness approaches the DC value only after a transient period where smaller length scales may dictate the behavior.

The figure shows that etch times lasting at least $\sim$ 0.3-0.5τ are required before a steady current at the desired, or designed, limiting current is reached. Applied to short etches on porous materials, this could lead to significant in pore etching leaving a sharp, high porosity surface. From a control standpoint, this sets a limit on the minimum amount of material which can be removed without taking extra precautions to ensure smooth surfaces during low etch times for porous materials. This issue will be demonstrated and addressed experimentally in Chapter 6 when attempting to tailor the fabricated emitter geometries with short secondary etches.

The problem of removing products when not etching can also be considered using the second boundary condition, for $t^* = t^*_{\text{off}}$ in equation 4.15. Equation 4.18 gives the resultant concentration field as a function of time in this scenario, again for an arbitrary initially prescribed field $c^*_0(x^*)$. Using this equation, the normalized concentration is plotted in Figure 4-7 for the indicated values of t^* for the case where the field is initially filled, $c^*_0(x^*) = 1 - x^*$.

$$\begin{aligned} c^*_{\text{off}}(x^*, t^*) &= \sum_{n=1}^{\infty} B^*_n \cos(\frac{n\pi}{2} x^*) e^{-\frac{\pi^2 n^2}{4} t^*} \\ B^*_n &= \int_0^2 c^*_0 \cos(\frac{n\pi}{2} x^*) dx^* \end{aligned} \tag{4.18}$$

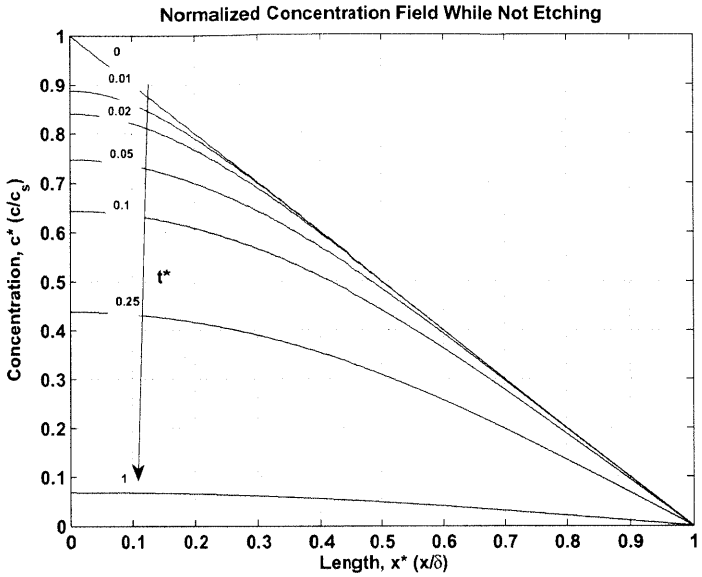

Figure 4-7: Concentration field dissipating over time when not etching.

4.4.1 Pulsed Dissolution on Porous Electrodes

Time varying signals for transport dominated electrochemical processes have been investigated theoretically and experimentally by numerous authors. In particular pulsed currents have been used frequently in electrodeposition processes[145, 146, 147, 148, 143] and anodic dissolution applications[121, 149, 143] where they have been credited with increasing deposition uniformity under certain conditions. Chin[143] and Dukovic[148] in particular provide summaries of experiments where enhanced uniformity was reported using pulsed dissolution. In the cited reference, Chin attributes enhanced uniformity for both electrodeposition and electrochemical etching to the ability for pulsed operation to enforce a large apparent Wagner number while yielding high instantaneous currents. However; Ibl[144] predicted that for pulses under constant mass transport control, enhanced deposition on protrusions may be avoided as the diffusion layer "follows the profile" as it evolves. Clerc[150] alludes that one interpretation for enhanced uniformity with due to a reduced effective diffusion layer thicknesses, could be a more conformal layer which remains consistent over the evolving surface. Meanwhile, for electrochemical etching, Datta and Landolt[149] focused on thermal benefits of operating at very high (100's of A/cm^2) instantaneous currents but low average currents while also noting that the reduced average current can lead to enhanced control during timed processes[121]. Applied to etching on porous electrodes, the two later

phenomena may be beneficial while the argument of high Wagner numbers is disconcerting. As discussed in section 4.3, operation in the secondary current regime at high Wagner numbers, can be analogous to high penetration depths on porous materials. This would correspond to significant etching within pores rather than the desired surface smoothing. Indeed, in the same review Chin notes that, as part of their experimental research using alternating (bipolar) signals[151, 152], their group obtained enhanced electrical penetration when performing electrodeposition through a porous zinc electrode. During one study[152] those authors noted that alternating voltage anodic dissolution at 60 Hz resulted in increased pitting and material removal along grain boundaries. However; that work used relatively high speed rotating disc electrodes suggesting operation outside the transport limited regime.

Despite this concern, the possibility that pulsed etching could yield enhanced uniformity led to the following theoretical treatment and, in section 6.4.4, experimental application of the technique.

4.4.2 Modeling Pulsed Voltage Conditions Under Diffusion Control

Several models for electrochemical processes under pulsed current conditions exist in the literature. These include the linearized model of Ibl[144] in which a duplex diffusion layer composed of a frequency and duty cycle dependent inner thickness is bound within a thickness prescribed by the constant current behavior. This model has been adapted to electrochemical machining by Datta and Landolt[149, 121]. Both Cheh[145] and Chin[143] developed analytical models using series solutions to the transport problem, similar to the approach used here but again applied to pulsed current electrodeposition. The model of Chin also includes a kinetic model for the electrical interface to predict voltage transients under galvanostatic (enforced current) conditions.

These previous works were concerned with enforcing current pulses rather than voltage pulses. Pulsed voltage conditions have previously been applied to dissolution by, for example Datta and Landolt in developing an electrochemical saw[132] and, to a lesser degree by Chin[152] on zinc electrodes. Under pulsed current operation the concentration at the interface may grow and decay over time, eventually approaching the saturated condition for salt film formation discussed previously. Under these conditions, the reaction may not be limited by transport throughout the pulse. When etching porous materials, transport

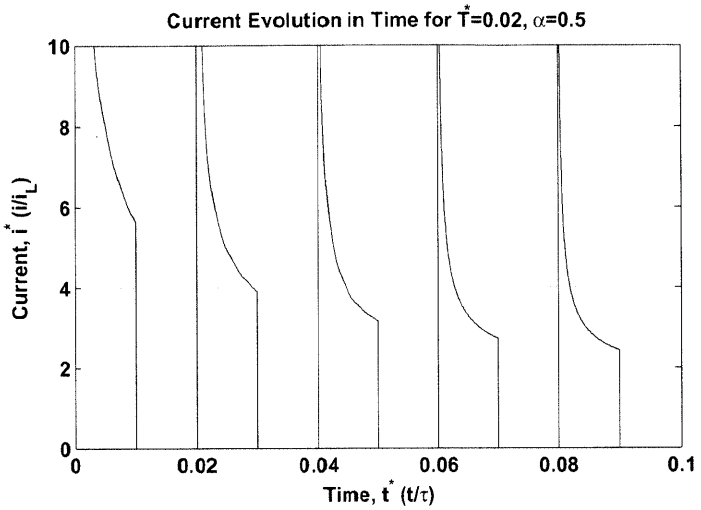

Figure 4-8: Non dimensional current evolution in time during pulsed voltage etching.

limited conditions are always desirable. Enforcing an applied potential well within the limiting current plateau has been selected as an alternative to promote these conditions as quickly as possible. In the model described above, this condition was extended to assuming the current is Faradaic for a negligible amount of time such that the reaction is entirely transport controlled. Even under these conditions whereby the overall reaction may initially be limited by mass transport, the scenario may not favor smooth etching at the porous surface throughout a pulse. However; as transport effects dominate, the current decrease will be accompanied by an increase in the length scale for concentration changes, leading to the desired smoothing effects at the porous surface. This desire supports using pulsed voltages over currents.

If the pulsing time scales are long enough for the assumption, made in the earlier analysis above, that the time required to form a salt film is negligible remains valid, the problem can be explored using equations 4.16, 4.17 and 4.18. Consider voltage pulsing at a non-dimensional period $T^* = T/\tau$ and duty cycle α such that etching occurs for the portion αT^* of each period. The evolution of the concentration field, and corresponding etch current, can then be determined iteratively such that, at each period, the field defined by equation 4.16 at $t^* = \alpha T^*$ is input as the initial condition for dissipation of the layer, in equation 4.18. Subsequently the field at $t^* = (1-\alpha)T^*$ in equation 4.18 becomes the initial condition at the next period of reforming the layer when etching continues. The current over time has been calculated in this manner in Figure 4-8 for the case where T^*=0.02.

After several periods, a steady state condition will be reached, where the field calculated at the end of a given period matches that found at the end of the previous period. This condition, equation 4.19, is equivalent to a zero net filling rate for the diffusion layer over the total pulse, such that the net amount of material added from the metal surface to the layer when etching is identical to that diffused out of the layer when not etching.

$$c^*_{\mathsf{off}}(x^*, t^* + T^*) = c^*_{\mathsf{off}}(x^*, t^*) \tag{4.19}$$

The steady state condition is demonstrated in Figure 4-9 for an example case where $T^* = 0.02$. The figure presents the steady state minimum and maximum concentration fields, corresponding to the beginning of the period and end of the etching segment ($t^* = \alpha T^*$) respectively for three different duty cycles. At a 50% duty cycle, Figure 4-9(a), the field nearly becomes linear indicating that the etching current at the end of the cycle approaches the limiting current density i_L. However; at lower duty cycles, Figures 4-9(b) and 4-9(c), the steady state condition instead resembles a dual layer structure. Here the concentration field near the surface is again roughly linear but has a relatively steep slope throughout the pulse. This result is in good agreement with the linearized theoretical treatments of Ibl[144] and Datta[149] for pulsed current reactions discussed above.

Figure 4-9 presents a concern when applied to porous materials where at low duty cycles, the length scale for variations in concentration can be seen to oscillate between values consistently lower than the enforce diffusion layer thickness δ. Thus, one interpretation of pulsed voltage etching is that it reduces the steady state effective diffusion layer thickness, δ_{eff}(introduced in the previous section). This interpretation is consistent with one conclusion of Datta[149], that pulsed current dissolution can achieve high mass transport rates at decreased electrolyte flow rates. These results also echo those of Ibl[144] for electrodeposition, where the same linear model used by Datta was used to predict reduced enhancement of surface roughnesses at lower effective diffusion layer thicknesses during pulsed operation at high frequency and low duty cycle. Referring to Fig. 4-2 of section 4.3, reduced reaction rates on protrusions are analogous to reduced shielding of pores on a porous structure.

Recall that the effective diffusion layer thickness was defined previously to be proportional to the inverse of the etch current when the surface is activated. This metric was used by Ibl[144] in determining a pulse limiting current, representing what current could be

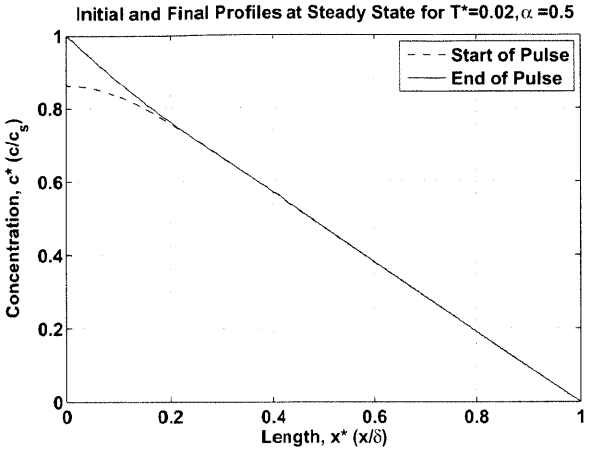

(a) Concentration fields at the start and end of a voltage pulse for $\alpha = 0.5$

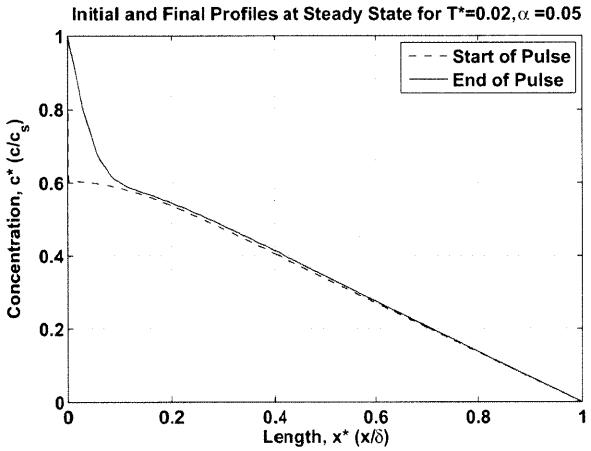

(b) Concentration fields at the start and end of a voltage pulse for $\alpha = 0.05$

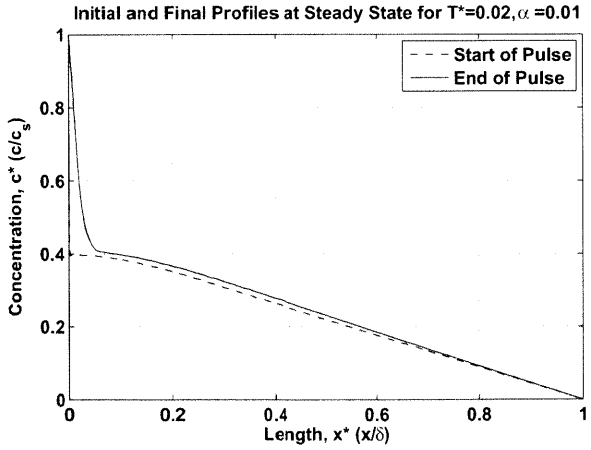

(c) Concentration fields at the start and end of a voltage pulse for $\alpha = 0.01$

Figure 4-9: Normalized concentration fields at the beginning and end of pulses once the steady condition of equation 4.19 has been reached for $T^* = 0.02$ and the indicated periods. At low duty cycles a duplex diffusion layer structure becomes evident.

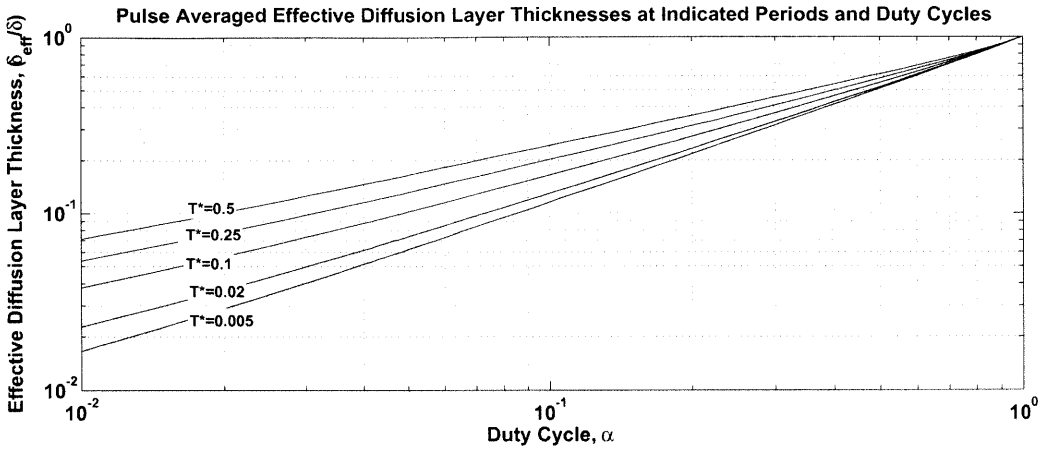

(a) Effective diffusion layer thickness averaged over flux.

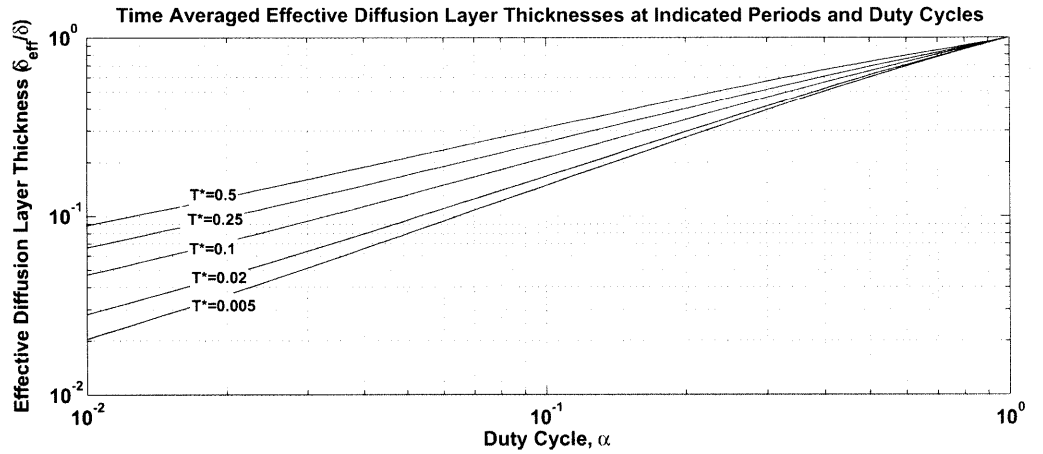

(b) Time Averaged Diffusion Layer.

Figure 4-10: Effective diffusion layer thicknesses averaged over current (upper) and time (lower).

enforced during pulsed current operation such that the rate became transport limited at the end of each pulse. When etching porous materials, the diffusion layer thickness throughout the pulse, rather than simply at the end of the pulse, will impact the etch quality. In Figures 4-10(a) and 4-10(b), the average thickness has been calculated for pulses at steady state. In Fig. 4-10(a), the average has been calculated over the flux (or current).while in Fig. 4-10(b) the average has been made over time. The former may be a more useful metric as it takes into account that relatively more material is removed during the initial portion of each pulse. The trends show that for high frequencies (low periods) and low duty cycles the effective diffusion layer thickness may become significantly smaller than the nominal (constant voltage) value.

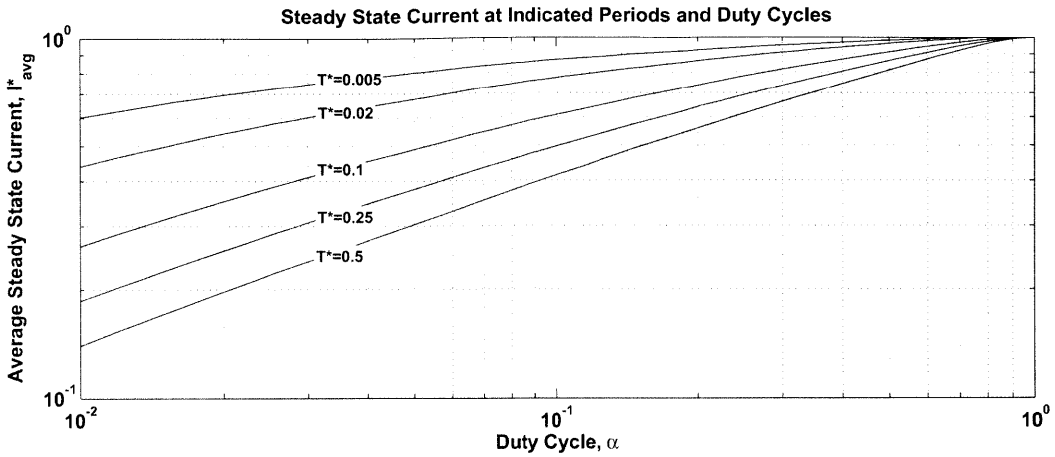

Figure 4-11: Current averaged over the entire pulse at the indicated periods and duty cycles.

One of the benefits of pulsed dissolution may be the ability to reduce the average current on a substrate and hence the average power being deposited by Joule dissipation through both the saturated salt film and electrolyte[149]. To this end, Figure 4-11 gives the time averaged current, over an entire period, at the steady state condition as a function of duty cycle for the indicated non dimensional pulsing periods. The figure shows that, in general, the average current is reduced at lower duty cycles, particularly at longer periods. At high periods, the ability for the duty cycle to reduce the average current becomes more significant because the concentration field, when on, will approach the limiting state for a relatively long portion of the pulse, thereby making the initially high current transients less significant. However; at lower periods, the transient behavior dominates and, although the substrate may only be active for a short period of time, the current during that period is very high.

Finally, the pulse limiting current, defined as the current at the end of each pulse (a minimum) has been plotted in Figure 4-12. The trends here are consistent with those observed using pulsed current models[143, 144, 145], demonstrating that at high frequencies and low duty cycles, relatively high pulse currents can be sustained when etching.

This highly simplified model suggests that while high frequencies and low duty cycles may lead to poor smoothing of porous materials, operation at relatively low frequencies and high duty cycles should be possible. However; it remains to be seen if any uniformity benefits remain under these conditions as many of the previous works cited above operated within the opposite extreme, high frequency and low duty cycle, where significant reductions in

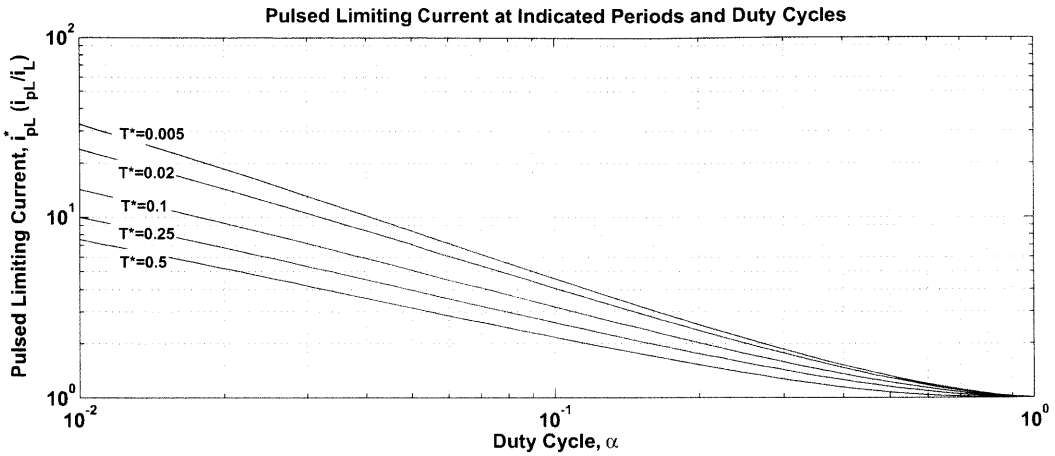

Figure 4-12: Transport limited current at the end of each voltage pulse at the indicated periods and duty cycles.

average current are achieved. It should be stressed that by assuming an instantly saturated layer, this model overestimates the current to, possibly, a significant degree. In reality, a maximum current either due to the reaction kinetics, electrolyte conductivity, or power supply limitations would place an upper bound on the surface current. This would have the effect of reducing the average current and hence the filling rate of the concentration field while etching. Once a steady state condition has been reached, this issue may become less significant depending on the initial concentration field at the start of each pulse.

4.5 A Numerical Simulation for Etch Profiles

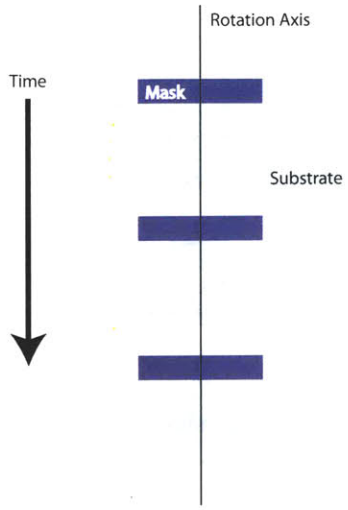

Figure 4-13: Emitter fabrication by undercutting of a circular mask.

Under the appropriate conditions, electrochemical etching may yield predictable, smooth, surface micromachining on porous materials. Applied to this research, the technique can be used to fabricated emitters from a bulk porous substrate using an undercutting procedure similar to that shown in Figure 4-13. A script has been developed using MATLAB solvers to numerically predict emitter geometries under conditions of mass transport control. This section begins with a review of some similar codes in the literature before describing the script developed here and presenting selected results.

4.5.1 Previous Simulations of Electrochemical Microfabrication

Under diffusion control, when an estimate of the diffusion layer thickness can be made, etching profiles at the feature scale can be modeled numerically[138, 153, 125] using equations 4.6 and 4.7. Although considered for a primary current distribution, the model of West[154] is mathematically identical to those cited above since in both cases Laplace's equation describes the relevant field. In all cited literature the feature to be etched has been defined by a trench, or cavity, within an otherwise masked substrate. Those results demonstrated that undercutting of the mask will occur with a degree of isotropicity dependent on time, the mask geometry and flow conditions.

The Alkire models[138, 153] are focused on the influence of transverse flow over a rectan-

gular cavity and include a numerical calculation of the flow field for varying Peclet numbers. With increasing flow rates, and hence Peclet number, the model predicts locally enhanced, but less uniform, etch rates with the electrolyte flowing over a masked rectangular cavity. However, as confirmed experimentally[153] at excessive Peclet numbers, the salt film necessary to sustain transport limited etching may be washed away in high flow regions leading to locally high etch rates which are not diffusion controlled.

Both the Madore and West solutions employ a moving boundary method where the etching rate, equation 4.6, and Faraday's law, equation 4.3, give the local rate of boundary recession. A modified concentration distribution for the adjusted boundaries is then determined at each time step using equation 4.7. The model of Madore[125] for titanium etching is notable in that it achieved good agreement with experiments performed in parallel. Specifically both the predicted etch profiles and observed (total) current were found to be in agreement with experimental measurements over time. The resultant profiles showed that although initially relatively anisotropic, the degree of undercutting can be expected to increase in time and approach an isotropic profile.

4.5.2 Model Formulation

A moving boundary routine has been developed to simulate electrochemical etching under transport limited conditions for prescribed geometries and hydraulic boundary layers. The method is similar to that of Madore[125] in that the surface profile and corresponding modified concentration field are updated at each time step by assuming a quasi-static solution to the concentration profile remains valid. Equations 4.20 through 4.22 govern the problem. The code is limited to 2-D problems but can accept either cartesian planar coordinates or cylindrical coordinates assuming an axi-symmetric problem. Unlike in the 1-D approximations described earlier in this chapter, δ in this case refers to a contour within the simulation space prescribed to satisfy $c_\delta = 0$, as in equation 4.21. Similarly s refers to the substrate profile at a given time step, while m refers to the mask surface where perpendicular concentration contours are enforced. In equation 4.22, $\overrightarrow{ds}$ is a vector displacement of the etched surface proportional to the flux of material leaving the surface, equation 4.5 and the simulation time step. The effective density, ρ_{eff}, is equal to the density of the solid material modified by the porosity, such that $\rho_{\mathsf{eff}} = \rho(1 - \phi_p)$, where ϕ_p is the material porosity introduced in section 2.4.3.

$$\nabla^2 c = 0, \tag{4.20}$$

$$c_\delta = 0$$

$$c_s = c_{sat} \tag{4.21}$$

$$\nabla_n c_m = 0,$$

$$\vec{ds} = -dt \frac{DM}{\rho_{\text{eff}}} \nabla_n c_s \tag{4.22}$$

The general process employed to generate etch profiles has been summarized in Figure 4-14. The routine accepts an initial surface profile to be etched and a corresponding masking geometry. This initial profile will typically be a flat surface but can also be, for example, a partially etched structure to be further etched under altered masking conditions. The substrate profile is described by an array of n coordinate nodes. An initial concentration boundary curve, δ, is then prescribed such that equation 4.21 will be enforced in the concentration solver. Both a static and dynamic model for estimating this boundary curve have been investigated here and they will be discussed in more detail below. Once the initial problem is established, the concentration field is calculated using a MATLAB finite element routine to solve equation 4.20. Here a triangular mesh is generated such that at least 1 element edge lies between each surface node. A sample mesh has been plotted in Figure 4-15 for an axisymmetric etch. The field gradient is then solved for each element within the simulation space. The normal component of the gradient at the midpoint between each surface node is approximated by an average over the gradients at each triangle with at least one point touching the surface between nodes. Finally, the gradient at each node is taken as the average of the values at adjacent midpoints.

Displacement vectors are then calculated using equation 4.22 and used to move the substrate nodes. The resultant substrate profile is subjected to some conditioning before proceeding to subsequent iterations. First, non physical nodes including crossed node points and nodes which would lie outside the simulation space are identified and removed. A new curve is then fit to the substrate profile such that the node points are redistributed at uniform spacing along the profile. As the net length of the substrate profile may increase significantly at later iterations, this procedure also allows for extra nodes to be added such that the inter node spacing never strays far from that of the initial profile. If a prescribed

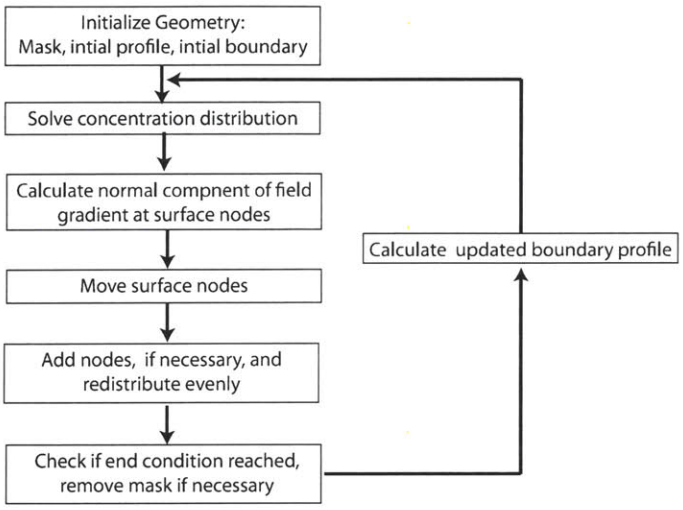

Figure 4-14: Process flow used in a moving boundary code to predict etching profiles for ILIS emitters assuming mass transport limited conditions.

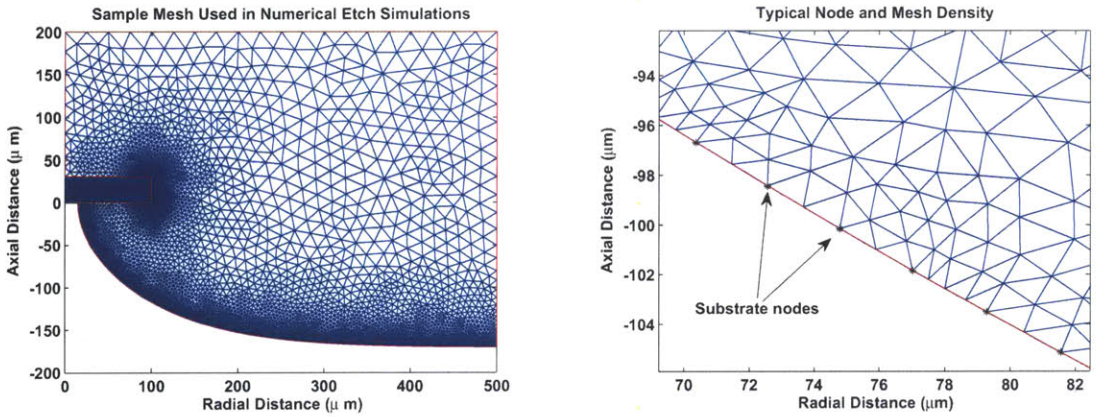

(a) Typical mesh generated using the MATLAB pdetool mesh generator. The dark blue shaded region connected to the origin represents the photoresist mask.

(b) Zoomed in view of the adjacent figure showing a typical distribution of nodes and mesh triangles.

Figure 4-15: Example of the simulation mesh used during simulations. Although a more dynamic boundary model was also used, this example was calculated using a flat simulation boundary above the substrate.

end condition (eg. etch depth, net mass removed etc...) has been met, the simulation ends. Otherwise, a new concentration boundary is determined, depending on the boundary model (see below) before beginning a new iteration. At each iteration, a new mesh is created to reflect changes to the surface and concentration boundaries. The time step during masked simulations has been scaled such that the substrate boundary is moved by 1 μm far from the mask where a planar solution to the concentration problem remains a good approximation. For simulations on sharp edges, such as when the etch has fully undercut the mask, the time step is reduced by a factor of 10.

4.5.3 Model Verification

While similar to the simulation of Madore et. al., this code differs in that a finite element method is used to solve for the concentration profile. However; the quasi-static approach remains identical. Before proceeding with the problem at hand, predicting emitter geometries, this code was applied to reproduce the results of Madore for etching titanium trenches as a means of verifying the code. As in the reference, a hemi-spherical boundary layer of radius 2L was applied and remained fixed above a trench of width 2L during the simulation. Sample results for a mask thickness to trench size, L, ratio of 0.14 are shown in Figure 4-16(a). In the figure, the time step was adjusted at each simulation step to maintain consistency with the reference. However; this practice was not adopted in all other simulations presented here where fixed time steps were used.

The comparison is particularly beneficial in that Madore also confirmed strong correlations between their code and experimentally etched profiles. Profiles generated using the code developed in this research using the same conditions as Madore are shown in Figure 4-16(a). These profiles are in excellent agreement with those found in the reference. It is interesting to note that at early times, the profile is characterized by enhanced etching near the corners of the mask relative to the center of the substrate. This phenomenon has been observed in experiments[125, 133] and has been suggested as a means for creating isolated islands of material when etching a thin film[155]. At longer times a more isotropic etch results. This shift from an-isotropic to isotropic etching can be quantified by an etch factor, E_F, defined as the ratio of etch depth to transverse etching distance (see equation 4.23 and more discussion on this parameter below).

The calculated time dependent current is also in good agreement with the trend pre-

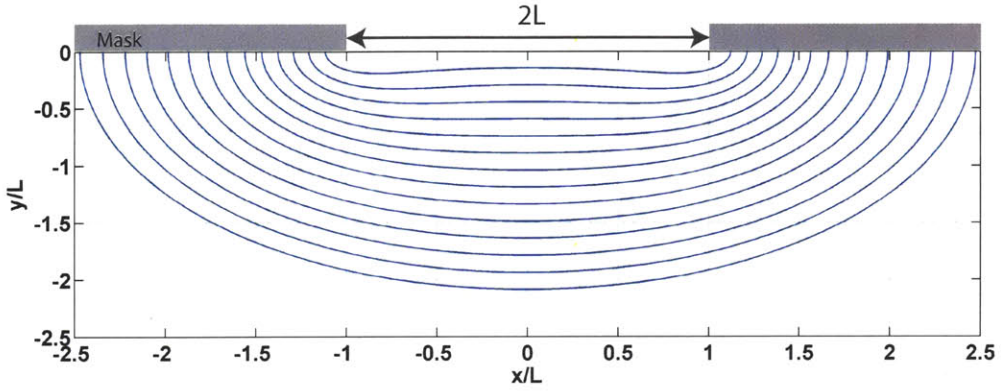

(a) Etch profiles simulated with the code developed here for the same conditions as Madore[125]. The reference used a boundary element method while this code uses a finite element routine.

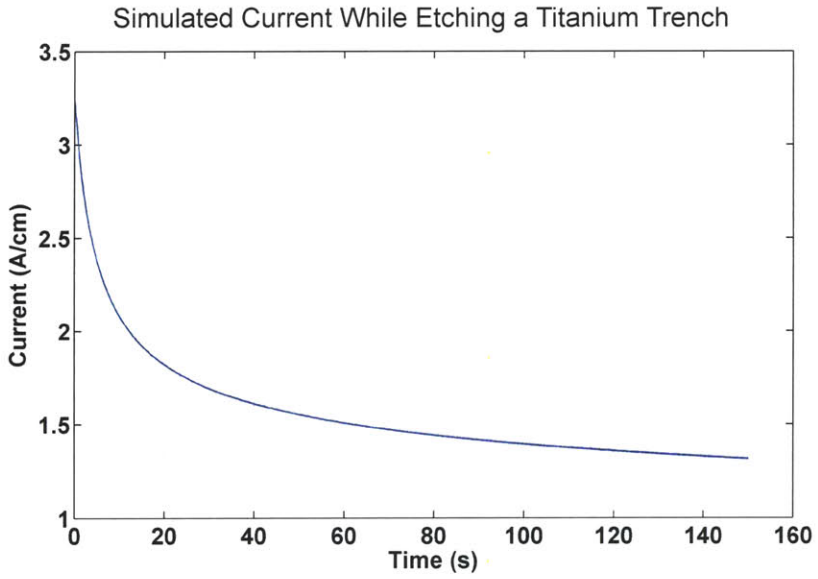

(b) Current versus time (per unit length into the page) for a trench etch in titanium.

Figure 4-16: Reproductions of the results of Madore[125] generated using the code developed here. Both the simulated profiles and predicted currents are in good agreement with the reference.

sented by Madore for a similar geometry. This is of particular note in that it highlights the discrepancy between current decay due to the changes in the substrate profile and that due to forming a boundary layer. Effects of the later, discussed in detail in section 4.4, are not present here as transients are not considered in this simulation. The decay in current shown in Figure 4-16(b) is then only due to the surface boundary relaxing to a state which minimizes concentration gradients as time progresses. According to these simulations, this relaxation dominates over the increasing active area.

4.5.4 Summary of Assumptions for Predicting Emitter Profiles

Applied to the current problem of estimating emitter shapes for porous ILIS arrays, many assumptions have been made. Some of the important assumptions are noted here along with a discussion of their impact on the applicability of the results.

- Surface machining : Applied to porous surfaces, the model assumes that etching progresses at the surface only, with the rate across each pore approaching that for a solid material, as discussed in section 4.3.

- Single emitter : The results assume a single isolated structure and do not take into account interactions with neighboring emitters. This validity of this assumption is therefore reduced at increasing packing densities.

- Quasi-steady state : At each time step, the time-independent diffusion equation (equation 4.7) is assumed valid within the boundary layer. The concentration profile is varied in time only by the alterations to the boundary profiles at each step.

- Stagnant diffusion layer : The diffusion layer is assumed to be stagnant such that equation 4.20 defines the concentration profile. Convection effects are lumped into the estimation of δ, the boundary layer profile.

- Time independent diffusion layer : The problem is assumed to be instantly mass transport limited such that a fully formed concentration boundary layer exists initially. This assumption ignores the transient decay considered in section 4.4, limiting the applicability to cases where the actual etch time far exceeds the decay time scale.

- Axisymmetric model : The linear motion of the etch station agitator used in this research (see Chapter 6) could result in strong variations along the direction of paddle

motion. However; as will be shown with the results in that chapter, at the feature (emitter) length scale, this assumption appears to be adequate in practice when using the final etch process.

- Stiff mask : The mask is presumed to remain stiff and fixed in position as the etch progresses. This may not be valid for thin masks where as material is removed the mask may curve due to flow, residual surface stresses etc... Similarly for very thick masks (as have been used in some tests here) this assumption may no longer hold as the structure becomes too fragile to support the mask.

- Far field behavior : The radial simulation extent was set to 5 times the mask radius where a Neuman type boundary (zero radial gradient) has been enforced. This assumption is analogous to assuming a planar electrode far from the emitter and could lead inaccuracies when applied to arrays with high emitter densities.

4.5.5 Defining an Appropriate Boundary Layer

In the 1-D model of section 4.4 the boundary layer thickness δ was sufficient to describe the problem. However; when estimating profiles for ILIS emitter arrays the situation becomes more complicated. An accurate model for the boundary would require a model of the complex flow pattern around the emitters during fabrication. This pattern would depend on both the shape of fabricated emitters and, at a larger scale, on the overall substrate dimensions and distribution of emitters. Such a model has not been attempted here. Instead, two alternatives have been considered and are demonstrated in Figures 4-17 and 4-18.

The first boundary model, Fig. 4-17, uses a static, planar simulation boundary at a level much greater than the mask thickness. The moving substrate is taken into account by globally scaling the gradients such that a constant etch rate is maintained far from the feature.

As an alternative to this scaled boundary layer, a geometry dependent, boundary curve has been generated using solutions to Laplace's equation. This technique is shown in Fig. 4-18. Here, an arbitrary field $\Phi(r, z)$ has been solved for $\nabla^2\Phi = 0$ with $\Phi([r_s, z_s], [r_m, z_m]) = 1$ and $\Phi(r, A) = 0$ where A is an arbitrary height much larger than the mask thickness. This differs from the solution for c in that Dirichlet conditions are assigned on both the mask and substrate for this initial calculation. The code then selects the value of Φ at large r and

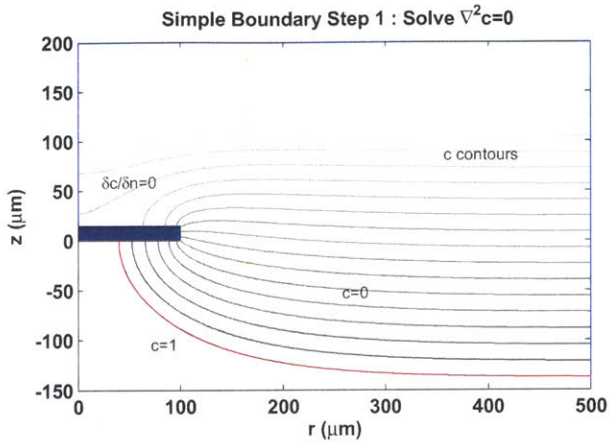

(a) Step 1: Solve Laplace's equation using a boundary a planar boundary at 200 μm.

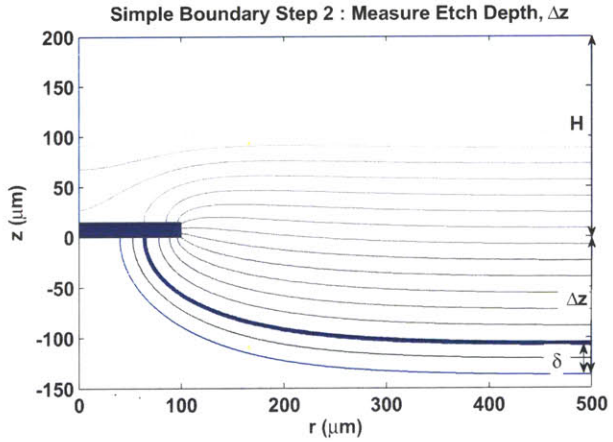

(b) Step 2: Determine the etch depth at 500 μm, from far from the mask.

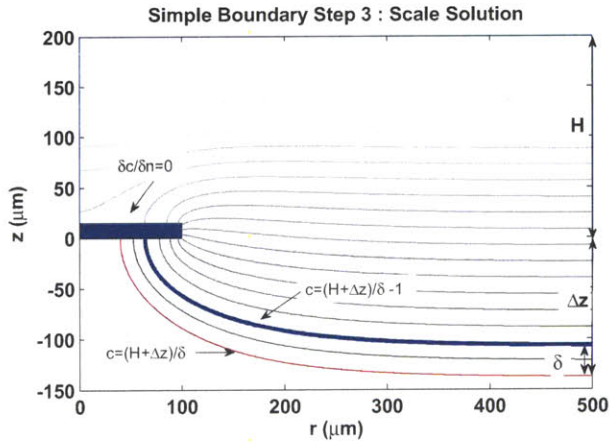

(c) Step 3: Scale the gradients to maintain a constant etch rate in the far field.

Figure 4-17: Steps used for the relatively simple boundary approach. In step 1, the concentration profiles are solved using a fixed boundary. In steps 2 and 3 the gradients are then scaled uniformly to maintain a constant etch rate, as prescribed by the selected diffusion layer thickness, δ, far from the structure.

a height of δ above the surface. The contour of Φ through this point is then selected as the new boundary layer for the subsequent calculation of $c(r, z)$ using equations 4.20 through 4.21. Here the solution again assumes a planar electrode far from the mask; however unlike the simple scaling approach it introduces greater dependence on the mask and emitter geometry as the shape evolves.

As demonstrated in Figure 4-18(c) the moving boundary model leads to an effectively larger boundary thickness, corresponding to reduced convection, under the mask than using the simple scaling model (Figure 4-17(c)). In that regard it is a crude estimation for the impact of the mask on flow hydraulics. However, this alternative scheme for predicting the boundary profile should not be interpreted as an attempt to accurately predict the complex flow description around the emitters during etching.

4.5.6 Results and Sensitivity to Mask Geometry

The script has been executed for a variety of mask geometries and effective boundary layers. The following plots offer insight into the predicted trends. The profiles are presented as 2-D profiles within the coordinate system introduced above. For simplicity the mask itself has not been plotted below. In addition to the profiles themselves, the etch factor E_F, has also been calculated for select conditions. This metric, given by equation 4.23 below[122], has been selected over an aspect ratio (height over diameter) since the tip diameter ($2r_{min}$) is intentionally driven to zero as etching progresses.

$$E_F = \frac{h}{r_{mask} - r_{min}} \tag{4.23}$$

Before presenting the plots it is important to note that these profiles represent general cases for given geometries and are not dependent on the electrochemical cell parameters c_s, M, D or ρ_{eff}. This is so because in each case the time step has been adjusted to ensure a fixed etch depth per time step far from the emitter. Thus, while the real time required to achieve a given profile will depend on the physical conditions, the number of simulation steps remains fixed. For example, if a desired profile is reached after 20 time steps, the predicted time to reach such a profile can be calculated by multiplying the time step for the particular electrochemical conditions by 20 and will therefore differ for different materials and effective densities.

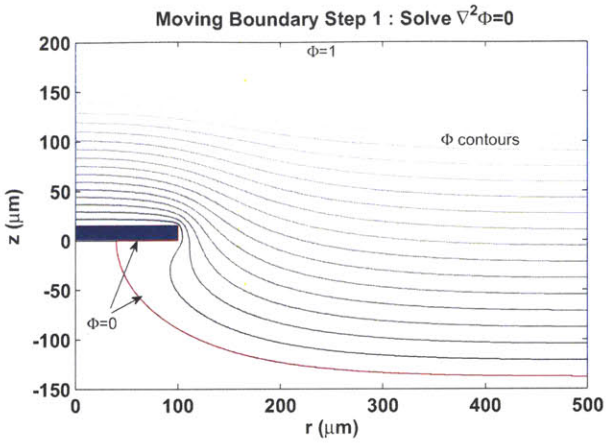

(a) Step 1: Solve Laplace's equation for an arbitrary field Φ using a planar boundary at 200 μm and Dirichlet conditions on both the substrate and mask surfaces.

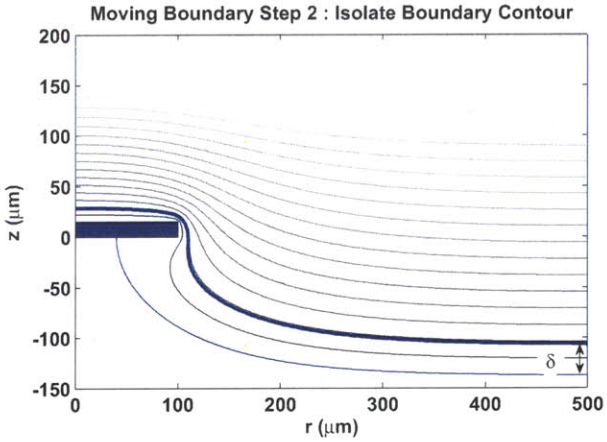

(b) Step 2: Isolate a contour of Φ passing through a point δ above the substrate far from the emitter.

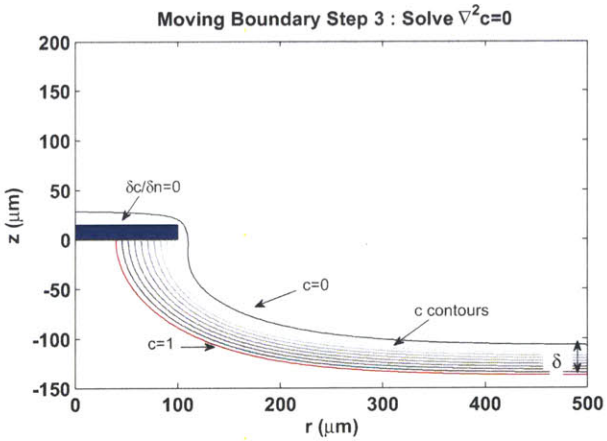

(c) Step 3: Solve Laplace's equation using the contour from step 2 as a concentration boundary. Here a zero gradient Neumann condition is restored on the mask.

Figure 4-18: Steps used to calculated the concentration fields using the moving boundary approach. Here a profile which conforms to the surface is generated in steps 1 and 2 and used as a boundary for solving the concentration field in step 3.

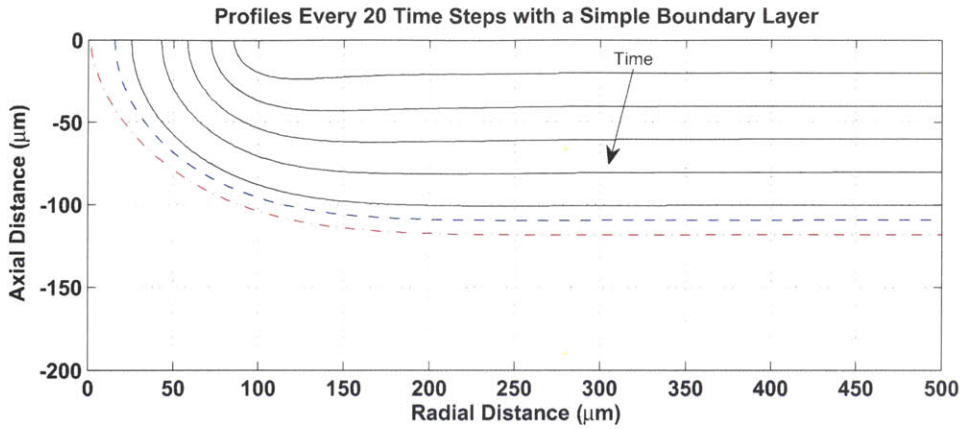

(a) Simulated profiles every 20 time steps for a simple, static boundary layer.

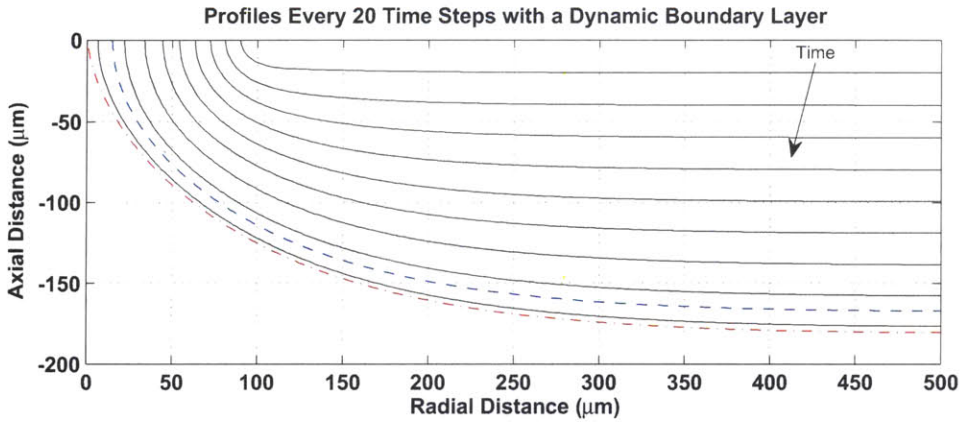

(b) Simulated profiles every 20 time steps using the moving boundary layer approximation.

Figure 4-19: Simulated profiles every 20 times steps for the two boundary models with a 200 μm diameter, 15 μm thick mask. The two dashed lines on each figure are the predicted profiles for maximum undercutting and for a 15 μm radius termination.

Comparing Profiles Predicted by the Static and Moving Boundary Definitions

Figures 4-19(a) and 4-19(b) demonstrate the evolution in time of emitter profiles predicted for the two different boundary layer options considered here. In both cases, a 15 μm thick, 200 μm diameter mask has been considered with 40 μm thick effective diffusion layer thickness. In Fig. 4-19(a), the diffusion layer thickness only manifests as a scaling parameter while in Fig. 4-19(b), the more dynamic boundary layer model introduced above has been used.

In Figure 4-20 the calculated etch factors as a function of the far field etch depth (equal to the emitter height) are plotted. Using the simple boundary model, the etch factor is generally small, beginning nearly isotropic before reaching a maximum at moderate etch

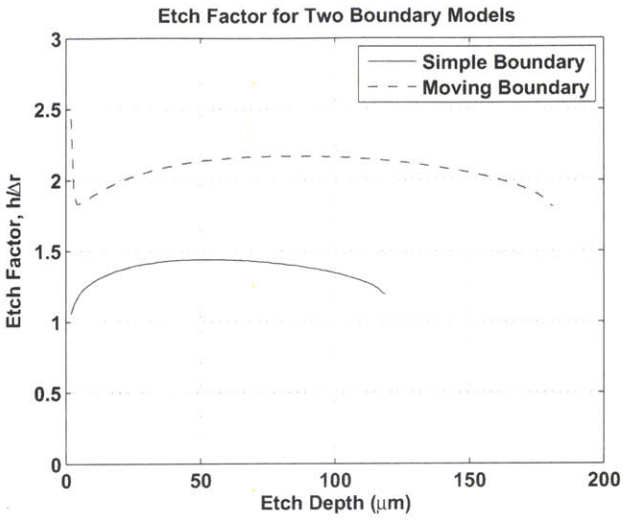

Figure 4-20: Comparing the etch factors predicted using the two boundary models considered here.

depths then decreasing again. Since the boundary thickness was only expressed by a scale factor, the profiles of Figure 4-19(a) are representative of the predicted profiles for any value of δ given this mask geometry. Figure 4-21 below demonstrates the weak dependence on, for example, mask thickness predicted by this type of boundary layer. This simplified model is therefore very restrictive in terms of simulating variations in etch profile due to the boundary conditions. In Chapter 6, section 6.7, we will see that the etch factor and emitter profiles are more accurately simulated with the moving boundary layer model described below.

Profiles Generated with the Moving Boundary Definition

The second, more dynamic, boundary description produces profiles which are significantly more dependent on the geometrical conditions. In general this boundary results in significantly larger etch factors compared with the static boundary model, as shown in Fig. 4-20. The impacts of the diffusion layer thickness on the predicted shapes are explored in the following plots. Figures 4-22 presents the profiles predicted at the point when the emitter tip radius reaches 15 μm for different values of δ. Both plots consider a 200 μm diameter mask which was set to 15 μm and 65 μm thick for Figs. 4-22(a) and 4-22(b) respectively. In the figures, the boundary layer thickness has been stepped from 10 μm to 150 μm in 10 μm increments. Note that for both resist thicknesses with a thin, 10 μm thick, boundary

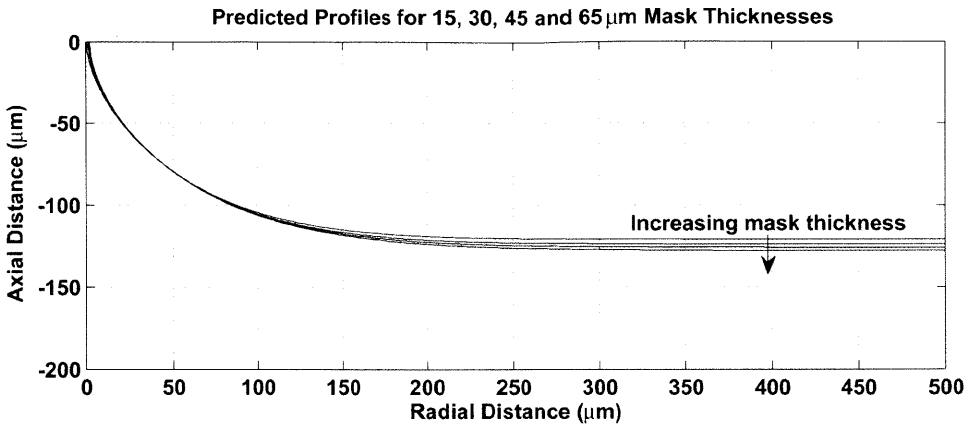

Figure 4-21: Using the static/scaling boundary model, only a weak dependance on mask thickness was observed.

layer the simulations predict a necking behavior. Experimental evidence of this type of phenomenon has been observed and will be discussed in Chapter 6.

In Figure 4-23, the etch conditions were identical to Fig. 4-22 but the etch was allowed to progress to a point where the tip radius approaches zero. This corresponds to the sharpest emitter which can be fabricated before the mask falls off, assuming idealized support for the mask itself.

The impact of inputs on the etch factor has also been explored. Figures 4-24 and 4-25, show the etch factor as function of etch depth with varying diffusion layer thickness for 15 μm and 65 μm thick masks respectively. In the figures, the diffusion layer thickness has been stepped from 20 to 100 μm in 20 μm increments. As in Fig. 4-20, the curves terminate at a depth equivalent to the emitter height when r_{min} goes to zero. These results indicate a trend for increased etch factor for decreasing diffusion layer thickness, δ.

Using this moving boundary definition, the mask thickness can also impact the etch profile. This has been explored again using the etch factor as a metric in Figure 4-26. Here a constant diffusion layer thickness of 40 μm has been enforced while mask thicknesses of 15, 30, 45 and 65 μm were input. For low etch depths, these results predict a transition to larger etch factors, hence reduced undercutting, as the mask thickness is increased.

Figures 4-27(a) and 4-27(b) are an attempt to discern the more dominant trend between mask and diffusion layer thicknesses parameters. Here the ratio of diffusion layer thickness to mask thickness has been held constant at 4 : 3 for three curves and altered slightly to 16 : 13 in the fourth. These correspond to diffusion layer thicknesses of 20, 40, 60 and 80

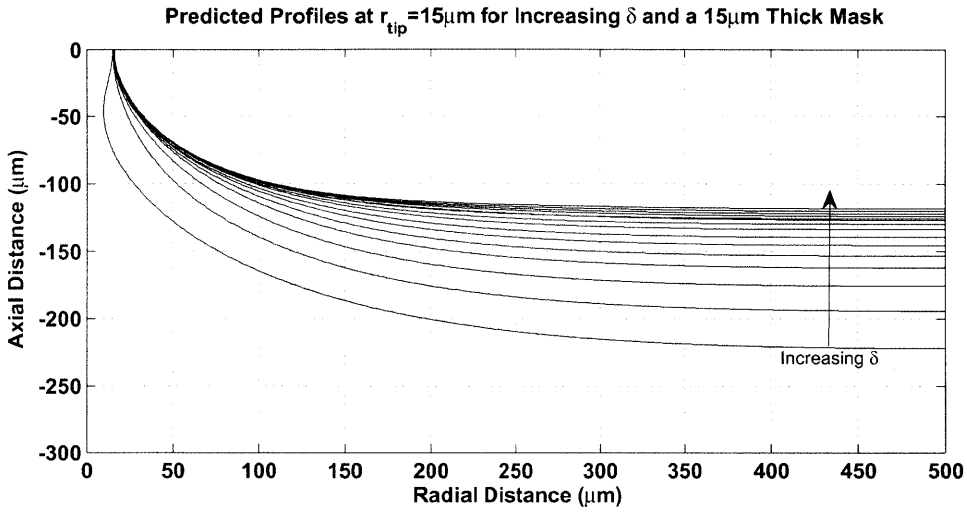

(a) Simulated profiles, terminating at 15 μm radially, for a 15 μm thick, 200 μm diameter mask.

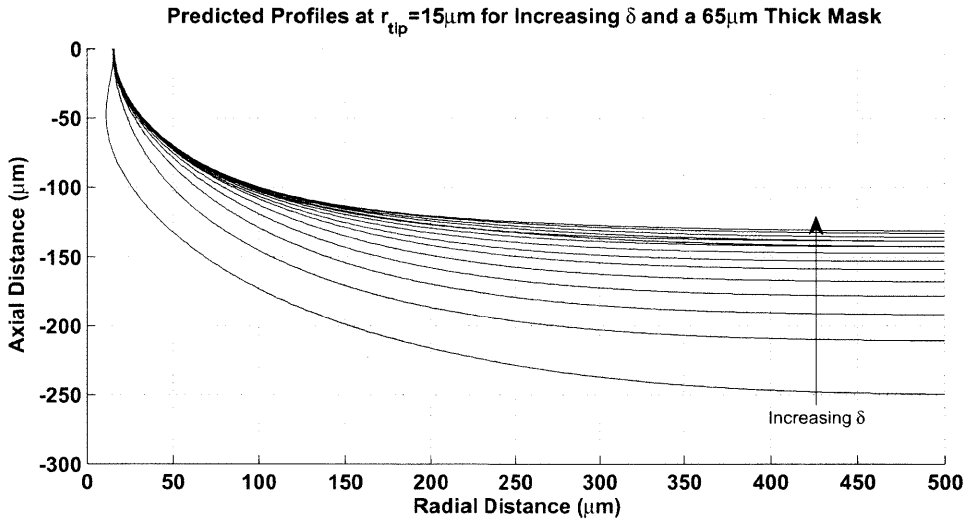

(b) Simulated profiles, terminating at 65 μm radially, for a 15 μm thick, 200 μm diameter mask.

Figure 4-22: Simulated profiles, terminating with a 15 μm plateau radius for two mask thicknesses and varied diffusion layer thicknesses. The diffusion layer has been stepped from 10 to 150 μm in 10 μm increments.

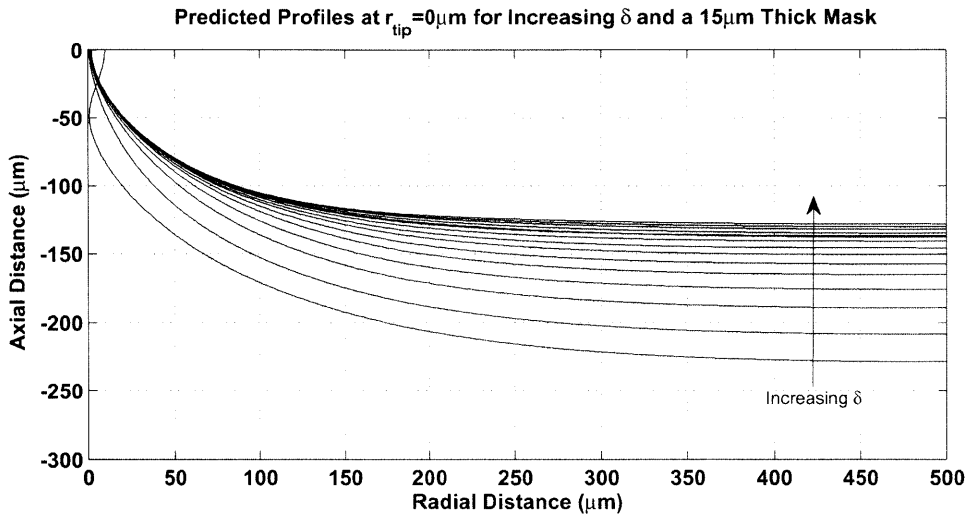

(a) Simulated profiles, terminating at 0 μm radially, for a 15 μm thick, 200 μm diameter mask.

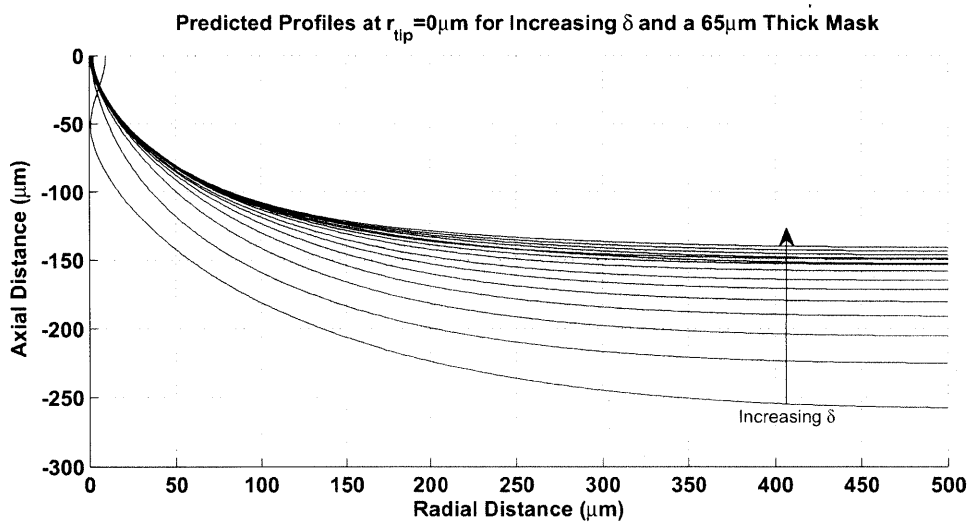

(b) Simulated profiles, terminating at 0 μm radially, for a 65 μm thick, 200 μm diameter mask.

Figure 4-23: Simulated profiles, terminating with when $r_{min} \sim 0$ μm for two mask thicknesses and varied diffusion layer thicknesses. The diffusion layer has been stepped from 10 to 150 μm in 10 μm increments.

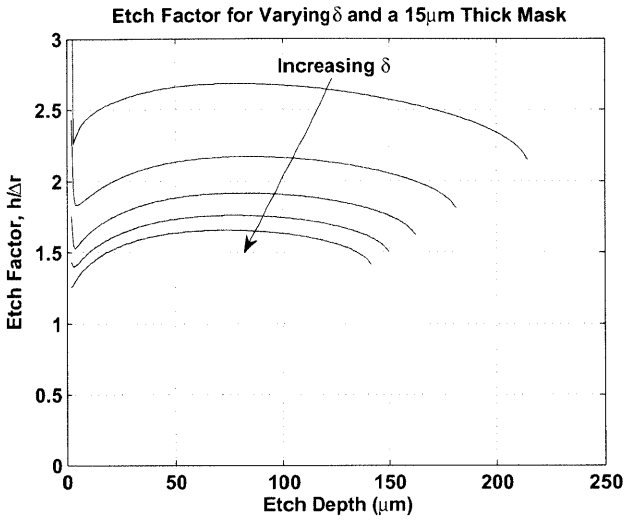

Figure 4-24: Predicted etch factors for a 15 μm thick, 200 μm diameter mask with diffusion layer thicknesses from 20 to 100 μm in 20 μm increments.

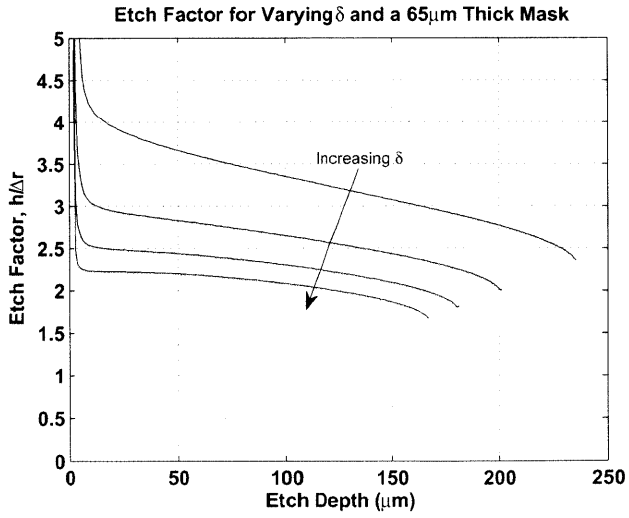

Figure 4-25: Predicted etch factors for a 65 μm thick, 200 μm diameter mask with diffusion layer thicknesses from 20 to 100 μm in 20 μm increments.

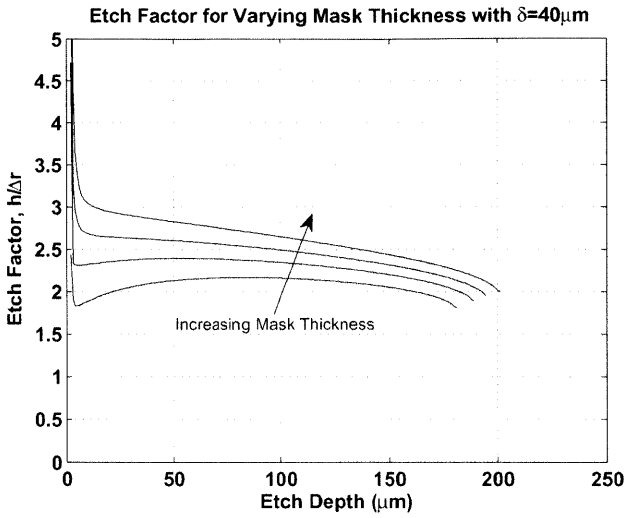

Figure 4-26: Predicted etch factors for a 200 μm diameter mask and a diffusion layer thicknesses of 40 μm with mask thicknesses of 15, 30, 45 and 65 μm.

μm with mask thicknesses of 15, 30, 45 and 65 μm for the four curves respectively. The selection of a 65 μm mask over 60 μm (which would fit with the sequence) was done to coincide with the experimentally tested masks thicknesses (15, 33 and 64 μm, see Chapter 6). The figures indicate the direction of increasing δ beginning from the δ =20 μm, 15 μm thick mask case. These plots demonstrate that the diffusion layer thickness is the dominant trend governing the etch.

The examples presented above have only considered a 200 μm diameter mask. However; since the governing expression, equation 4.20, is linear the results can be geometrically scaled to other conditions if all three geometrical inputs are scaled in constant proportion (δ, mask thickness and mask diameter). In Figure 4-28, the etch factor has been calculated for two cases, first a 100 μm diameter, 15 μm thick mask with a 20 μm diffusion layer thickness. Second, these parameters were doubled and the simulation was run again for a 200 μm diameter, 30 μm thick mask and a 40 μm thick diffusion layer. When the etch factor (a relative property) is plotted as a function of the height relative to the maximum height in each case, the curves are in agreement. Some deviation at low heights may be due to a decrease in accuracy for the 100 μm diameter etch where the time step scaling was not adjusted and remained at a rate of 1 μm per step in the far field.

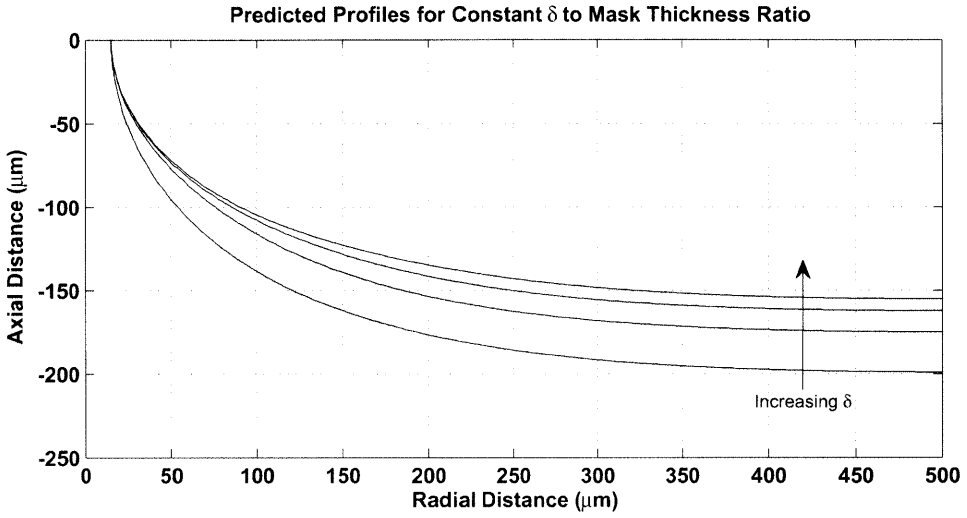

(a) Predicted profiles etching to 15 μm at the apex with a constant diffusion layer to mask thickness ratio of 4:3.

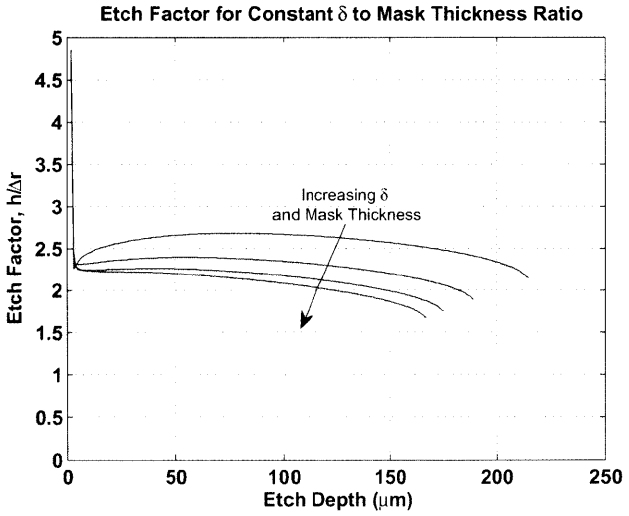

(b) Predicted etch factors etching to 15 μm at the apex with a constant diffusion layer to mask thickness ratio of 4:3.

Figure 4-27: Results for a constant diffusion layer to mask thickness ratio of 4:3.

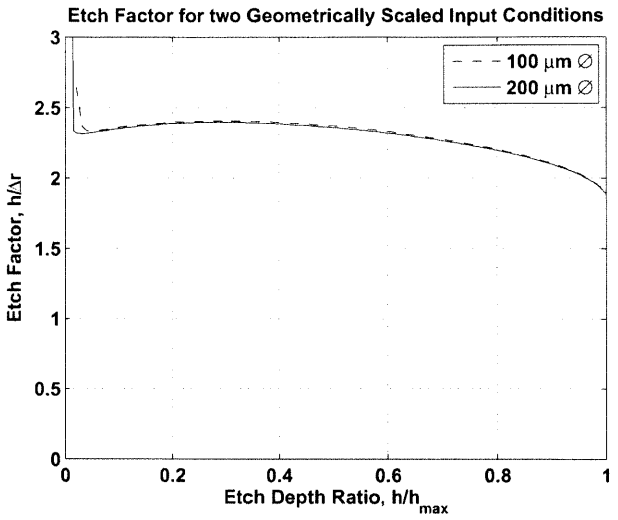

Figure 4-28: The results presented above are applicable to any mask diameter through scaling the solutions. This is demonstrated here for a 100 μm diameter, 15 μm thick mask etched with a 20 μm diffusion layer and a 200 μm diameter, 30 μm thick mask etched with a 40 μm thick diffusion layer.

4.5.7 Discussion and Applications to Forming Porous Emitter Arrays

This simulation has provided insight into what may be expected when forming individual emitters. However the high sensitivity to the effective boundary layer thickness, δ, combined with the highly approximate method used to generate boundaries from this single metric may limit the applicability of the model. Furthermore, the model does not predict the behavior between emitters or at the edges of a substrate where the masked pattern may end. However; the trends may still be insightful when considering the experimentally produced structures in Chapter 6. Furthermore, these simulations give approximations to the emitter geometries which can be used to predict the electric field distribution when used as an ILIS emitter.

The various sample plots presented in the previous section offer insight into the trends predicted by this model. Comparing the results achieved using the alternative boundary definitions, it is clear that the moving boundary can have a significant impact on the etch profiles. However; this significance is decreased for large diffusion layer thicknesses where the two solutions become comparable, as seen comparing Figs. 4-20 and 4-24 where the etch factor at large δ approaches that predicted for the static boundary. This comparison highlights how the moving boundary has provided an additional parameter which can be

employed when attempting to match the experimentally etched shapes and etch times with the simulation. Given a specified mask geometry (diameter and thickness), the only parameter which can be adjusted is the diffusion layer thickness. Using the moving boundary solution, this thickness may be adjusted to yield final profiles which match experiments, however; this does not guarantee that the simulation will also predict consistent etch times. Instead, a combination of these definitions may be more suitable in attempting to predict both time and etch shape such that the diffusion layer thickness is treated as simply a shape modifying parameter and the entire solution scaling is adjusted to match the time dependence. The magnitude of this correction will depend on how accurately this simple moving boundary model matches the complex flow patterns around fabricated structures.

The achievable etch factor, or aspect ratio, can also be interpreted as a limit to the density of emitters, of a targeted geometry, which can be fabricated using electrochemical etching. Clearly the spacing between emitters of a certain geometry must be greater than the mask diameter (assuming circular masks). Consider an isotropic etch such that the etch factor is constant and equal to 1. Under these conditions, a 150 μm tall emitter, as targeted for field enhancement in the emitters fabricated here, would be achieved with a 300 μm diameter mask and hence the array would be limited to $>\sim$ 300 μm spacings. The results presented here suggest that higher etch factors may be possible, resulting in proportionally tighter spacing. However; even for small diffusion layer thicknesses and thick masks, these results predict etch factors no greater than $\sim$ 2.5 at completion. Hence, a practical limit on emitter density for 150 μm tall emitters using electrochemical etching may be reached as the spacing approaches $\sim$ 120 μm. Finally, since etching porous materials requires the diffusion layer thickness to be much larger than the pore size, targeting high etch factors by reducing the diffusion layer thickness may lead to pore damage and/or an ill defined structure. Recall that we have selected 150 μm tall emitters for pores a few μm in size given the arguments of section 2.4. Using other materials, smaller emitters could, of course, be more tightly packed if deemed suitable for operation as ILIS given the pore size and permeability.

4.5.8 Electrostatics and the Need for Secondary Etching

In Chapter 2, $\sim$ 150 μm tall emitters terminated by $\sim$ 15 μm rounded tips were, as an example, motivated to be electrostatically suitable for achieving ion emission from porous

materials. Using the simulations developed in this section, the field distribution for fabricated emitters can now be predicted. In the discussion of emitter electrostatics the tip radius was confirmed as a dominant parameter governing field strength and enhancement. However; these simulations predict a range of tip geometries ranging from a flat plateau (under etched), a very sharp point or a dulled tip (over etched) depending on the etch time for given conditions. The situation becomes more complicated when one considers the effect on tip geometry due to a small perturbation in the diffusion layer thickness.

For a planar etch, equations 4.3, 4.5 and 4.6 reduce to equation 4.24; the etch depth as a function of time is inversely proportional to the diffusion layer thickness. Here ζ is a proportionality constant.

$$\frac{\Delta h}{\Delta t} = \zeta \frac{1}{\delta} \tag{4.24}$$

Hence, for a small perturbation in the diffusion layer thickness such that $\delta = \delta_0 + \delta'$, where δ_0 is a nominal case and δ' is a perturbation, after etching for Δt seconds, the etch depth Δh will be perturbed by h' given by equation 4.25. Here $\Delta h = \Delta h_0 + h'$.

$$\begin{aligned} \frac{\Delta h}{\Delta h_0} &= \frac{\delta_0}{\delta} \\ 1 + \frac{h'}{\Delta h_0} &= 1 - \frac{\delta'}{\delta_0} \end{aligned} \tag{4.25}$$

As an example, consider the three profiles plotted in Figure 4-29. Here the far field (planar) etch depths are $\sim$ 170.9, 180.4 and 188.1 μm. These were generated for a 200 μm diameter, 15 μm thick mask, with a 40 μm diffusion layer thickness. Taking the 180.4 μm deep etch, curve A2, as the nominal case and referring to equation 4.25, these three etches represent approximations to the profiles that can be expected due to a diffusion layer thickness perturbation equal to their percent change from the nominal case. Specifically, curve A1 at 170.9 μm, equates to a roughly 5 % increase in the diffusion layer, or 2 μm, while curve A3 at 188.1 μm approximates a 4 %, or 1.5 μm, decrease in the diffusion layer. Numerous sources for errors of this magnitude could exist, including flow and temperature non uniformities across a wafer.

The discrepancies are highlighted by considering the electrostatic distribution for a scenario as in section 2.4.2. Here the potential distribution for an electrostatic grid has again been solved to determine the electric field magnitude along the emitter surface. As in section 2.4.2, a 200 μm diameter, 50 μm thick grid positioned 100 μm above the emitters

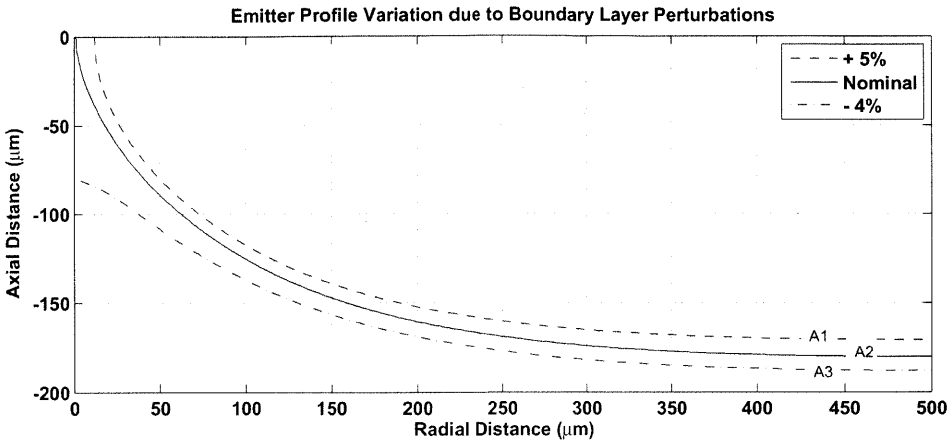

Figure 4-29: Single step etching example with a small variation in diffusion layer thickness.

has been used in simulating the electrostatic fields. The relative field strength and angle relative to the central axis are plotted in Figure 4-30. The peak field strength is also listed, in the form of a field enhancement compared with the far field (planar) solution. Ideally the peak electric field would occur at the emitter tip (path length 0 in the plot), be axially aligned (have a 0^o angle) and drop off quickly preventing off axis spurious emission. This configuration would support emission focused near the tip with low beam divergence angles. Thus, in the figure, an ideal emitter is one where the peaks of the upper and lower plots are spaced as far apart as possible. The figure demonstrates that the under etched, A1, and nominal, A2, cases yield strong field enhancement but could result in highly divergent beams as strong fields are expected on highly off axis surfaces. Meanwhile, the over etched case features a peak field at low surface angle but the field enhancement is small due to the reduced emitter height. Hence in practice, emission may be dominated by curves A1 and A2 due to strong electric fields but yield poor performance due to the highly divergent beam expected.

This discussion also neglects the hydraulics of the resultant emitters. As discussed in section 2.4.3, very sharp emitters, such as A2, may not support strong emission at the tip due to the high flow impedance or an ill defined flow path as the pore and tip dimensions become comparable. Similarly, depending on the selected pore geometry, the sharp edges of curve A1 may not yield emission sites (pores) at the peak field location.

Although a slightly over etched emitter could be suitable for ILIS emission from a practical standpoint, this discussion demonstrates that an array of uniform emitters targeted

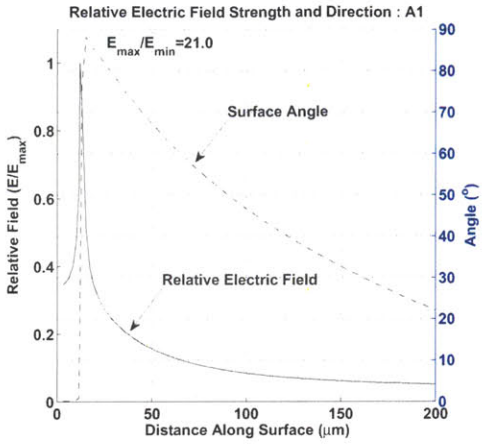

(a) Electric field magnitude and direction with $\delta \sim 1.05\delta_0$.

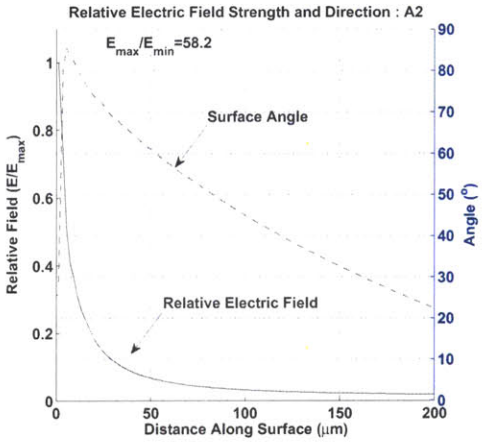

(b) Electric field magnitude and direction with $\delta = \delta_0$.

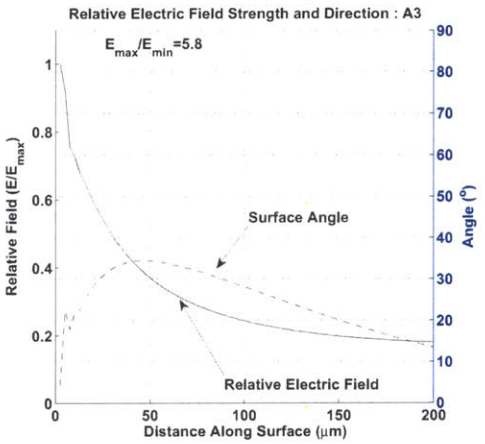

(c) Electric field magnitude and direction with $\delta \sim 0.96\delta_0$.

Figure 4-30: Relative electric field strength and surface angle relative to the axis of symmetry as a function of distance along the surface from the apex.

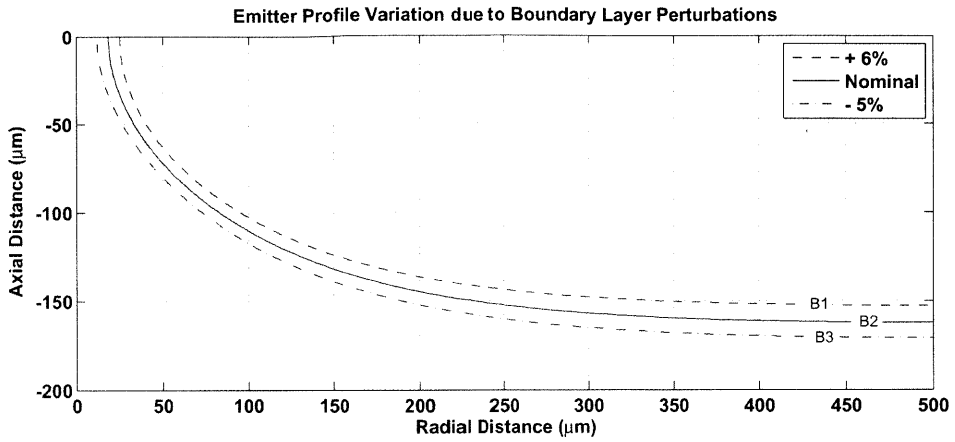

Figure 4-31: Simulated first step of a two step etch process. The etch has intentionally been stopped with relatively large plateau radii.

to such a profile would be extremely difficult to achieve. As an alternative, a two step etching method has been considered. Here an initial etch targeted to create under etched plateaus with a moderate diameter can be performed before the mask is removed chemically and the sample is etched again. This procedure is comparable to that performed by Tajmar et. al. as a post processing step for porous tungsten liquid metal ion source thrusters[30], although the overall geometries are significantly different. The benefits of this procedure are again more clear with an example.

Consider the same etch conditions used above, but with the etching stopped at a nominal case where the maximum depth is 162.4 μm leaving a 19 μm diameter plateau at the tip. This case has been plotted in Figure 4-31 as curve B2 along with two more profiles again corresponding, through equation 4.25, to a small deviation in the diffusion layer thickness. Specifically, curve B1 was terminated at a 152.8 μm depth while curve B3 was terminated at 170.9 μm and is identical to curve A1 of Fig. 4-29. Compared with the previous example, these curves correspond to similar percent deviations in δ; 6 % larger and 5 % smaller for curves B1 and B3 respectively.

These curves have then been input to the code but without a masked region. A secondary etch was then simulated such that a far field etch depth of 2 μm was approximated in each case, see below for a discussion of the challenges inherent in implementing such an etch. The resultant profiles are plotted in Figure 4-32. The secondary etch has favored the sharp edges of the plateaus leading to rounded tips with minimal impact on the shape far from

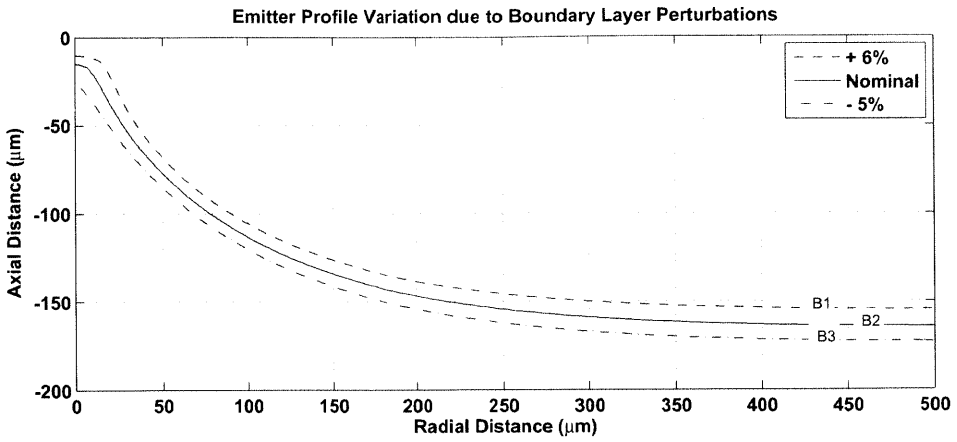

Figure 4-32: Simulated second step of a two step etch process. The etch has intentionally been stopped and then etched again with the mask removed in between.

the tip. Simulated 3-D plots of the resultant profiles from both processes are also presented in Figure 4-33.

The electrostatic distributions for this two step etching process have been simulated as in the single step process above yielding Figure 4-34. Again, the plots present the variation in field relative to the peak field for that structure while also indicating the field enhancement over the planar solution. In this case, curves B2 and B3 feature strong fields close to the emitter tip and at much lower surface angles compared with curves A1 and A2 above. Curve B1, derived from the largest diameter plateau, may be less desirable as the peak field is reached farther from the tip and at slightly larger surface angles. However; note that in this case the more ideal curves, B2 and B3 feature significantly stronger field enhancement than curve B1. Thus, unlike the scenario above where curve A3 resulted in an axial peak field but very low field enhancement, on a wafer scale emission from more ideal tips could dominate if a two step etch process is used. Finally, the broadened electric field peaks may be more accommodating to configurations where the distribution of allowable emission sites is finite (for example a relatively large pore structure).

Given these examples it appears that emitters formed using a two step process may yield better performance across a wafer, particularly by increasing robustness to variations in the etch conditions. However; referring to the discussion in section 4.4, smooth short etches may be inherently difficult to achieve, particularly on porous materials. There it was motivated that etch times larger than $\sim 0.5\ \tau$ would be required to fully form a diffusion

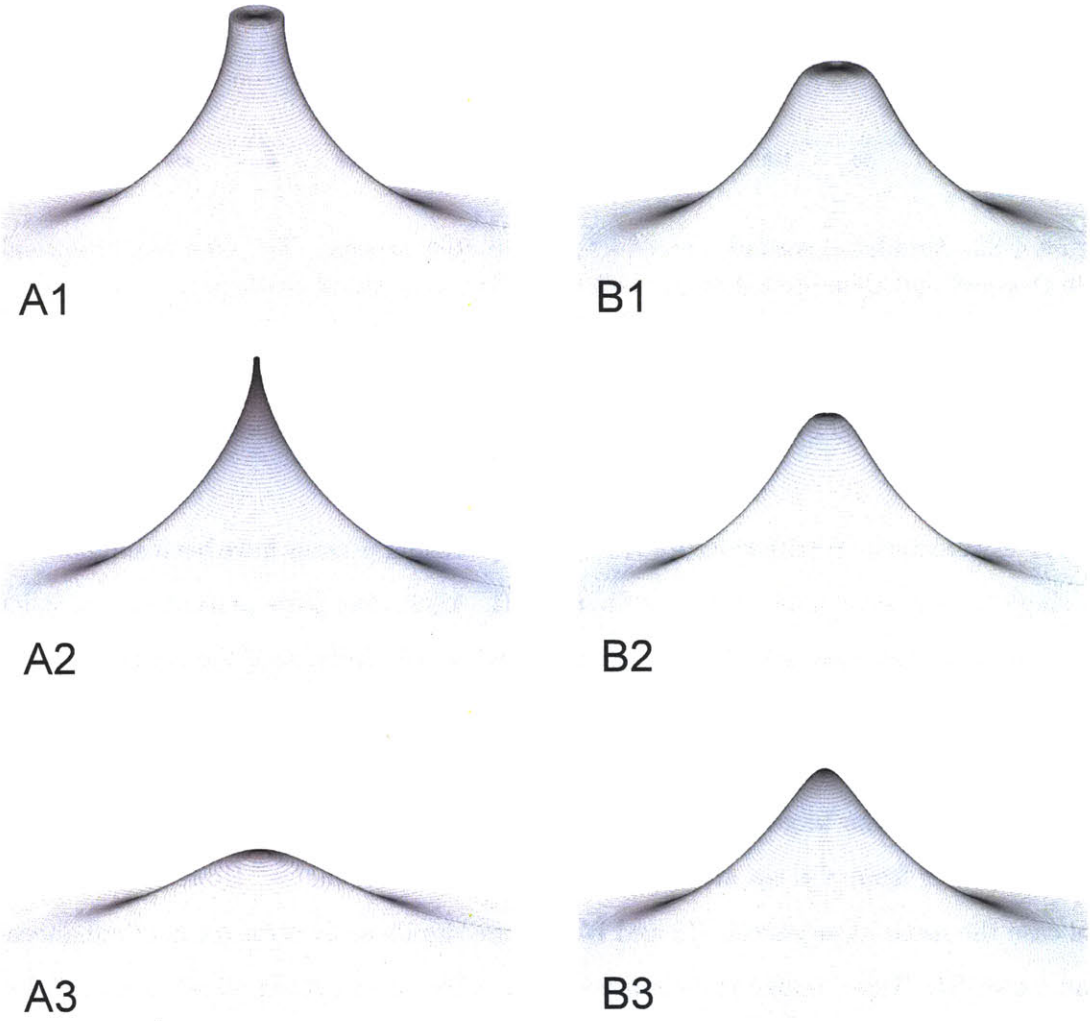

(a) Emitter variability for a roughly ± 5 % diffusion layer variation when attempting to target very sharp emitters (A2) with a single etch step.

(b) Range of emitter shapes predicted for similar variability to the adjacent figure but using a two step etch process.

Figure 4-33: Simulated 3D visualizations of predicted emitter shapes using one and two step etch process with a roughly 5 % variation in diffusion layer thickness.

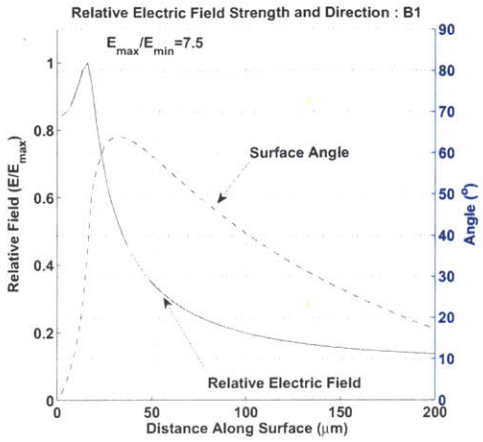

(a) Electric field magnitude and direction with $\delta \sim 1.06\delta_0$.

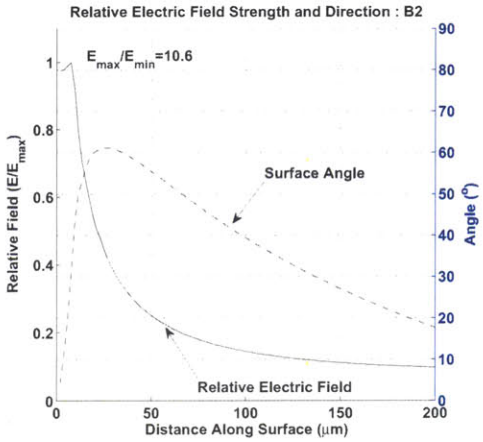

(b) Electric field magnitude and direction with $\delta = \delta_0$.

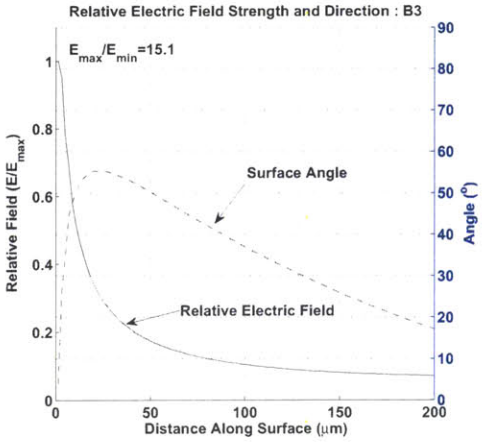

(c) Electric field magnitude and direction with $\delta \sim 0.95\delta_0$.

Figure 4-34: Relative electric field strength and surface angle relative to the axis of symmetry as a function of distance along the surface from the apex.

layer. For $\delta \sim$ 40-60 μm and a diffusivity of 6.6 x 10^{-6} cm^2/s, this corresponds to $\sim$ 1.2-2.7 seconds. Meanwhile, using Faraday's law, equation 4.3, etching 2 μm of solid nickel with an effective valence of 2 and $C_{sat} \sim$ 4.8 M/L[130] through a planar configuration would require at least 3.8 to 5.7 seconds over the same range of diffusion layer thicknesses. Because the current is significantly higher during the transient phase, these values are a significant over approximation. Therefore, in practice, the secondary etch step simulations may not be valid in that they were assumed to occur for an initially fully formed diffusion layer, ignoring the transient phase. Applied to porous material, the situation may be more dire in that significant etching within the surface pores may occur during the transient phase. In this research, an attempt has been made to overcome this challenge through additives to the electrolyte (see section 4.1.4). This process and its results applied to forming arrays of porous ILIS will be demonstrated in Chapter 6.

Chapter 5

Design of a Demonstration Thruster Array

The electrochemical method described in the previous chapter has been integrated into a design for a complete thruster developed in collaboration with colleagues within the MIT Micro Technologies Laboratory (MTL) and the Space Propulsion Laboratory (SPL). This chapter summarizes the design goals and the overall fabrication process developed by the group.

5.1 Target Performance

An array of 480 emitters spaced, 450 μm apart has been targeted within a 12.2 x 12.2 x 2 mm package. Given the previous emission tests using porous emitters, wetted with EMI-BF_4, by Legge where beams of more than 1 μA of current and $\sim$ 0.1 μN of thrust per emitter were measured, the arrays here were targeted to approach $\sim$ 500 μA of total emitted beam current and thrusts up to $\sim$ 50 μN. The corresponding thrust density, $\sim$ 0.3 N/m^2, would therefore begin to approach that available from gridded ion engines[10] while confining the source and feed system to a very small and modular device. In practice, a number of modules (at least two for charge neutrality) would be operated at any given time on a spacecraft. As was discussed in Chapter 1, a controlled set of these thrusters could provide sufficient thrust to achieve both simple orbital manoeuvres and attitude control.

Given the results in section 2.4.2, for planar emitters over $\sim$150 μm tall, the field strength for a $\sim$ 15 μm radius tip, as used by Legge for porous emitters, is similar to that

for an infinite paraboloid. Hence for emitters with similar tip radii, this design was targeted to operate at applied potentials comparable to those used by Legge ($\sim$ 1-3 kV). However; the relatively small grid orifices and separation distances, see section 5.5 below, along with larger pores, see section 5.4, could lead to somewhat lower starting potentials compared with Legge. For an ion beam produced at $\sim$ 1 kV, composed of equal parts monomer and dimer ion species the equivalent specific impulse would be $\sim$ 3000 s and 2200 s for EMI-BF_4 and EMI-Im respectively.

5.2 Thruster Package Overview

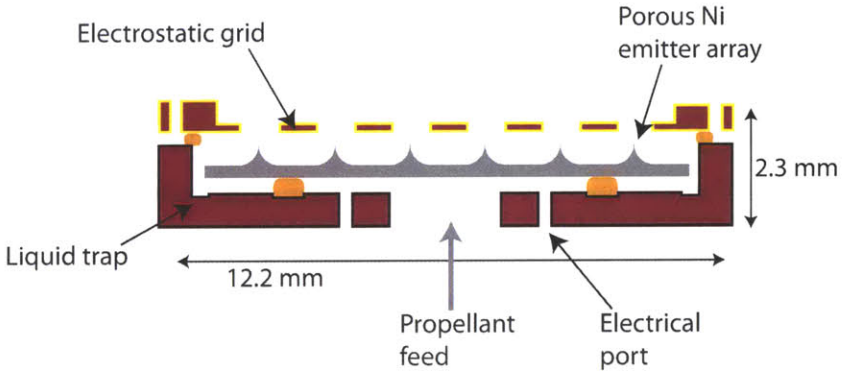

Figure 5-1: The complete thruster package includes a silicon frame, the porous emitter array and an electrostatic grid. This first generation design includes a shallow liquid trap, a 4 mm diameter propellant feed port and two small 0.7 mm electrical ports.

The complete thruster package is shown schematically in Figure 5-1. A porous nickel emitter array has been bonded to a silicon frame using epoxy. A single electrostatic grid has been bonded, again using epoxy, to the silicon frame such that it is aligned with the emitters below. The 4 mm diameter hole at the center of the frame allows ionic liquid to be added to the substrate, an external propellant tank (not used here) could alternatively be coupled through this port. Two 1.2 mm diameter electrical ports have also been included in this design. However; in practice for this research since no external propellant tank has been used, electrical contact was made using the larger central orifice. A small liquid trap, 0.7 mm wide, bounds the base of the frame. This trap was intended to prevent any excess propellant from reaching the extracting grid. Both the substrate to frame and frame to grid

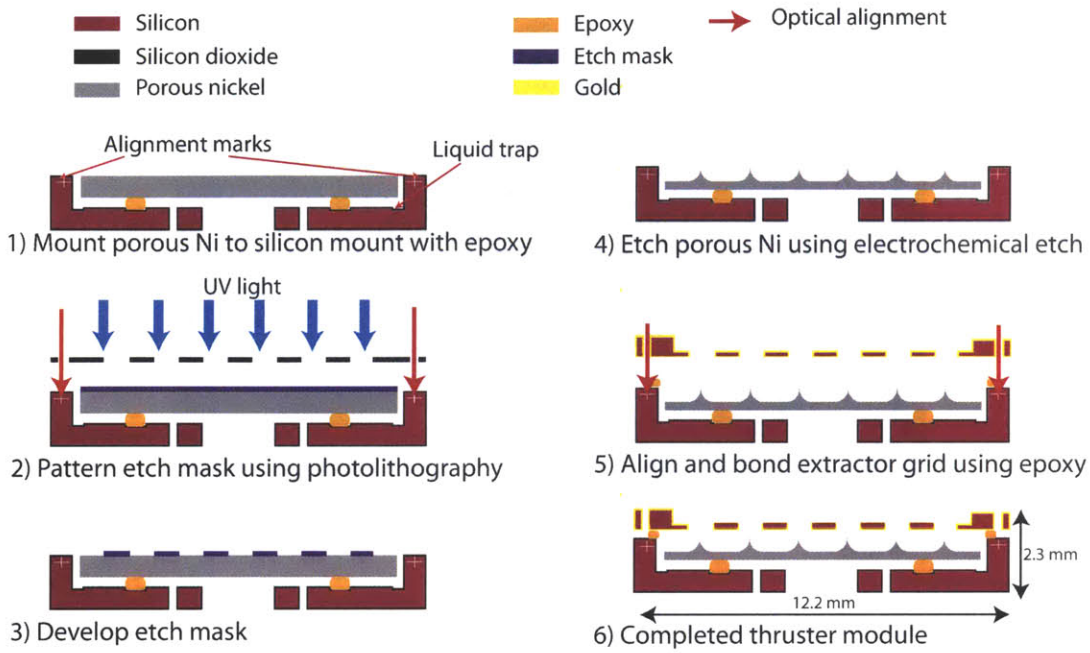

Figure 5-2: An overall fabrication process for aligned, arrays of porous ILIS featuring electrochemical etching of a bulk porous substrate.

epoxies were electrically insulating (see details below) while 1 μm of silicon oxide was also grown on the frame to enhance electrical isolation.

Once assembled, the empty mass was roughly 0.7 ± 0.1 g varying with the grid material type and dimensions along with the amount of epoxy used in bonding. The porous nickel wafer, discussed below, allowed for $\sim$ 35-40 μL of propellant to be stored within the device, varying with the emitter geometries and epoxy technique.

5.3 Overall Fabrication Process

Electrochemical etching under diffusion control will be used to effect surface micromachining of a bulk porous metal substrate through a dry film polymer mask. The electrochemical etching process has been integrated into an overall process for the thruster package, including aligned extractor grids, shown schematically in Figure 5-2. This procedure has been developed in tandem with Hanginq Li of the MIT Microsystems Technologies Laboratory (MTL)[156]. All silicon processing has been performed by Dr. Li within MTL. Here an oxidized silicon frame houses a bulk porous sample from the beginning of the processes. Dry

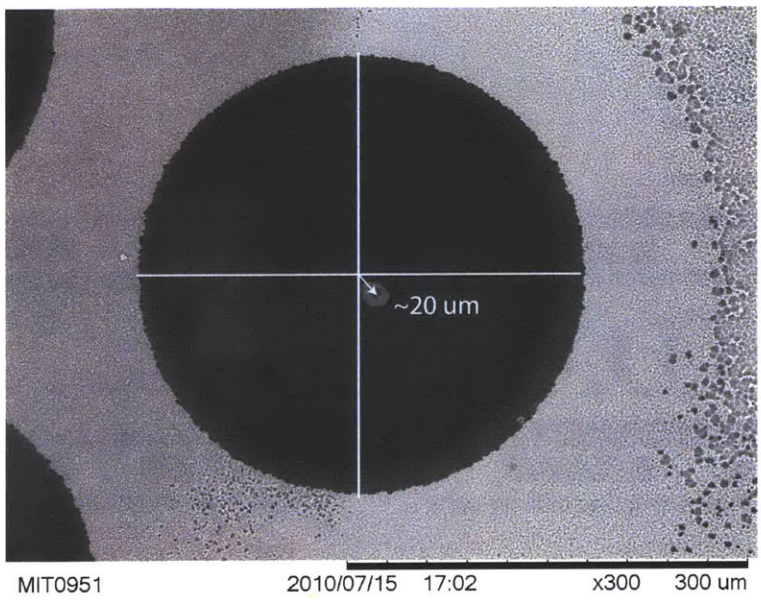

Figure 5-3: An example of the typical alignment accuracy achieved using this process during this research. Alignment has been made to markings on the silicon frame during both the array lithography and grid bonding steps, yielding 10's of μm alignment. In this image a solid emitter is shown.

film photoresist is applied to the surface and patterned using photolithography, see section 6.2.1. Alignment of the mask pattern during lithography is performed with reference to alignment marks on the frame, removing any dependance on the initial position of the porous metal within the frame. The entire sample is then inserted into an electrochemical etching station where, even for electrolytes which may electrochemically react with the silicon frame, unwanted reactions can be avoided by isolating electrical contact to the porous metal sample.

Finally, after etching and cleaning the array, an electrostatic grid can be bonded to the package. Here the alignment is performed using the same alignment marks, located on the silicon frame, used when masking the porous metal. Under this scheme the overall alignment uncertainty can be reduced to that inherent with the equipment used during the lithography and bonding steps (10's of μm to date). Figure 5-3 is a typical example of acceptable alignment, achieved using the alignment marks shown. This example used a solid emitter array to test the alignment technique.

Figure 5-4 contains sample photographs of the empty silicon frame, a frame including an etched porous emitter array and a complete package. The alignment markings shown

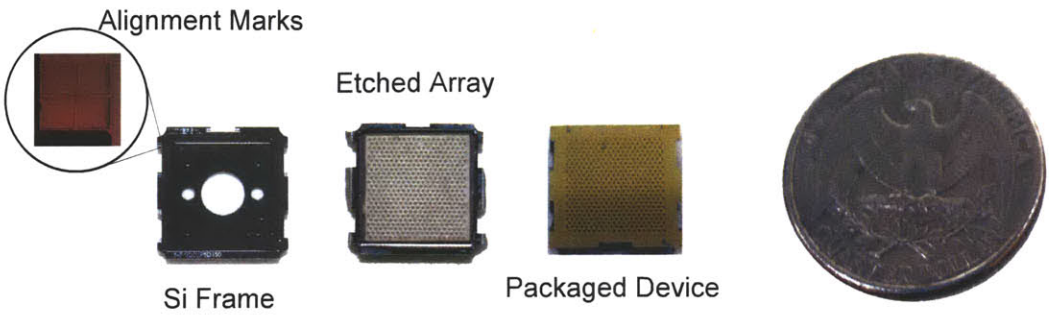

Figure 5-4: Examples of an empty silicon frame, highlighting the small alignment marks, a package after etching the emitter array and a completed device.

are matched with similar features on the electrostatic grids.

5.3.1 Available Epoxies and Application Technique for Porous Materials

Three epoxies have been used successfully for the two epoxy bonding points, between the frame and porous sample and between the frame and grids. The process of selecting suitable epoxies and determining an application method has been done in collaboration with Pablo Diaz Gomez-Macqueo of the Space Propulsion Laboratory. Some details of the epoxy requirements, along with the final process used to apply epoxy to porous samples are discussed here.

The silicon frame to porous metal bond must satisfy several requirements. First, this epoxy must be chemically compatible with the variety of solutions used throughout both the etching and cleaning processes. Specifically, as detailed in the next section, the cured bond was exposed to sodium hydroxide (1N), hydrochloric acid (2N), nickel chloride ($\sim$ 3M), sodium carbonate ($\sim$ 1%), acetone, methanol, isopropanol and both EMI-Im and EMI-BF_4 ionic liquids. The bond was heated to over 115 ^{o} after curing during the masking process (section 6.2.1). Electrically, the oxide coating described above was intended to insulate the bond from the, possibly, charged frame. However; good electrical insulation was nevertheless desirable for redundancy. Finally, all epoxies were required to have minimal outgassing rates such that continued operation in vacuum would not degrade the bond. Two products supplied by Epoxy Technologies, Billerica MA, were identified to meet these requirements. Specifically, a combination of EPO-TEK 377 and H72 epoxies have been used. Both epoxies meet NASA's low outgassing standards[157] and have a specified resistivity greater than

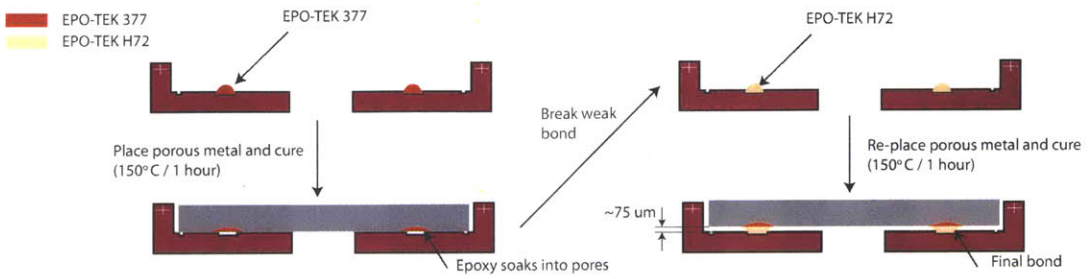

Figure 5-5: The bond between the porous sample and the silicon frame, made before etching, was done with two epoxies. The first epoxy was allowed to penetrate the pores and cure. The second, more viscous, epoxy formed the final bond and a roughly 75 μm gap between the metal and silicon frame.

10^{13} Ωcm.

The two part bond process, outlined in Figure 5-5, was developed after extremely poor yields were achieved with these, and several other, epoxies when used in a single step. Specifically, relatively viscous epoxies were desirable to minimize the amount of epoxy wicked into the porous media before the epoxy was sufficiently cured to harden. However; the majority of the epoxies tested tended to transition through a relatively low viscosity phase when heated but not fully cured. This resulted in, typically, weak bonds and poorly cured epoxies even with numerous attempts at refining the curing schedule. In the final process, small drops of the low viscosity 377 epoxy were allowed to wet the porous metal at points in line with the frame bond pads. After 1 hour at 150^o C, this epoxy did cure, although completely within the pores. However; this then provided a patch of clogged pores such that the relatively high viscosity H72 epoxy could be used to make the final bond. The combined samples were then heated for another hour at 150^o C to complete the curing process. During this final cure, a microscope slide was placed on top of the samples to promote a flat surface, this was, of course, not particularly accurate and should be updated if future work continues with this process. If properly cured the bond showed good resistance to the listed chemicals.

The silicon frame to electrostatic grid bond was extremely problematic, these issues are discussed in section 7.4. The original design intended to use the H72 epoxy listed above. However; the most successful arrangement, detailed in that section, used a viscous, single component, epoxy resin supplied by Epoxies Etc. of Cranston RI. Specifically, type 10-3784 epoxy resin was used and cured for 1 hour at 150^{o}C on a hot plate. In all tested cases, the

grid to silicon frame gap was controlled using thin sheets of kapton or teflon tape to form temporary spacers. These spacers were removed after curing prior to any testing.

5.4 Porous Material

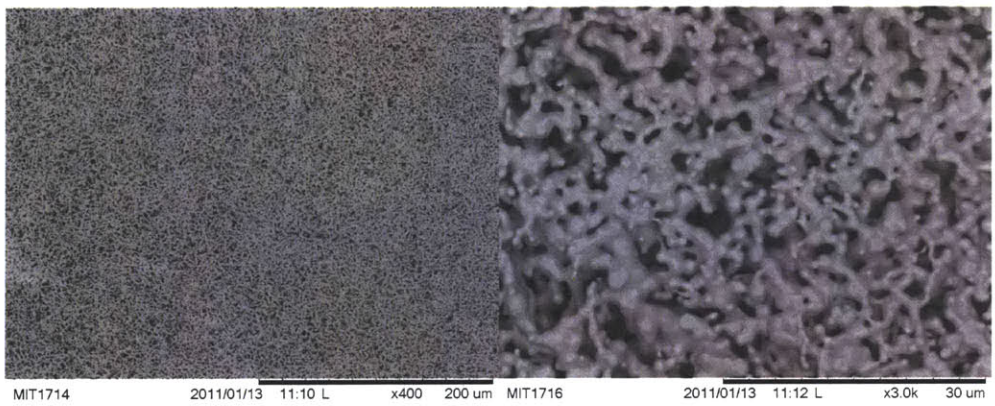

Figure 5-6: SEM images of the porous nickel material used to fabricated emitter arrays within the overall process of Fig. 5-2.

Porous nickel has been supplied by Chand Eisenmann Metallurgical of Burlington, CT. The material has been sintered using nickel powders produced using a nickel-carbonyl process. The supplied specifications for the material were 0.05 micron grade with a relative density of 65 %. However; direct measurements of the material volume and mass suggest the density may be closer to 55 %. Figure 5-6 shows an example of the initial material as supplied from the manufacturer before processing. Once nickel was identified as a suitable material for the electrochemical process (section 6.3), selection of this particular material was largely based on commercial availability and cost. The apparent pores are quite large compared with the porous tungsten used previously (section 2.2.3), with void spaces reaching roughly 5 μm in some cases. As motivated in section 2.4, changes to the porosity, and therefore permeability, may impact the performance compared with previously tested tungsten emitters. For example, an increased pore size could lead to reduced starting potentials as discussed in section 2.4.1. Finally, the relatively large pores, compared with the targeted tip radii, were expected to yield emitters which could no longer be considered as a continuum at the tips. Instead the pore structure could have a significant influence on the final topography for electrostatics and the ultimate beam emission characteristics (angle,

intensity). Despite these possible concerns; this material was found to be sufficient to both demonstrate the fabrication scheme (Chapter 6) and achieve electrospray emission (Chapter 7).

5.4.1 Emitter Lithography Masks

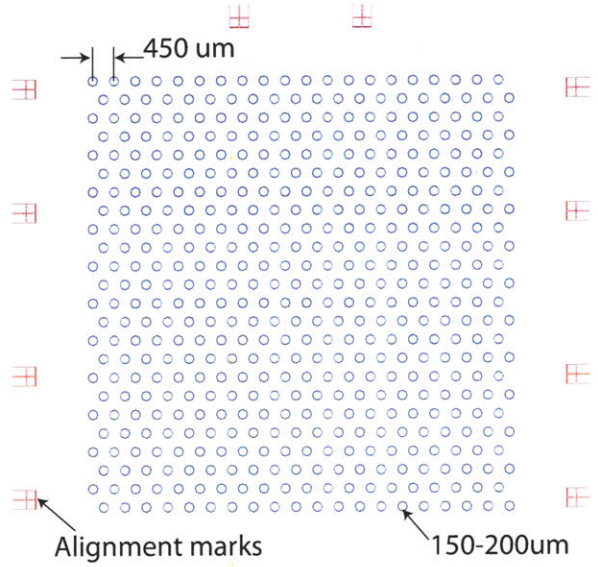

Figure 5-7: An example (outline) of the photolithography masks used to pattern porous metal housed within the silicon package described above.

Figure 5-7 shows an example of the masks used in patterning porous nickel for fabricating the emitter arrays. The features around the perimeter of the mask are the alignment marks, used to maintain alignment between the emitters and the package regardless of the physical position of the porous metal substrate.

The simulation results in section 4.5 predicted etch factors between $\sim$ 1.5 and 2.5 depending on the prescribed conditions. Two mask diameters expected to yield emitters greater than 150 μm tall have been used during development of the fabrication process, 150 and 200 μm. The final process used to create successfully operated emitters used a pattern of 200 μm diameter masks.

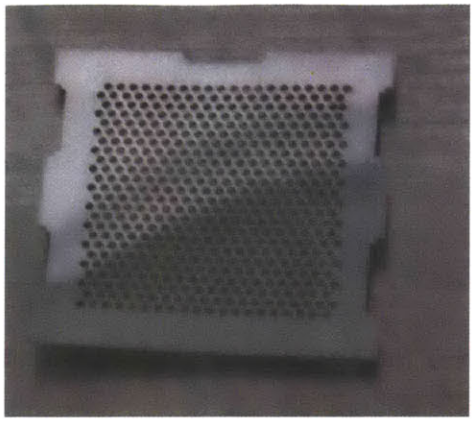

Figure 5-8: Photograph of a stainless steel, laser cut grid. These grids were very thin but inherently wavy, leading to uneven tip to emitter heights.

5.5 Electrostatic Grids

Two types of grids were available: the microfabricated, gold coated silicon grids shown in the designed process flow, Fig. 5-2, and laser cut stainless steel grids. The final silicon grids used here were approximately 100 μm thick, at the orifices, and grid diameters of both 250 and 300 μm were available. The stainless steel grids featured 300 μm diameter orifices and were roughly 90 μm thick. The latter grids were used successfully in a relaxed package, explained in section 7.5, intended to demonstrate the array capabilities while avoiding some electrical isolation issues with the complete package (see section 7.4.1). An example of this type of grid is shown in Figure 5-8 demonstrating that they were inherently not flat. As such, these grids required a support structure, discussed in section 7.5.

5.5.1 Grid Orifice Sizing

Lozano[36] measured the spreading angles from externally wetted ILIS and found typical beam angles, θ_B of roughly 15-20^o. However; in porous ILIS, where multiple emission sites could occur, the location of the emission site should also be considered. In section 4.5.6, the simulated surface fields after etching revealed that surfaces with electric fields close to the maximum case may be titled by up to $\sim$ 35 ^{o} off the central axis even after secondary etching. Hence the net beam, consisting of several beamlets (see Fig. 5-9), could have non negligible intensities at angles up to $\sim$ 55^o (Net θ_B in the figure). For emitters without secondary etching, significant portions of the beam at even higher divergence angles would

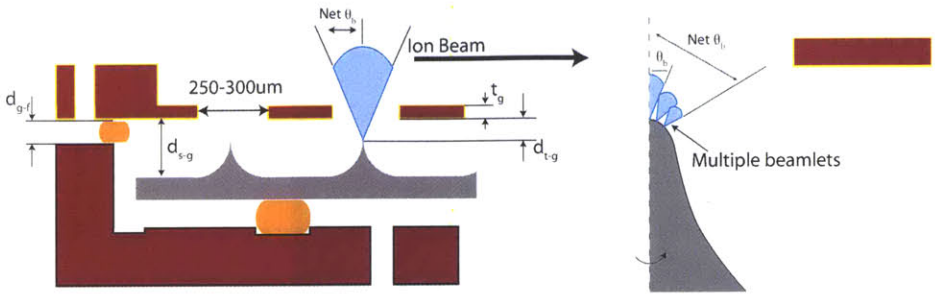

Figure 5-9: Schematic showing the key geometric factors considered when sizing and positioning the electrostatic grids.

be expected.

All tests presented in chapter 7 used grids with 300 μm orifices (although some attempts with 250 μm grids have been made). Typical tip to orifice distances, d_{t-g}, were $\sim$ 150 μm. For 100 μm thick grids, the tip to outer grid surface angle was roughly 30^o while the angle to the inner (emitter side) surface was roughly 45^o. Hence, some beam interception was possible. However, increasing the grid orifice size also decreases the peak electric field (at the emission site) for a given applied potential, while reducing the grid thickness could lead to structural issues (see below). Despite this concern, the testing presented in Chapter 7 found that with secondary etching this design could achieve good transmission, with only a few percent of the total beam current intercepted by the grid for one sample device (section 7.5.3).

5.5.2 Grid Deflection due to the Electrostatic Field

At these length scales the electrostatic stress on the grid, due to the applied fields, could become sufficient to deflect, or even fracture, the grids. For a distributed loaded P on a rigidly clamped square plate with side lengths a, Timoshenko[158], gives equations 5.1 and 5.2 for the maximum plate deflection (at the center) and stress (at the edges) respectively. Here w_{max} is the plate deflection at the center, Y is Young's modulus, t_g is the plate thickness, D_{plate} is the plate modulus, ν_p is the Poission ratio and σ_{max} is the maximum stress at the edge of the plate.

$$w_{max} = 0.00126 \frac{Pa^4}{D_{plate}} \tag{5.1a}$$

$$D_{plate} = \frac{1}{12}\left[\frac{Yt_g^3}{1-\nu_p^2}\right] \tag{5.1b}$$

$$|\sigma_{max}| = \frac{6}{t_g^2} 0.0513 Pa^2 \tag{5.2}$$

Two failure modes should be considered. First, the maximum stress should not exceed the fracture stress for the plate material. Second, for large deflections the plate may become dynamically unstable, a condition known as electrostatic pull-in. As shown by Senturia[96], for an electrostatic problem with a linear relationship between applied load and deflection (as in this case), pull-in occurs when $w_{max} \sim 2/3 d_{s-g}$, where d_{s-g} is the grid to substrate separation.

Thin grid thicknesses were desirable to reduce the interception angles discussed above. Estimates for the critical thickness at which either fracture or pull-in can be considered for the two available grid materials. Assuming the electric field over the majority of grid surfaces to be roughly V/d_{s-g}, the applied load can be calculated as $P \sim \epsilon_0/2(V/d_{s-g})^2$. Typical emitters fabricated here were taller than 150 μm and roughly 150 μm from the grid orifices such that $d_{s-g} \sim 300 \mu m$. Typical operating potentials are less than 2 kV. The square, thin portion of the grids has side lengths of $a = 10.5$ mm.

The material properties of silicon depend on the crystal orientation with respect to the load direction, but for the purposes of this estimate a Young's modulus of $\sim$ 145 GPa and Poisson ratio of $\sim$ 0.3[96] are typical. Silicon may fracture when stress levels exceed $\sim$ 5 MPa[159]. Using these values, the grids may fracture for thicknesses, t_g, less than $\sim$ 35 μm, while pull-in could occur for t_g less than $\sim$ 10 μm. Similarly for stainless steel using Young's modulus of 190 GPa and a yield strength of 200 MPa, the limiting thicknesses are 9.5 and 5.7 μm for pull-in and deformation respectively. Hence for the 100 μm thick grids used here, these effects should be avoided for both materials.

These simple calculations have ignored the perforated nature of the grids and have assumed they are rigidly supported at the edges. As future iterations move to higher emitter densities and thinner grids, more detailed calculations should be made. In addition,

for the testing in section 7.5, using a partially assembled version of this design, the stainless grids were only supported at the corners. However; no pull-in was observed.

Chapter 6

Experimental Development of an Electrochemical Technique for Porous Emitter Array Fabrication

The intentions of this chapter are to both present the results of the process used to fabricate the porous nickel emitter arrays tested in this research (Chapter 7) and to provide insight into the evolution of that process, which may be helpful in applying the technique to alternative metals and porosities in the future. The etching tool and masking techniques used while exploring mass transport controlled electrochemical etching are described first. Subsequently a series of simplified experiments are presented. These experiments had two goals; first to establish appropriate cell potentials and electrolyte conditions for transport limited etching on porous nickel and second to verify that the tool developed here can modify mass transport rates through variable agitation rates. The remaining bulk of this chapter is devoted to establishing conditions for fabricating uniform porous emitter arrays, suitable for ILIS operation, within the silicon mount described in the previous chapter.

6.1 Electrochemical Etching Tool

As described in Chapter 4 an appropriate tool is crucial when performing electrochemical microfabrication under transport controlled conditions. It was indicated in that section that a paddle agitator would be suitable for etching emitters. Specifically a cathodic paddle has

been selected in order to simultaneously achieve both a close proximity counter electrode (to minimize Ohmic losses) and agitation near the surface. Agitation provides directional control that can not be achieved through, for example, temperature variations. Enforcing forced convection has been used to normalize the transport properties across samples, which would otherwise be dictated by local conditions and geometry (for example, products etched from the edges of an activated sample could diffuse more freely than from the center without forced convection).

The paddle design here has been used to impart desirable hydraulic and electrostatic conditions simultaneously. The paddle motion is inherently periodic and the gap between itself and the sample has been small. The resulting regime of dissolution could be somewhere between two extremes depending on the specific sample and paddle configuration. In the case of a primary current distribution not far from the paddle, it could be used, as was done by Datta[132], to impart highly localized, high current, etching. Here the region immediately below the paddle is favorably etched while its motion simultaneously dictates the hydraulics of the problem. In this case, for any fixed position on the sample being etched, the paddle motion could be modeled, to a first approximation, by a pulsing problem, similar to that of section 6.4.4, so long as mass transport continues to dominate the process directly below the paddle. In the alternative extreme, where the overpotential for the reaction is primarily localized near the metal surface, the potential drop through the electrolyte may be small, equivalent to a secondary current distribution around the paddle. In this case, the paddle motion could be thought of as simply a mechanism for periodically enhancing mass transport. In either case, for sufficiently high dissolution rates such that mass transport limits the reaction rate, the conditions at a given position may be well described by an average diffusion layer thickness. However; the active area would only approach the complete electrode area if operation is near the second extreme.

The design outlined below was developed without prior knowledge as to which regime (or somewhere in between) would be optimal. Therefore; in some respects, flexibility to expand and modify the system has been favored over accuracy for a particular operation. The follow sections provide an overview of the device

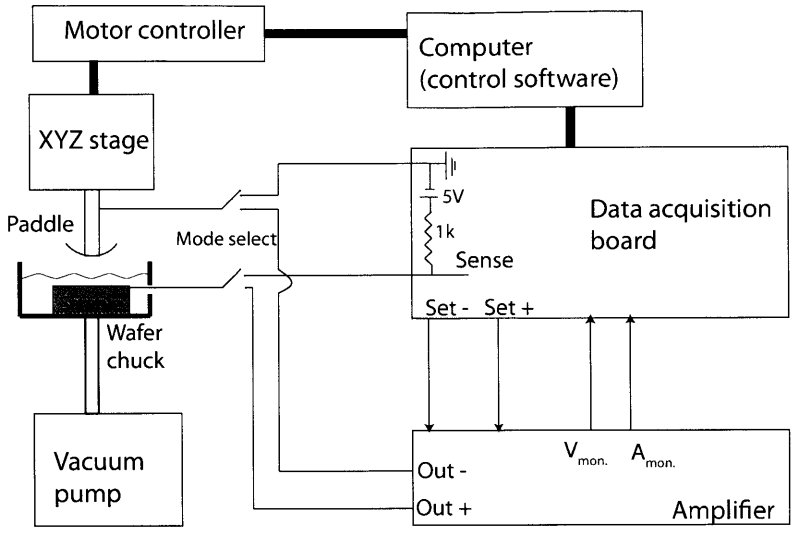

Figure 6-1: Schematic overview of the etch station constructed during this research. A potentiostat was incorporated into this setup for some preliminary tests but is not shown here.

6.1.1 Etching Station Overview

The etching station consists of 4 key components, shown schematically in Figure 6-1. The sample is held by a vacuum chuck which doubles as liquid bath for the selected electrolyte. The cathodic agitator is positioned using a three axis stage controlled using a computer interface. Simultaneously, the electrical conditions are controlled by the computer through a data acquisition system used to drive and monitor an amplifier. More details on each component are described below.

Three Axis Gantry Style Stage

Three Newmark Systems linear eTrack stages are configured to provide, x, y and z motion via computer controlled motor controllers, using an RS232 interface. The vertical (z) and transverse (y) axes are driven by relatively high resolution (0.04 μm), low speed (up to 40 mm/s) stages while the primary (x) axis uses a lower resolution (0.24 μm) high speed (up to 220 mm/s) stage for agitating the electrolyte. Figure 6-2(a) shows a CAD drawing of the completed stage. The stages have been mounted to a structure made from 80/20 Inc. modular framing components mounted to a 20 x 40 inch optical plate. Teflon friction bearings, available from 80/20 Inc. and designed to straddle the frame, were used on

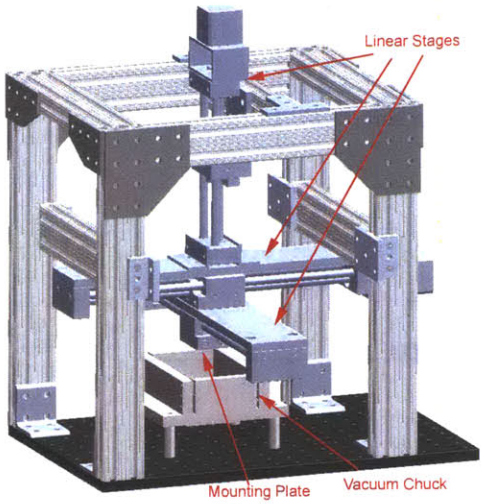

(a) CAD drawing of the etching station built for electrochemically etching emitter arrays in this research.

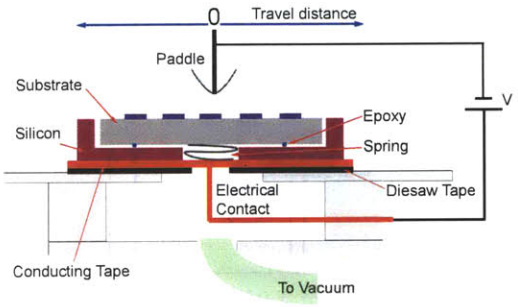

(b) Schematic of the vacuum chuck connections for a porous sample. The (copper) conducting tape is required to achieve electrical contact without breaking the vacuum seal.

Figure 6-2: Drawings of the etching station used here, the wafer chuck doubled as a bath for holding the electrolyte solutions.

the vertical axis. Although the moving parts are protected by thin teflon sheets during operation, the stages must be cleaned, using simple detergents, and lubricated using a chemically resistant lubricant, after each etch session (or every few days if under heavy use). Failure to do so will result in damage to the stages.

The total planar travel range, roughly 12 by 12 inches has been selected to accommodate future upgrades to the station, such as 6 inch wafer level processing. The vertical component has a maximum travel distance of approximately 100 mm and must be operated at slow speeds to prevent slipping due to the relatively high weight of the planar stages.

Power Supply and Feedback

A Kepco BOP 36-12M, 400 W bipolar amplifier supplies the etching current and is driven by a National Instruments NI-DAQ USB 6229 data acquisition board. The Kepco supply can be operated in current or voltage control configurations driven by an analog signal from the NI-DAQ board. The amplifier can provide up to $\pm$ 36 V and $\pm$ 12 A. Analog monitoring lines from the power supply are read back by the NI-DAQ allowing for realtime feedback of the cell current and voltage.

Vacuum Wafer Chuck

The wafer chuck holds samples to be etched in place, provides electrical contact and serves as a bath for the electrolyte during etches. Figure 6-2(b) shows, schematically, how the vacuum seal and electrical contacts are achieved in this design. A small Venturi type vacuum pump, driven by the building air lines, provides suction which both secures the sample and compresses a small conducting spring, or wire, making electrical contact to the sample. When etching samples within the silicon frame described in Chapter 5, a layer of conducting tape has been used to maintain electrical contact without breaking vacuum, as shown in the figure.

The vessel used here measured 124 by 78 mm, was 40 mm deep and consists of teflon walls secured to a polyethylene base covered in Viton rubber. The Viton sheet also serves as a gasket for the vacuum seal. During all tests 150 mL of the selected electrolyte was poured into the vessel after securing the sample.

Etch Control Software

A LabView script controls and monitors the electrical conditions while simultaneously controlling the paddle position and motion. Sequences of consecutive processes can be loaded into a stack and can proceed continuously. This feature is beneficial when etching within transport controlled conditions where initial transients can occur over long periods. By preparing a sequence in advance, the conditions can be modified, significantly or slightly, in quick succession. These sequences can be saved and reloaded for future use or to be tailored by a user to achieve a particular goal.

Etching can be set to occur for a fixed amount of time, or alternatively, a set mass of material to be removed can be prescribed. In the later case, the software integrates the cell current and calculates an estimate for the mass removed, using equation 6.1, where the reaction valence, z, molar mass, M, and etch efficiency, θ, depend on the material being etched.

$$\Delta m = \frac{M\theta}{zF} \int I dt \tag{6.1}$$

As discussed at the end of this chapter, significant uncertainties would be expected in etching to a certain mass, primarily due to etching at the edges of arrays, however; in practice this etch stop has been typically more reliable than simple prescribing a time.

6.1.2 Height Calibration

A small control box permits the anode and cathode connections to be simultaneously switched over to a sensing circuit on the data acquisition system, as shown in Fig. 6-1. This allows for contact calibration of the sample height whereby the stage, with a conducting protrusion (usually the paddle) is lowered slowly to a dummy sample of known height until it makes contact. When contact is made it is detected and passed on to the control software which stops the paddle motion and notes the calibrated height. The paddle can then be raised slightly from this new reference point and moved laterally aside such that the dummy and working sample can be exchanged. The desired electrolyte is then be added and the paddle is positioned over the working sample for etching. This method has significantly increased the accuracy in paddle to cathode gaps during experiments but was not installed until the experiments beginning in section 6.4.2. Previously the height was input from the home position (with the paddle fully raised) and was prone to near mm level accumulated errors due to slipping as the stage descended through 10's of mm. In the future, full automation could be achieved by replacing the manual switch by a relay controlled through the data acquisition board.

6.1.3 Paddle Designs

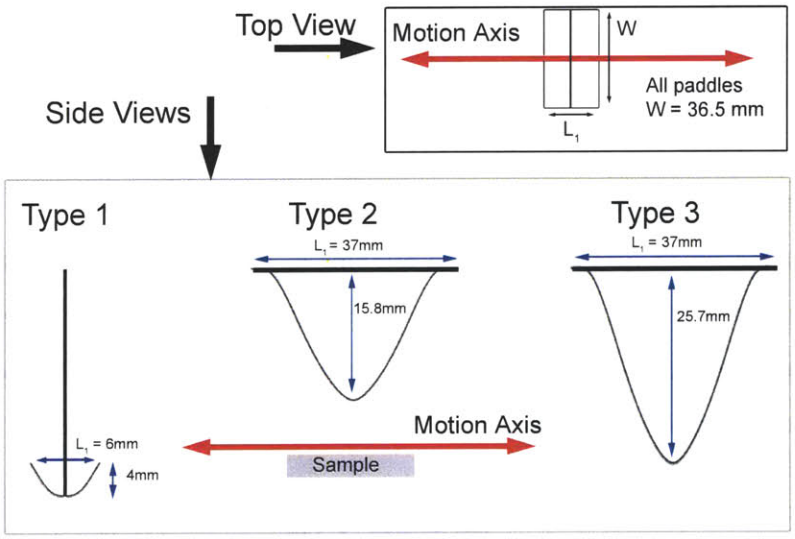

Figure 6-3: Schematic views of the three paddle designs used during this research.

The paddle agitators mounted within the etch station have generally been wedges. This

design was first selected with the intention of achieving localized etching directly below the paddle. However; as discussed in the initial results section below this may have been the case in practice. The wedge design was also desirable as a means for inducing both perpendicular and parallel flow towards the material surface. Three shapes have been tested here, shown schematically in Figure 6-3. The type 1 paddle was used during preliminary experiments and initial tests on solid wafers, while only type 2 and type 3 paddles were used when etching porous samples. The transition from a type 1 to a type 2 paddle was made based on numerous concerns, including low cathode area, recirculating flows and the poor resilience to damage/bending. Details concerning the motivations for changing paddles are provided within the results sections below. In general the evolution of these designs has been developed qualitatively from experimental results. The paddles were not designed using any quantitative analysis. Explorations of the performance sensitivity to paddle geometry are highly recommended. Figure 6-4 is a photograph of a type 1 paddle etching a solid nickel array. In all cases the paddles were 36.5 mm wide (as shown in the inset) and were made from stainless steel sheets 0.3 mm thick.

Figure 6-4: Photograph of a type 1 paddle etching a solid nickel sample within hydrochloric acid.

6.1.4 Recommended Expansion to Wafer Level Processing

As stated above the etch station developed here was designed to accommodate future upgrades for wafer level processing. Specifically the total travel of the tool head could allow for wafers up to 12" in size. This would require constructing a new wafer chuck/bath to be

coupled with the existing vacuum pump and electrical connections. Wafer level processing could be accomplished relatively easily after optimizing an etch process at the die level due to the selective nature of electrochemical etching. Specifically, using a multiplexer, the control software could select each die mounted on a wafer and position the paddle above that region. Using this technique wafer level alignment and packaging could be achieved, possibly leading to more efficient fabrication of these sources. Due to the significant amount of material removed when etching in bulk, the system may also need to be upgraded with a method for maintaining fresh electrolyte.

6.1.5 Additional Equipment

SEM Images have, unless noted otherwise, been obtained using the MIT Space Propulsion Laboratory, Hitachi TM-1000 tabletop SEM. Two imaging modes are used here and are shown in Figure 6-5, where an image has been repeated in each mode. As shown in the figure, the topographical mode, intended to highlight elevation changes, is useful when imaging porous materials as it highlights the structure contours while softening the appearance of the pores themselves. This benefit comes at the expense of some sense for the feature topography when viewing structures at an angle.

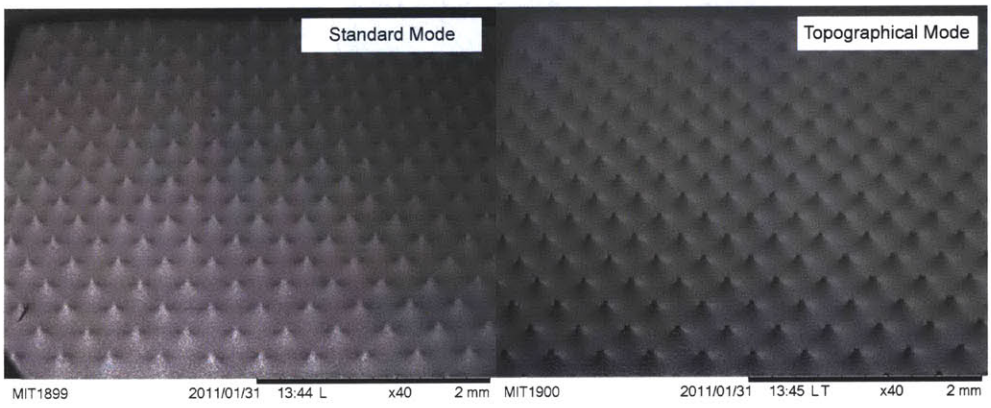

Figure 6-5: The Hitachi TM-1000 was used in two modes, in the 'topographical' mode, the contours of porous structures can be seen more clearly at the expense of the pores themselves.

Potentiostatic scans have been made using a Princeton Applied Research VersaStat 3F potentiostat. The potentiostat maintains an input potential between the working sample and a reference electrode by controlling the current between the working sample and an aux-

iliary electrode (such as the paddle). This device was used whenever possible to measure reaction rates with cell voltages measured with respect to a platinum reference electrode. However; the device output could not exceed 300 mA, limiting its applicability to simplified samples rather than complete arrays. The specific setup used in those experiments is described in section 6.3.

6.2 Sample Preparation

This section describes the preparation of the simplified test electrodes used in section 6.3 and the nickel arrays etched in section 6.4. The resists which have been used, and the corresponding masking procedures, are detailed along with the cleaning procedure used on most samples.

6.2.1 Masking Procedures

As identified in the review of techniques presented in 3.3, dry film photo resists are well suited for masking porous materials. Three dry resists have been used in this research. In all cases, lamination has been done by hand due to the lack of specialized equipment suitable for masking the size of samples used here. Table 6.1 contains details of the resists and lithography procedures used during this study. These instructions reflect the best conditions for obtaining good yields on the samples studied here. Specifically, these settings assume 1 mm thick nickel samples and, in the case of the MP525 and FX515 resists, are tailored to 1 x 1 cm samples bonded within the silicon packages described in section 5.3. Significant alterations to the lamination instructions may be required for different materials or packages but these conditions should serve as a good starting point. The MP513 resist was primarily used on solid samples. The listed recipe was tailored to those samples but was also used to successfully pattern porous samples on a few occasions. The resists typically have a lifetime of roughly 6 months and quickly degraded once expired. Due to the large minimum order sizes (thousands of square feet), the resists were tested and ordered in the sequence (left to right) shown in the table. Unfortunately this prevented direct comparisons between samples as the entire process evolved along with the available resists. Figure 6-6 shows examples of masks created using the very (64 μm) thick MP525 and the relatively thin (15 μm) FX515 resists.

Table 6.1: Dry film resist properties and recommended conditions for laminating 1 mm thick nickel samples mounted in Silicon frames.

Resist	**MP513**[a]	**MP525**	**FX515**
Manufacturer / Brand	MacDermid Aquamer	MacDermid Aquamer	DuPont Riston
Thickness	$33\mu m$ / $1.3mils$	$64\mu m$ / $25mils$	$15\mu m$ / $0.6mils$
Lamination Temperature	110^oC	115^oC	115^oC
Lamination Time (s)	$120s$	$90s$	$80s$
Pressure Time (s)	$60s$	$60s$	$60s$
Exposure Time (s)	$30s$	$15s$	$95s$
Developer Concentration (Na_2CO_3)	2% W/V	1% W/V	1% W/V
Developer Volume	$200mL$	$200mL$	$250mL$
Developer Stirring	-	300-400rpm	300-400rpm
Developer Temperature[b]	75^oC	80^oC	50^oC
Develop Time	$\sim 120s$	105-135s	$25s$
DI Rinse Spray / Dunk	- / $15s$	$\sim 10s$ / $5s$	$10s$ / $5s$
Drying	Ni spray	Ni spray	Ni spray

[a]Available MP513 was a sample stock which was past its expiry date upon delivery. The resist was primarily used on solid nickel samples.

[b]Listed temperatures are set points on a hotplate and were not measured directly.

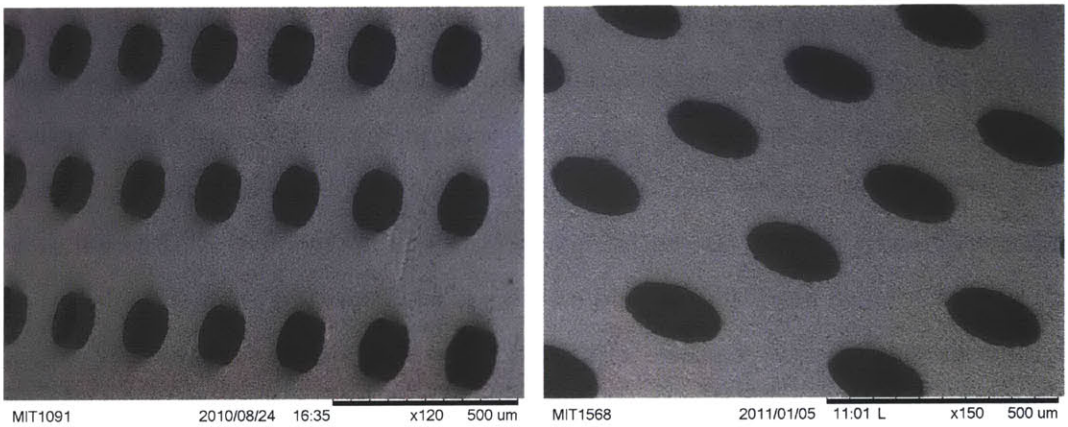

(a) SEM image of the, very thick, MP525 resist after patterning to create 150 μm diameter masks on porous nickel.

(b) SEM image of the FX515 resist after patterning to create 200 μm diameter masks on porous nickel.

Figure 6-6: Examples of the dry film photo resists used to mask porous nickel samples.

Before lamination, the samples, set on a microscope slide, were heated to the listed temperature. They were then removed, quickly (but gently), laminated and then returned, face up, to the hot plate. Lamination consisted of simply smoothing the resist over the sample using a cotton applicator to provide gentle pressure for a few seconds until the resist was smooth and visually uniform. Pressure was continually applied with the applicator, for the time listed in the table, but with a thin microscope slide positioned on top of the sample. This assisted in distributing the applied pressure. Samples laminated without some applied pressure were often characterized by non uniformities across the sample which became apparent after developing. Other, more consistent, methods for applying pressure during lamination were explored but did not yield any improvements. For example, placing a known weight on the sample aided in ensuring a uniform force but the large thermal sink appeared to be more detrimental compared with the manual method described above.

Photolithography has been performed using a Karl Suss MJB3 mask aligner located within the exploratory materials laboratory (EML) at the MIT Micro Technologies Laboratory. All dry film samples were developed within aqueous Na_2CO_3 at the listed concentrations. These solutions were mixed from solid Na_2CO_3 first dissolved in water to form a 10 % W/V concentrated solution before finally being diluted immediately prior to use during each lithography session. The listed temperatures reflect the plate settings, the actual temperature of the solution was not monitored.

For a small set of solid nickel samples, the experiments in section 6.3.2 below, a spin on resist was used instead of the dry film. Here a 10 μm thick layer Shipley 1813 resist was applied using a spin coater. The samples were soft baked on hotplates for 50 s at 70^oC followed by 45 s at 90^oC. Lithography was performed using the aligner described above with a 90 s exposure followed by development through immersion in MF-319 developer for 50 s. Finally, the samples were hard baked at 90 ^oC in an oven for 30 minutes.

6.2.2 Cleaning Procedure

The samples were cleaned using a solvent procedure before masking and after etching, including between the first and second etch steps detailed below. Step 0, using sodium hydroxide, was used to dissolve the dry film resists and was only performed after etching masked samples. After cleaning the samples were either processed, or tested, immediately or stored in a nitrogen desiccator at $\sim$ 20 % relative humidity.

- Step 0 : 30 minutes ultrasonic cleaning in 1N sodium hydroxide
- Step 1 : 30 minutes ultrasonic cleaning in acetone
- Step 2 : 30 minutes ultrasonic cleaning in methanol
- Step 3 : 30 minutes ultrasonic cleaning in isopropanol
- Step 4 : 30-60 minutes drying on a hotplate at 80^o C

6.3 Exploration of Electrochemical Etching

Several experiments on simplified substrate geometries were performed to explore and identify suitable etching conditions for forming emitter arrays on porous metals. First, an appropriate electrolyte demonstrating a clear limiting current plateau has been identified for both nickel and titanium etching. Further experiments were aimed at estimating the thickness of the diffusion layer and at experimenting with its dependence on the enforced hydrodynamic conditions using solid nickel samples.

6.3.1 Experimental Configuration

These experiments used samples as shown in Figure 6-7 to explore electrochemical reaction rates using the available potentiostat (described above). The solid samples were masked with either the MP513 or Shipley 1813 resists. For the former, dry film resist, the mask revealed a 15 mm long, 0.5 mm wide strip of nickel. While using the spin on resist a strip 10 mm long and 0.75 mm wide was exposed. The exposed area was hence 0.075 cm^2 for all tests. The edges of the sample were sealed with kapton tape, not shown in the figure, to prevent any activation of those surfaces. By limiting the active area, current densities up to 4 A/cm^2 over the entire surface could be achieved with the potentiostat. As will be shown later in this chapter, current densities of this order were often observed when etching complete arrays. A long strip was selected in order to capture the effects of the paddle motion in a manner comparable to etching emitter arrays. In lieu of a more standard reference electrode (see Bockris[119] for examples) a simple platinum wire was selected such that it could be placed along the exposed region. This was done to provide a measurement of the potential within the electrolyte near the activated surface in the event the cathodic

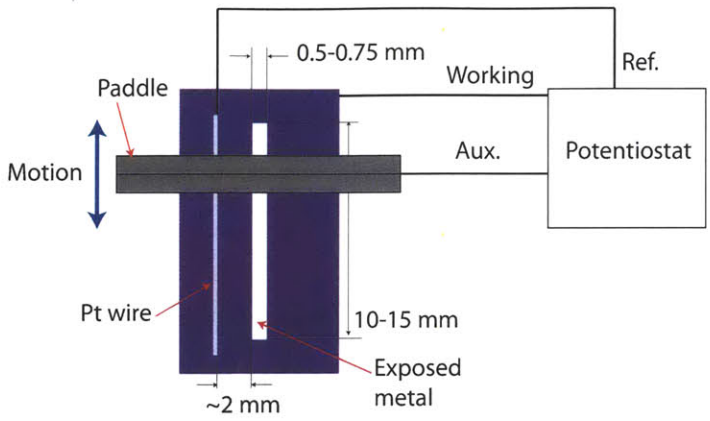

Figure 6-7: Schematic of the simple electrodes, and associated connections to the potentiostat, used during these initial experiments. The exposed area was 0.075 cm^2 for all tests.

paddle selectively etched the surface directly below its position. The sample was held, and electrically contacted, using the vacuum chuck vessel described in section 6.1.1.

The potentiostat has been operated in both potentiodynamic (sweeping potential) and potentiostatic (constant potential) configurations. During potentiodynamic scans a rate has been selected which attempts to seek a tradeoff between the time required for transients to settle and the changing active area due to evolution of the electrode itself.

6.3.2 Electrolyte Selection : Achieving Mass Transport Control

Potentiodynamic sweeps for both nickel and titanium samples have been performed using test samples patterned with the Shipley 1813 resist within the apparatus described. Sample results are presented in Figure 6-8 for nickel. For all cases the potential was ramped at 100 mV/s from 0 to 4 V beginning with a new sample for each scan. The data has been plotted versus the respective open circuit potential (for a platinum reference electrode). At low voltages, all samples were characterized by a low but fast rising current. However; at increasing potentials both the HSO_4 and HNO_3 cells quickly passivated while the HCl system continued to rise until a clear plateau was established at roughly 1 V beyond the open circuit potential. As the potential was increased further, violent reactions with visible gas evolution were observed for all electrolytes. During these tests a type 2 paddle was used. The paddle to electrode gap was roughly 1-2 mm with the paddle oscillating to $\pm$ 10 mm about the center of the sample at 50 mm/s.

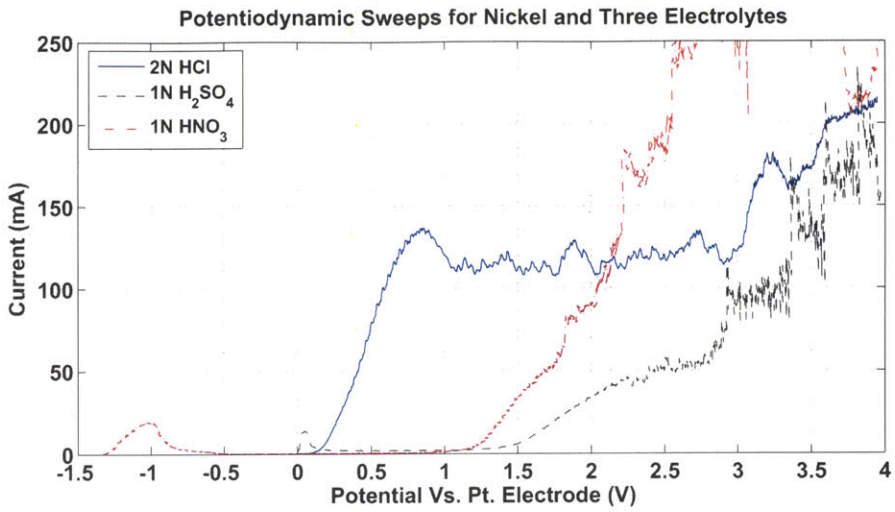

Figure 6-8: Potentiodynamic sweeps for three electrolytes at the indicated concentrations with nickel samples. The H_2SO_4 and HNO_3 solutions passivated the nickel surface while the HCl solution demonstrates a wide limiting current plateau.

The magnitude of the current density plateau observed for 2N HCl can be compared with the approximate values of section 4.1.3. There for a rectangular flow cell current densities on the order of 1-4 A/cm^2 were expected depending on the diffusion layer thickness and saturation concentration. The total electrode area in this case was 0.075 cm^2, however; the active area at any given time may differ significantly. As proposed in the tool description above, the active area may range from a value comparable to the paddle width to the complete electrode area. If the former case, the active area could be as much as an order of magnitude less than the total depending on the paddle size, position and electrostatics. It will be motivated below that the situation approached the later condition, within the complete area activated. Under those conditions, the plateau with HCl in the figure corresponds to roughly 1.5 A/cm^2.

Earlier tests used non acidic solutions, such as aqueous LiCl and NaCl. These were abandoned as, even for small samples, the etch products quickly saturated and precipitated throughout the solution. Using these solutions for the relatively large amounts of material removed here would likely require a constant supply of fresh electrolyte which would complicate the overall process. Given these results, 2N HCl has been selected for nickel etching in this research.

A similar experiment has been performed using titanium samples. These data are pre-

sented in Figure 6-9 for systems of aqueous 2N HCl, aqueous 1N H_2S0_4 and 10% V/V ($\sim$ 1.9 M/L) H_2SO_4 in methanol. A clear plateau was observed using H_2SO_4 in methanol. However; using HCl, the current appeared to be transpassive in that the current decayed after initially climbing but then continued to rise at moderate levels. The plateau magnitude observed using H_2SO_4 in methanol was in agreement with those of Piotrowski et. al[160] who avoided passivation of titanium samples in aqueous solutions by using methanol as a solvent as opposed to water. However; the strong oscillations at low potentials warrants further discussion.

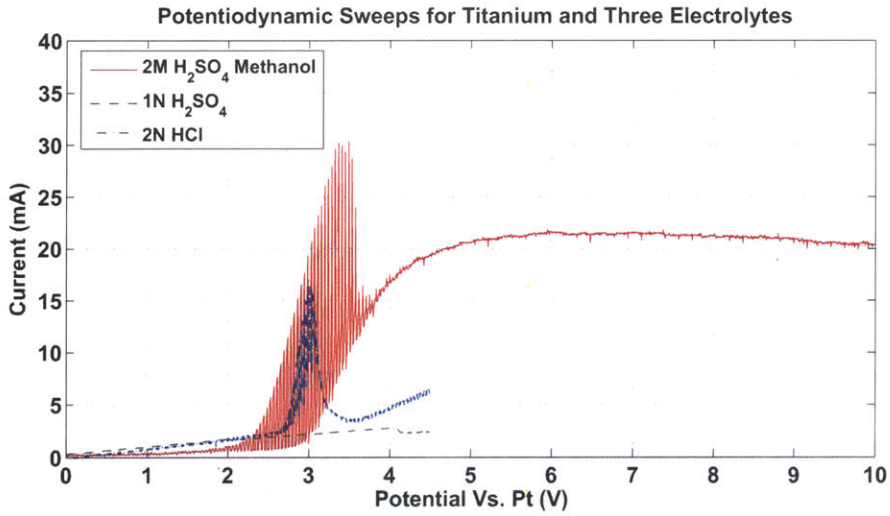

Figure 6-9: Potentiodynamic sweeps for three electrolytes at the indicated concentrations with titanium samples. The aqueous H_2SO_4 and HCl solutions passivated the surface while the H_2SO_4 in methanol demonstrates a wide limiting current plateau.

The measured current of Figure 6-9 has been plotted again in Figure 6-10 as a function of time focusing on the high oscillation region. These high magnitude oscillations have a frequency of approximately 2.3-2.5 Hz while the paddle motion prescribed (50 mm/s over 20 mm) would yield time dependent variations at 2.5 Hz. This strong correlation suggests that for titanium etching at moderate potentials, the etch rate was far more dependant on paddle position than when etching nickel in aqueous HCl. This trait suggests that at low potentials, the dissolution was of the primary kind, governed by the potential distribution over the cell at a given time. The data of figure 6-10 are consistent with a cell passing through a primary current regime before becoming limited by mass transport over the entire sample such that the dependence on potential distribution, and hence paddle position, is

reduced, and eventually becoming secondary. Similar, but lower amplitude, oscillations were observed for titanium etching in aqueous HCl near the current peak.

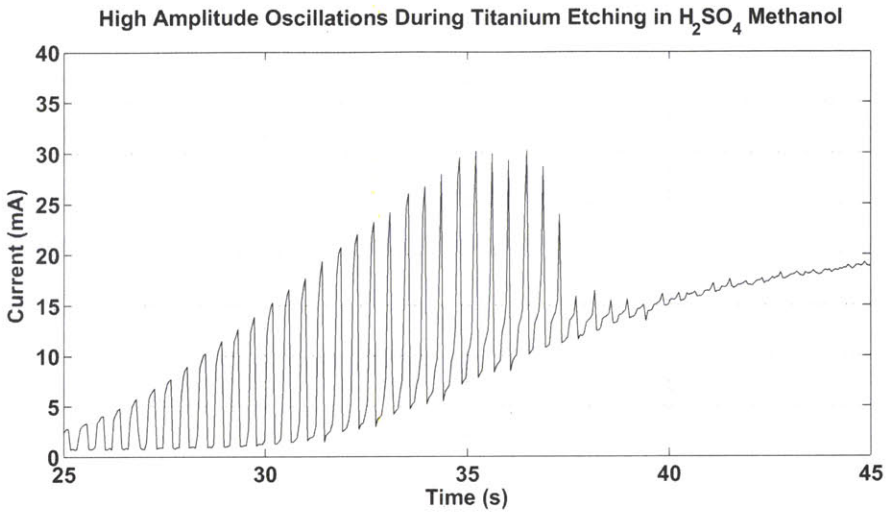

Figure 6-10: High magnitude oscillations during Titanium etching.

6.3.3 Visual Confirmation of Mass Transport Limited Conditions

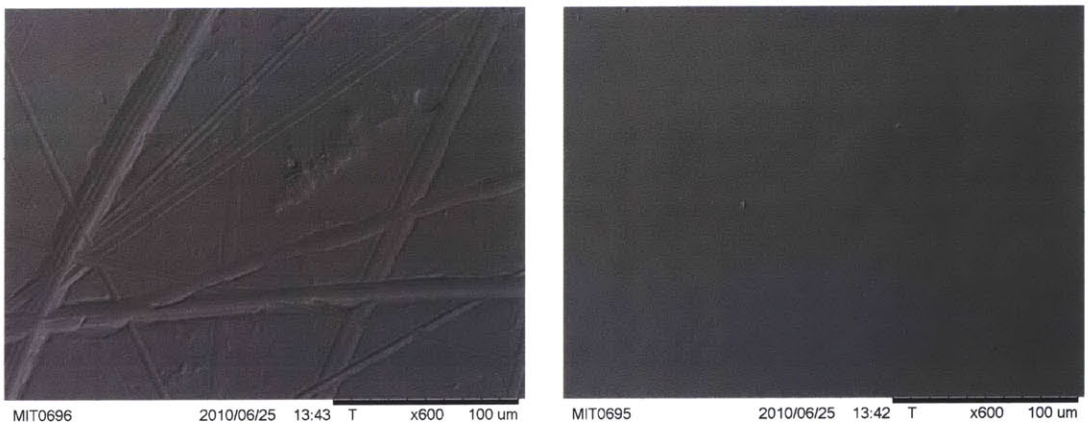

(a) An SEM image, in topographical mode, of a piece of solid nickel before etching.

(b) An SEM image, in topographical mode, of a piece of solid nickel after etching.

Figure 6-11: Etching below and above the transport limit on solid nickel samples.

Figure 6-11 shows topographical images taken before and after etching a solid sample at settings with the current plateau observed in Fig. 6-8 for nickel etching in HCl. After etching, Fig. 6-11(b), the sample is locally smooth with only slight imperfections remaining compared with those visible before etching, Fig. 6-11(a). As stated in the review, section

4.2, smooth etching is a characteristic of etching under mass transport control these images are therefore further confirmation that transport limited etching was achieved.

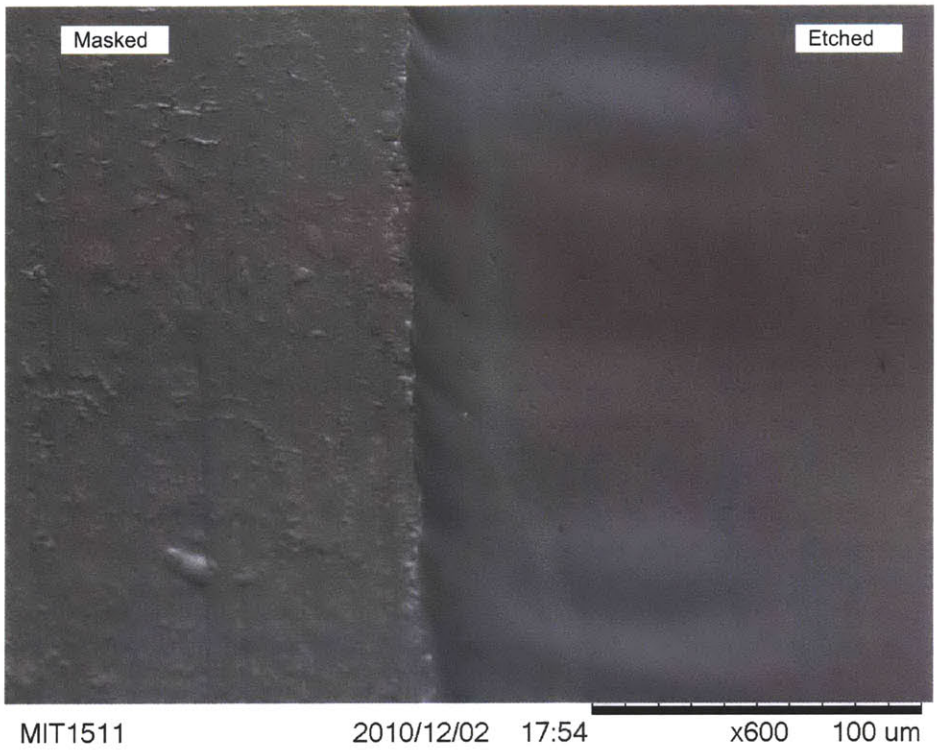

Figure 6-12: Titanium etching under mass transport limited conditions. The left portion of the figure was masked while the right side was etched. The simple kapton tape mask was poorly bonded, resulting in significant non-uniformities.

Similarly, the image in Figure 6-12 was achieved when etching titanium through a simple kapton tape mask at 10 volts in H_2SO_4 methanol, under the same hydrodynamic conditions as Fig. 6-9. Again, smooth surfaces are achieved on the etched surface, although the kapton mask was poorly bonded resulting in large scale non uniformities along the trench edges.

6.3.4 Applied Cell Potential

An important practical note, identified in section 6.1, is that due to the high currents expected when etching emitter arrays, the available potentiostat was not used. Instead fixed voltages were set between the working electrodes only. It was therefore important to compensate for the additional potential required to sustain the cathodic reaction.

Figure 6-13 demonstrates this shift for a 0.075 cm^2 strip sample with a potential scan rate of 50 mV/s from 0 to 6V measured with respect to the indicated electrodes. Here a

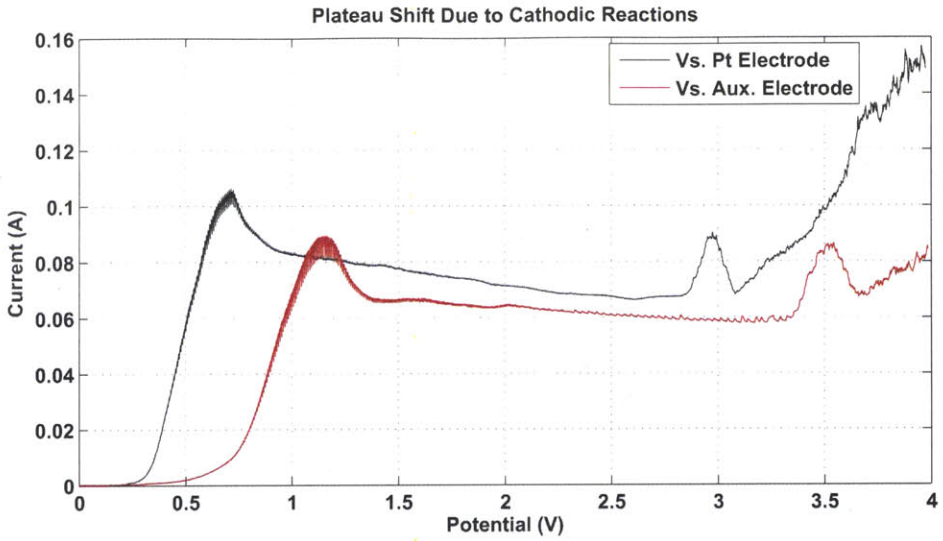

Figure 6-13: Shift in potential due to cathodic reactions when measuring the anode potential against the cathode rather than against a platinum reference.

type 1 paddle was positioned $\sim 1.5\ mm$ above the sample and agitated at 150 mm/s over $\pm$ 10 mm. The data demonstrate a shift of roughly 0.5 V when enforcing a potential between the cathode (auxiliary) and anode instead of enforcing a reference potential with respect to the anode. This experiment represents a single, low current example. When etching arrays at much larger currents the shift might increase depending on the cathode geometry and surface conditions. Given these experiments a point to the far right of the shifted curve, 3.5 V, was selected as an initial set point for the array etching experiments in the next section, where ensuring transport limited etching across the entire sample was desirable.

6.3.5 Influence of Cell Geometry and Hydraulics

The preceding experiments verified that a wide limiting current plateau could be identified using nickel etched in 2N HCl. In section 4.1.3 it was stipulated that under these conditions the reaction rate (or equivalently the current) should be controlled by hydraulic conditions. This has been investigated in Figure 6-14. Here a strip sample was etched with the paddle roughly 6 mm above the sample. The potential was swept at 100 mV/s from 0 to 4 Volts while varying the paddle speed from 25 to 150 mm/s as indicated in the figure.

In Chapter 4, section 4.1.3 two correlations were introduced for predicting variations in the diffusion layer thickness at varied hydraulic conditions within a rectangular flow

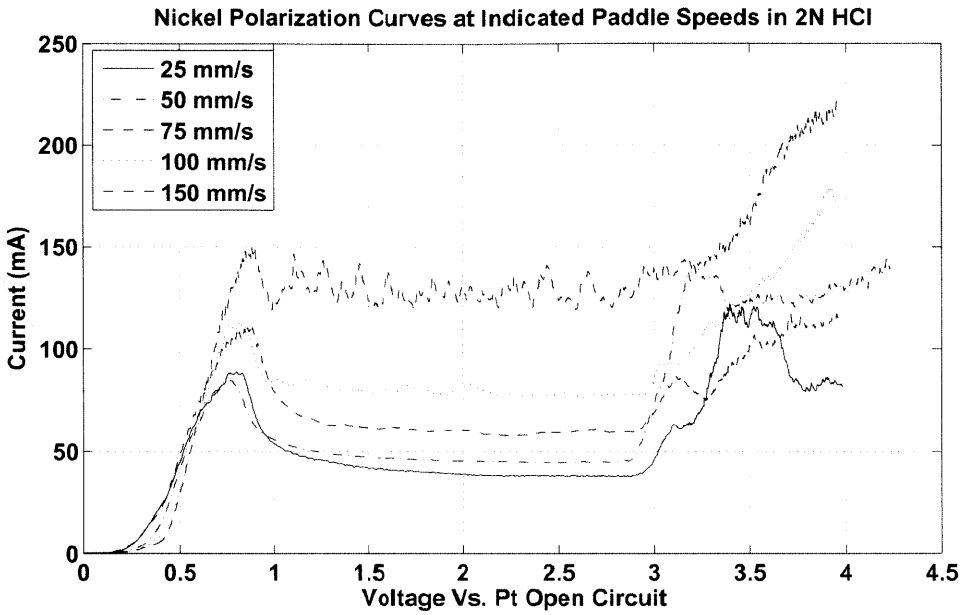

Figure 6-14: Potentiodynamic sweeps with the paddle motion set to oscillate at the indicated speeds. As agitation, and hence transport, is increased the limiting current plateau rises.

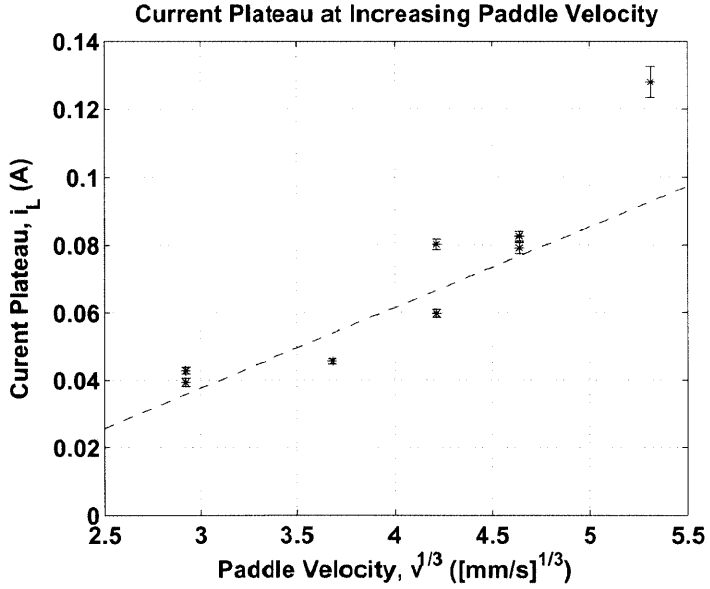

Figure 6-15: Average limiting currents with increasing velocities. A linear fit has been made given the Sherwood number relations for rectangular flow cells described in section 4.1.3.

channel. Although this configuration, an oscillating paddle cell, differs significantly from a simple flow channel, the data in Fig. 6-14 can be compared with the trends predicted for those conditions using the paddle speed as a characteristic velocity. Specifically both correlations, equations 4.9 and 4.11, predict the Sherwood number will increase with the Reynolds number, and hence velocity, to the 1/3 power. The data of Fig. 6-14 along with repeated scans at 25, 75 and 100 mm/s have been plotted against the paddle velocity to the 1/3 power in Figure 6-15. Here the average current has been taken between 1.5 and 2.5 V, with the error bars indicating the standard deviation within that band. A least squares fit to the data has also been plotted. The correlation is poor, particularly due to the scan at 150 mm/s where high currents and current oscillations were observed and the small data set. Nevertheless, these data confirm that increasing agitation can effectively increase the amplitude of the limiting current potential within a nickel, 2 N HCl cell.

Potentiostatic Measurements

In addition to the potentiodynamic sweeps above, where a current density plateau can be observed as evidence of transport control, potentiostatic methods can also be employed. Here a fixed potential, relative to the platinum reference electrode, within the plateau of figure 6-8 for HCl can be set and the current observed over time using the potentiostat. Under ideal conditions of constant area and a planar electrode, these data would be described by the model introduced in section 4.4 for mass transport time scales that far exceed the double layer charging time. Specifically for an initially clean surface with no reactant products in the solution, the measured current evolution in time can be compared with equation 4.17. Figure 6-16 shows two examples of such data along with a curve fit using the 1-d model. The limiting current has been approximated from the average current between the 15 and 25 second marks in each plot, where the current was relatively stable. Normalizing the curve as shown removes a dependence on the unknown saturation concentration and active area (so long as the area remains constant). With an estimate for the Ni^{2+} diffusivity, 6.6 x 10^{-6} cm^2/s, a least squares fit to the measured data produces an estimate for the diffusion layer thicknesses.

In Fig. 6-16(a), a type 1 paddle roughly 1 mm above the sample was oscillated at 50 mm/s while in Fig. 6-16(b), a type 2 paddle at approximately the same height was also oscillated at 50 mm/s. The enforced potential was 2.5 V in both cases. The fits yield

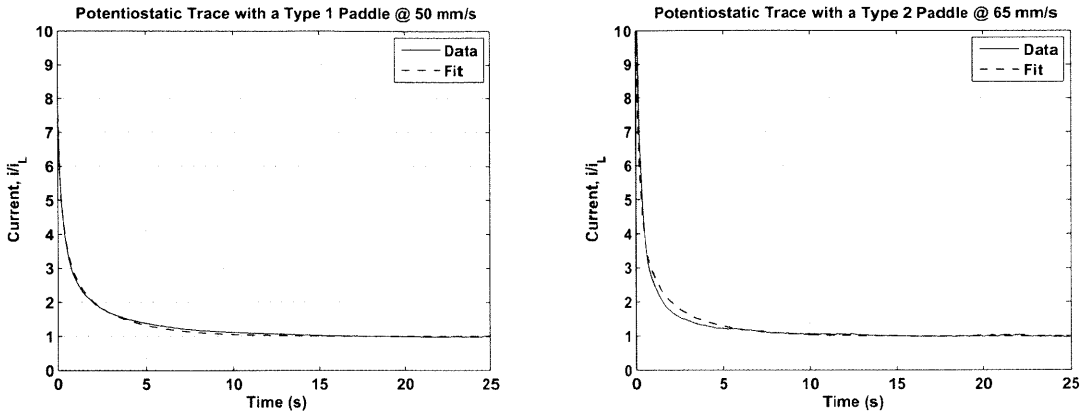

(a) Potentiostatic scan with a type 1 paddle oscillating at 50 mm/s roughly 1 mm above a strip sample.

(b) Potentiostatic scan with a type 2 paddle oscillating at 65 mm/s roughly 1 mm above a strip sample.

Figure 6-16: Potentiostatic scans within 2N HCl using solid nickel strip samples.

estimates of 136 and 131 μm diffusion layer thicknesses for the two cases respectively.

These estimates are higher than the values predicted using correlations for rectangular flow channels in section 4.1.3. However; a number of factors contribute to the uncertainty in the estimate made here. Specifically, although much wider than the photo resist thickness, the area of the sample cannot be assumed constant over the time period considered, which would lead to an increase in measured current for all other conditions constant. Conversely, referring to the simulation results of section 4.5.6, for etching within a trench, significant current decay was expected to occur due to the shape evolving to one which minimized concentration gradients.

The samples used here, patterned with MP513 had a resist thickness to trench half width ratio of $\sim$ 0.13, compared with 0.14 for the the trench simulations presented previously. However; estimated diffusion layer thicknesses here range from $\sim$ 50 μm predicted by the Sherwood number correlations in section 4.1.3 to $\sim$ 135 μm using the potentiostatic fits shown here. These correspond to boundary layer to transport layer thickness ratios from $\sim$ 1.5 to 4.5, significantly less than in the trench simulations where the fixed boundary radius was set at 14 times the resist thickness. Hence, in these experiments the assumption of a constant hemi-spherical boundary may not be valid and more detailed simulations would be required to estimate the current evolution in time due to shape evolution.

For this research, a planar experiment cannot be expected to yield identical hydrodynamic conditions to the patterned porous samples etched later. Therefore; this estimated

diffusion layer thickness is sufficient in that, along with previous correlations, it strongly suggests that the tool developed here can support transport limited conditions with diffusion layers several 10's of μm thick. If more accurate measurements were desired for this type of geometry, it would be imperative to de-convolve the competing time scales predicted by the 1-D transient model and quasi-steady numerical simulations.

6.3.6 Conclusions and Discussion Based on Preliminary Experiments

The relatively stable currents observed in Fig. 6-13, at low velocities in Fig. 6-14 and particularly during the potentiostic scans above do not show any correlation between paddle position and current. Recall that during these tests the exposed sample was 15 mm long while the paddle traveled over a 20 mm distance. Hence for a portion of each cycle the paddle was not positioned above the exposed region. This suggests that, for nickel and the conditions shown, the paddle description favors the second extreme discussed in section 6.1.3. Specifically these conditions may not result in highly localized dissolution only below the paddle. One possible exception to this observation was the 150 mm/s case in Fig. 6-14. During titanium etching, high amplitude oscillations were initially apparent at a frequency equal to that of the paddle displacement but these oscillations appear to be quickly suppressed under mass transport control.

This observation suggests that, at least to a significant degree, the complete exposed area was activated during these scans. As discussed above, in so far as the diffusion layer thickness can be kept constant on average this operating state should not prevent the tool from being applied to etching arrays. Under this assumption, the limiting plateaus in Fig. 6-14, can then be used to estimate a range of effective diffusion layer thickness over the sample as a function of velocity. Using the same estimates for diffusivity and the saturation concentration as in section 4.1.3 (6.6 x 10^{-6} cm^2/s and 4.8 M/L respectively), these plateaus correspond to diffusion layer thicknesses from 110 to 35 μm, decreasing with increasing velocity.

Given the results of this section, a paddle velocity of 50 mm/s over $\pm \sim 10$ mm with the sample potential of 3.5 V within 2N HCl was selected as an initial set point for electrochemical etching arrays of emitters for ILIS thrusters. These tests are presented in the next section, beginning with initial tests using solid nickel.

6.4 Microfabricated Emitter Arrays

The techniques developed in the previous section have been applied to fabricating porous ILIS emitter arrays as desired for the thruster design presented in Chapter 5. In this section, arrays etched on solid nickel will be presented first followed by examples of etching on porous material, leading to the final process used to developed the arrays tested for emission.

6.4.1 Etching on Solid Nickel

Solid nickel was used to establish a baseline from which to build the porous metal process. These experiments used the MP513 Aquamer resist on both isolated samples and squares mounted within the thruster package described in Chapter 5. In all cases a type 1 paddle was used and the photo mask diameter for the resist masks was 150 μm. Although many samples beyond those shown here were attempted, this discussion focuses on samples which particularly advanced the process. All samples were cleaned prior to and after etching; however many of the images shown here are taken before the final cleaning step to highlight accumulations of residue and the condition of the mask after etching. It should be noted that prior to placing the samples in the SEM they were lightly rinsed in de-ionized (DI) water to prevent corrosion within the microscope.

Figure 6-17 is typical of a 10 x 10 mm patterned solid nickel sample etched alone, without the silicon package, under DC conditions and with low speed paddle agitation. Here with the paddle oscillating to $\pm$ 7.5 mm at 50 mm/s significant variations across the wafer are evident in a direction parallel to the paddle motion. At the center of the sample some structures were formed with highly symmetric and smooth features, as in Figure 6-17(b). These features have dimensions similar to those desired ($>$ 150 μm, with $\sim$ 15 μm tip radii). This sample was etched for 150 s with 3.5 V applied between the sample and cathodic paddle based on the results of Fig. 6-13.

Given that some qualitatively desirable structures were fabricated, as in Figure 6-17(b), subsequent efforts focused on obtaining enhanced pattern scale uniformity. These included very low frequency (0.07 Hz, 15 s period), high duty cycle (75 %) trials which showed very little improvement over the sample shown in Figure 6-17. Much larger 20 x 20 mm samples were also tested to determine if flow non uniformities could be eliminated by moving the sample edges far from the patterned region. For these samples the central 10 x 10 mm

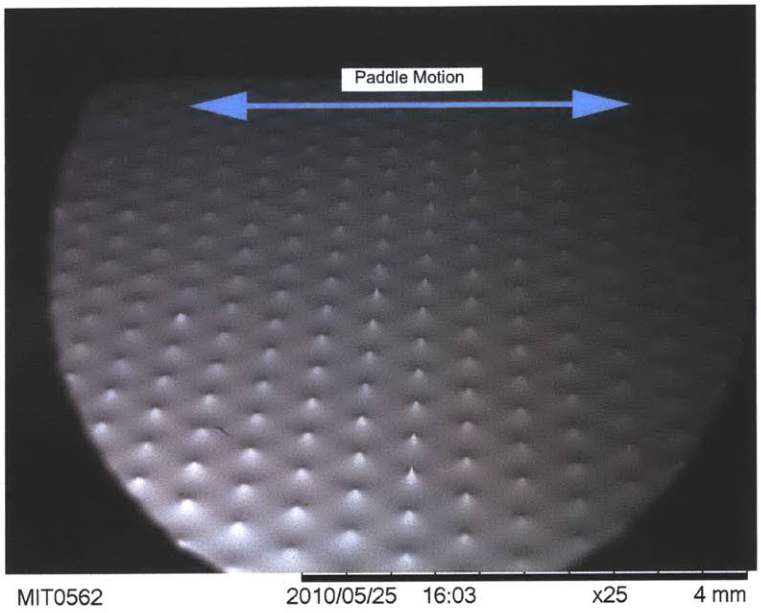

(a) Wafer level non uniformities in a direction parallel to the paddle motion. Here the paddle was roughly 1 mm from the sample and agitated at 50 mm/s.

(b) SEM image of a structure formed at the center of the array shown in the adjacent figure.

Figure 6-17: Sample of etching a solid nickel sample with low agitation using a type 1 paddle.

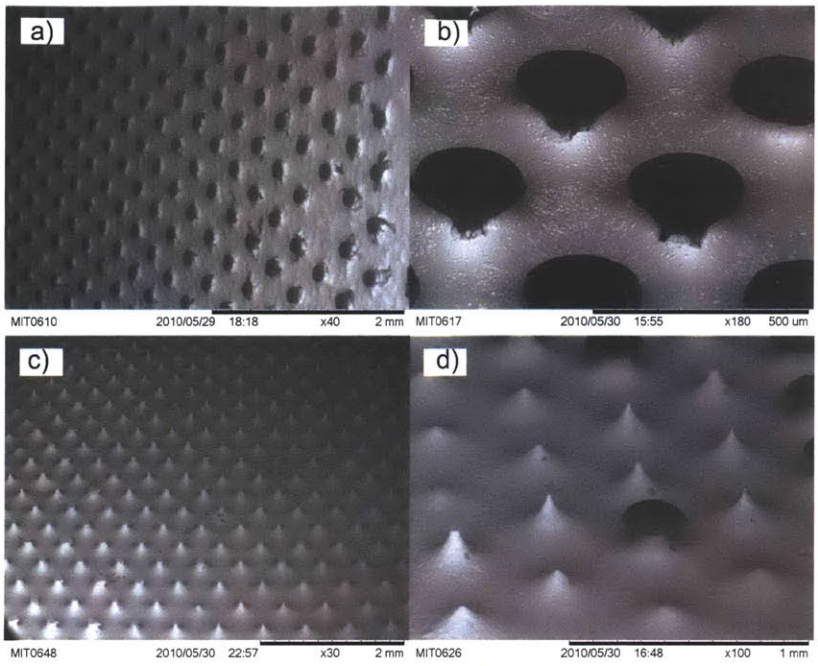

Figure 6-18: Examples of features etched on large, 20 x 20 mm samples with the center 10 x 10 mm patterned and the remaining area exposed.

of the sample was patterned with the standard 150 μm diameter masks leaving 5 mm of additional material around all edges. At the same paddle speed and approximate separation as above this technique succeeded in increasing uniformity. However, the etch rate was greatly decreased as shown in Figure 6-18(a) where the same conditions as in Fig. 6-17(a) were maintained for 180 seconds but the etch was far from complete. The measured current was typically $\sim$ 3.5 A using 10 x 10 mm samples and 4.5 A for the 20 x 20 mm samples. Hence the current density (for a completely activated sample) decreased from 3.5 to 1.1 A/cm^2 between the samples. In Figs. 6-18(a,b), residues are clearly visible stuck to the remaining masks. However; it is not clear if this was due to the mask degrading or etch products precipitating from the solution. Another feature of these etches were the small irregularities visible in Fig 6-18(b), particularly for short duration etches. Figures 6-18(c) and 6-18(d) were achieved with the etch potential raised to 4.2 V to compensate for the increase in overall measured current. Figure 6-18(d) shows a typical portion of Fig. 6-18(c) at increased zoom. Rather than result in smooth etching, this potential induced surface roughening which may indicate a transition to the oxygen evolution regime to the far right of Fig. 6-8.

These preliminary etches demonstrated a how a variety of etch qualities can result depending on the prescribed conditions. While varying the sample size increased uniformity to some degree both attempts reinforced the dominant role of the mass transport conditions on etch quality. One of the major proposed benefits of electrochemical etching is the ability to etch samples selectively, within a package, compatible with the proposed overall process of section 5.3. Clearly the package itself can be expected to influence the fluid motion induced by an oscillating paddle above, hence all further experiments were performed using samples mounted in the silicon frame.

A set of arrays was then etched with solid nickel mounted to the silicon thruster package (see Fig. 5-1). Here, the paddle agitation rate was found to have a dominant impact on both the pattern scale uniformity and the feature (emitter) scale. In Figure 6-19 SEM images for three samples etched at increasing velocity are shown. In all three cases the etch potential was set to 3.5 V. This potential was applied in pulses, but at very large periods and duty cycles, 20 seconds on and 5 seconds off. The paddle to sample gap was roughly 1.5 mm, while the paddle oscillated over $\pm$ 10 mm at the indicated velocities.

Figure 6-20 shows an SEM image taken near the edge of the upper sample in Fig. 6-19. The highlighted regions, observed on other samples under similar conditions, appear to indicate regions of enhanced mass transport leading to local increases in the etch rate. Furthermore, under these agitation conditions, the space between structures is characteristically uneven with spacial variations in etch depth at length scales comparable to the structure spacing. Compared with the lower image of Fig. 6-19, these non uniformities are absent at increased agitation rates.

At the pattern, or wafer, scale the uniformity was seen to increase dramatically from 65 mm/s to 75 mm/s paddle motion. The image on the left of Fig. 6-21, etched at 65 mm/s is similar to Fig. 6-17(a) in that the etch rate again varied across the sample with enhanced etching at the sample edges compared with the center. Again, this non-uniformity coincided with the direction of paddle motion. With increased agitation the sample uniformity increased significantly, although some over etched regions are present at the bottom of Fig. 6-21(b).

In section 4.5 the expected variations due to small $\sim$ 5 % variations in the diffusion layer thickness were considered. Two examples of local non uniformity are shown in Figure 6-22. Figure 6-22(a) is an SEM image at the center of an array etched at 50 mm/s. The

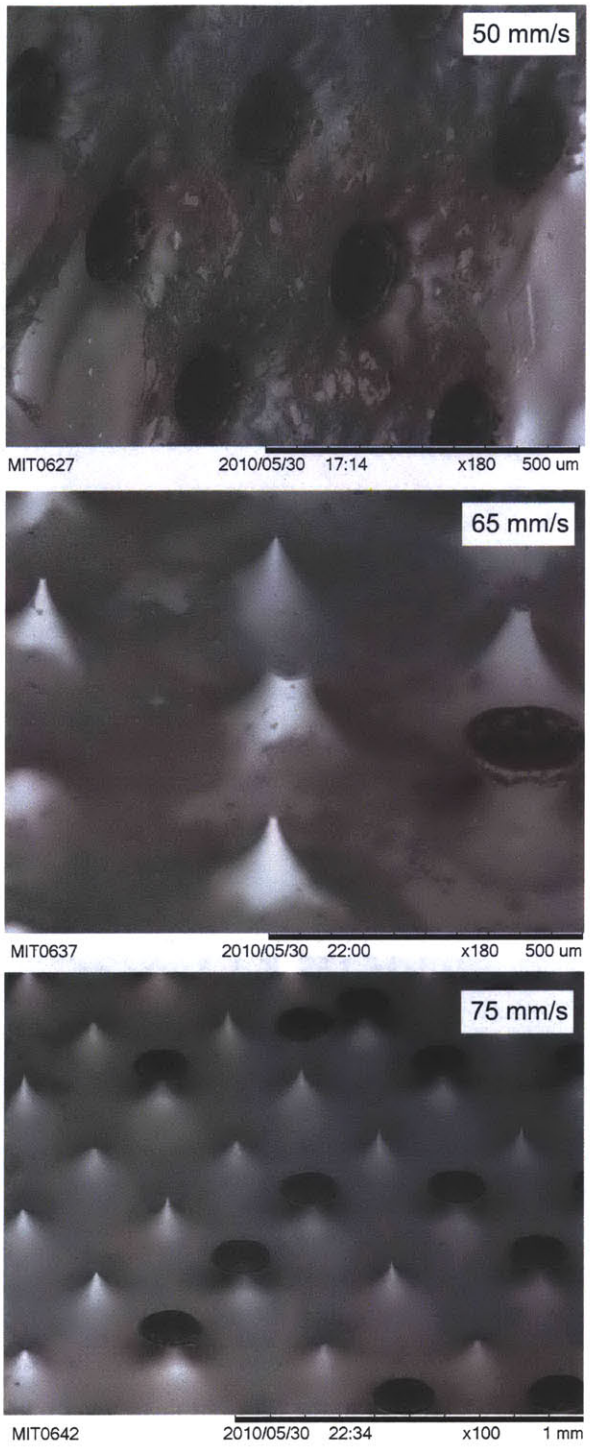

Figure 6-19: Solid nickel arrays etched with increasing velocity. The samples have not been cleaned to highlight the accumulated residue in each case.

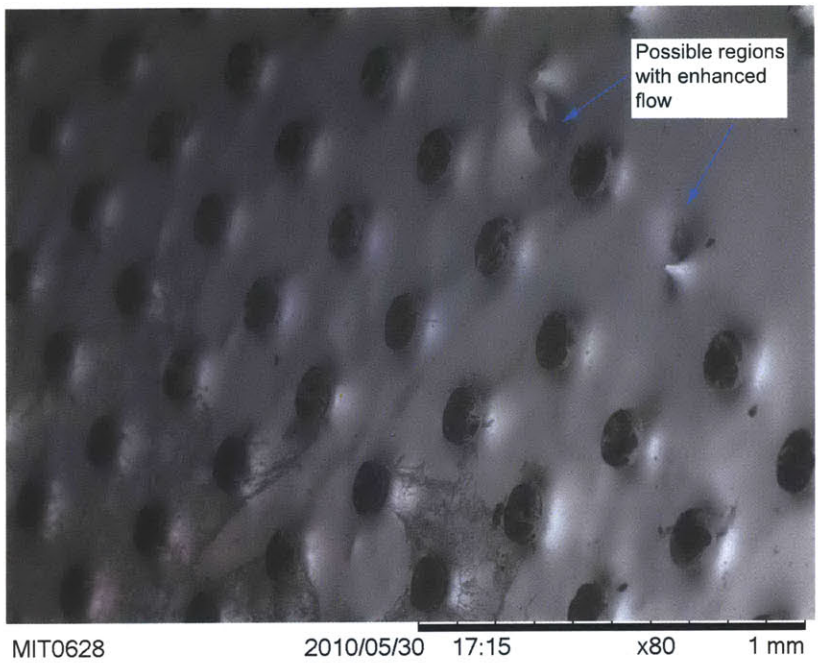

Figure 6-20: An example of possible regions of enhanced etching due to flow patterns around the etched features on solid samples.

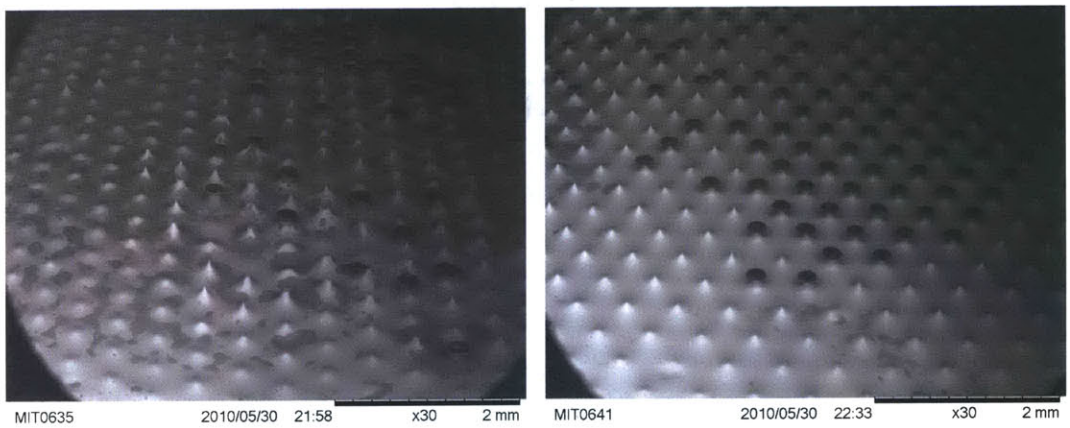

(a) SEM image for a solid array fabricated in the silicon package with a paddle speed of 65 mm/s.

(b) SEM image for a solid array fabricated in the silicon package with a paddle speed of 75 mm/s.

Figure 6-21: Samples demonstrating an increase in uniformity and less etch residues at increased agitation rates.

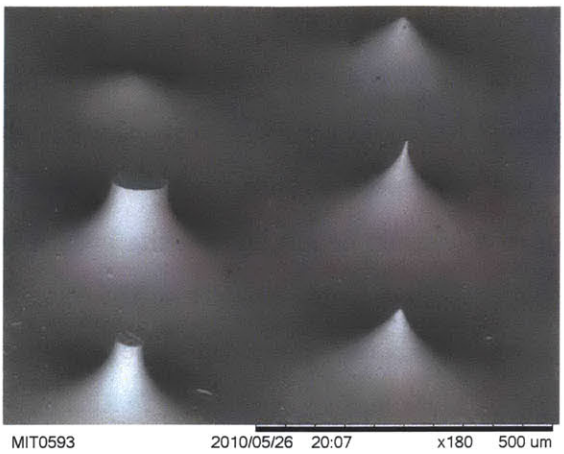

(a) SEM image of solid emitters showing a high degree of non uniformity between adjacent emitters.

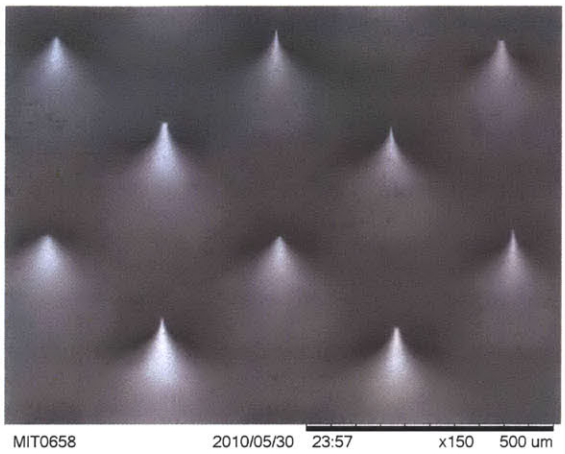

(b) SEM image of solid emitters demonstrating non uniformities similar to that predicted in Chapter 4.

Figure 6-22: Examples of the local non uniformities experienced when etching solid arrays..

discrepancies between adjacent structures are very large. While the large scale variations in Figs. 6-17(a) and Fig. 6-21(a) may be explained by enhanced transport near the edges of the samples, these variations are much more localized. Figure 6-22(b) presents an SEM image of emitters near the center of the 75 mm/s etched sample shown above. In this case the variations resemble those predicted numerically for small variations in the diffusion layer. These images show that, in addition to enforcing more uniform transport hydraulically, slightly higher paddle rates may also yield enhanced local stability.

Summary of Observations from Solid Array Etching

These experiments demonstrated that structures similar to those predicted in section 4.5 can be formed. The etch quality was found to be highly dependent on the agitation conditions. At low agitation rates pattern scale non uniformities and feature scale irregularities are prominent. Increasing the agitation rate was shown to lead to enhanced pattern scale uniformity. However; both the increased etch rate and decreased average boundary layer thickness may hinder control and accuracy for etches targeting specific emitter heights or tip radii. Further; recall that in the preliminary experiments above, the effective diffusion layer thickness was estimated to decrease to as low as 35 μm for 150 mm/s paddle oscillations. When etching the $\sim$ 45 % porosity porous nickel used here, with pores and particle sizes several μm in size, high agitation rates may begin to prevent pore level smoothing and

surface micromachining.

Increasing the potential such that operation outside of the measured current limiting plateau resulted in reasonable pattern scale uniformity but surface roughening at the feature (emitter) scale. On porous structures this could lead to in pore etching.

These results again enforced the dominance of hydraulic conditions on the etch rate and uniformity (at all scales). This prompted two significant design changes to the etching station prior to proceeding to experiments with porous arrays. First, the type 2 paddle shown in Fig. 6-3, was installed to enhance the cathode surface area (due to the large observed currents). Second, the height calibration scheme described in section 6.1.2 was installed. This reduced the uncertainty in paddle to electrode gap by roughly an order of magnitude, from up to 1 mm to approximately 100 μm (measured using shims). With, effectively, a new parameter to vary, initial tests with porous material included exploring how the paddle to sample gap would impact etch quality.

6.4.2 Constant Voltage Etching on Porous Nickel : 65 μm Thick, 150 μm Diameter Masks

Initial tests on porous metal using the MP513 mask were plagued by poor resist quality. The MP525 resist was acquired as an alternative and, initially, produced moderate yields during the lithography steps. The results presented in this section used this resist patterned to create 150 μm diameter masks.

As described above, prior to these experiments, the etch station was upgraded to include a more accurate method for setting the sample to paddle height. The impact of this metric on etch rate and uniformity was explored using a set of 7 patterned samples. All etches were performed at 4.2 V with the type 2 paddle set to oscillate between $\pm$ 10 mm over the sample at 75 mm/s. Using this paddle no obvious signs of, or problems due to, gas evolution were observed even at 4.2 V. Figure 6-23 presents the measured current over time for the different sample to paddle heights used here. As these were masked samples with highly variable geometries over time as the etch progresses, a final stable limiting current was not expected in any case. Nevertheless it is interesting to compare the relative currents after the dominant initial transients. Figure 6-24 plots the average current for the period from 40 to 60 seconds as a function of the paddle to sample gap to the -1/3 power. Recall in chapter 4, the variation in diffusion layer thickness for a rectangular flow channel was

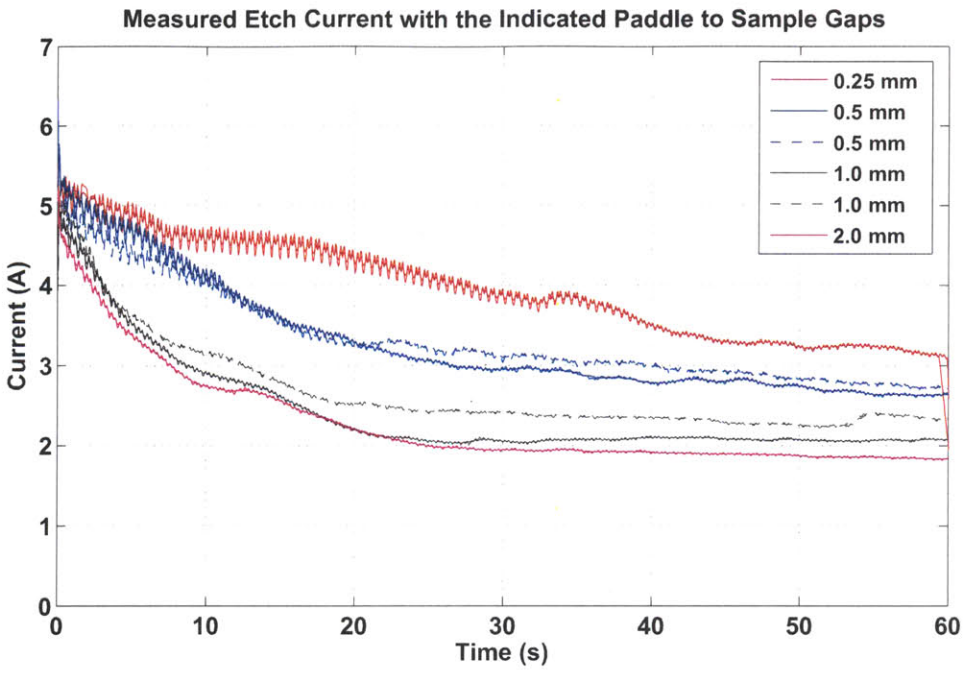

Figure 6-23: Measured currents over time, at fixed potentials (4.2 V) and paddle motion (75 mm/s over 15 mm) at the indicated electrode gaps.

expected to vary like the height to the 1/3 power. For all other properties constant, the measured current should vary with the the inverse of diffusion layer thickness. Hence, the linear relationship between current and electrode gap to the -1/3 power shown in Figure 6-24 appears consistent with the correlation, despite the significant differences between this arrangement and a rectangular flow channel.

The simulation results presented in section 4.5, predicted an increase in emitter aspect ratio with decreasing boundary layer thickness, and hence electrode gap. In Figure 6-25 and 6-26, SEM images for emitter arrays etched using gaps of 0.25, 0.5 and 1.0 mm are presented as an example. In each case the net mass removed was calculated to be within $\sim$ 3 % of 63 mg. The images include the remnants of the photoresist mask as it is interesting to consider the impact of the mask itself on the etch.

Although a limited data set, some observations are evident from the images. For smaller electrode gaps, many sharp structures on the order of the desired $\sim$ 150 μm height were produced, although significant non-uniformities were present across the wafers. For a large electrode gap, Figs. 6-25(c) and the far right of Fig. 6-26, very shallow structures are present. However, the mask appears to have separated from the structures at very large

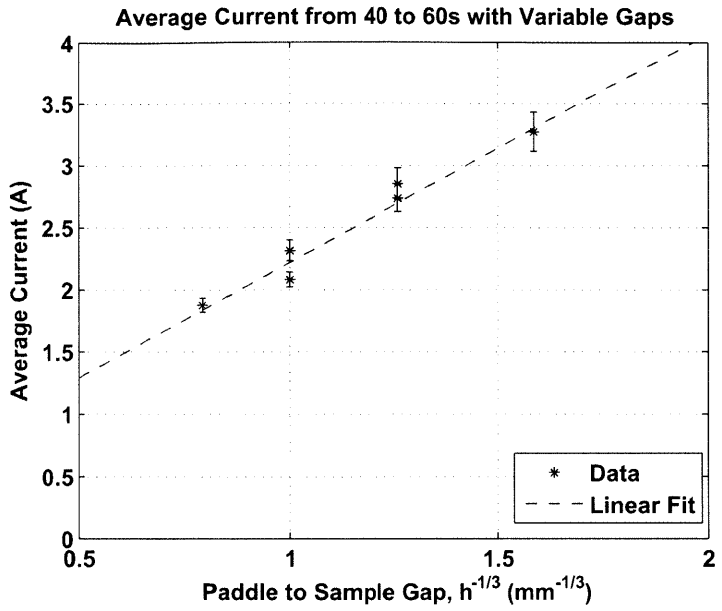

Figure 6-24: Average current after initial transients plotted versus the electrode gap to the $-1/3$ power. Although a paddle agitator was used, the linear (r=0.981) relationship agrees with the empirical correlations for a rectangular flow cell, equation 4.11, under mass transport control.

emitter tip diameters. Figures 6-25(c) and 6-26 are representative of the behavior observed during two other attempts at large gaps (1.0 and 2.0 mm) with all other hydraulic conditions constant. For both the 0.25 and 0.5 mm gaps, instances of the mask bending the structure were observed. Hence although tall structures were observed for smaller electrode gaps (smaller diffusion layers), problems with the mask prevented any rigorous comparisons with respect to the numerical simulations.

While pockets of well formed porous structures were observed at both 0.25 and 0.5 mm electrode gaps, on some occasions repeated scans at 0.25 mm resulted in periods of extremely high current etching, including attacks to the pore structure. This may have been due to the inherent non uniformities in the thickness of epoxy bonding the porous sample to the silicon frame leading to electrode gap variations which would become more significant at reduced set gaps. Furthermore, the transient behavior with a 0.25 mm gap, upper curve in Fig. 6-23, differed greatly, with significantly more oscillations over a longer time period compared with all other gaps. As shown in the Figures, operation at 0.5 mm produced comparable results at both the emitter and pattern scales but without these issues. Subsequent etches were made with a 0.5 mm electrode spacing and did not encounter either

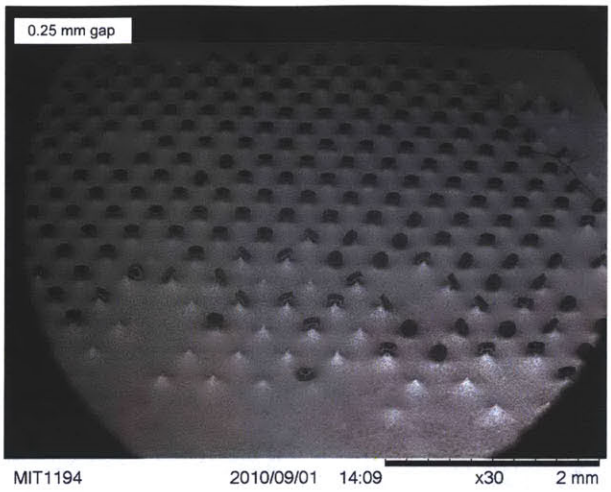

(a) Etched array with an electrode gap of 0.25 mm.

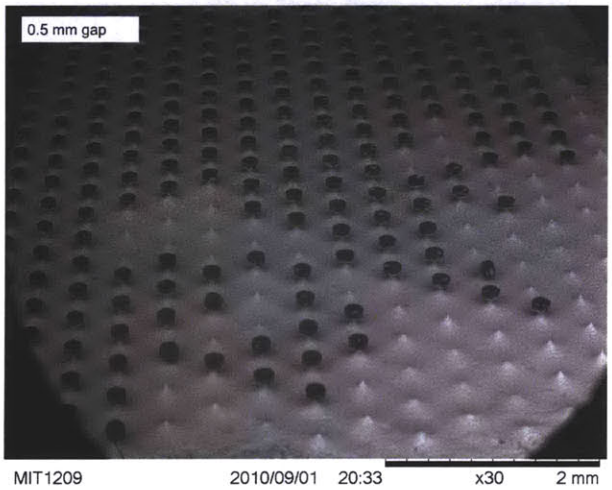

(b) Etched array with an electrode gap of 0.5 mm.

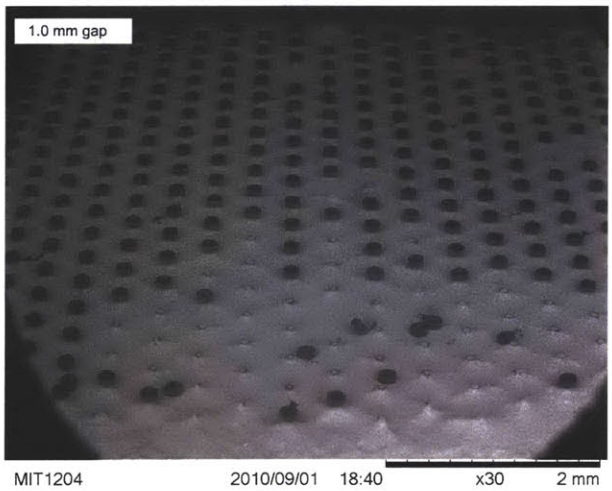

(c) Etched array with an electrode gap of 1.0 mm.

Figure 6-25: Porous nickel arrays etched using the indicated paddle to sample electrode gaps with all other variables constant.

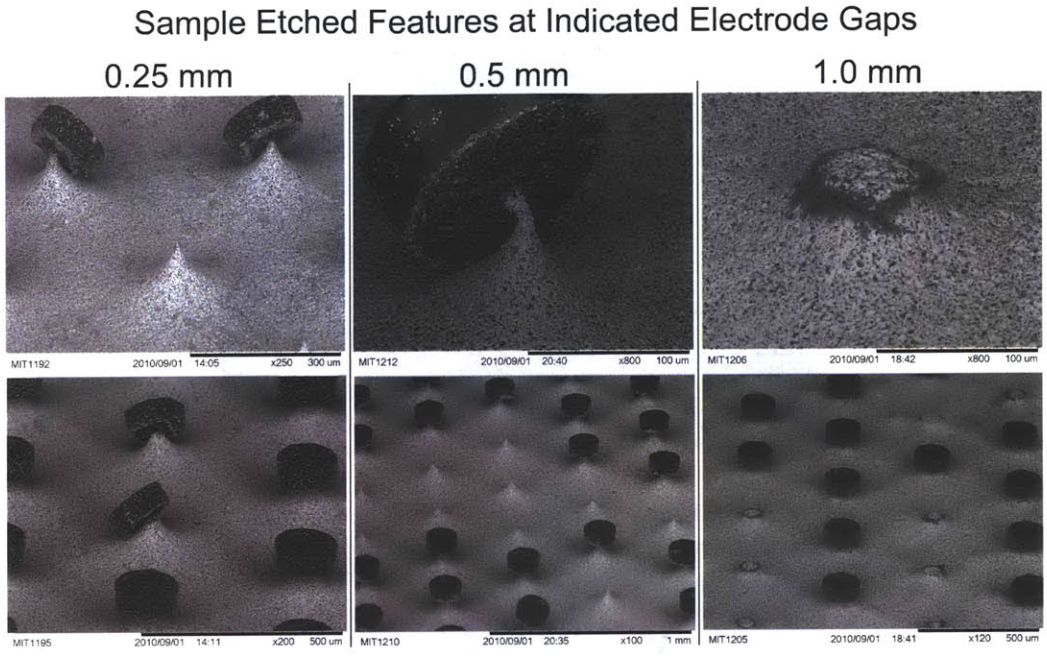

Figure 6-26: Examples of features formed when etching with the indicated paddle to electrode gaps. Although repeatable, it was unclear why the mask often detached prior to completing the etch with relatively large gaps (eg. 1 mm here).

of these problems.

Figure 6-27 demonstrates the typical degree of uniformity which could be achieved using a 0.5 mm gap and the paddle and electrical conditions described above. The target etch mass was increased slightly between these samples with a few more mg removed between samples beginning with the upper figure at 63 mg and increasing with each subsequent figure. The results demonstrate that although pockets of consistent emitters could be formed under these conditions, the arrays were characterized by regions of significantly over, or under, etched emitters.

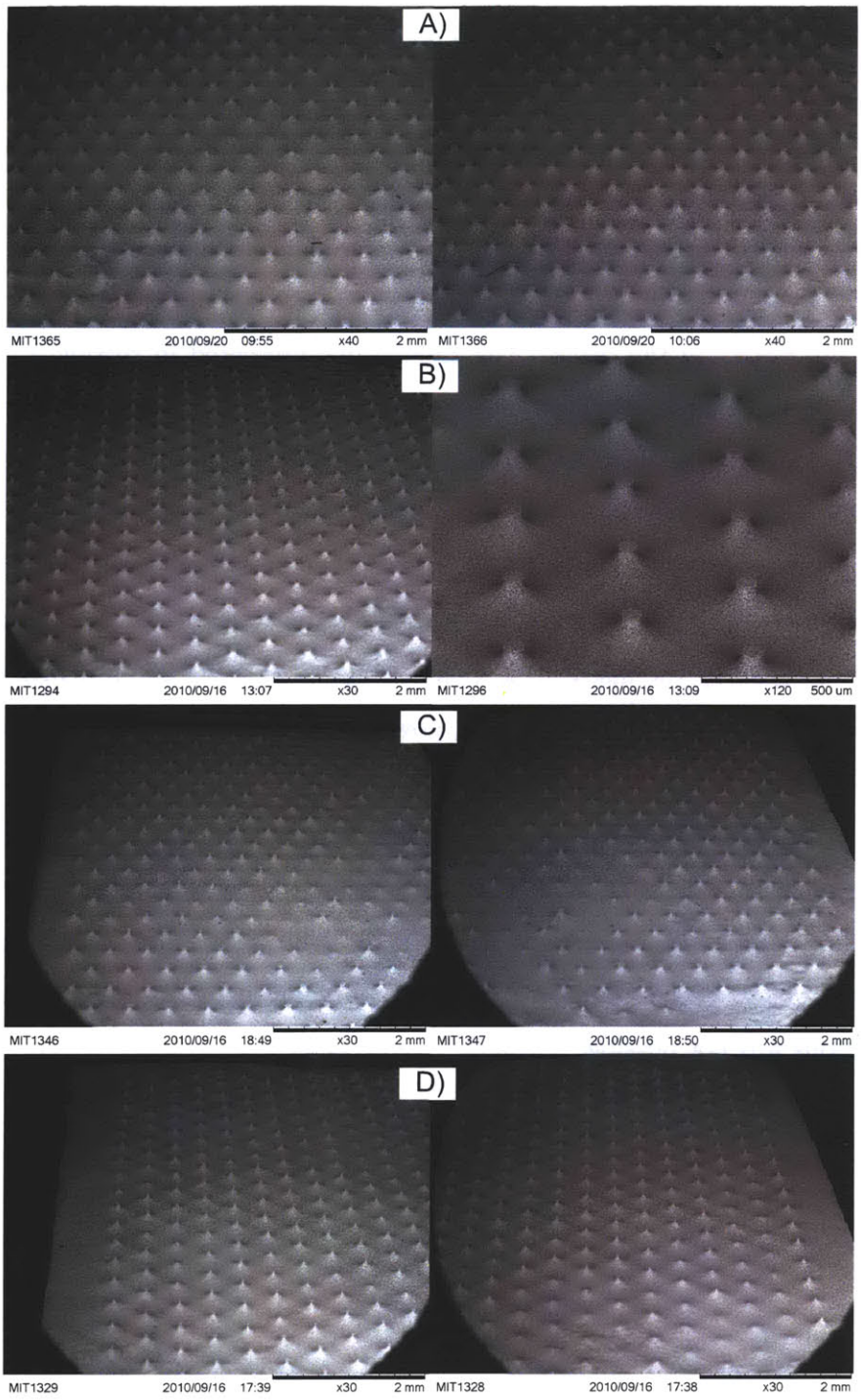

Figure 6-27: Non uniformities at the wafer scale when etching under constant voltage conditions.

As mentioned above, when etched under these conditions, the structures were characterized by significant necking and frequent deflections due, apparently, to the massive size of the mask compared with the structure. In addition to the instances shown in Fig. 6-26, Figure 6-28 presents several examples of problems attributed to the large mask. In the first figure a piece of porous nicekl can be seen stuck to a detached mask. This figure is also interesting in that it reveals the degree to which the dry film masks penetrates the porous surface, as seen by the imprint on the reverse side of the mask. In Fig. 6-28(b) a structure with a $\sim$ 15 μm diameter neck has been significantly bent but remained intact after chemically removing the mask. The simulations presented in section 4.5 predicted necking for very small diffusion layer thicknesses. Although the boundary model used in those simulations cannot be verified with these results, more generally the necked structures suggest locally enhanced flow was occurring some distance just below the mask.

The trials summarized above identified two primary concerns with the MP525 resist. The thick mask was not ideal for etching emitters with 150 μm diameter masks as the features were dwarfed by the mask itself. Some attempts at using 200 μm with the 65 μm thick mask did not improve matters as the, now even more massive, mask again resulted in deflected emitters at even larger neck diameters. Problems with this MP525 mask were not limited to emitter deflections. In practice lithography with this resist had low yields, although an improvement over the MP513, and frequently lead to patches where the resist detached during developing or etching as in Fig. 6-26. This made a more detailed parametric evaluation of the effect of etch conditions on etch quality impractical as maintaining constant initial conditions was not possible.

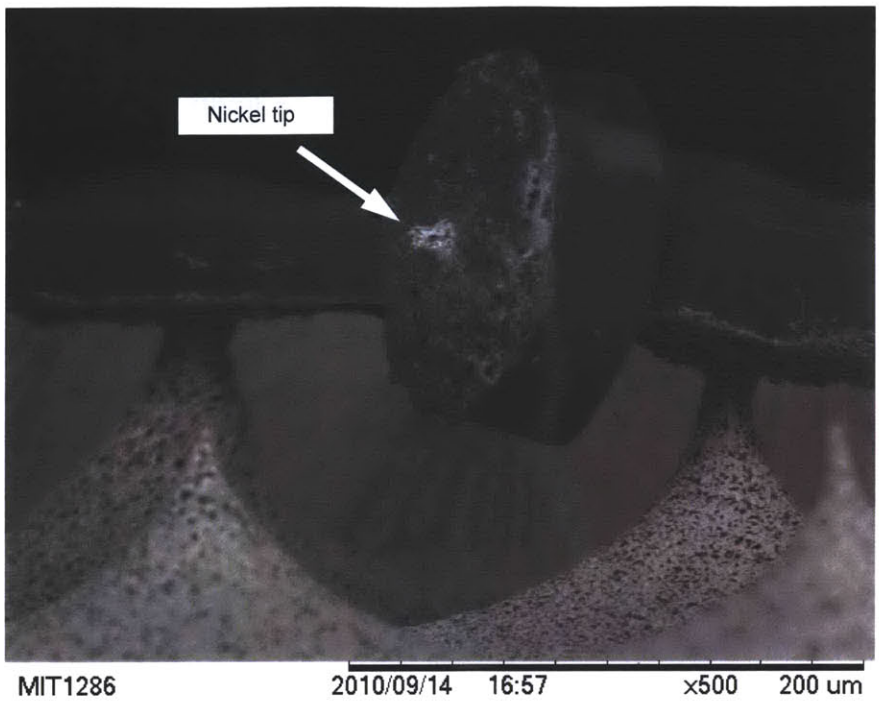

(a) A detached MP525 mask with the tip of an emitter embedded in the mask.

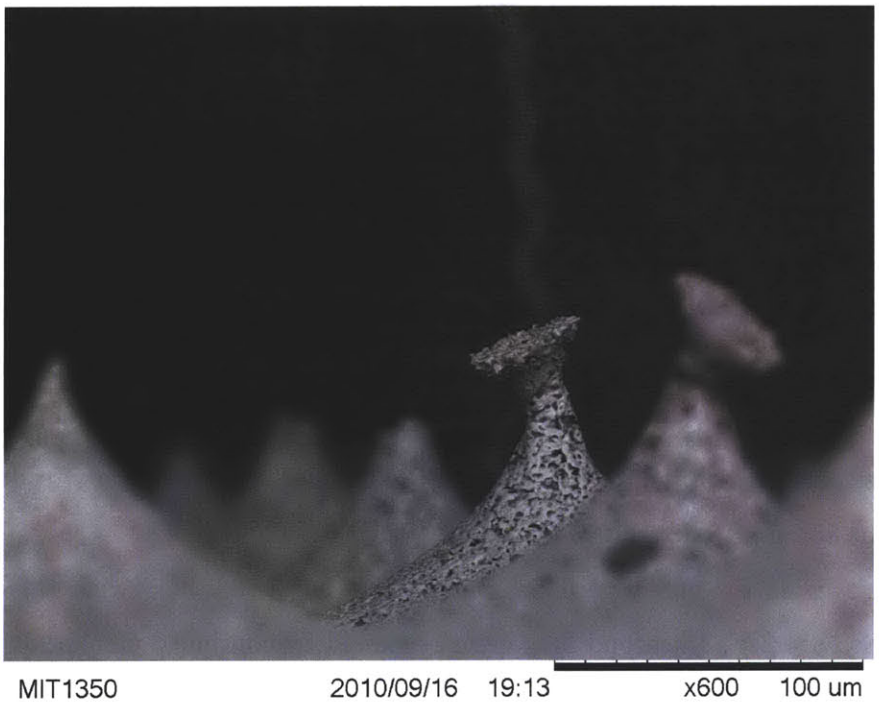

(b) Examples of bent emitters observed with the MP525 mask. The emitter in focus has a $\sim$ 15 μm neck diameter.

Figure 6-28: Examples of damage attributed to the extremely thick MP525 mask.

6.4.3 Constant Voltage Etching on Porous Nickel : 15 μm Thick, 200 μm Diameter Masks

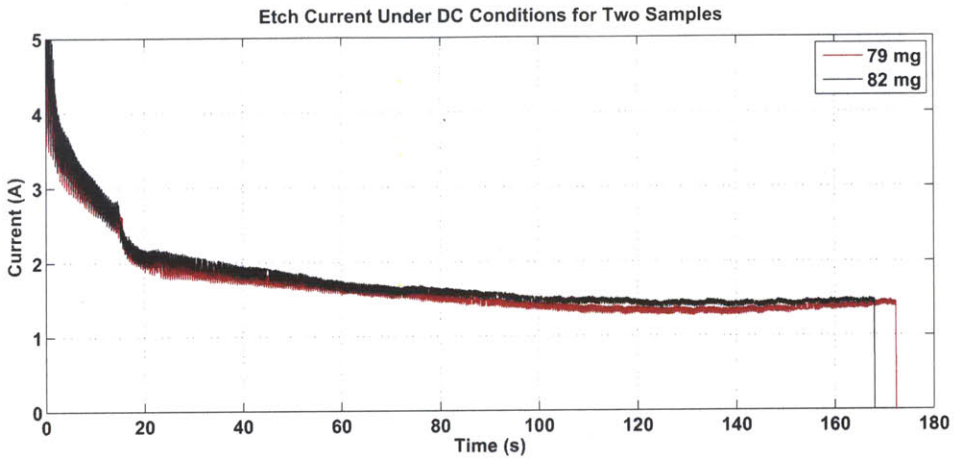

Figure 6-29: Samples of etch currents measured over time using etching under constant voltage conditions with the 15 μm thick, 200 μm diameter mask.

The DuPont Riston FX515 mask was a natural progression at this stage due to both its reduced thickness (15 μm) and its listed suitability for acid based etches. Using this resist and the lithography process outlined in table 6.1, samples were patterned to create 200 μm diameter masks. It should be noted that this resist had a much larger yield at the lithography stage both at the pattern scale, meaning masks were consistently formed up to the sample edges, and at the batch level, allowing for much more efficient experimentation. The decision to increase to 200 μm masks was partly motivated by attempted emission tests being performed in parallel which were not successful. Increasing the mask was expected to increase the emitter height (see section 4.5) and hence the field enhancement. This had been deemed unwise with the 65 μm thick MP525 mask which was already resulting in bent structures at 150 μm in diameter.

The best cases for etching under constant voltage conditions with this mask were achieved with a 4.2 V, 15 second long signal followed by continued etching at 3.8 V using the type 3 paddle while oscillating over $\pm$ 7.5 mm at 75 mm/s. The current recorded when etching two samples has been plotted in Figure 6-29. The reduced travel distance compared with the previous section and the lower voltage during the majority of the etch were both efforts to reduce the impact and severity of the initial transients as the diffusion layer builds. During this time the paddle position appears to play a greater roll (hence the oscillations in

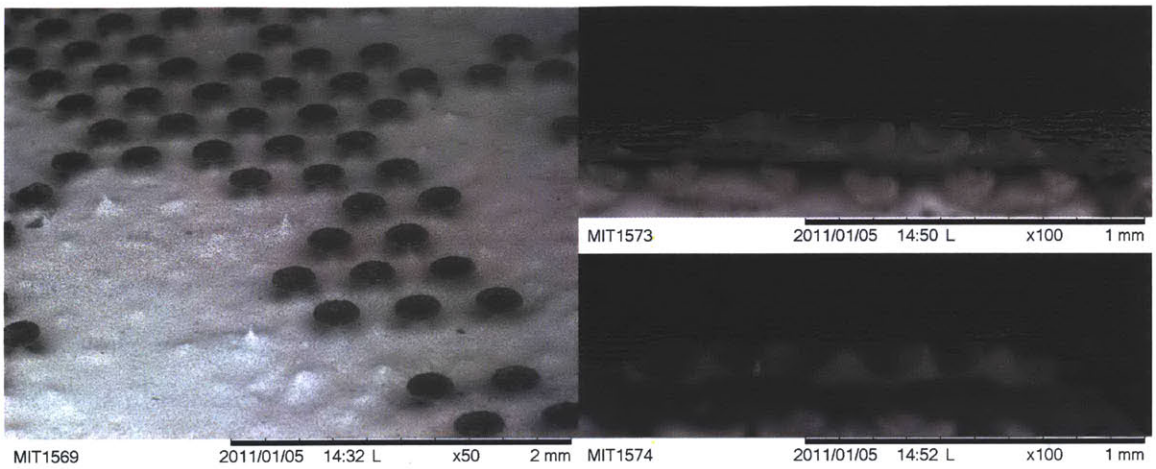

Figure 6-30: Examples of the significant non uniformities resulting during constant voltage etching with the 200 μm, 15 μm thick Riston mask. Although locally non-uniform, no particular edge or direction was favored.

Fig. 6-29), reducing the travel distance was intended to reduce non-uniformities which could arise during this time and then be compounded throughout the etch. Meanwhile increasing the potential could lead to initially higher currents in regions that are not transport limited, leading to more material removal and, possibly, a faster approach to diffusion control.

Figure 6-30 shows two examples of etching under these conditions. Despite consistent masks and relatively repeatable current traces, Fig. 6-29, initial etch results with this mask again lacked uniformity. In the solid array experiments presented earlier in this chapter, a relatively small variation in the paddle velocity lead to both an increase in pattern scale uniformity and enhanced local uniformity between small groups of structures. The porous arrays etched in this section were typically characterized by only the latter, poor local uniformity. Instead of varying the hydraulic conditions, which may have reduced the pattern scale uniformity, pulsed etching was considered as an alternative to enhancing local stability.

6.4.4 Pulsed Voltage Etching on Porous Nickel

During Chapter 4, it was motivated, using numerical simulations, that even small perturbations in the diffusion layer thickness could result in significant non uniformities when comparing emitters on a single wafer. One of the possible explanations[150] for pulsed etching achieving enhanced uniformity during electrochemical etches was that it may result in a more conformal diffusion layer near the surface as it evolves. The frequently non uniform

constant voltage etches presented above often displayed conglomerates of etch products on or around some remaining masks when viewed after etching, suggesting that to some degree the diffusion layer was interacting with the mask causing precipitates in a non-uniform manner. Given these observations, pulsed etching was attempted.

The 1-d model in section 4.4 showed that for low duty cycles and high frequencies, the average effective diffusion layer thickness during pulsing could reduce to length scales much smaller than the constant voltage diffusion layer thickness. As noted above, the etch may have already been pulsed to some degree due to the paddle motion in the tests above. However, current oscillations at the paddle frequency were typically low after initial transients.

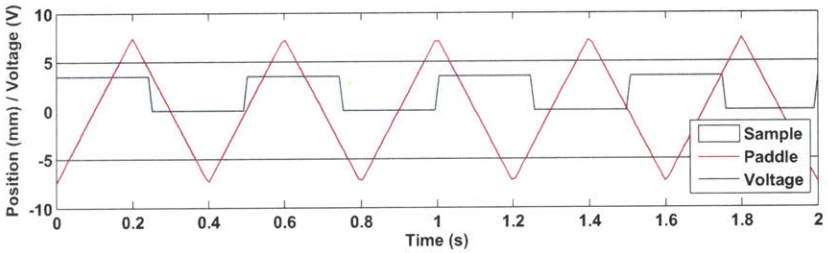

Figure 6-31: While the paddle oscillated over the sample at 2.5 Hz, the electrical signal was pulsed at 2 Hz.

Based on the results of the previous sections a diffusion layer thickness between $\sim$ 50-75 μm would be consistent the enforced hydraulic and observed electrical conditions. In the experiments presented here, the electrical pulse frequency was set to 2 Hz with a 50 % duty cycle. For a diffusion layer thickness between 50 and 75 μm, this corresponds to a non dimensional period, T^* in the model, between 0.13 and 0.06 respectively. Referring to the estimates from that model, this selection may result in a reasonably significant ($\sim$ 50 %) decrease in the effective diffusion layer thickness. However; in order to observe any effects from pulsing, a relatively small pulse period, T^*, was desirable and hence a trade off was required. Since the paddle may have already induced perturbations at 2.5 Hz, a value close, but not equal, to that of the paddle was chosen. Figure 6-31 demonstrates how, by selecting a frequency different than that of the paddle, the possibility for locking the paddle and electrical signals in phase was avoided. If the two signals were in phase such that the electrical signal was activated over one portion of the paddles travel more than others, it could result in non-uniformities.

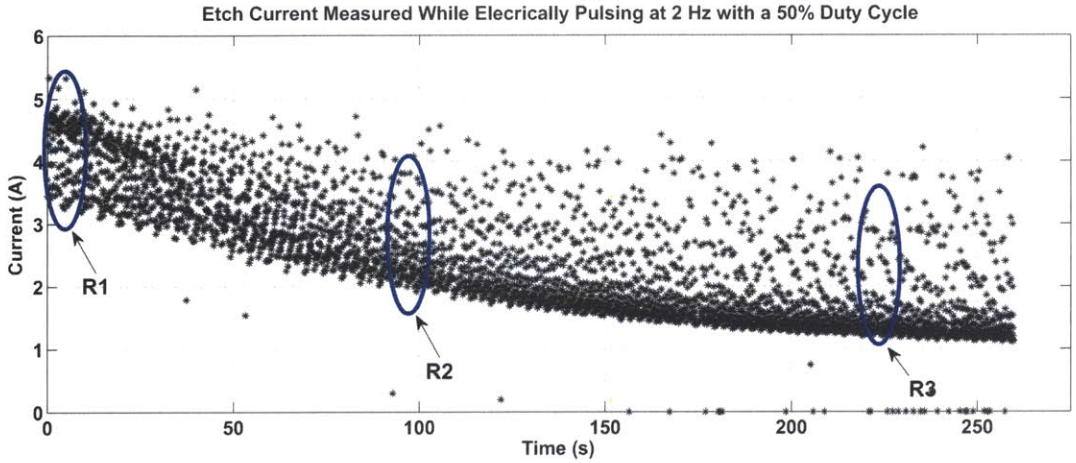

(a) Measured current over time throughout a complete etch while pulsing the applied potential at 2 Hz with a 50 % duty cycle.

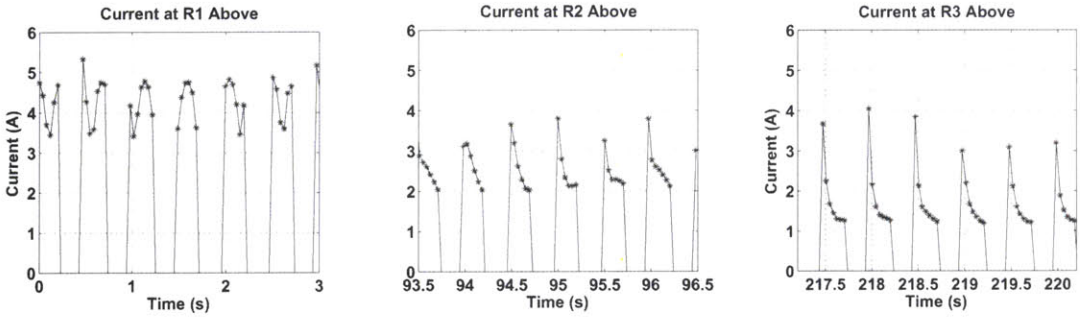

(b) (c) (d)

Figure 6-32: Measured current over time using pulsed etching. Figures b,c and d show the behavior at the regions highlighted as R1,R2 and R3 respectively in the upper figure.

Plots of the observed current while using a 3.8 V, 2 Hz signal with a 50 % duty cycle are shown in Figure 6-32. Note that during this test the sample was first subjected to 0.5 V for 15 seconds in an attempt to activate the surface, this had been attempted previously with no discernable effect and its influence here is unknown. Otherwise, the paddle conditions were identical to those in the constant voltage case above (75 mm/s over $\pm$ 7.5mm, 0.5 mm gap). The overall etch time to the same mass of removed material was roughly 1.5 times longer than under constant voltage conditions, demonstrating that, as expected, the average current did not decrease by an amount equal to the duty cycle (as would be the case without transients). The lower figures show the circled regions, R1, R2 and R3 in the upper figure for representative 3 second segments. These subplots demonstrate that, when pulsing, the current pulses transition from nearly square, high amplitude, currents in R1, to traces strongly resembling the diffusion controlled 1-d pulsing model of section 4.4 in R3. Compared with Fig. 6-29, the transient behavior occupies a significantly longer portion of the etch, even when considering the sample is only active for half of the time shown in Fig. 6-32(a).

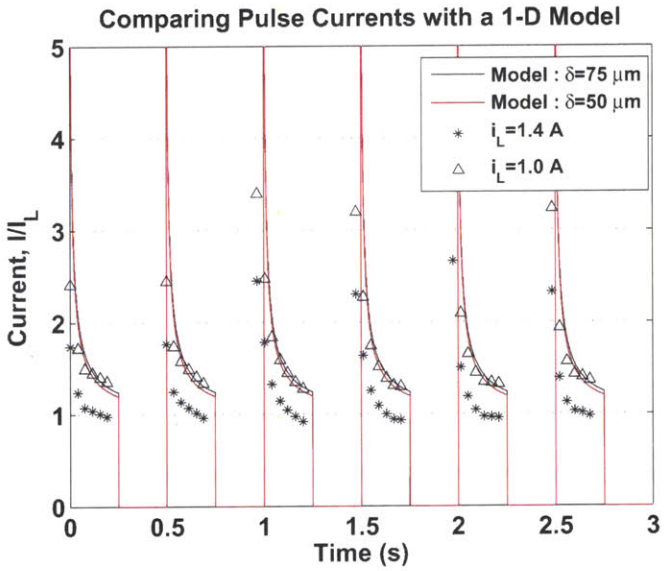

Figure 6-33: When compared with the 1-D theory of section 4.4, the measured current within the developed region, Fig.6-32(d), shows reasonable agreement depending on the selection of I_L and δ.

In Figure 6-33 a section of data from 200 to 203 seconds in Fig. 6-32(a) has been normalized and plotted alongside theoretically predicted non dimensional currents using

the 1-d model. This plot has been included as a simple comparison only, no rigorous fit to the data has been performed. The two curves for the model, assume a 50 μ and 75 μm total diffusion layer thickness. The first trace of the data has been normalized by, 1.4 A, the average current over the last 20 seconds of Fig. 6-29 where constant voltage etching was performed with the same hydraulic conditions. Meanwhile, if normalized by $\sim$ 1 A, equivalent to increasing the equivalent constant voltage diffusion layer by 1.5 times, the data appears more consistent with the model.

Pulsed etching was found to yield significant enhancements to the etch uniformity at both the pattern and feature (emitter) scales. Figure 6-34 compares results of etching under constant voltage conditions with those achieved using pulsed voltages for identical, hydraulic, paddle conditions. Not only did pulse etching yield more uniformity between emitters and across the waver, but the overhead topographical images shown in the figure reveal that the emitters themselves appear more axially symmetric.

Given the results shown for the sample case above, this technique has been adopted for all arrays yielding significant batch yields. For example, the four arrays shown in Figure 6-35 have been etched to a consistent etch mass (104 mg) under identical paddle motion and electrical conditions. Compared with the example in Fig. 6-34, the potential has been decreased slightly to 3.5 V in an effort to reduce the impact of the initial section (R1) in Fig. 6-32(a), however all other conditions were held constant. After etching sample 1, a small error in the paddle center position (about which oscillation takes place) was found which could have lead to uneven agitation. This was corrected before etching samples 2 through 4. Although sample 3 appears slightly over etched compared with samples 2 and 4, the results are generally consistent. This pulsed etch, at 3.5 V, has been adopted as the final etch configuration used to develop the functioning emitter arrays presented in the next chapter.

Pulsed etching has increased uniformity immensely at the pattern, or wafer, scale, however; at the pore scale the degree to which the surface has been smoothly etched without impacting the pores has been reduced. Figure 6-36 demonstrates some of the worst examples of this phenomenon observed using this process. Compared with, for example, Fig. 6-26 under constant voltage conditions, these emitters are characterized by relatively rough protrusions. This phenomenon was not unexpected in the context of the 1-d transient model. There it was argued that pulsing would reduce the effective diffusion layer thickness, and

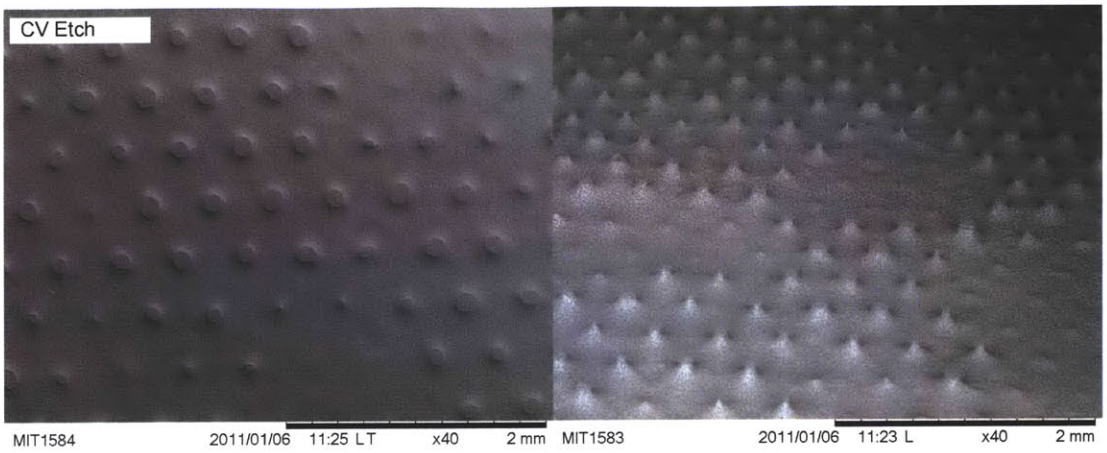

(a) An array etched under constant voltage (CV) conditions demonstrating strong non uniformities between patches of structures and highly irregular shapes where view from above.

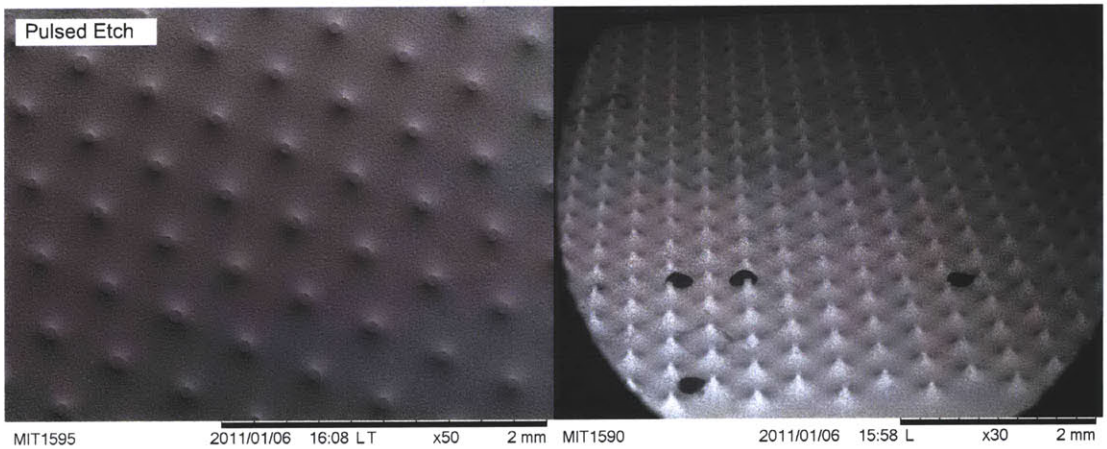

(b) An array etched to the same removed mass and with identical hydraulic conditions to the adjacent figure but using a square pulsed voltage at 3.8 V, 2 Hz with a 50 % duty cycle.

Figure 6-34: Arrays of porous emitters etched under constant voltage and pulsed voltage conditions. Pulsing increases both pattern and feature (emitter) scale uniformity..

hence the length scale for smoothing. Although disconcerting, it should be stressed that the images in Fig. 6-36 represent particularly poor emitters to highlight the concern and are not representative of all emitters on a typical array. Additionally, the secondary etch step discussed in the next section typically was effective in smoothing these surfaces.

An important observation made when pulsing was the presence of a contiguous layer of etch products visible on the sample throughout the etch which was only removed with a mild DI water rinse. This layer has been observed consistently during all pulsed etches. The layer appears to be extremely thin and must be less than $\sim$ 200 μm thick as the emitter masks were clearly visible protruding from this layer.

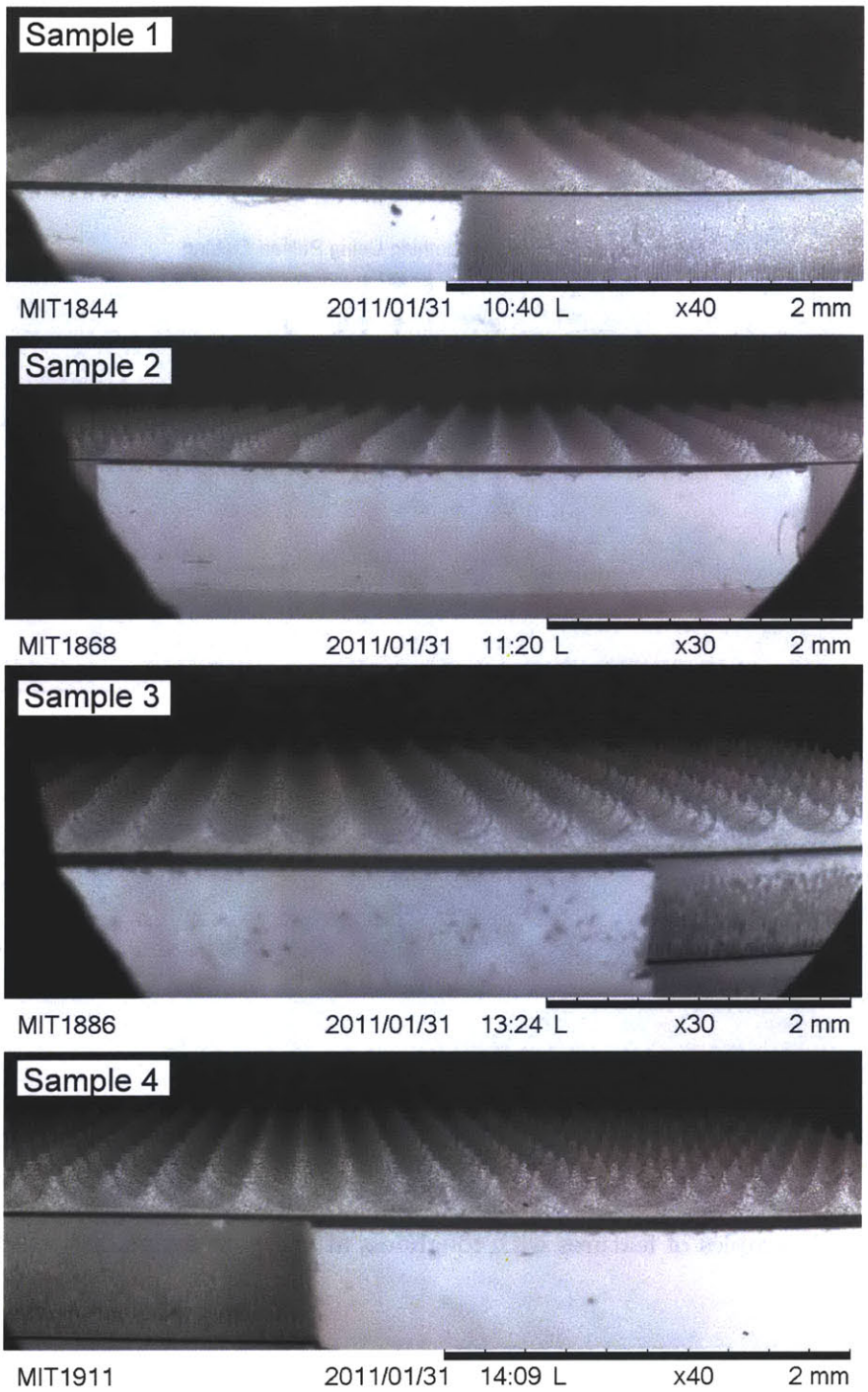

Figure 6-35: An example set of arrays etched using the pulsed technique. The paddle center was realigned after the first sample, all other conditions are constant between samples.

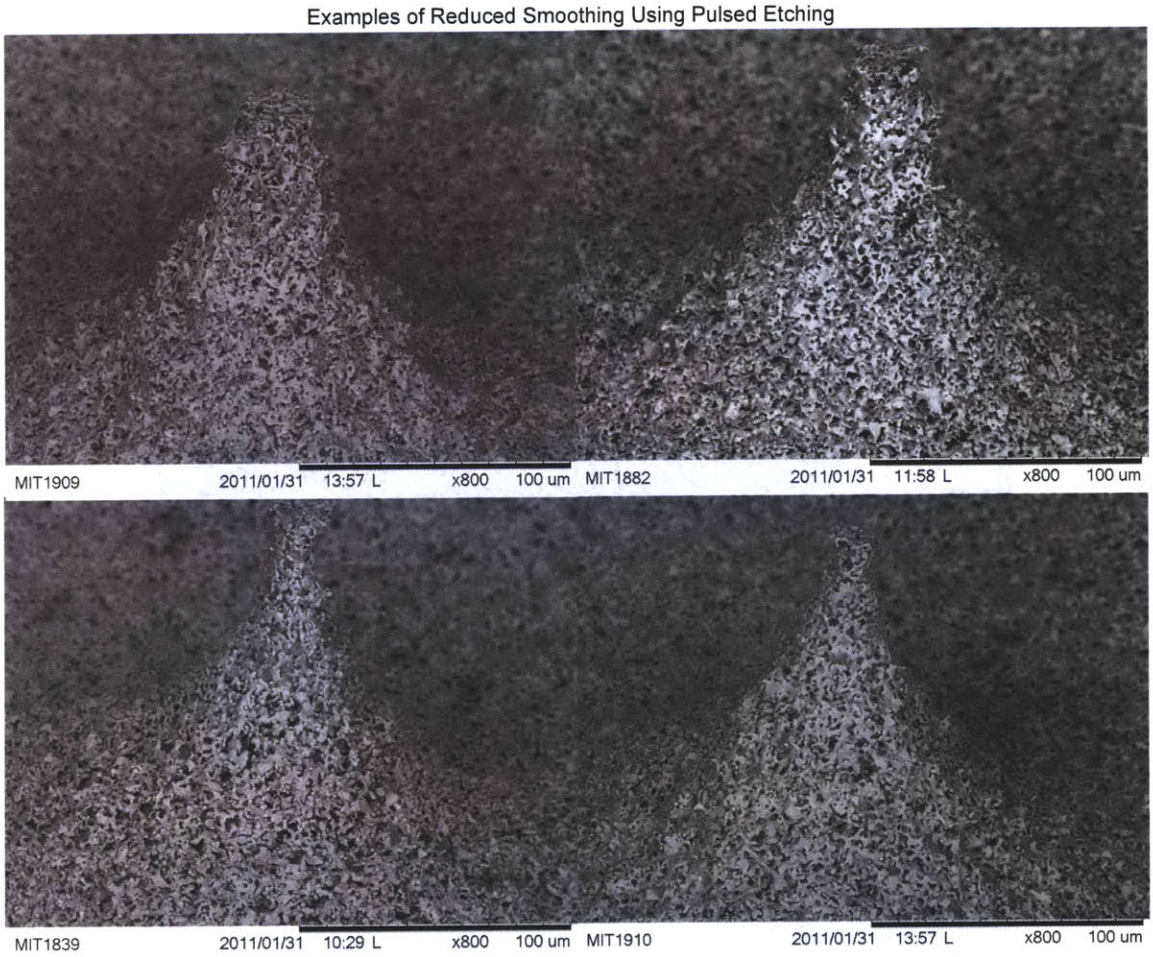

Figure 6-36: Examples of features with roughness at the pore scale after pulsed etching.

6.5 Secondary Etching to Achieve Rounded Emitters

Section 4.5.7 identified a two step etch processes as a possible method for relaxing the constraints on etch uniformity while achieving arrays of useful emitters. However; that discussion also identified that for such short etch times, the target of smooth surface machining on porous metals may not be valid.

This concern was validated during initial attempts at rounding the resultant emitters. For example, the case shown in Figure 6-37 where an initially etched array was cleaned and etched again for a short period of time. Specifically, a secondary etch sequence consisting of 5 seconds at 0.75 V and 5 seconds at 3.1 V, presumably within the transport limiting plateau, was performed in 2N HCl. The initial low voltage etch segment was intended to activate the surface prior to increasing the etch rate. The current during this first portion was significantly lower than during the higher voltage etch, such that less than 10 % of the material removal was calculated to have occurred during this segment. The images demonstrate how, under these conditions, the second etch has attacked the internal pore structure aggressively. The resulting sharp edges and ill defined structure would not be desirable for application as ILIS.

6.5.1 Adding Salts to Reduce Transient Effects

In chapter 4, section 4.1.4, the use of added salts containing the etch products, nickel ions in this case, to offer additional control over the etch conditions was considered. Two experiments have been performed to verify this and its impact on short electrochemical etches on porous materials. First an unmasked sample of nickel, in the standard package, was etched in 2N HCl at 4 V, with increasing concentrations of added nickel chloride ($NiCl_2$). Second, two clean samples were etched for short time periods in electrolyte with and without added salts.

The first experiment, summarized in Figure 6-40, was performed with the type 1 paddle set to oscillate at 65 mm/s roughly 1 mm above the sample. This experiment was performed before the etch station gap control was upgraded. The results are shown in Figure 6-40. A single sample was used throughout while fresh electrolyte was prepared for each scan.

The results confirm that by adding nickel ions to the electrolyte, the limiting current has been reduced. In Fig. 6-38(b) the data are plotted as a function of nickel chloride

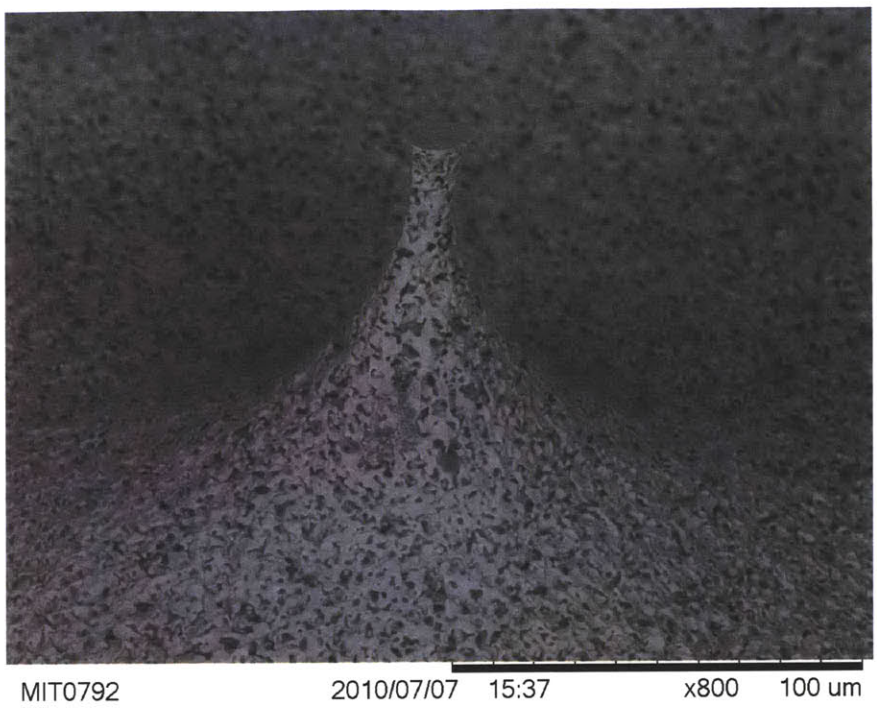

(a) A porous emitter tip prior to secondary etching. Note this emitter was fabricated on material with closed pores at the surface.

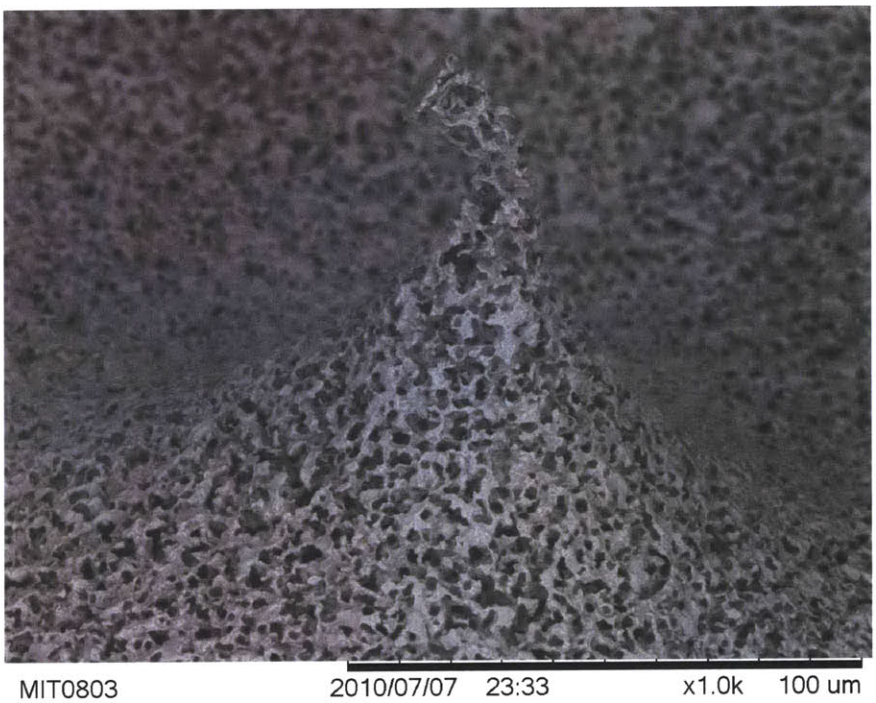

(b) A porous emitter from the same array as above, after etching for 5 seconds at 0.75 Volts and 5 seconds at 3.1 Volts. Less than 10 % of the material removal was calculated to occur during the low voltage portion of the etch.

Figure 6-37: Initial attempts at a second etch step within 2N HCl without any added salts.

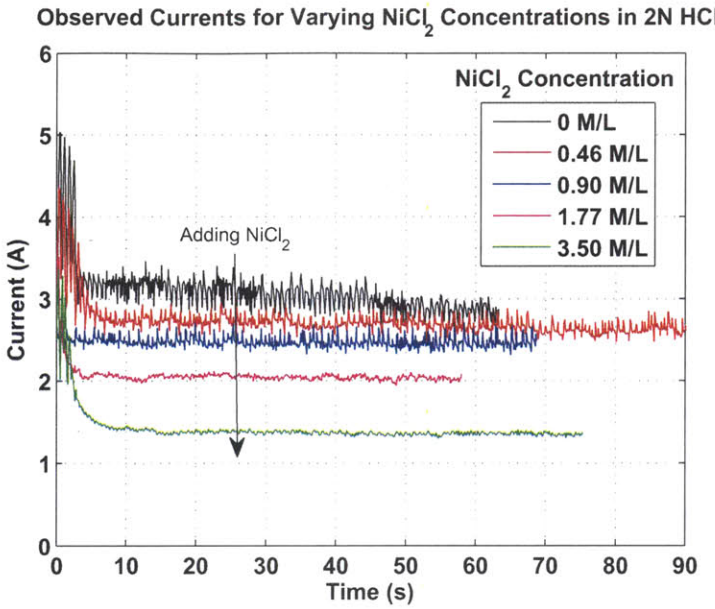

(a) Measured currents at the indicated $NiCl_2$ concentrations for a single porous nickel sample.

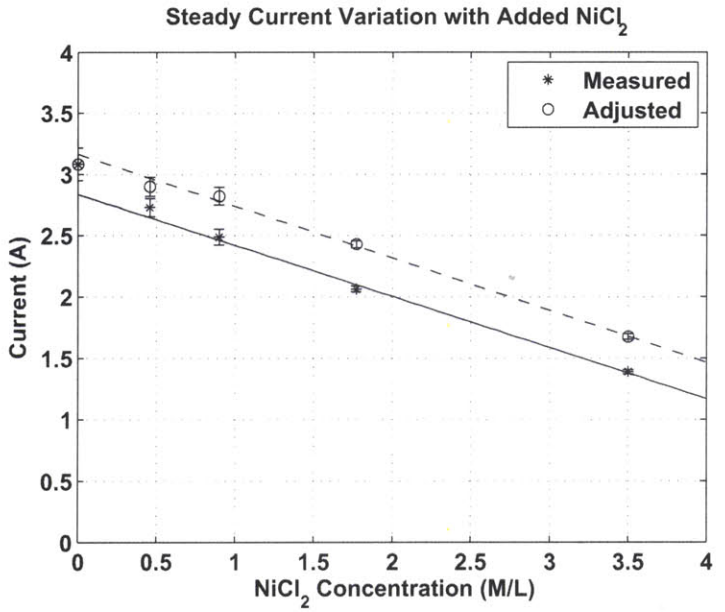

(b) Mean currents, evaluated between 15 and 40 seconds, as a function of added $NiCl_2$. The adjusted data include a correction due to the increasing paddle to sample gap as material was removed from the sample.

Figure 6-38: Dependence of $NiCl_2$ concentration on measurements of the limiting current using unmasked porous samples mounted in the silicon frame.

concentration. Here the average value between 15 and 40 seconds has been selected to minimize the deviations due to the sample area changing as time progresses. The second set of data has been adjusted to include some consideration of the cell geometry changing throughout the experiment. As these data were collected for a single sample, the material removed would effectively lower lower the sample away from the paddle. The amount of material removed has been calculated using Faraday's law, equation 4.3 by integrating the current and assuming a 1 cm^2 exposed area and 90 % etch efficiency (see the discussion below). After each scan in Fig. 6-38(a) an estimate for the net etch depth has been made and correlated to give a relative change in diffusion layer thickness, using equation 4.11. Finally the measured currents are scaled by the inverse of this relative change to provide an estimate for the effective current changes due to concentration alone. In both cases a weighted linear fit has been made and used to estimate the effective saturation coefficient, where the limiting current would go to zero for this cell. The fits predict 6.8 and 7.2 M/L for the measured and adjusted curves respectively. These values are of the correct order but roughly 1.5 times larger than the 4.8 M/L cited in the references[130]. Including the height adjustment increased the linear-correlation coefficient from 0.992 to 0.999.

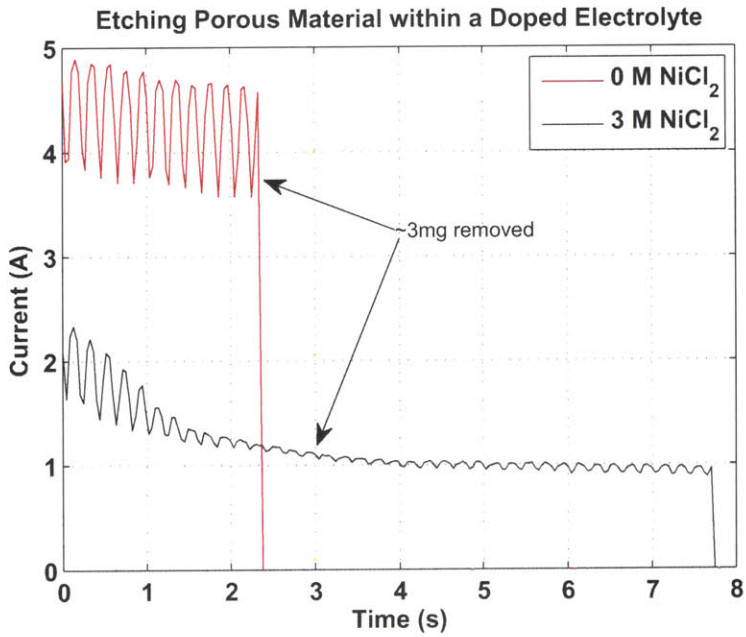

Figure 6-39: Two porous samples were etched until $\sim 3\ mg$ of material was removed within two different electrolytes. With added $NiCl_2$, a transition to a smooth, steady current occurs within a relatively short portion of the total etch time.

The second experiment was performed using the type 3 paddle with the final etch station configuration. The paddle design differed significantly from the design above. Only qualitative agreement with the data in Figure 6-40 was expected. In this experiment two unmasked samples have been etched until approximately 3 mg of of material has been removed. The etches were made with 3.8 V applied while the paddle was set to travel at 75 mm/s over $\pm$ 7.5 mm with an electrode gap of 0.5 mm. Without added $NiCl_2$ the etch lasted 3.3 seconds and was highly dependent on paddle position (causing high amplitude oscillations), with current amplitudes between approximately 5 and 3.5 A. With 3 M/L of $NiCl_2$ added to the solution, the etch took 7.7 seconds with moderate oscillations decaying, along with the average current, over the first few seconds before becoming relatively stable around 1 A. For a planar surface of the porous nickel used here, this corresponds to roughly 0.6 $\mu m/s$ of material removal.

Figure 6-40 presents SEM images of the initial porous nickel surface, as supplied from the manufacturer, and the surfaces after the two etches discussed above. Without $NiCl_2$, Fig. 6-40(b), the short etch has resulted in significant damage to the pore structure, consistent with etching before the reaction has become limited by transport. With added $NiCl_2$, Fig. 6-40(c), the surface has been smoothed with reduced signs of etching within the pore structure and regions of high surface area, as expected during transport limited etching.

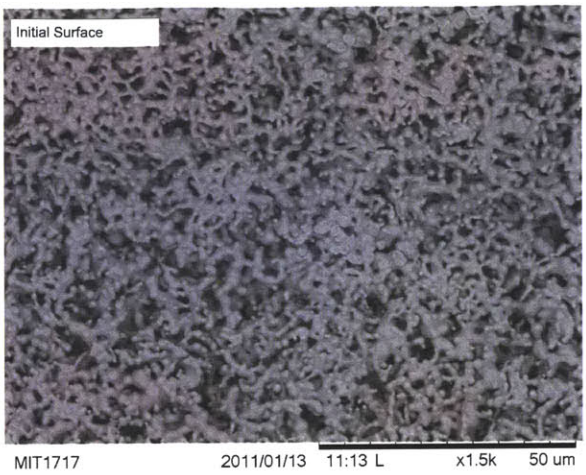

(a) Initial porous surface after cleaning but no other processing.

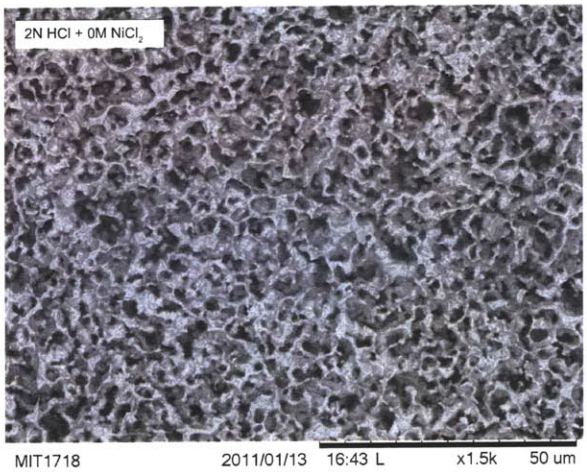

(b) Porous surface after removing $\sim 3\ mg$ of material in 2N HCl without added salts.

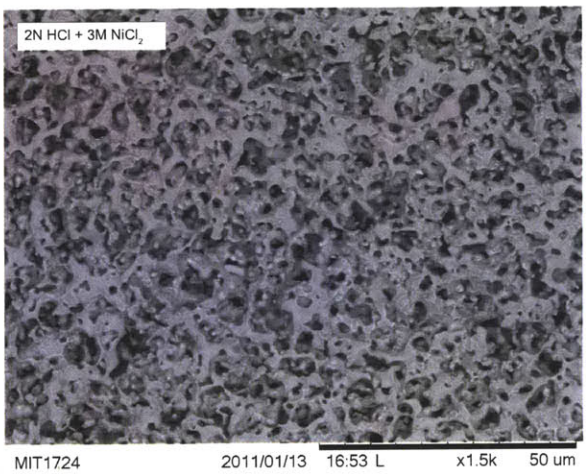

(c) Porous surface after removing $\sim 3\ mg$ of material in 2N HCl doped with 3M $NiCl_2$.

Figure 6-40: Demonstration of the ability for doped electrolytes to achieve surface machining on porous nickel during short etches.

6.5.2 Smoothing Emitters with Doped Electrolytes

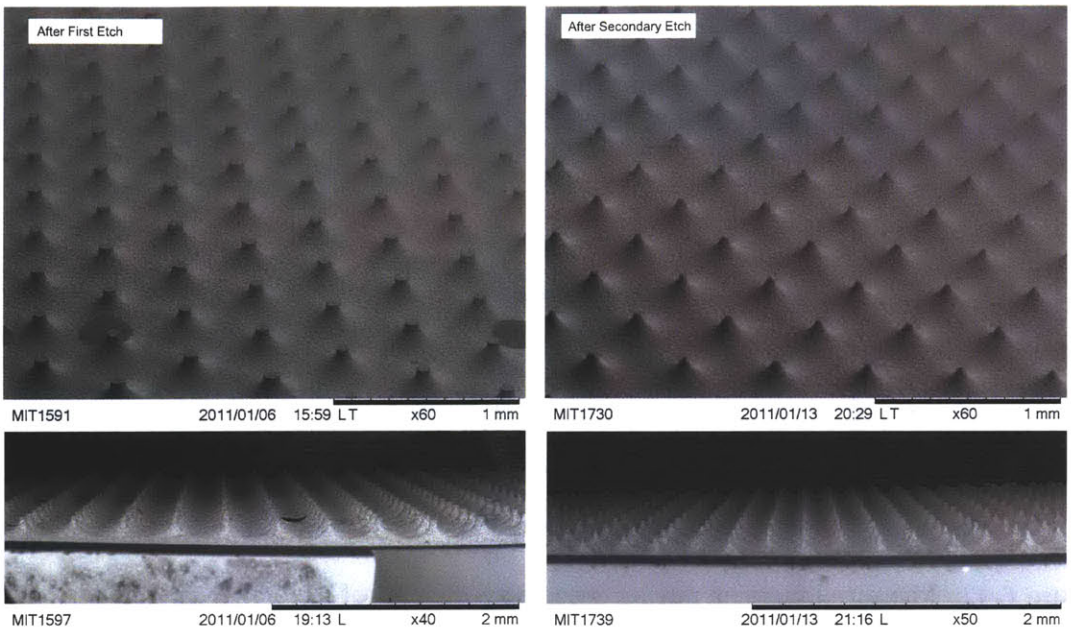

(a) Topographical and perpendicular SEM images of a sample after the first etch step.

(b) Topographical and perpendicular SEM images of a sample after the second etch step.

Figure 6-41: Secondary etching to round plateaus, forming more desirable structures for application as ILIS.

These results have been applied to performing the desired secondary etching of emitter plateaus while maintaining smooth etching on porous emitter arrays. Using the array shown in Fig. 6-34(b), etched using the pulsed etching processes described above, a 15 second etch within 2N HCl doped with 3M $NiCl_2$ yielded the transition shown in Figure 6-41. Fig. 6-41(a) is a topographical SEM image before the secondary etch, while Fig. 6-41(b) shows the same array after secondary etching. The etch was controlled based on mass, stopping after 5 mg of calculated mass removed.

The measured current during the etch is shown in Figure 6-42. The figure demonstrates that, despite adding $NiCl_2$, high amplitude oscillations remain during the initial portion of the etch before decaying along with the average current. The 15.3 second total etching time was typical for this process. However, as discussed in section 6.7.2, the total etch time disagrees significantly with that predicted numerically.

As desired, the additives supported smooth etching on the porous materials yielding emitters as in Figure 6-43. Compared with Figure 6-37, where secondary etching without

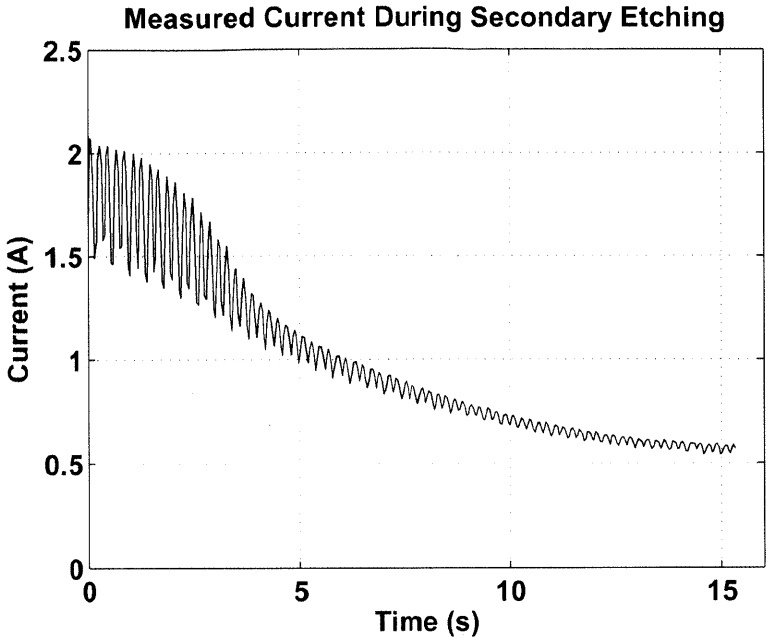

Figure 6-42: Measured current during secondary etching of an emitter array to remove 5 mg of material. The total etch time was approximately 15.3 s.

doping resulted in etching within the pores, the discrepancies are clear. This processes has been repeated on four additional arrays with good results. In all cases the type 3 paddle was oscillated at 75 mm/s over $\pm$ 7.5 mm with an electrode gap of 0.5 mm.

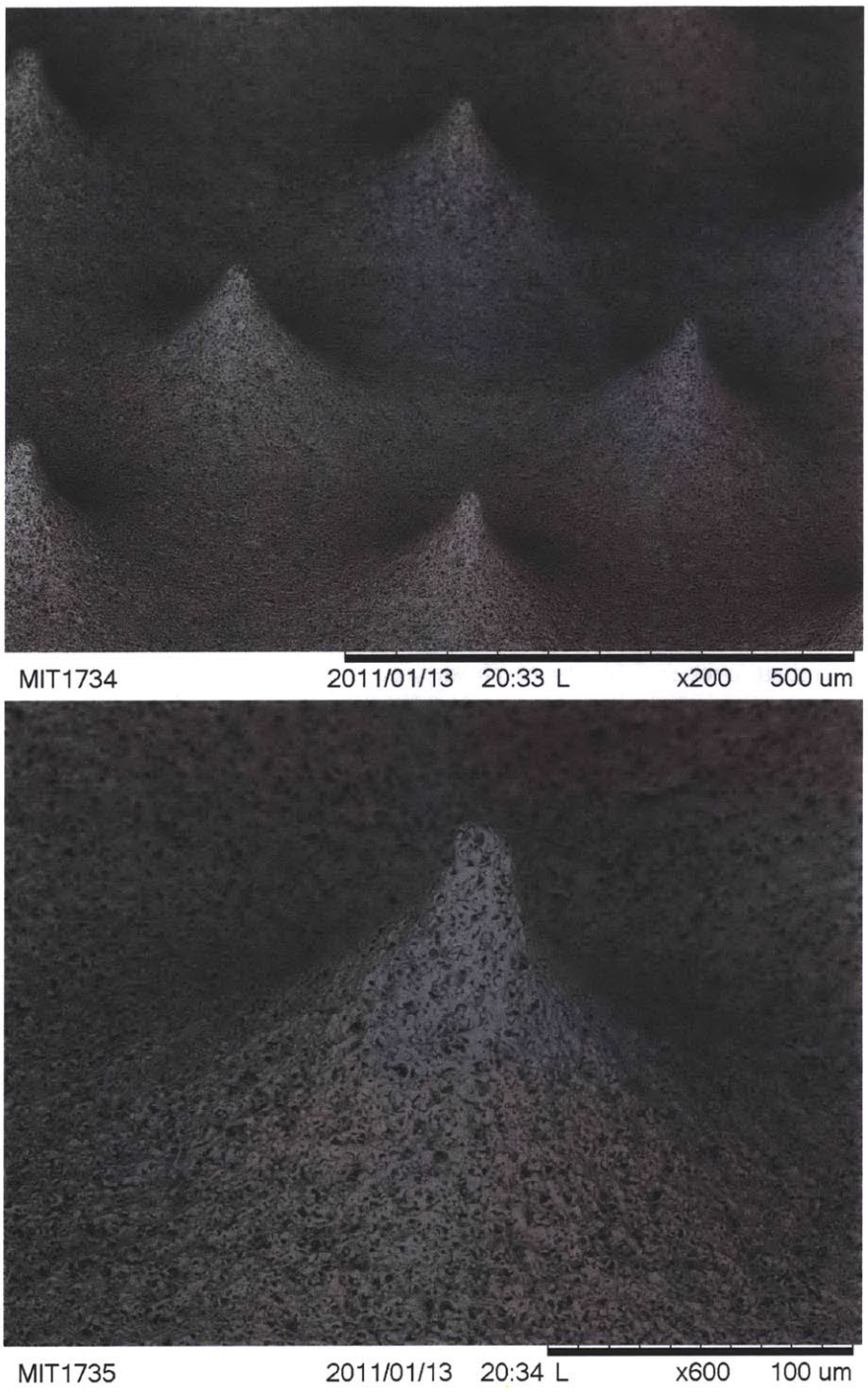

Figure 6-43: SEM images of emitters formed after secondary etching. The structures are generally smooth with no signs of etching within the pores, despite a short etch time.

6.6 Final Process Summary

The complete process, including two etch steps, has been tested on 5 samples over three separate sample batches. Further etching has been forgone in favor of testing the performance, in terms of operation as ILIS, of the fabricated arrays. The final process used remains relatively straight forward and several changes are suggested in the discussion below. The two etch steps have been adjusted slightly over the example discussed in section 6.5.1 in that the first etch step has been increased from 97 to 104 mg while the secondary etch was reduced from 5 to 3 mg.

Final process:

1. Solvent clean
2. Pattern with FX515 resist, 200 μm mask diameters
3. Pre-Etch : 0.5 V DC for 15 seconds with the type 3 paddle set to a gap of 0.5 mm and oscillating over $\pm$ 7.5 mm at 75 mm/s.
4. Etch step 1 : 3.5 V at 2 Hz, 50 % duty cycle in 2N HCl with the type 3 paddle set to a gap of 0.5 mm and oscillating over $\pm$ 7.5 mm at 75 mm/s. Etch to 104 mg of material removed.
5. Solvent clean
6. Etch step 2 : 3.8 V DC within a 2N HCl and 3M $NiCl_2$ solution with the type 3 paddle set to a gap height of 0.5 mm and oscillating over $\pm$ 7.5 mm at 75 mm/s. Etch to 3 mg of material removed.
7. Solvent clean

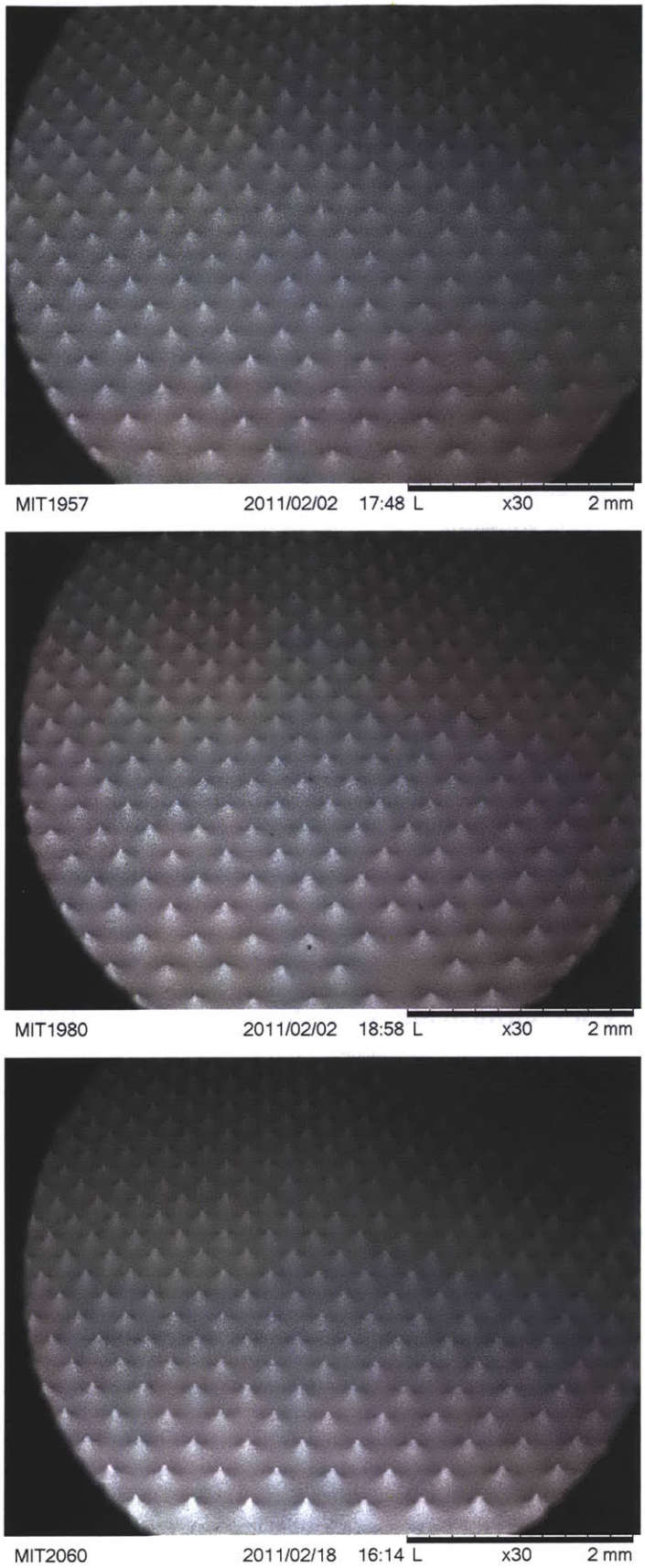

Figure 6-44: Examples of arrays etched using the complete process developed here.

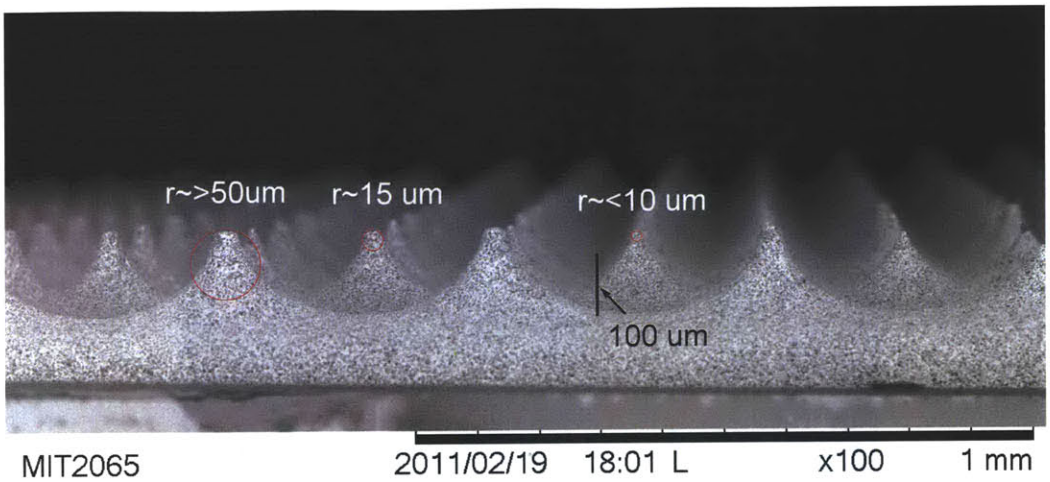

Figure 6-45: Using the full process described, emitters consistently *sim* 150 μm tall are achieved but with variable tip radii.

6.7 Discussion and Recommendations

The transition from constant voltage (or very low frequency) etches to pulsed etching has significantly enhanced uniformity at the feature and pattern scales, with some minor degradation at the pore scale. Perhaps more importantly, pulsed etching appears to be a more robust technique with far greater consistency between samples, as demonstrated in Fig. 6-35. However; much room for improvement remains.

6.7.1 Suitability for Operation as a Porous ILIS Thruster

This fabrication scheme has produced emitters, typically in excess of 150 μm tall, as desired. However, despite the progress made in developing this process some degree of non uniformity remains. Figure 6-45 demonstrates the typical range of emitter tip diameters produced using this technique. The emitters are typically $\sim$ 150-170 μm tall (relative to the lowest points on the wafer) with tips ranging from sharp points, with diameters less than $\sim$ 10 μm, to smoothed plateaus with much larger apex diameters. Ultimately, the performance as ILIS emitters will be the driving metric for the success of this process. As shown in the next chapter, when well aligned and electrically isolated, strong beam currents can be sustained from these devices despite the non-uniformities.

One of the challenges required of any fabrication scheme used to create porous arrays for ionic liquid ion sources is the ability to package the device. This etch technique has been

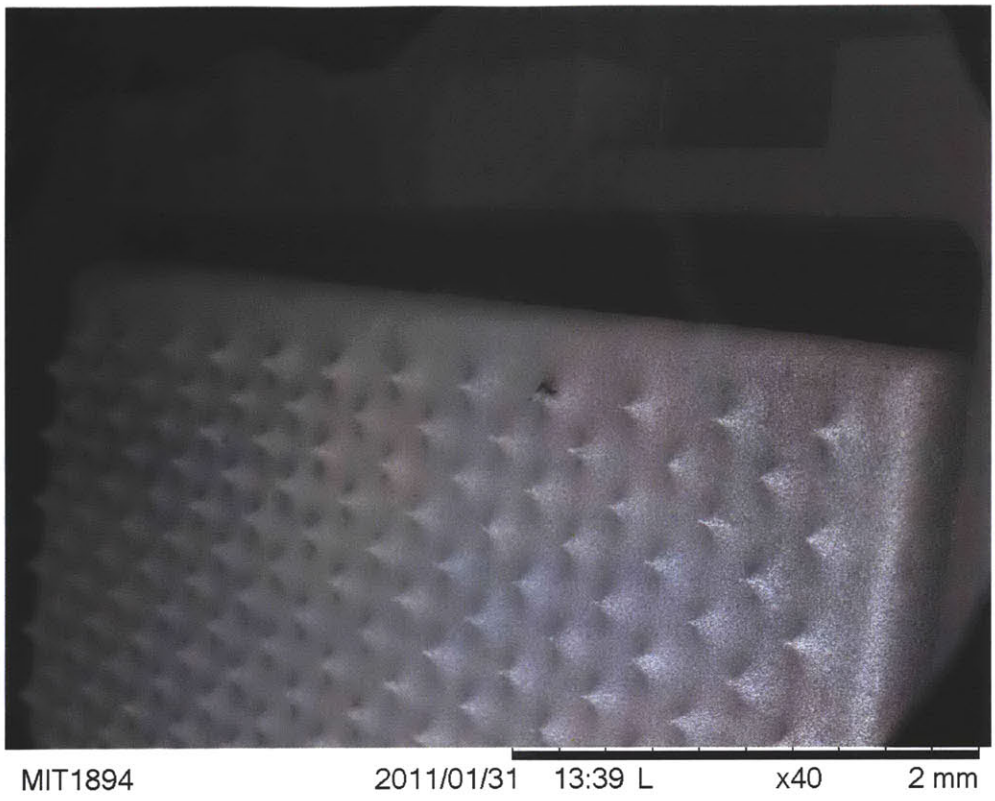

Figure 6-46: SEM image showing an etched porous nickel sample with emitters formed within a few 100 μm of the substrate edge. The rounded substrate edge was desirable as sharp edges could have resulted in spurious emission to the nearby silicon frame.

demonstrated to be capable of selectively etching a patterned porous metal sample while housed in a silicon frame. This accommodates the array and grid alignment to be made with respect to the silicon package in a relatively simple manner. A key to this has been the ability to etch emitters, to relatively high uniformity, right up to the edge of the samples. As shown in Figure 6-46, the technique developed here results in useful structures within a few hundred μm of the nickel sample edge. This may be a significant benefit over other techniques which could require a porous array and package to fabricated independently and then joined later in an aligned manner. Operationally, the tendency for this method to inherently etch the edge of the material to a significant degree is beneficial as it removes sharp edges that would be present if, for example, a sample was cut to size using a die saw after forming the emitters. Sharp edges could lead to high electric fields and spurious emission from the sides of the array.

6.7.2 Correlations Between Numerical Simulations and Observed Results

The numerical simulations presented in section 4.5 have been useful in gaining insight into the trends and expected behavior during etching. However; as a predictive tool, they have only provided an approximation to the etch time and profiles to be expected for the majority of results presented here.

Simulated First Etch Step

In general, the structures had etch factors typically larger than those predicted using the simple, static, boundary model discussed in section 4.5.6. Much better agreement has been observed using the more dynamic moving boundary model.

Necking was, to some degree, predicted by the simulations but only as the etch nears completion and for very thin $\sim$ 10 μm boundary layer thicknesses. Using the 65 μm thick, MP525 mask, significant necking occurred even for etches stopped well before this, as was shown in Figs. 6-27 and 6-28. However; in those images the surface remains smooth at the pore scale, suggesting that although relatively more etching has clearly occurred to form the neck, the boundary model used in the simulations may not accurately capture this behavior. This is not unexpected given the somewhat arbitrary nature of the boundary definition.

During pulsed etching, the arrays are typically much more uniform, to the extent where some qualitative comparisons can be made between the observed and predicted profiles. Using the technique shown in Figure 6-47, profiles for two pulsed etches have been plotted in Figure 6-48. In each case 6 profiles were selected from images taken perpendicular to the emitters. Here an estimate for the axis of symmetry has been made based on the plateau diameter. Radial measurements have then been made at fixed vertical increments.

In Figure 6-48, a boundary layer thickness of 35 μm has been selected and the resultant profiles after every 10 time steps (equivalent to $\sim$ every 10 μm in the far field) are plotted. Here, a 35 μm thickness was found to yield profiles similar to the measured profiles but was not measured directly. However; a value on this order would not be unexpected given the estimates in section 4.1.1,$\sim$ 35-110 μm combined with the predicted reduction in effective boundary layer thickness during pulsing.

In Fig. 6-48(a), the etch was stopped after removing 97 mg material. This was achieved after etching for roughly 260 seconds (the plot shown in Fig. 6-32(a) shows the actual data

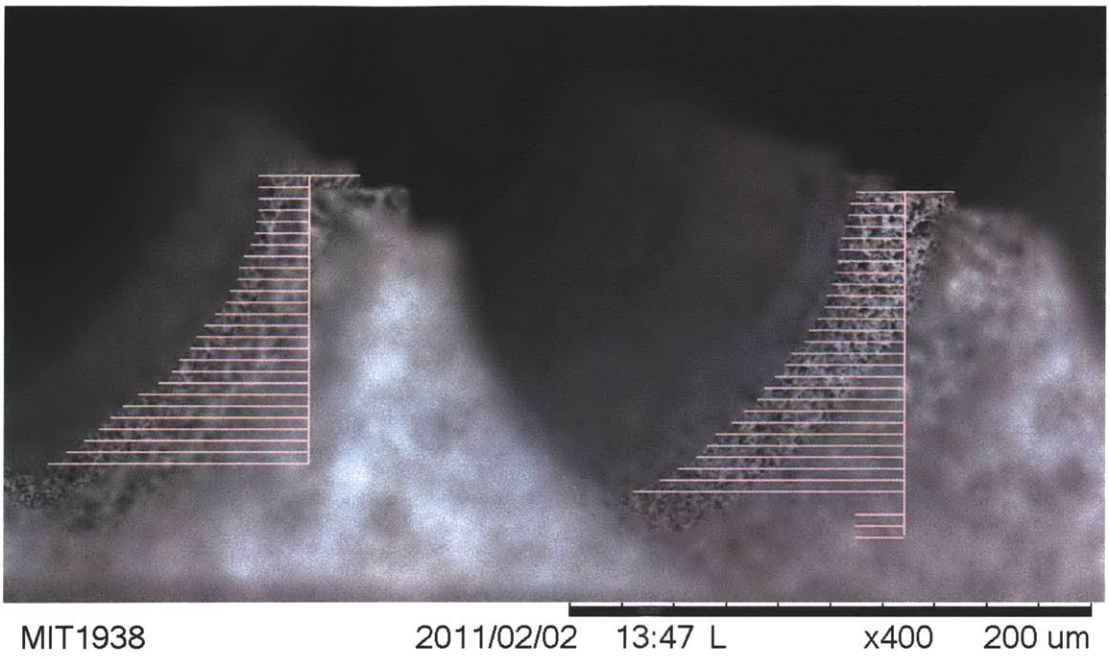

Figure 6-47: Fabricated arrays were traced using this method for comparison with the profiles simulated using the code described in section 4.5.

for this sample). At a 50 % duty cycle this corresponds to 130 seconds of actual etching. The height of the emitters after etching was measured, using a microscope to be 152 $\pm$ 5 μm, in reasonable agreement with the profiles extended to the simulation boundary. For a 35 μm diffusion layer thickness the predicted etch time to this height was $\sim$ 140 seconds for a saturation concentration of $C_s = 4.8\ M/L$, a diffusivity of $D = 6.6$ x $10^{-6}\ cm^2/s$ and a bulk density of 55 %.

In Fig. 6-48(b), the etch was stopped after removing 104 mg material under identical hydraulic and pulse timing to the sample above. This was achieved after etching for roughly 320 seconds while pulsing. At a 50 % duty cycle this corresponds to 160 seconds of actual etching. The height of the emitters after etching was not measured however, in so far as the profiles agree with those simulated, the far field height was between roughly 160 and 175 μm. For a 35 μm diffusion layer thickness the predicted etch time to this height was between $\sim$ 145 to 160 seconds using the same physical properties as in the previous example.

These qualitative comparisons show reasonable agreement with the model. However; both of these examples, and all others available, were etched to very similar set points. A truly validated model would be one that not only fits the data towards the end of the etch

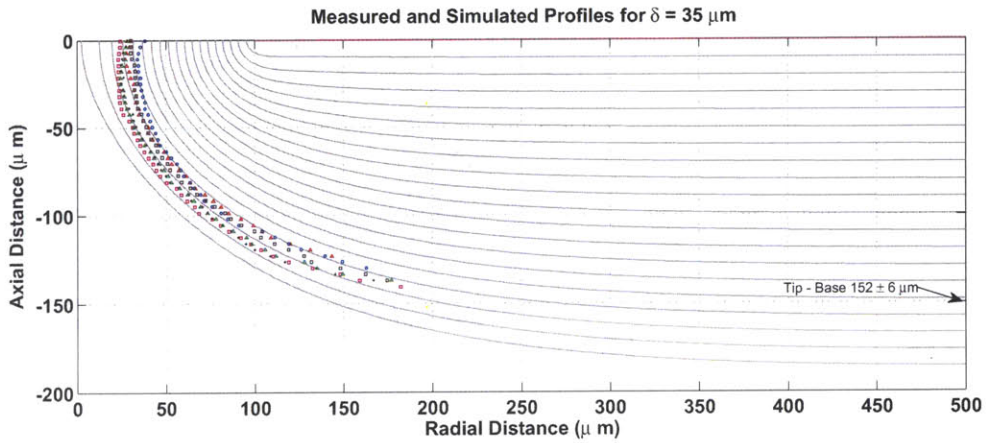

(a) Simulated and measured profiles for a 35 μm boundary layer thickness, etched to a target of 97 mg.

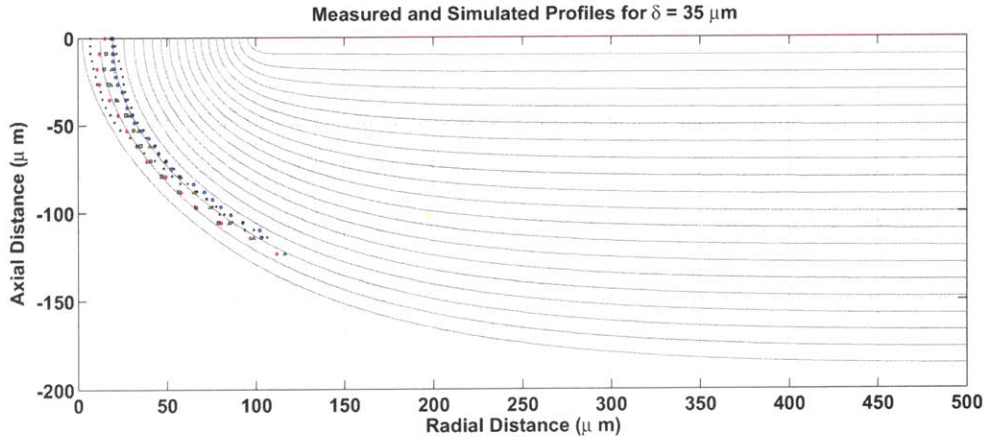

(b) Simulated and measured profiles for a 35 μm boundary layer thickness, etched to a target of 104 mg.

Figure 6-48: Comparisons between numerically simulated and measured etch profiles. The selection of $\delta = 35$ μm was based on approximate agreement with the model. The simulations were not run as a predictive tool prior to etching.

but is also consistent with samples etched to a lesser degree. Hence a number of samples would need to be sacrificed, in terms of use for operation as ILIS, to generate a set of data spanning the entire etch. This has not been performed. Further refinement of the model could include an attempt to include the pulsed nature of the dissolution by varying the diffusion layer thickness in time.

Simulated Secondary Etching

In Figure 6-49, measured and simulated profiles are compared before and after secondary etching to round the emitters. In Fig. 6-49(a), the experimental profiles shown in Fig. 6-48(a) are plotted along with a selected simulated profile, the solid line in the figure. The simulated profile was then input to the code to simulate secondary etching. Experimentally, the array was etched to remove 5 mg, taking 15.3 s of total etching. After secondary etching, the measured emitter heights were 143 ± 5 μm, reduced from 152 ± 6 μm after the first etch step. In Fig. 6-49(b) a simulated profile has been plotted after terminating the simulation when the emitter height was reduced by 9 μm, in keeping with the measured behavior.

Referring to Fig. 6-40, the after etch rate was expected to be reduced by roughly 60 % with 3 M/L of added $NiCl_2$ after forming a diffusion layer. The simulated profile shown in Fig. 6-49(b) reached the measured change in emitter height after only 1 s of simulated etching, or 1.7 s after correcting for dopants. Thus the simulation dramatically under predicts the actual etch time (15.3 s). Considering the simulation assumes a fully formed diffusion layer, actual etch times are typically expected to be much shorter than simulated. However; the strong gradients at the emitter edges could lead to high current densities limited by the applied potential (the primary distribution) during the initial part of the etch. This situation is consistent with the high amplitude oscillations shown in Fig. 6-42 for the first few seconds of etching. As with the first etch step, further, more accurate, characterization of the etch transients would be required before the simulations could be used as a predictive tool for secondary etching.

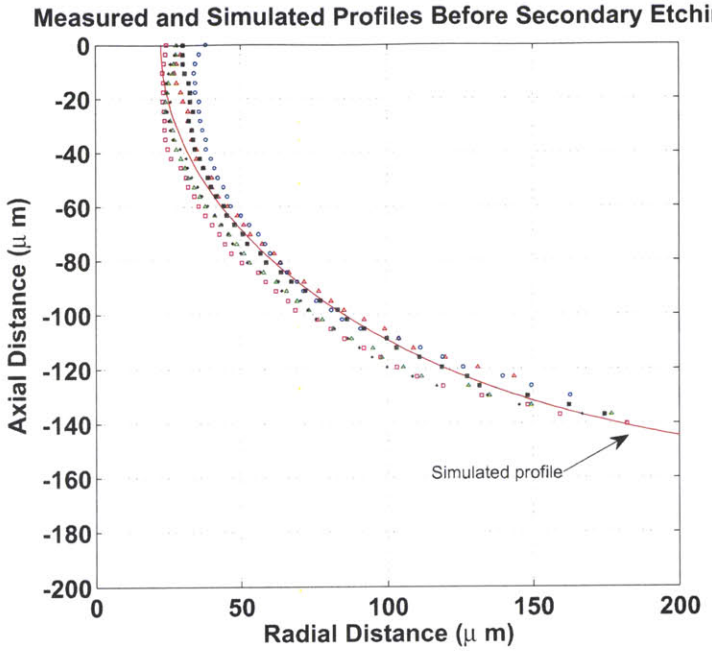

(a) Measured profiles, after etching 103 mg, plotted with a calculated profile after $\sim$ 150 s of simulated etching.

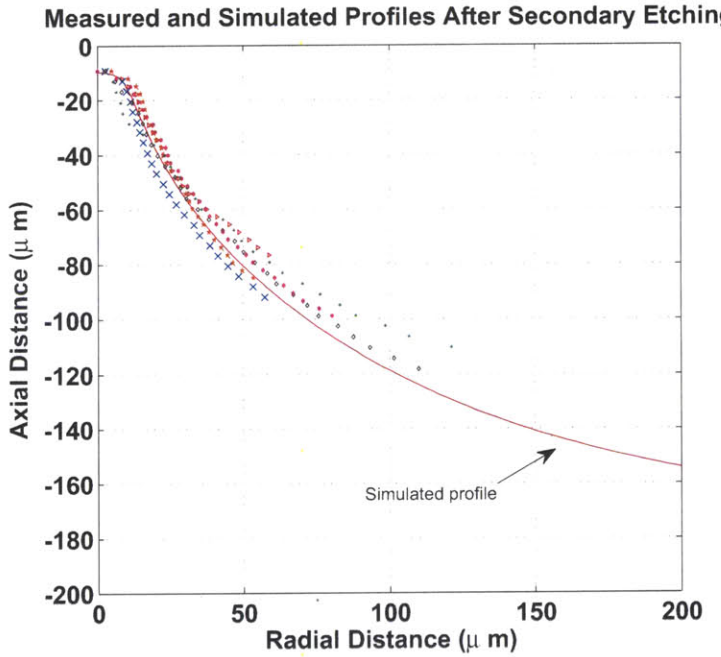

(b) Measured profiles after removing 5 mg through secondary etching plotted with a selected calculated profile set to terminate .

Figure 6-49: Comparisons between numerically simulated and measured etch profiles before and after secondary etching. The second etch was targeted to 5 mg of material removed. The actual total etch time was 15.3 s while the predicted etch time, adjusted for the added $NiCl_2$, was less than 2 s.

6.7.3 Recommendations for Increasing Etch Uniformity and Control

Several sources of error remain in the current setup. Particularly, the paddle position, along the axis of oscillation is not known to a high degree. Another calibration step and sensing circuit could be added to the structure such that, before each scan, the paddle home is redefined on a scale much closer to the sample, just as has been done with the vertical axis. The impact of the paddle shape and composition has not been explored to any great degree here. The versions used to in this research have been made from simple sheets of stainless steel and, under some occasions, were prone to bending or, if not cleaned properly between runs, corroding. An investigation of these effects could include varying the paddle geometries in search of an optimum before fabricating a more permanent structure.

The final form of the etch station control software allows for much more complex and carefully designed etch processes. Particularly due to the ability to stack and queue instructions during any particular run. This could, for example, be used to adjust the paddle motion throughout the process to minimize the initial transients. One suggestion would be to begin with the paddle oscillating over the sample only (traveling over $\pm$ 5 mm) at a relatively slow speed during the beginning of the scan where its position is significant. The velocity could then be increased along with the travel, to approach the conditions used here after some initial period. Similar steps could be made with the electrical signals, for example beginning with a high constant voltage before a transition to pulsing. This may reduce transients effects by quickly forming an initial diffusion layer prior to pulsing.

Many other parameters warrant exploration in an effort to enhance uniformity. For example, no adjustment to the pulse duty cycle or period has been made in this research. A simple experiment aimed at confirming the limits of pulsed etching, when dissolution occurs within the pores, at low duty cycles and high frequencies would be interesting. Furthermore, recall that in section 6.4.4 the pulsed etching currents were in reasonable agreement with the 1-d pulse model developed in section 4.4 but only when normalized by an equivalent constant voltage limiting current of 1.0 A. This was in contrast to the roughly 1.4 A limiting current observed when etching with the same paddle settings but using a constant voltage. Meanwhile, a thick and stable residue was observed on the surface after these etches. One explanation for these observations could be that under pulsed conditions, a large stable overall diffusion layer forms while pulsing ensures a smaller effective diffusion layer near the

surface (ultimately dictating the etch). Further experimentation could aid in developing an understanding of this phenomenon.

6.7.4 Selecting Mass or Time as an Etch Stop

Selecting mass as an etch stop for the control software has typically yielded more consistent results compared with timed etches. However; this has been somewhat unexpected given two observations. First, the etch efficiency, defined as the ratio of actually removed to calculated material mass has varied within several percent for similar target masses. Figure 6-50 provides some examples of the etch efficiency calculated by measuring the sample masses before and after etching (and cleaning) during an assortment of batches. Although the efficiencies are typically high, the scattered nature could translate to a similar degree of uncertainty to be expected when targeting mass as an etch stop.

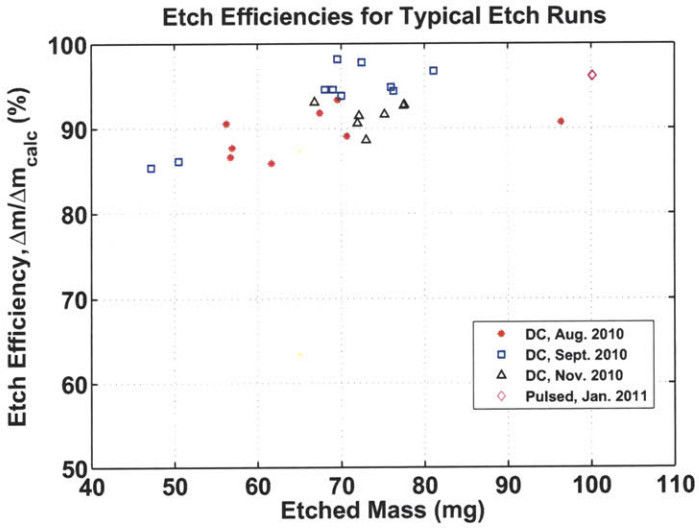

Figure 6-50: On some occasions the mass targeted, and verified by integrating the output current, has been compared with the actual mass difference measured with a scale.

Furthermore, the amount of material removed is highly dependent on the degree of etching at the corners of the material. As shown in Figure 6-46, the substrate edges are round and have been etched to, at least, a level consistent with the average planar etch depth. Measurements of samples removed from their silicon frames after etching have shown that as much as 40 % of the total etch mass may be due etching at the edges. Some attempts at simulating the etch here been made, an example of which is shown in Figure 6-51. This simulation used the moving boundary type definition of the boundary layer but assumes a

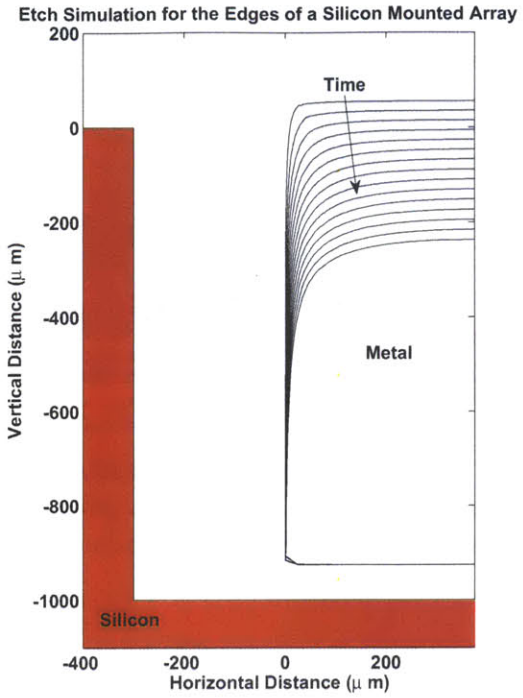

Figure 6-51: Simulations of the boundary evolution at the edge of a sample mounted in a silicon package as in described in chapter 5.

planar (Cartesian) geometry with infinite extent in and out of the page. The simulation appears reasonable at first glance, however it significantly under estimates etching at at the lower corner of the metal, deep within the frame. Figure 6-52 demonstrates this for arrays where the silicon frame has been snapped off at one edge to reveal the sample edge before and after etching (these images are representative of the process but do not show the same sample before/after etching). In this model that region has been heavily shielded, while in reality a transient model would be required which takes into account the time required for a stagnant boundary layer formed in the corner to begin interacting with the frame. Finally, recall that one of the benefits of this overall process has been the ability to relax the spatial accuracy requirement for the metal within the frame, since the mask is applied after bonding and aligned to the frame. Hence, the gap between the metal and silicon frame shown in Fig. 6-51 will typically vary around the sample perimeter.

Despite these concerns, etches targeted for mass have been used in fabricating all of the emitter arrays tested in the next chapter.

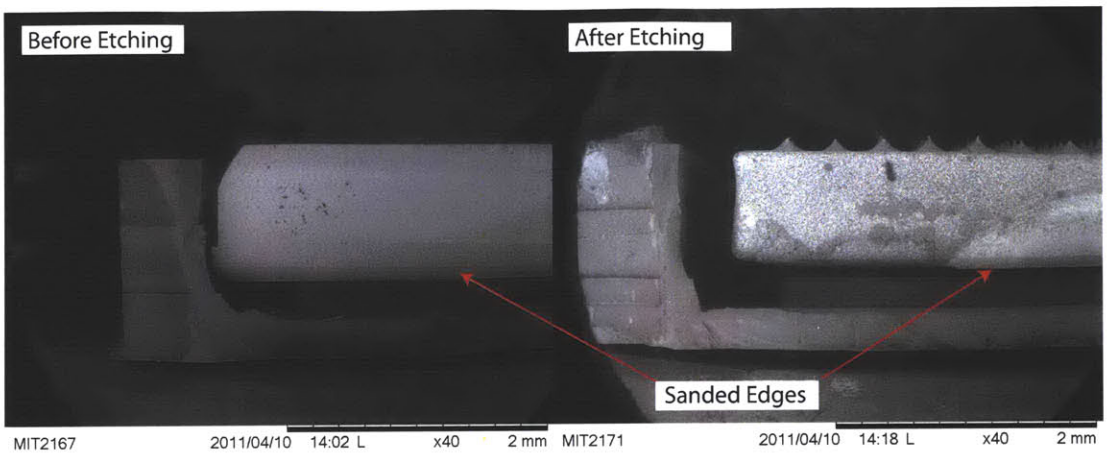

Figure 6-52: SEM images of typical samples before and after etching. The edges have not evolved in the manner predicted by Fig. 6-51. Significant residue, possibly due to the epoxy, can be seen on the etched sample. The samples were de-burred by sanding before etching, leaving chamfered edges.

6.7.5 Impact of Photoresist Quality and Dimensions

Although using the Riston FX515 thin resist resulted in a dramatic increase in the yield at the photolithography step of this process, some adjustments are recommended. For example, the mask in Figure 6-53 below was patterned with a 200 μm diameter photo-mask but somewhat larger resist discs have resulted. This may be due to excessive heat or pressure during lamination, or just as likely, a problem at the exposure stage. If, for example, the photo-mask and sample are not in good contact, diffraction could occur at the edges off the pattern[96]. If the metal sample was not perfectly flat during epoxy bonding to the silicon frame, this issue could arise.

As this process was developed, three different thicknesses of photo resist made by two manufacturers were used. However; the most reliable etching technique, pulsed etching, was not developed until the third, thinnest, resist was acquired. Since the resists have a finite lifetime, comparison between all three resists with identical etching conditions was not possible. Some reasonably uniform arrays were created using the 65 μm thick, MP525 with 150 μm masks, although on only a few occasions. Using images of these arrays, the technique shown in Fig. 6-51 could be used to trace and compare these emitters with the FX515 results. New samples etched with 150 μm diameter, 65 μm thick masks using the final process would make quantitative comparisons of this sort more applicable.

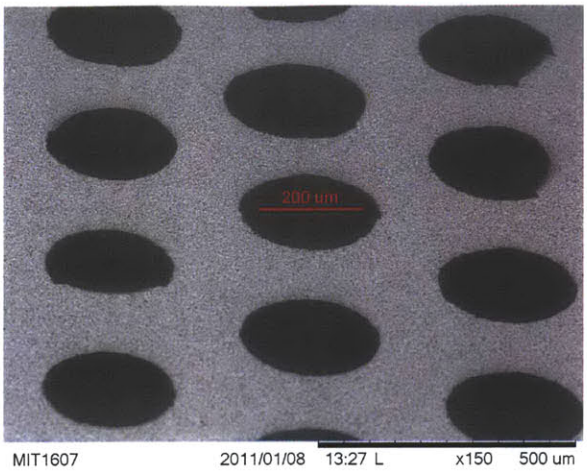

Figure 6-53: Over sized masks created using a 200 μm photo mask with the FX515 resist. This resist has been generally more reliable than the MP513 and MP525 but further refinement to the process is recommended.

6.7.6 Smooth Etching on other Porous Metals

The results presented here have been largely focused on solid and one grade of porous nickel. However; the general technique should be applicable to a number of metals. In section 6.3 a limiting current plateau was observed during a potentiodynamic sweep for titanium in H_2SO_4 methanol. Using available estimates of the diffusivity and saturation conentration[125] along with the measured data, the transport layer thickness, δ, would be roughly 40 μm in this case assuming a fully activated surface. This estimate, along with the observed smoothing in Fig. 6-12, suggests that porous titanium could also be etched in a manner similar to that shown here for porous nickel. Wide limiting current plateaus have been observed for many other metals, for example iron in chloride electrolytes[121], leaving many opportunities for applying this research to other porous metals.

The porous ILIS emitters fabricated on porous tungsten, both during the early phases of this project and by Legge[70] can also be considered in the context of transport limited etching. Those etches were typically done at low voltages and low to moderate currents. However; at the final stage of etching, only the emitter tips were etched at relatively high current densities. Figure 6-54 demonstrates two tips fabricated in this fashion. Given the results of this work, it appears that this porous tungsten process may have occasionally etched below or within the transport limited regime as evidenced by the figure. No further experimental confirmation of mass transport control when etching porous tungsten has been

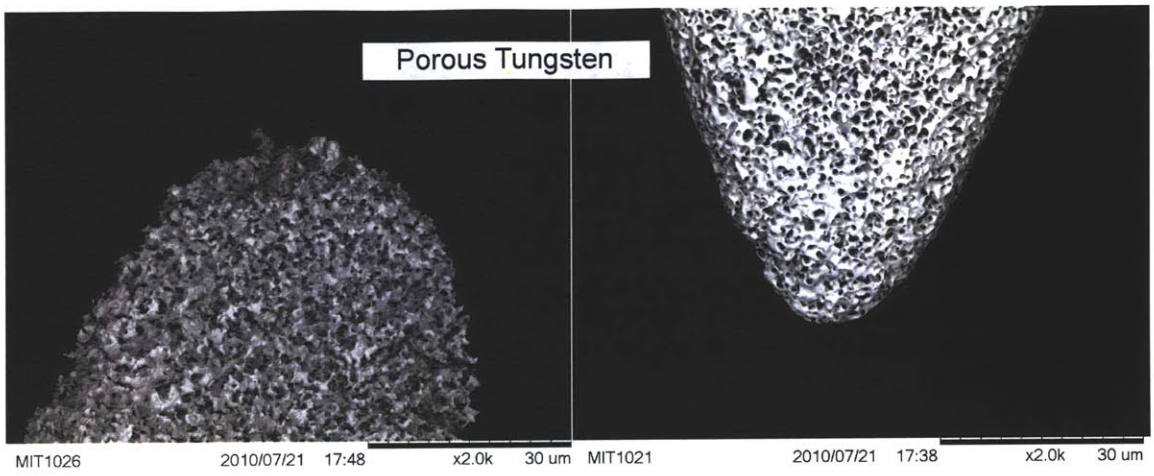

Figure 6-54: SEM images of two flat type porous tungsten emitters fabricated during the early stages of this research using the method of Legge[70]. Qualitatively, the smooth surface on the right appears to have been etched under diffusion controlled conditions.

done during this research due to the mask compatibility challenges in the sodium hydroxide electrolyte and the high cost of purchasing this material.

Finally, it is important to note the similarities between structures formed on solid nickel, in section 6.4.1 and those formed using the final process on porous nickel. This observation supports the anticipation, stipulated in Chapter 3, that transport limited electrochemical etching would be applicable to a wide range of porosities. In this regard, these two examples suggest any material with porosity and typical particle sizes lower than the porous nickel used here should be compatible with the etch process. If verified, this could allow for interesting explorations of the impact the pore structure may have on emission by allowing for relatively constant geometries to be formed using a variety of materials.

6.7.7 Other Applications and Emitter Densities

The emitters fabricated here used a 200 μm circular mask and will be shown, in the next chapter, to operate well as arrays of ILIS. The emitter spacing for all examples above has been 480 μm, however with a 200 μm diameter mask, higher density arrays could be fabricated on the same material without altering the etch conditions. An initial attempt at etching an array of 952 emitters spaced 318 μm apart, Figure 6-55, has been made and did not show any problems. This etch was made using the same porous nickel material used in this chapter and was done on a 1 x 1 cm sample mounted within a silicon frame. The etch

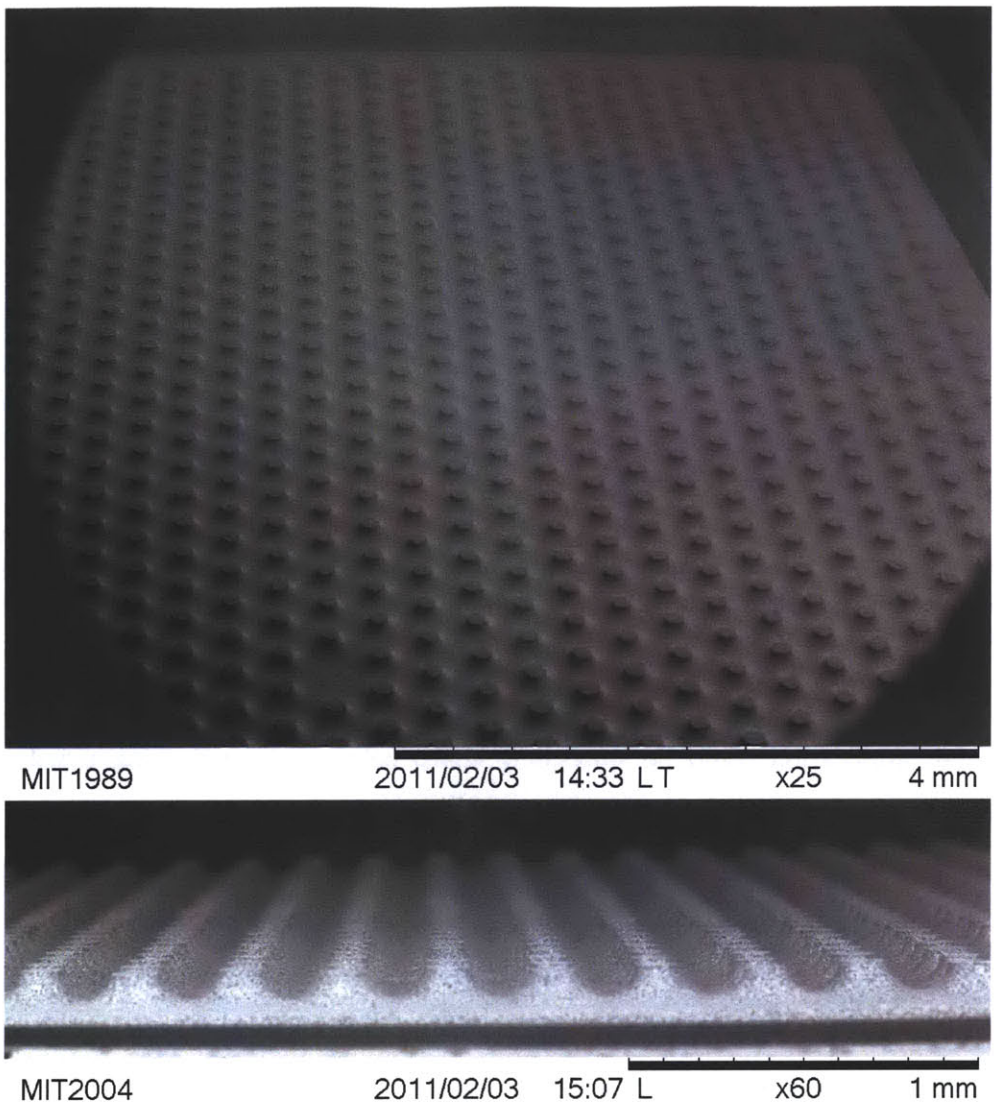

Figure 6-55: An example of an array of 952 emitters spaced 318 μm apart.

was stopped too early due to a calculation error.

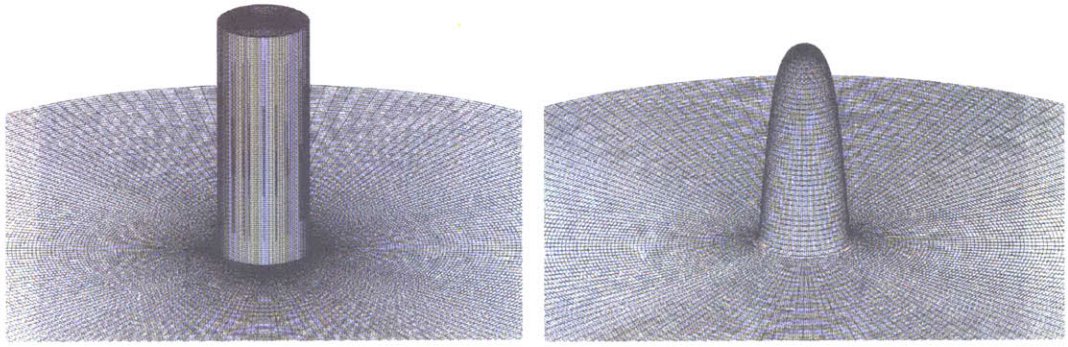

(a) Model of a sintered porous column before electrochemical etching.

(b) Sintered column after a simulated etch of a few seconds using the electrochemical technique developed here.

Figure 6-56: The techniques developed here could be applied to arrays of sintered porous metal columns. The initial columns may be cylindrical and required further adjustments to achieve rounded tips suitable for ILIS. After etching the column using doped electrolyte, a rounded tip could be achieved.

Another application could be smoothing sharp columns formed using powder metal sintering, as has been done by Tajmar[30] for long, needle like, porous tungsten LMIS emitters. As was mentioned in Chapter 3, electrochemical etching could be used on planar arrays of sintered columns to obtain tip geometries more suitable for use as ILIS. In Figure 6-56 this process as been simulated on a 200 μm tall, 50 μm diameter column using the code developed here. As with the secondary etching performed in this research, this type of etch may required added salts to suppress transient effects.

Chapter 7

Ionic Liquid Ion Source Experiments

The experiments presented in the beginning of this chapter are a series of tests which were performed in parallel with development of the fabrication scheme described in the previous chapter. The goal of these tests was to, ideally, identify any issues preventing operation of the porous nickel arrays prior to investing heavily in their development. First, emission from a single planar porous tungsten emitter was tested and compared with the emission from the flat/strip style emitters of Legge. Second, externally wetted nickel emitters were used to confirm if, when wetted with the available ionic liquids, ion emission could be sustained from nickel at levels comparable to those seen with externally wetted tungsten. Finally, some experiments with dual grid operation, to vary both beam current and energy, were made using an array of 80 flat style tungsten emitters, these results are provided in Appendix A.

The remainder of the chapter is then devoted to experimentally testing the porous nickel arrays shown in the previous chapter. Some limited testing has been achieved with the complete package described in Chapter 5; however, those devices have been plagued by electrical breakdowns and alignment problems. More successful testing has been performed using a temporary configuration which allows for separation of the grid and array structures. Using this arrangement, strong emission was observed from arrays fabricated with and without secondary etching, and using both EMI-Im and EMI-BF_4 ionic liquids.

7.1 Experimental Apparatus

The experiments performed here have all been carried out within the MIT Space Propulsion Laboratory Minivac vacuum chamber. The available equipment and generic configurations used for the majority of experiments carried out in this research are described in this section.

7.1.1 Test Facility

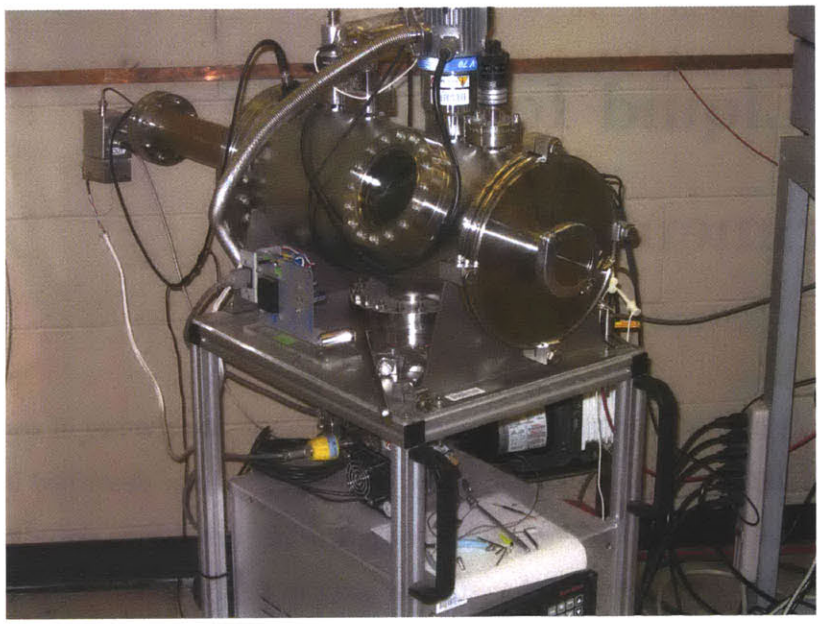

Figure 7-1: The Minivac vacuum chamber at the MIT Space Propulsion Laboratory.

The 20 cm diameter, 50 cm long cylindrical chamber, Figure 7-1, is pumped by two Varian V-70 turbopumps. Practically, the system can sustain operation at vacuum levels as low as 2.0x10^{-7} Torr if pumped for $\sim$ 12 hours. The available equipment used in these experiments are listed here:

- **High Voltage Amplifier:** Matsusada AMS-5B6 high voltage amplifiers capable of $\pm$ 5 kV. Two of these units were used, they are driven by an analog input voltage (1 V per kV) and include a monitor signal at 2 V per kV output voltage.

- **Electrometer :** Keithley 6514 high impedance electrometer and a Keithley 6517 electrometer. The later includes a built in voltage source frequently used to bias the beam collector plate.

- **Current Amplifier:** Keithley 338 current amplifier.
- **Signal Generator:** Agilent 33220A signal generator. Two of these units were available.
- **Oscilloscopes :** Agilent Inifinium 1 GHz, 4 Ga/S and Agilent DSO5014A 200 MHz
- **ScopeMeter :** Fluke 198 ScopeMeter, hand held digital oscilloscope

7.1.2 Beam Current Measurements

Figure 7-2 is typical of the beam current measurements performed here. The source was mounted some distance L_c from a collector plate which was biased to suppress secondary electron emission. The current collected on this plate was then measured using a Keithley electrometer. The distance L_c will be noted for each experiment and was typically set as far as possible from the source, to safeguard the electrometers against high voltage discharges, while continuing to capture the entire beam given an approximation to the beam angle. The Keithley output was then been fed to an oscilloscope for visualization and data logging. Any modifications to this generic setup are noted in the relevant sections. This includes some occasions where, in lieu of biasing the collector plate itself, a biased high transparency electrostatic grid was placed in front of the collector to suppress secondary electrons from the collector plate. The Fluke 198 ScopeMeter indicated in the figure was used to measure the emitted and intercepted currents whenever possible. The ScopeMeter itself is battery powered and left floating. Recorded data was saved and downloaded to a computer using an optical USB to serial adapter.

In processing the data from these measurements, the results have typically been plotted as the magnitude of the observed current. Hence, typical IV curves presented here often present both positive and negative beam currents as positive values with the polarity inferred from the sign of the applied potential.

7.1.3 Time of Flight Measurements

A time of flight spectrometry apparatus described in detail by Fedkiw[58] has been used to measure the composition of emitted beams whenever possible. Figure 7-3 is representative of this setup for a given source. The electrostatic gate consists of tungsten wires which, when

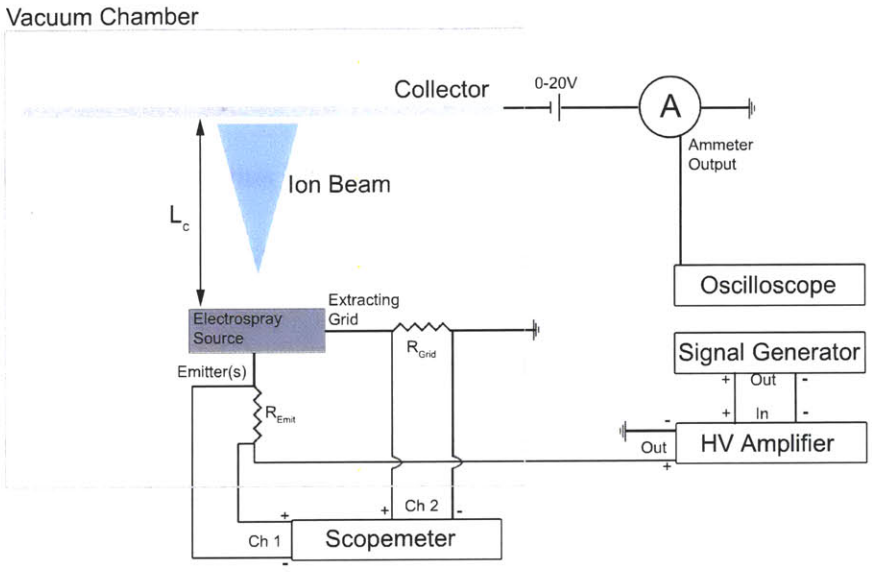

Figure 7-2: Schematic of the generic setup used to measure beam currents emitted from the various sources tested here.

activated, sustain an electrostatic field which deflects the incoming beam. This provides a fast interruption to the ion beam impinging on the collecting plate at L_t. When accelerated through a prescribed potential, a beam of charged species with distributed charge to mass ratios will manifest as a distribution of arrival times. For this research a primary goal of these measurements was to determine if operation within the purely ionic regime was being sustained using the various sources.

The data collected using this device has typically been recast into a species mass for singly charged ions. Specifically, for a singly charged, axially directed beam, equation 7.1 provides the species mass for a beam accelerated through a potential V over a distance L_t in time a time t. Plotting the data as a function of this metric, instead of time, provides a means for comparing observed steps with known ion masses but is not equivalent to assuming the beam is only singly charged. Current from multiply charged ions would create additional steps which do not coincide with the expected species masses from singly charged ions.

$$m_{spec} = 2qV\left(\frac{t}{L_t}\right)^2 \tag{7.1}$$

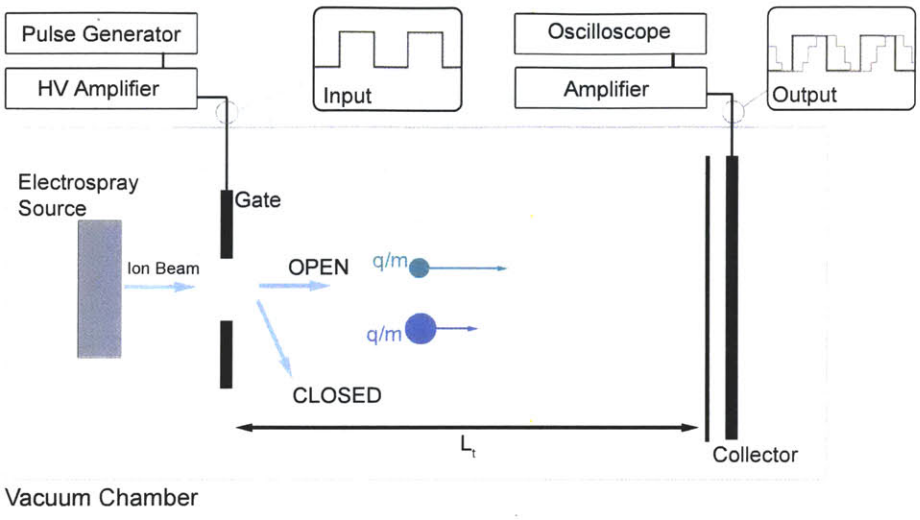

Figure 7-3: Schematic of the time of flight setup used here. Details of this setup are available in the references[58].

7.2 Preliminary Testing Part 1: Emission from a Single Planar Porous Tungsten Emitter

Prior to this research, flat strips of porous tungsten emitters had been developed and tested by Legge[70](see chapter 2). This experiment was intended to confirm the assertion of chapter 2, section 2.4.2, that planar porous emitters greater than 150 μ tall with tip radii $\sim$ 15 μm could sustain pure ion emission and performance levels comparable to the experiments made by Legge using flat arrays. A summary of the experiment and results is given here while more details of this experiment can be found in a paper published during the course of this research[73].

7.2.1 Source Description

Although electrochemical etching was used in this experiment, the test was carried out prior to developing the etch station and techniques developed in this thesis. Here 30 % porosity porous tungsten identical to that used by Legge was patterned with 30, 500 μm diameter circular discs spaced 2 mm apart using a DuPont Vacrel dry film mask. This procedure is described in more detail in the companion paper cited above. Etching was carried out electrochemically in a simple 1N NaOH cell. The resultant etch was highly non-uniform but yielded a few emitters of suitable geometry, one of which, shown in Fig. 7-4, was selected

Figure 7-4: The emitter selected for testing emission from a single porous tungsten emitter on a planar substrate.

for testing. This emitter featured an apex roughly 175 μm above the (uneven) tungsten surface with a roughly $\sim$ 15-20 μm radius of curvature at the tip.

The single emitter was isolated using the setup shown schematically in Figure 7-5(a). A 3D printed ABS plastic mount was secured to a larger teflon plate, upon which a manual three axis stage was attached. The stage was used to position a 1 mm diameter loop of 0.25 mm diameter stainless steel wire around the tip. Planar alignment was confirmed with a video microscope while the axial separation was set to a point where, using the microscope, the tip was as close to level with the base of the extractor loop as possible. Figure 7-5(b) shows a photograph of an initial attempt at alignment. The final configuration differed in that the extractor support was moved to be perpendicular to the emitter plate in an effort to reduce beam interception. Once aligned, the structure was loaded into the vacuum chamber as a source and configured as in Fig. 7-2. Here the collector plate was positioned 1.5 cm from the single emitter and was not biased. The collected current was measured using the Keithley 338 current amplifier. The array was wetted with EMI-BF_4 from the front by applying drops directly to, and in the vicinity of, the selected emitter.

7.2.2 Beam Current Measurements

Figure 7-6 presents the applied potential and collected current measured while ramping the applied potential magnitude from 0 to 2.5 kV over a 100 s period and simultaneously alternating polarity at 0.5 Hz. The data shown are an average over 6 consecutive scans

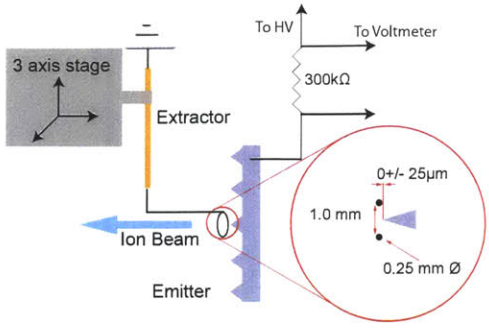

(a) Schematic of the source used in these experiments. This source was then integrated into the generic setup of Fig. 7-2 for testing.

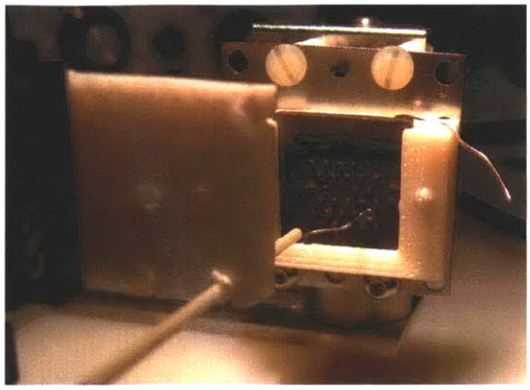

(b) Photograph of the configuration during development. When acquiring the results shown here the ring extractor support structure was modified such that it approached the sample parallel to the array surface in an effort to reduce beam interception.

Figure 7-5: This source consisted of a low density array with a 1 *mm* diameter wire ring extractor positioned over a selected emitter using a manual 3 axis stage. The entire assembly (including stages) was then loaded into the vacuum system and fired towards a collecting plate.

at these conditions. The vacuum pressure during these tests was below 5 x 10 $^{-5}$ Torr. (Note, the relatively low vacuum was likely due to the tendency for the ABS plastic mount to outgas significantly)

The collected current has been plotted again in Figure 7-7 as a function of the applied potential. In the figure, each data point has been generated using a least squares linear fit to the current versus potential measurements for each half period. The indicated error bars correspond to the statistical uncertainty resulting from the linear interpolation.

A limited set of measurements was performed at DC conditions to estimate the transmission fraction of this source. Here the emitted current was measured by monitoring the voltage drop across a 300 $k\Omega$ resistor (R_{emit} in Fig.7-2) using a hand held multimeter. The recorded emitted and collected currents are shown in Figure 7-8 and indicate that approximately 70 % $\pm$ 10 % of the emitter current was measured at the downstream collector plate. The intercepted current at the extractor was not measured.

7.2.3 Beam Spectroscopy

The source was then loaded into the time of flight configuration shown in Fig. 7-3. During this test a small collector plate, housed in a 36.8 *cm* long extension tube was used as a

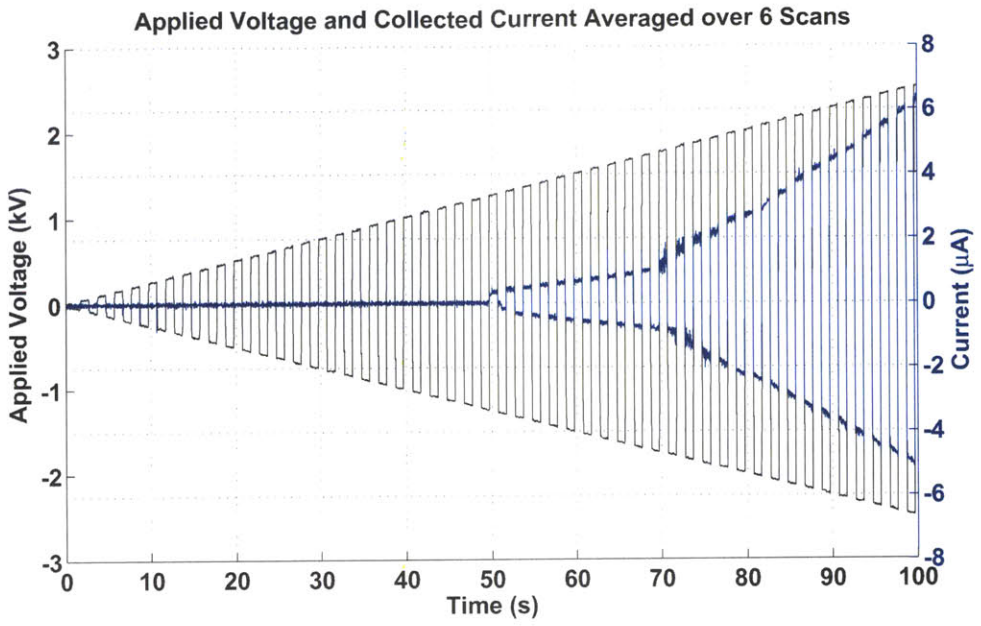

Figure 7-6: Applied potential and collected currents observed from a single porous tungsten emitter with a linearly ramped potential alternating in polarity at 1 Hz.

collector. The overall transit distance L_t was 72.6 cm using this configuration. With this extension, smooth signals could be achieved but at the expense of only capturing a portion of the beam. Time of flight measurements were made at 2.75 kV in both the positive and negative polarities. In figure 7-9 the collected data have been plotted as a function of species mass, using equation 7.1. As indicated in the figure the data coincide well with known masses for EMI-BF_4 monomer and dimer species with a possible population of doubly solvated negative ions.

7.2.4 Conclusions

These data can be compared with those measured by Legge for the flat arrays of the same porous tungsten material[72, 70]. Over similar operating potentials Legge observed stable currents from 10's of nA up to several μA. Specifically, up to 4.5 and 7.0 μA in the positive and negative polarities respectively. In the experiments presented here, the minimum discernable currents detected were a few hundred nA's in both polarities and reached 5.8 and 4.8 μA in the positive and negative cases respectively. Although similar in magnitude, the data collected here differ in symmetry compared with Legge where negative currents were typically stronger than positive. However; in this experiment the collector plate was not

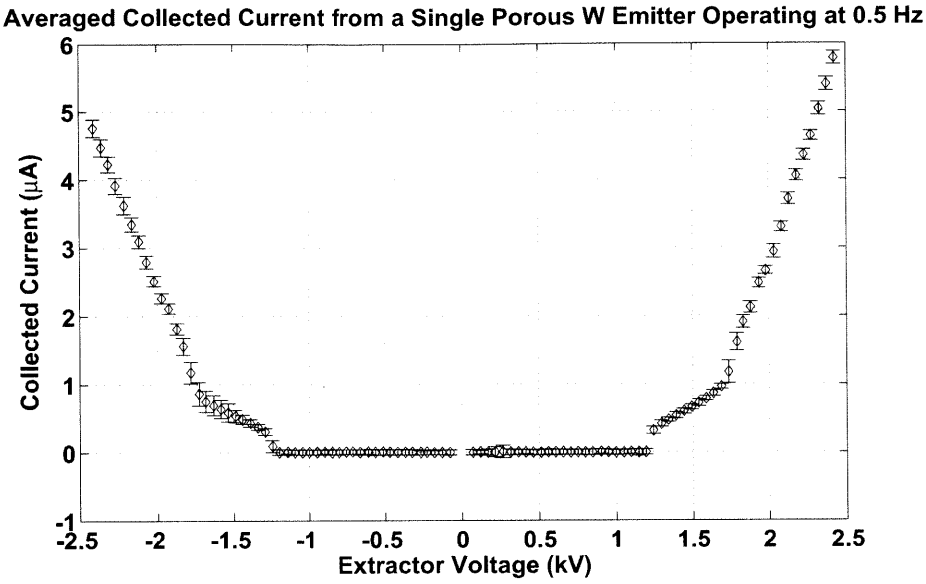

Figure 7-7: Collected current magnitude from a porous planar tungsten emitter. These data are averaged over 6 consecutive scans.

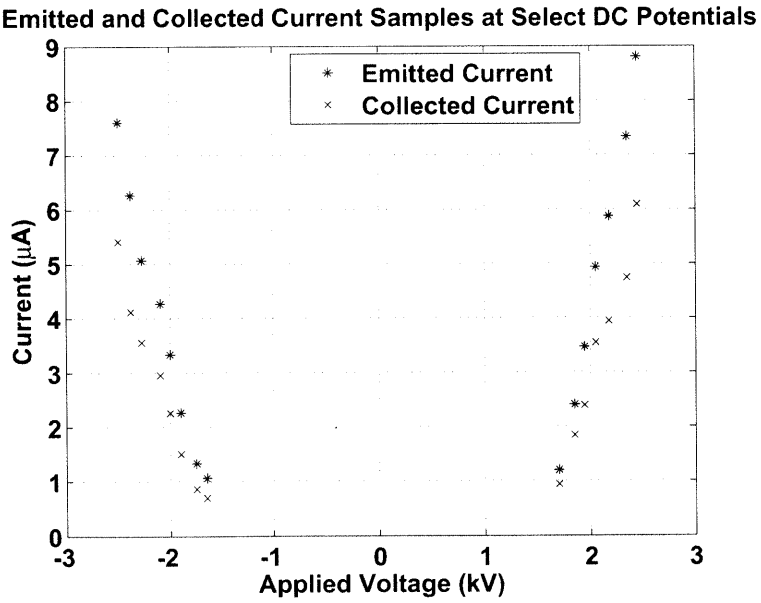

Figure 7-8: Emitted and collected currents at the indicated set points. The emitted current was not monitored continuously during the scans presented in Figure 7-7.

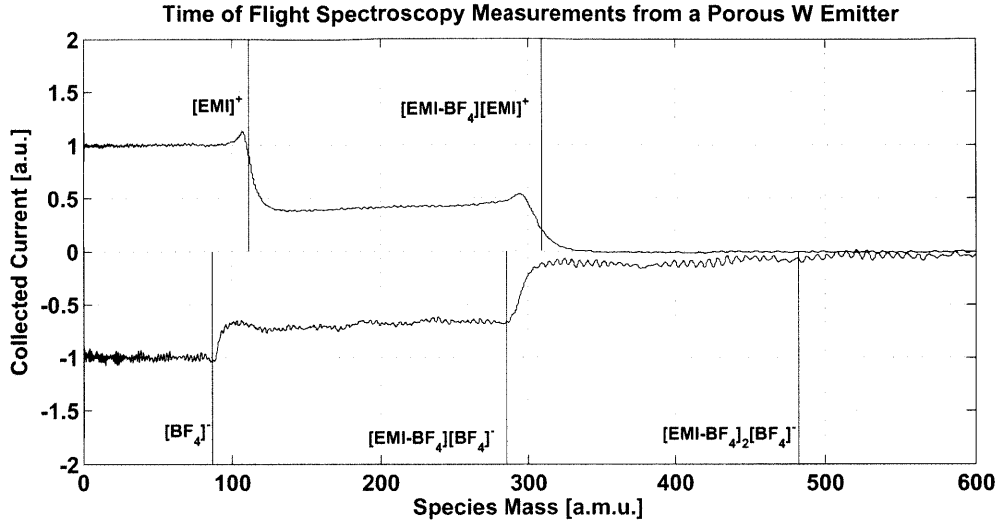

Figure 7-9: Time of flight data collected from a single planar porous emitter at $\pm$ 2.75 kV using EMI-BF_4 propellant. The collector used here was positioned in an axially aligned extension tube far from the source. As a result these data may not be representative of the entire beam.

biased and therefore could have been prone to spurious currents due to secondary electron emission from the plate to the chamber. These would manifest as an additional positive current detected at the collector plate and could therefore have, to some degree, contributed to the inverted symmetries.

The emitted and collected currents were not perfectly matched but, given the simple extractor configuration, these results were promising. Any significant emission from sites off the emitter tip would have been unlikely to reach the collector plate due to their high beam angles. Combined with the beam spectroscopy measurements, these results support the notion that a planar emitter can sustain pure ion emission at high currents using ionic liquid propellants.

7.3 Preliminary Testing Part 2: Externally Wetted Nickel Emitters

Ionic liquid sources were originally developed using externally wetted tungsten needles[37, 36]. Before proceeding with fabricating nickel based porous emitter arrays, this preliminary study using externally wetted nickel needles was performed. The goals were to establish if any unforseen chemical or, for example, hydraulic, interactions may be present when

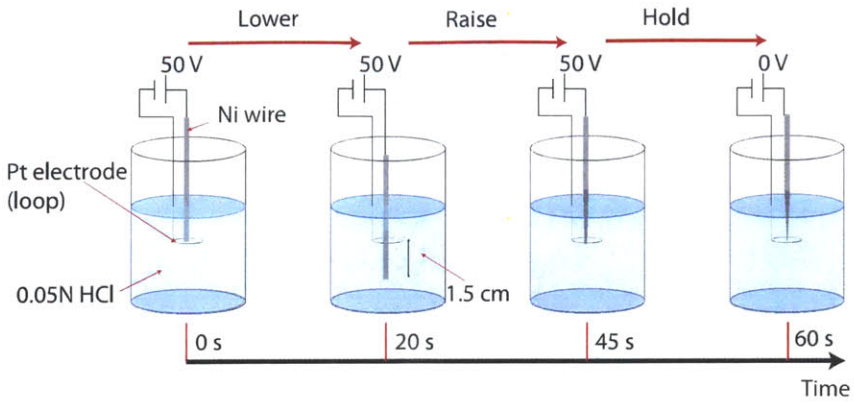

Figure 7-10: Externally wetted emitters were fabricated using a simple electrochemical process. A 0.5 mm wire was lowered slowly, over $\sim$ 20 s though a Pt loop electrode, and then retracted over $\sim$ 25 s. The wire was then held such that the tip was level with the loop for a further 15 s.

using nickel which could prevent further development. The description below supplements a paper presented at the 2010 Joint Propulsion Conference[61] focused on validating nickel substrates.

The tests used EMI-Im and EMI-BF_4 to obtain electrospray emission on externally wetted nickel emitters. Pure ion emission was confirmed by measuring the emitted current using time of flight measurements. Additionally, the electrochemical double layer between the ionic liquid and emitter was probed while alternating the emission potential. These probe measurements were performed on both nickel and tungsten emitters in an attempt to instill confidence in the ability for voltage alternation to suppress electrochemical reactions on nickel in a manner similar to that observed with tungsten[37].

7.3.1 Fabrication of Externally Wetted Nickel Emitters

The externally wetted emitters were etched using a modified form of the procedure Cavallani[161] used to create nickel field emission electrodes. Unlike the reference, physically rough emitters were desirable to promote wetting while a relatively large tip diameter, consistent with the 15-20 μm tips used on tungsten emitters[36], was targeted. The process is outlined in Figure 7-10. A 0.5 mm diameter nickel wire was initially positioned within a loop, roughly 1 cm in diameter, of platinum wire with both electrodes immersed in a weak 0.05N hydrochloric acid electrolyte. A constant cell potential of 50 V was maintained during the

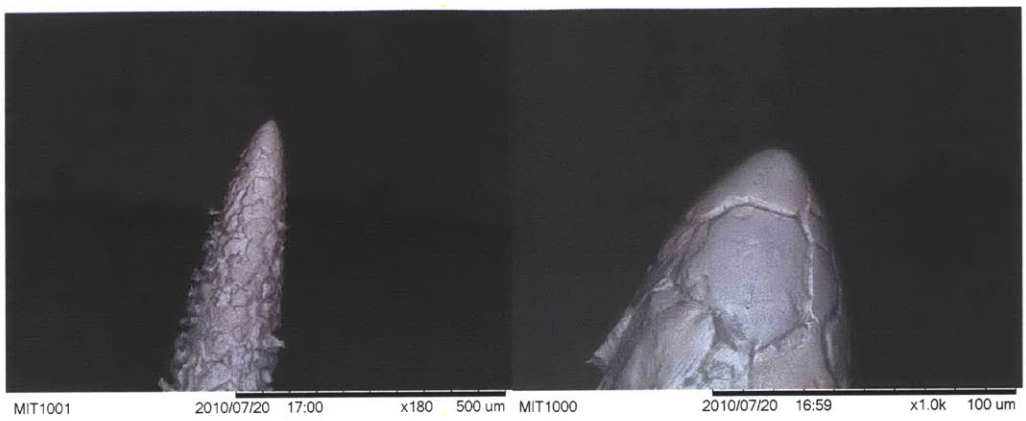

Figure 7-11: SEM images showing an example of the emitters fabricated using the procedure outlined in Fig. 7-10.

etch while moving the emitter within the platinum loop achieved variable shaping and surface roughness. Specifically, the emitter was first lowered such that after approximately 20 s the tip was roughly 15 mm below the loop. Subsequently, the emitter was raised to be level with the counter electrode over an additional 25 s before remaining level with the loop for the final 15 s of etching. The initial lowering and raising of the wire had the effect of inducing surface roughnesses along a suitable length of wire while the final, steady, phase achieved the desired tip radius. In the context of the electrochemical etching in the previous chapter, the behavior during roughening was largely consistent with an etch not limited by mass transport where etches favoring the crystal structure are typical. An example of the emitters fabricated in this manner is given in Figure 7-11.

7.3.2 Experimental Configuration

These experiments were performed within the facility described previously. Vacuum levels below $1x10^{-5}$ Torr were maintained throughout all experiments presented in this section. Externally wetted emitters were configured as shown in Figure 7-12. The high voltage signals were applied using the signal generator and both of the HV amplifiers listed at the beginning of this chapter. An identical signal was input to both amplifiers while that connected to the collector plate was biased to 50 V to prevent effects due to secondary electron emission. The Keithley 6514 electrometer was used to measure the probe to ground potential while the emitted current was monitored using the Keithley 6517 electrometer. The configuration differs from the generic setup shown in Figure 7-2 in that the emitter was grounded with

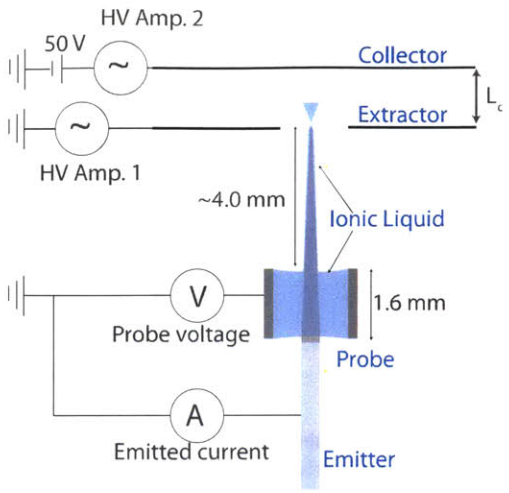

Figure 7-12: Experimental setup used to characterize the behavior or externally wetted nickel emitters.

high voltages signals applied to the collector and extractor electrodes. The setup includes a cylindrical platinum probe, 1.6 mm long with a 1.8 mm inner diameter, placed $\sim$ 4 mm from the tip of the emitters. The probe was filled with ionic liquid before the emitters were passed through the cylinder until the tip was inline with the extractor hole. This ensured wetting to the tip and continuous coupling between the probed and active ionic liquid. Probe signals were interpreted as a measurement of the electrochemical double layer at the ionic liquid to emitter electrode interface.

For time of flight measurements the collector plate was removed and the potential was applied in the standard manner with the grid grounded, as in Fig. 7-2. These measurements used a collector mounted within a 36.8 cm long extension housing as in section 7.2, such that the total gate to collector distance was 79.5 cm.

Three diagnostic tests were performed using these emitters and the ionic liquids EMI-Im and EMI-BF_4. First, the emitted current was measured as a function of potential. Second, time of flight data was collected and finally, the electrochemical double layer was probed at varying emitted currents and potential alternation frequencies.

7.3.3 Emission and Time of Flight Spectroscopy

Figures 7-13(a) and 7-13(b) show representative data for the emission current. Here the potential polarity was alternated at 1 Hz while its magnitude was ramped from zero. The

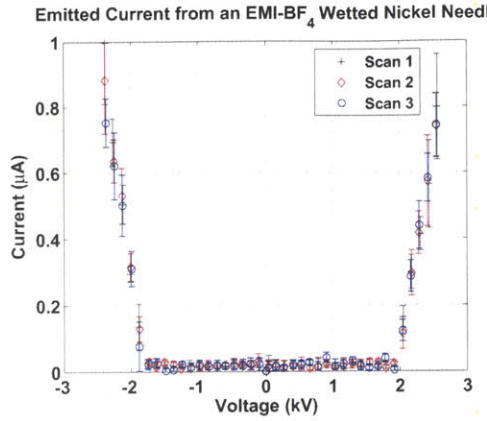

(a) Emission from an externally wetted nickel needle wetted with EMI-BF_4 over three consecutive scans.

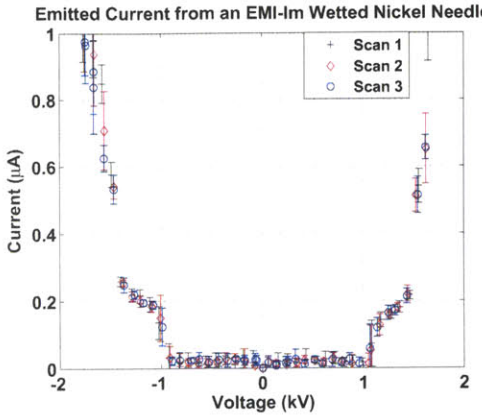

(b) Emission from an externally wetted nickel needle wetted with EMI-Im over three consecutive scans.

Figure 7-13: Emitted currents from externally wetted nickel emitters. The data points represent the mean current at the mean potential for a half period of voltage alternation at 1 Hz. The error bars give one standard deviation from the mean.

data give the mean and standard deviation of emitted current for each half period. The plots show three consecutive scans in each case and demonstrate that, although somewhat unstable, the behavior between scans was generally in agreement. For both liquids, current levels from a few hundred nA up to $\sim 1\ \mu A$ were recorded. Note that for EMI-Im, the emission increased gradually after roughly $\pm\ 1\ kV$ before increasing at a rate more comparable with that seen with EMI-BF_4. Unstable emission is not uncommon from externally wetted emitters and may indicate that the emitter geometries and wetting path were not ideal. This would not be surprising given the relatively untested etching scheme described above. However; for the purposes of demonstrating emission from nickel these data are acceptable.

Time of flight spectroscopy measurements using EMI-Im on an externally wetted nickel emitter are given in Figure 7-14. Here the known masses of EMI-Im monomer and dimer (singly solvated) ions, see table 2.1, are plotted along with the measured signal. The measurements are consistent with a beam dominated by monomer and dimer species at all potentials. However; the ratio of species was not consistent between all extracting potentials. For one case of positive emission, at 1.5 kV, a small portion of the signal decayed relatively slowly beyond the scale plotted here. This could indicate a small droplet population but the phenomenon was not repeated and may have been a measurement error. Similar agreement was achieved for positive ion emission using EMI-BF_4. Measurements

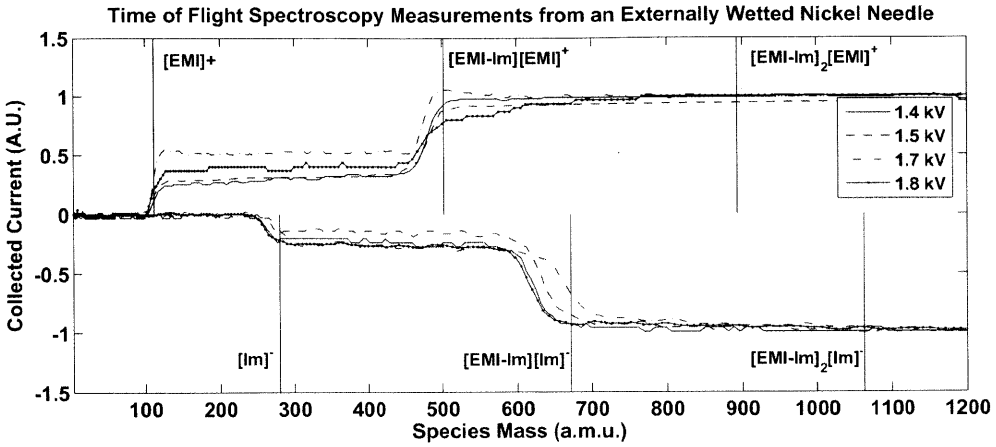

Figure 7-14: Time of flight data collected using an externally wetted nickel emitter wet with EMI-Im.

from negative ion beams with that liquid were not taken due to a malfunction within the time of flight measurement hardware.

7.3.4 Probing the Electrochemical Double Layer

Probe measurements were then taken while operating the sources at a variety of currents and alternation frequencies. Here the emitter potential polarity was alternated while the magnitude was held constant. Externally wetted tungsten emitters, fabricated using the method outlined by Lozano[36], were also mounted as in Fig. 7-12 and tested for comparison with nickel. The data shown here are samples of a larger data set. Sample data for both nickel and tungsten using EMI-BF_4 are given in Figure 7-15 at 10 s and 100 s alternation periods. Similarly, Figure 7-16 presents data collected using EMI-Im with a 100 s period of alternation for both nickel and tungsten. Finally, an example of the data for EMI-Im on nickel for a 10 s potential period is given in Figure 7-17. No detailed model for the expected, or predicted, probe behavior has been considered (see section 7.7.8 at the end of this chapter for discussion in this regard), instead only qualitative observations were made.

The results generally showed that for relatively long periods on nickel, the probe potential begins to saturate, while at lower periods a more saturated measurement was only observed for one polarity. Compared with tungsten, known to react with EMI-BF_4[37], the measurements are qualitatively similar for 10 s periods from a nickel emitter. However; at a 100 s period, the signal from positive emission on the tungsten emitter was quite unlike

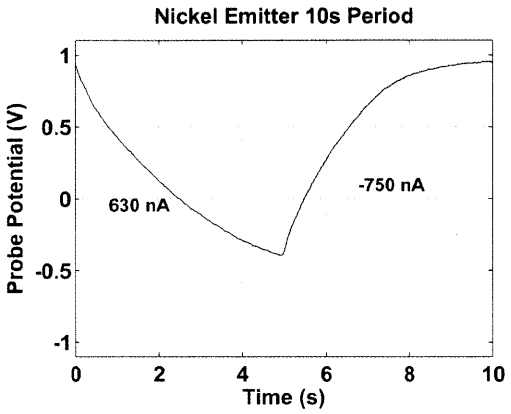

(a) Probe measurements with the indicated current draws in each polarity for a nickel emitter wet with EMI-BF_4 with a 10 s alternation period.

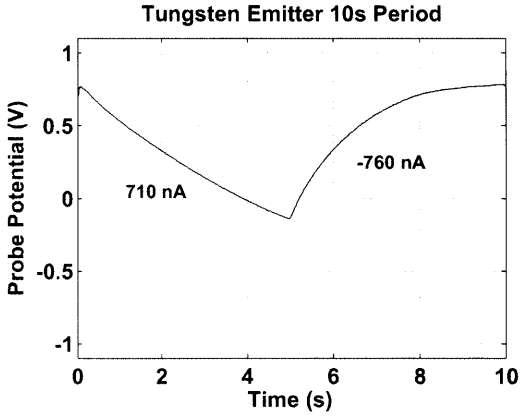

(b) Probe measurements with the indicated current draws in each polarity for a tungsten emitter wet with EMI-BF_4 with a 10 s alternation period.

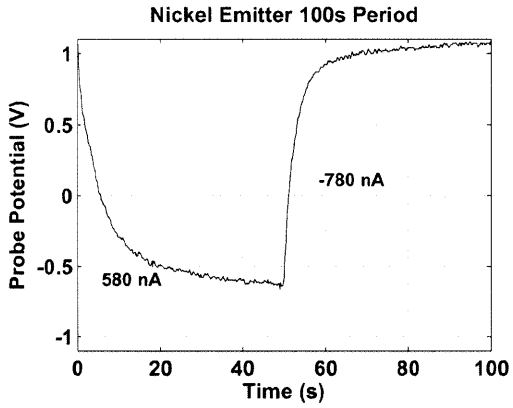

(c) Probe measurements with the indicated current draws in each polarity for a nickel emitter wet with EMI-BF_4 with a 100 s alternation period.

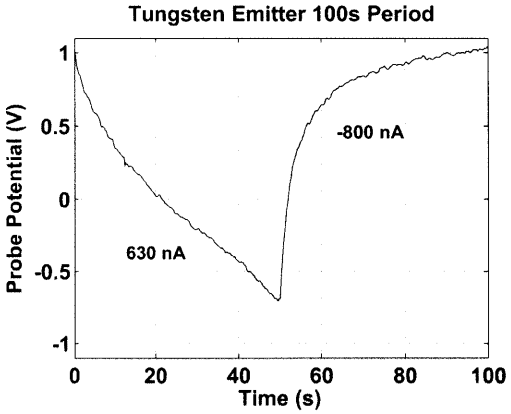

(d) Probe measurements with the indicated current draws in each polarity for a tungsten emitter wet with EMI-BF_4 with a 100 s alternation period.

Figure 7-15: Representative data showing the charging and discharging of the EMI-BF_4 ionic liquid to metal interface at the indicated periods and current levels for both nickel (left side) and tungsten (right side) emitters.

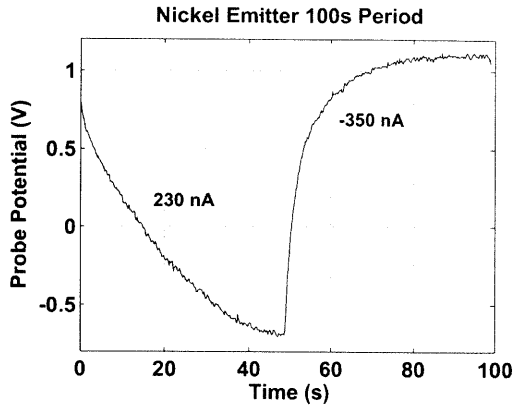

(a) Probe measurements with the indicated current draws in each polarity for a nickel emitter wet with EMI-Im.

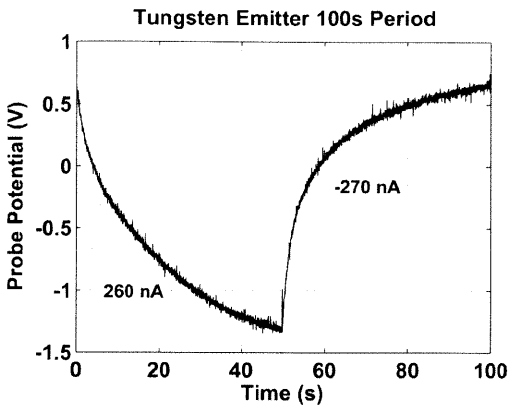

(b) Probe measurements with the indicated current draws in each polarity for a tungsten emitter wet with EMI-Im.

Figure 7-16: Representative data showing the charging and discharging of the EMI-Im ionic liquid to metal interface at the indicated periods and current levels for both nickel (left side) and tungsten (right side) emitters.

that for negative emission and both polarities on nickel. The previous work with tungsten found that when emitting postive ions, the resulting reactions resulted in a discoloration of the fluid, while when emitting negative ions gas evolution occurred. Hence, the irregular shape for tungsten and EMI-BF_4 could be consistent with contaminating reactions. This has not been confirmed directly. Using EMI-Im the measurements were relatively similar between both materials.

All tests shown here favored negative ion emission on average. It is interesting to note that this has been accompanied by a tendency for the probe measurements to approach a more saturated signal when emitting negative ions. Recall that the potential magnitude was constant while its polarity alternated. No circumstances of emission favoring positive ions were recorded.

A complete understanding of these results would be beneficial in determining optimum operation of these emitters, as will be demonstrated with the complete porous arrays tested below where the results strongly suggest electrochemical reactions do occur even when operated at 1 Hz. A successful model for such behavior would require understanding the complete (bi-polar) problem to establish the underlying mechanisms driving the probe signal. Despite the lack of a quantitative understanding, based on the similar results when operating at 10 s periods for both metals and ionic liquids, the anticipation that operating

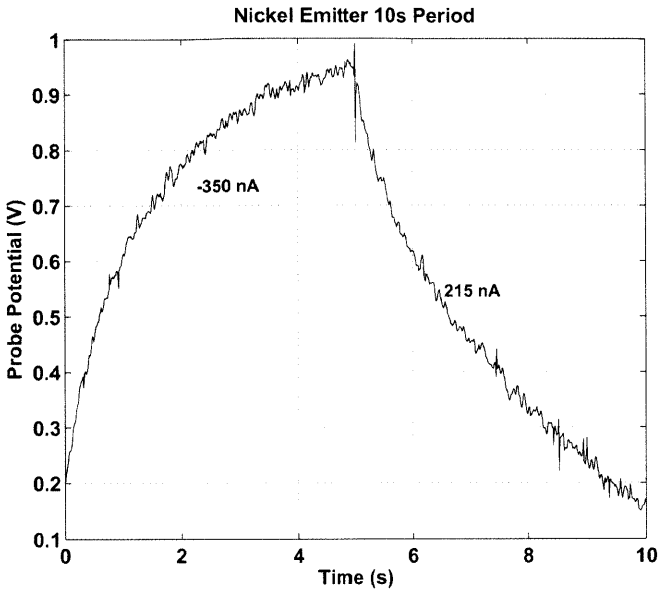

Figure 7-17: Probe measurements with the indicated current draws in each polarity for a nickel emitter wet with EMI-Im with a 10s potential alternation period.

at 1 Hz may suppress reactions was applied to the porous arrays tested below. Further discussion of these results is presented in section 7.7.8.

7.4 Microfabricated Porous Nickel Emitter Packages

The microfabricated arrays developed during this work have been tested both as part of the complete package described in Chapter 5 and in a laboratory configuration intended to demonstrate the array capabilities while relaxing some of the challenges inherent in the completely packaged devices. Some of the electrical isolation problems experienced and the best case of emission from a complete package are described in this section. Measurements demonstrating the array capabilities using the modified configuration are then presented in the next section.

7.4.1 Electrical Shorts Observed with Microfabricated Packages

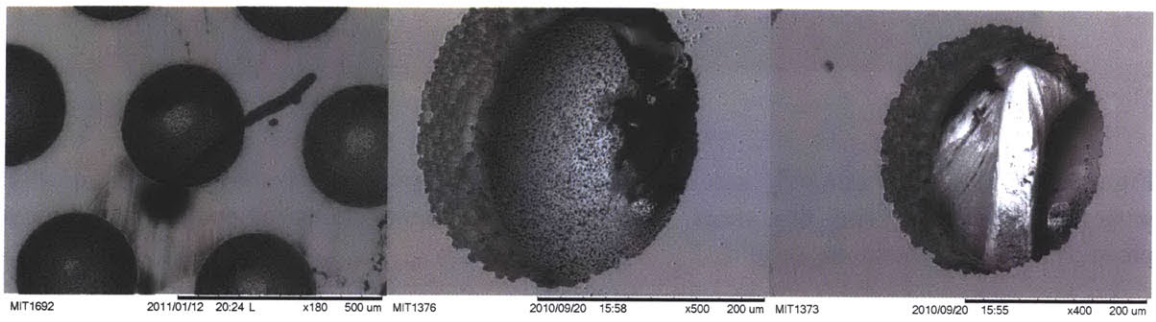

Figure 7-18: Examples of physical shorts found during attempted operation of the fully microfabricated thrusters. Maintaining a clean device throughout testing was difficult as the vacuum chamber was not housed within a clean environment.

Operation of the fully packaged thruster modules has been plagued by a number of faults which typically manifest as moderate ($k\Omega$'s) to large (100's of $M\Omega$) shorts between the porous nickel emitter array and the electrostatic grids. On many occasions these were, regrettably, found to be due to contamination during the assembly or testing phases. Examples of the resulting physical shorts are shown in Figure 7-18. On some occasions this type of contamination could be removed through cleaning but otherwise resulted in total loss of the sample due to the inability to disassemble the devices once fully bonded.

A more critical issue may be poor trapping of excess liquid by the silicon support structure. Two mechanisms were anticipated to prevent the conducting ionic liquid propellant from bridging from the emitter array to the electrostatic grid above. First, the porous nature of the substrate itself was formed of pores presumably much smaller than any other

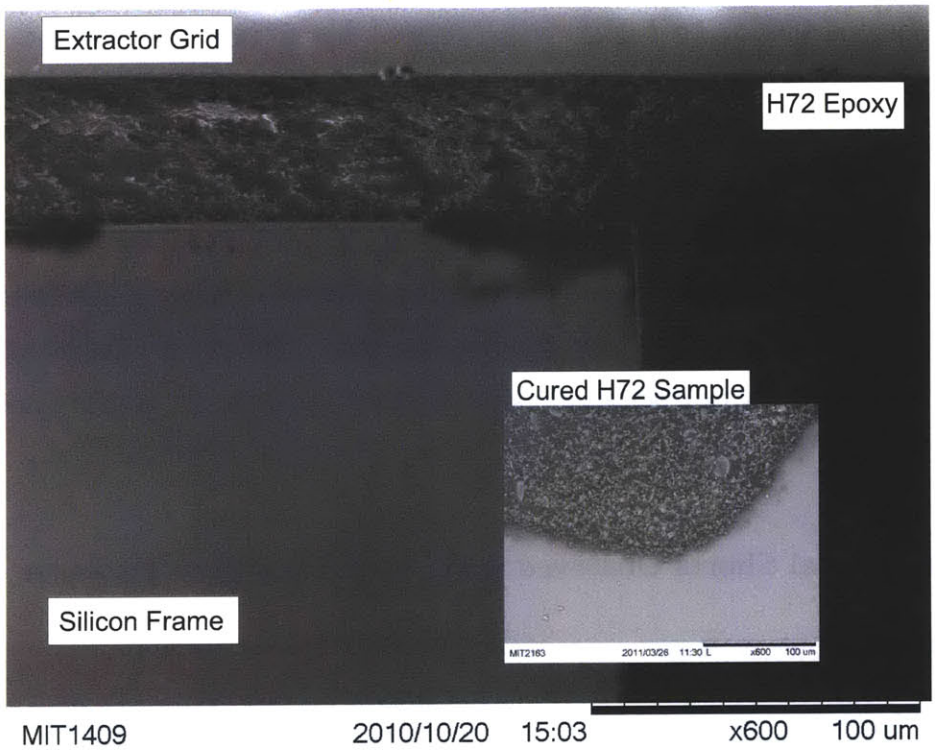

Figure 7-19: Side view of a fully assembled array showing epoxy which may be contaminated with ionic liquid resulting in a short. The inner image shows the same epoxy on a sample piece of silicon without any liquid.

feature on the device. Thus relatively strong capillary forces should maintain the liquid within the substrate, so long as it remains at or below saturation. Additionally, the small liquid trap described in Chapter 5 was intended to prevent any excess or errant liquid, added through the rear feeding site, from tracking along the silicon surface to the extracting grid.

Despite these measures, post failure inspections have suggested that liquid migration could have contributed to some of the observed shorts. Specifically, despite measured impedances greater than 200 $G\Omega$ during evacuation of the test chamber, many samples shorted as soon as a potential (typically a few 100 V) was applied to the assembly. For one such occasion the assembly was carefully broken to obtain an SEM image of the grid to frame bond, Figure 7-19. The figure also includes a test sample of the same (H72) epoxy cured on a sample silicon frame (oxide coated) without an array, extractor or ionic liquid. While not conclusive, the smooth regions between exposed points within the epoxy may be evidence of ionic liquid. It is unclear what path the liquid may have taken from the porous array to reach this point.

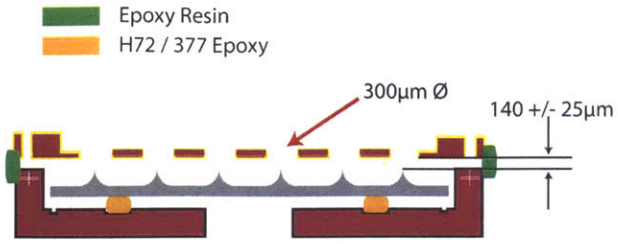

Figure 7-20: Modified epoxy locations for bonding the extractor grid and silicon frame along with average emitter to extractor distances for the sample assembly tested below.

To counter this issue, a slightly more successful approach, suggested by colleagues developing the overall process[113], used the alternative Epoxy Resin described in section 5.3.1. Here dots of the viscous epoxy resin were applied to the outside of the structure while the upper and lower components were secured. On some occasions this method resulted in the configuration, as in Figure 7-20, with the grid to frame epoxy kept outside the crucial gap. However; this technique was prone to poor alignment, possibly due to differential thermal drifts between the upper and lower support structures during curing. Furthermore, the epoxy was often drawn into the tight frame to grid gap when heated, nullifying the benefits. On a few occasions this technique held off electrical shorts long enough to gather some preliminary emission data. The next section presents one example case.

7.4.2 Best Case Operation of a Complete Thruster Package

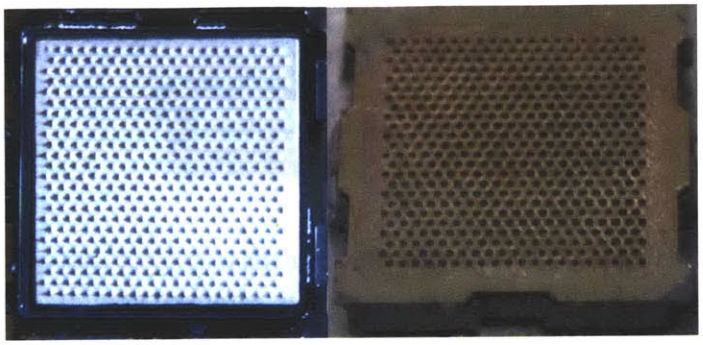

(a) Photographs of the porous nickel array before and after bonding to the gold coated silicon extractor grid.

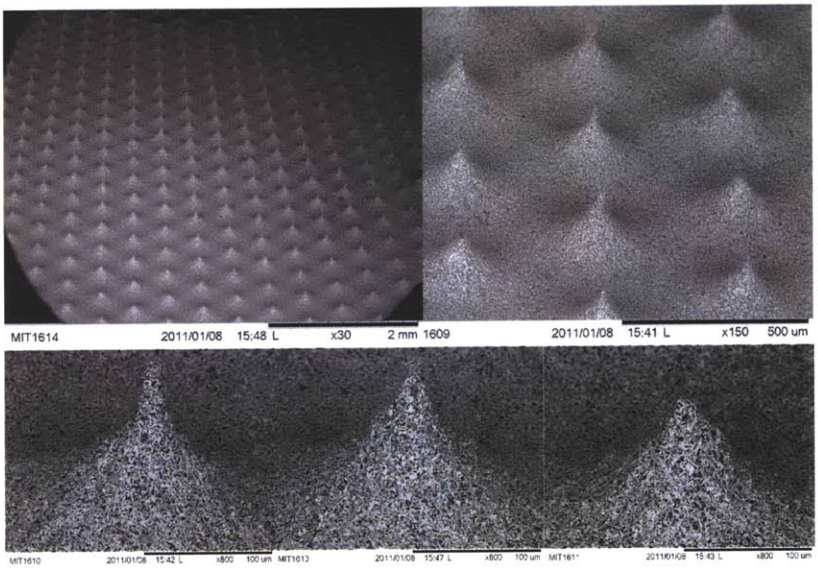

(b) SEM images of the porous nickel array, fabricated using the pulsed etching process developed in the previous chapter. This array was not treated with the secondary etch step to round the emitters.

Figure 7-21: Images of the sample array, before firing, used in this example experiment.

This array was fabricated using the pulsed electrochemical conditions described in the previous chapter but was not treated with the secondary etch step. The array was packaged using the externally applied epoxy as in Fig.7-20. The average emitter to tip distance was measured using a microscope to be 140 $\pm$ 25 μm. The silicon extractor grid used here was 100 μm thick, with 300 μm diameter holes and was coated with gold, as described in section 5.5. Photographs of the array and final package, along with SEM images of the fabricated emitters are shown in Figure 7-21. The package was wet with the ionic liquid EMI-Im, using the rear feeding port and a syringe. Drops were added until the porous nickel

substrate no longer quickly adsorbed the liquid. The package was then placed in a nitrogen desiccator overnight, at which point a few more drops were added and quickly absorbed by the material just prior to testing. The sample was not visibly saturated or overflowing.

The source was configured in the standard manner shown in Figure 7-2, with a biased collector plate at 20 V positioned 24.1 mm from the extractor. Only the current collected on this plate was measured during this test. Emission was started after evacuating the chamber to below 2.2 x 10^{-7} Torr, this level was maintained throughout the test. The potential polarity was alternated at 1 Hz at all times while the amplitude was ramped from zero over a 20 second period. Four consecutive scans from 0 to $\pm$ 2.5 kV were made followed by two scans from 0 to $\pm$ 2.75 kV. The collected data was typically noisy, but with no noticeable high frequency signal discernable from the equipment background noise, as shown in Figure 7-22(a). Due to this noise, a 10 point moving average was employed in Figure 7-22(b) where results have been grouped and averaged for the two maximum potential set points. Several 10's of μA were collected in both polarities. The current was typically higher for the positive polarity, at a given potential magnitude, during these tests.

After making the measurements above, the potential amplitude was set to 2.7 kV, while continuing to alternate at 1 Hz, and the collected current progression in time was observed. This test lasted less than 2 minutes before an electrical short occurred and the test ended. The data shown in Figure 7-23 are a compilation of three 40 second scans, omitting a short ($\sim$ seconds) delay between each scan ending and the next beginning. The data has been truncated at the point when, during the third scan, an electrical short was encountered.

Once these tests were complete, the array was examined in an effort to identify the cause of the electrical short. No obvious cause (such as contamination) could be identified. However; the inspection did reveal patterns of residue on the emitters, shown in Figure 7-24. Possible explanations for this residue, also observed in some tests below, will be discussed in section 7.7.7.

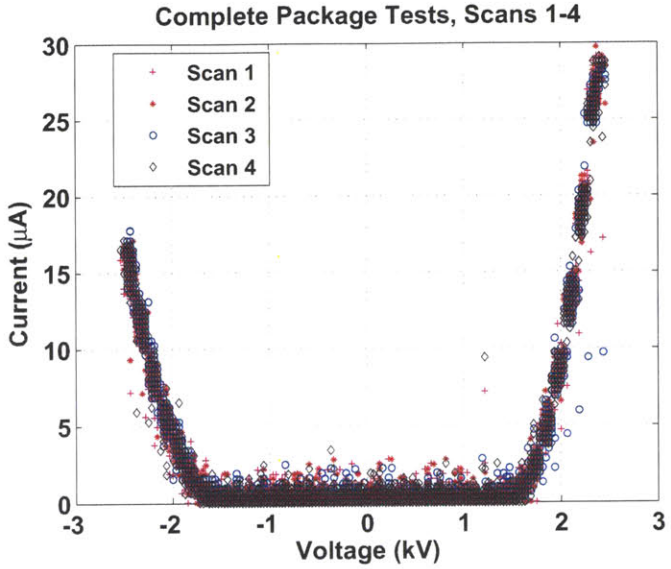

(a) Measured collected current from a complete thruster package at the indicated emitter potentials.

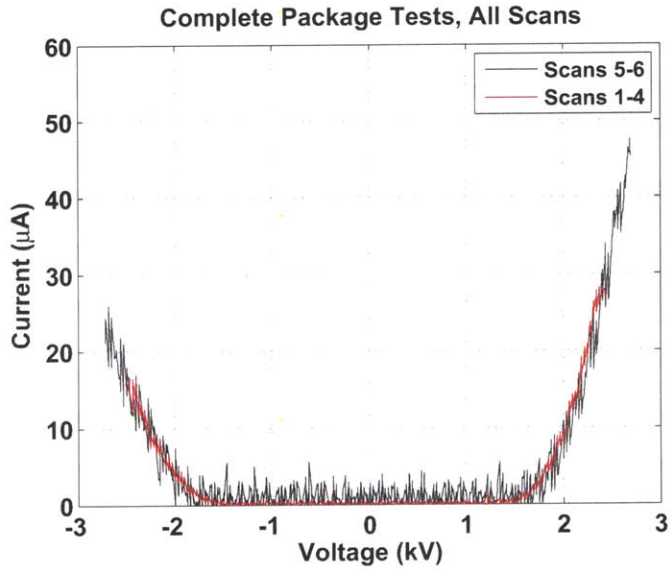

(b) Measured collected current from a complete thruster package at the indicated emitter potentials using a 10 point moving average for two sets of scans.

Figure 7-22: Magnitude of collected current from a fully packaged nickel array.

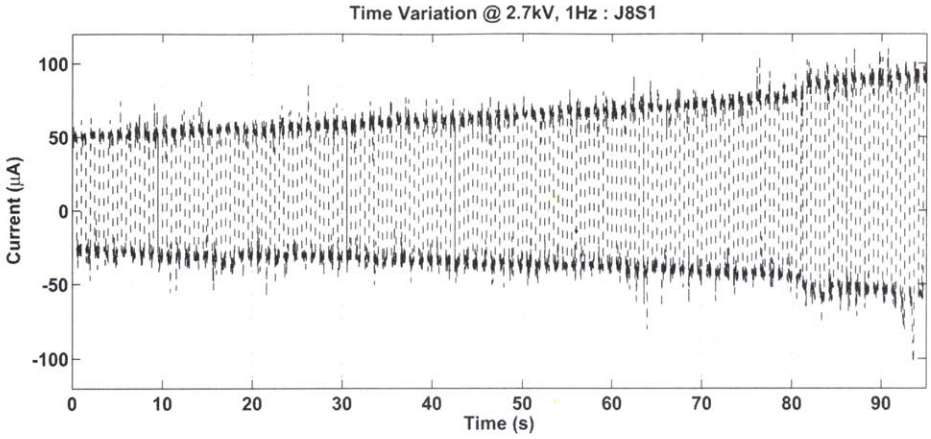

Figure 7-23: Collected current evolution in time with a fixed potential amplitude. 2.7 kV, while alternating the potential at 1 Hz. These data are a compilation of three 40 second scans, the third scan ended prematurely due to an electrical short.

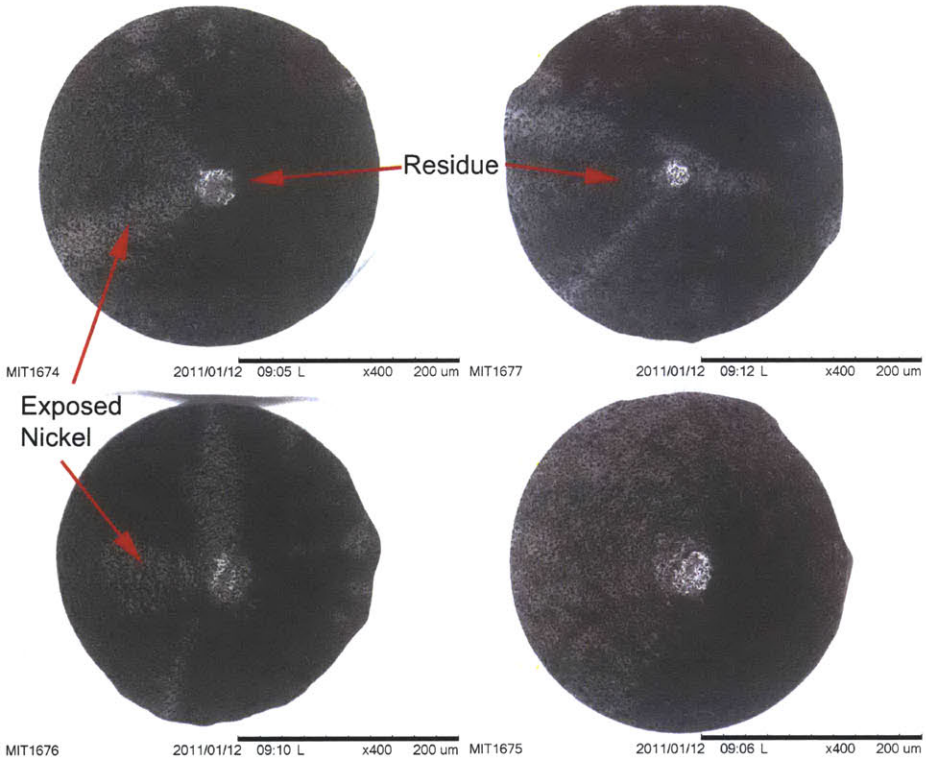

Figure 7-24: Residue patterns visible on an array fired using the complete thruster package.

7.5 Nearly Fully Microfabricated Emitter Packages

Due to the issues identified with the fully microfabricated packages, a simplified setup has been used to demonstrate the capabilities of the emitter arrays. This setup, shown schematically in Figure 7-25(a), uses the laser cut stainless steel grids spot welded, at the corners, onto larger support plates (Kimball Physics, stainless steel eV part plates). The emitter array has then been pasted to a separate support plate using double sided SEM tape. The two parts have been aligned with a simple 3 axis alignment jig using the markings and guides as described in section 5.3. In this setup, a temporary bond between the support plate and the grid has been made farther from the array itself compared with the completely packaged devices. The components were secured using double SEM tape pasted onto alumina spacers. These spacers were then positioned on silicon sheets layered with kapton tape to achieve good (see section 5.5) tip to extractor distances. These extra silicon spacers are not shown in the schematic. This technique has two advantages for laboratory testing. First, it typically eliminated electrical shorts by greatly increasing the electrical path between the emitter array and extractor grid and removed a path for excess ionic liquid to form a short. Second, it is a non destructive method. The grid assembly can be easily removed from the array without any damage to either, thus allowing the same grid to be used on multiple arrays and for mis-aligned or physically shorted arrays to be easily corrected with minimal damage to sensitive components.

Three beam emission experiments have been performed with this configuration. First emission from an array without secondary etching has been tested with EMI-Im, next a fully processed array is tested with the same liquid and finally another fully processed array has been tested with EMI-BF_4. In all cases the setup was loaded into the standard configuration of Fig. 7-2 for emission testing with the collector plate 24.7 *mm* from the extractor.

7.5.1 Sample Array 1 : Single Etch Step with EMI-Im Propellant

The array shown in Figure 7-26 was etched using only the first etch step in section 6.6. The array was somewhat over-etched leaving many emitters too sharp for secondary etching. A representative variety of emitters are shown in the figure. The upper right figure shows a topographic view of one particularly over etched region on the array. Structures in this

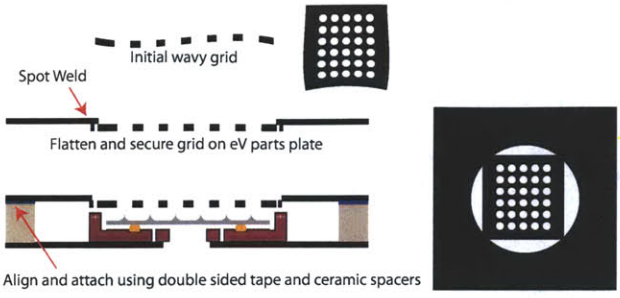

(a) Metal grids, shown in chapter 5, have been mounted on stainless steel plates and bonded, temporarily to the emitter arrays using double sided tape.

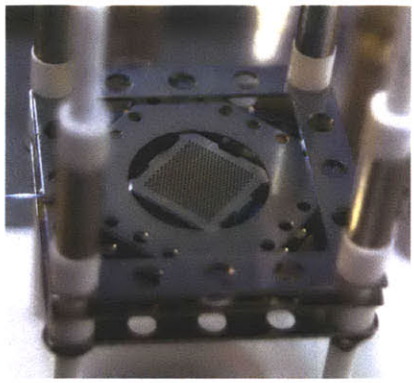

(b) Photograph of the simplified assembly used to test arrays in this section.

Figure 7-25: A simplified, non-destructive, assembly has been used to test the emitter array capabilities in this section.

region resembled the dull mound in the bottom right of the figure and were not expected to yield emission. After assembling the source as described above (Fig. 7-25(a)) it was wetted with EMI-Im through the rear feed port in the same manner as described in the previous fully packaged test, section 7.4.2. The emitted and intercepted currents were measured using the ScopeMeter with 97.8 $k\Omega$ and 106.8 $k\Omega$ resistors on the emitter and grid lines respectively. Typical emitter tip to extractor distances were roughly 120-150 μm, estimated based on the emitter heights and spacings on the support structures.

Initial measurements were performed with an alternating potential at 1 Hz and fixed magnitude. However; the recorded data were highly unstable, see Figure 7-27. This issue was later tracked down to a breakdown in the Fluke ScopeMeter leading to a current leak at negative potentials (see the next section). With positive potentials only, stable and relatively steady collected currents were achieved when ramping the applied potential from 0 to 2.0 kV with a 10 second period. Once the minimum potential for measurable current was observed to be greater than 1 kV, subsequent scans were made from 1.0 to 2.5 kV, again over 10 seconds. Examples of these results are summarized in Figure 7-28. Figure 7-28(a) gives the emitted, collected and intercepted currents as measured during one scan. Although every effort was made to ensure these data were taken during the same 10s scan, this was difficult due to the inability to externally trigger (and hence ground) the ScopeMeter. The data may therefore have been offset by a period of the complete ramping signal on some occasions. The collected current was roughly 70 % the emitted current. The

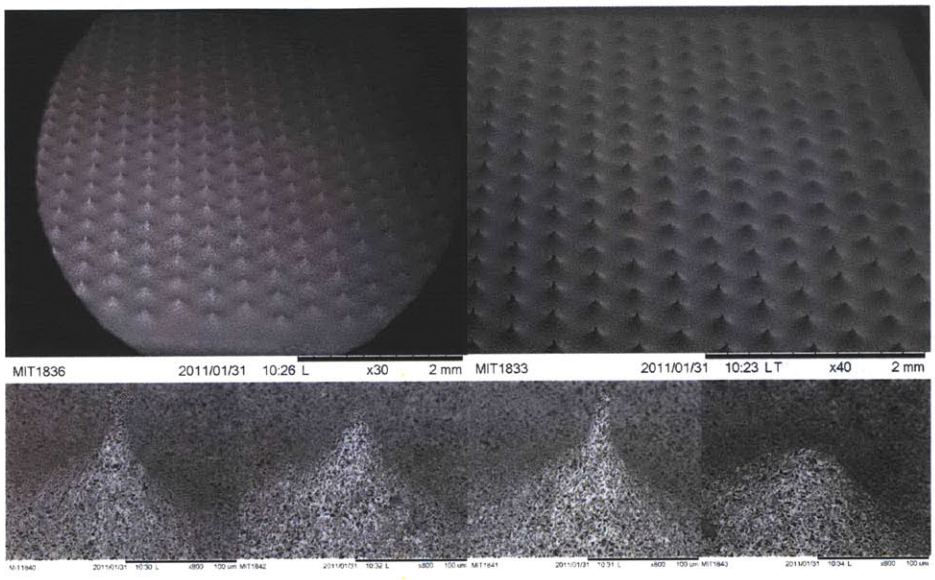

Figure 7-26: SEM images of the array tested here. This array included a large swath of over etched structures localized to one side of the array, a portion of this region can be seen in the upper right corner.

current generally decreased as time progressed, as shown in Fig. 7-28(b) where subsequent scans of the collected current (every 10 seconds) are plotted after smoothing each curve with a 10 point moving average.

These tests were halted before any short was detected. The setup was then disassembled and examined visually and using the SEM. Evidence of interception was clearly visible on the extractor grid and some discolouration was observed on the emitter array, Figure 7-29. The discolouration and grid damage were both localized to the region of sharp emitters suggesting that, as expected, the large number of over etched structures, shown in Fig. 7-26 may not have been active during emission.

Inspection within the SEM revealed that, unlike Fig. 7-24, although residue was present it was concentrated in regions between the emitters rather than around the emitters themselves. An important distinction, to be discussed in the context of electrochemical reactions in section 7.7.8, was that this array was primarily operated in the positive mode only. Although some alternating potential scans, as shown in Fig. 7-27 were performed, they occurred at relatively low potentials, and hence currents, and only exceeded 10 μA of ap-

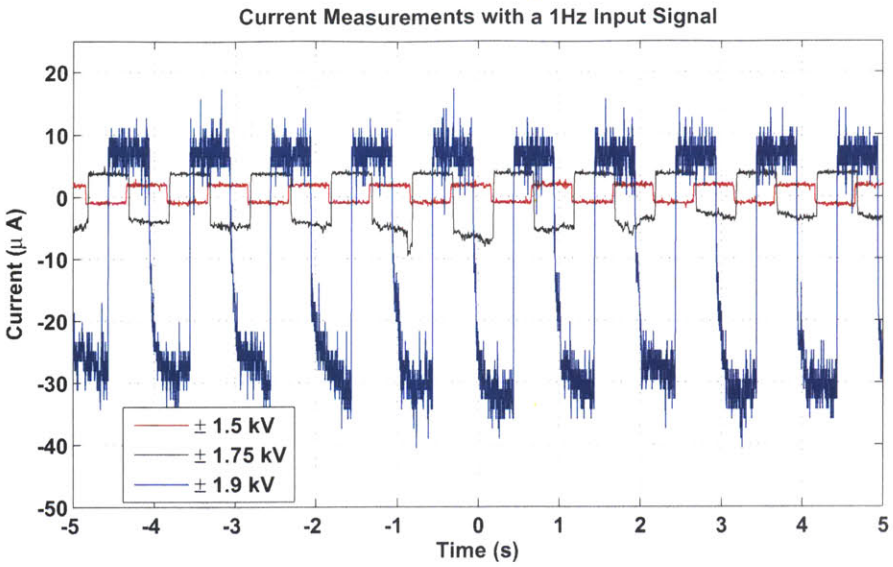

Figure 7-27: Preliminary testing while alternating the potential polarity at 1 Hz revealed strong, unsteady, emission at negative polarities.

parent negative emission for roughly 1 minute. As mentioned above, the actual device current in the negative mode may have differed from these measurements due to hardware malfunctions.

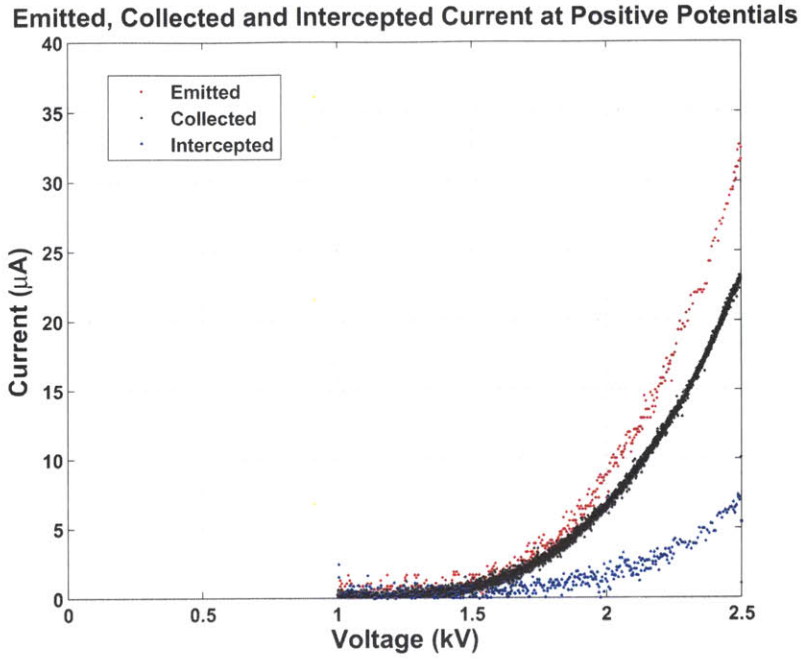

(a) Samples of the emitted, collected and intercepted currents measured with this device. The collector current was typically 70 % of the emitted current.

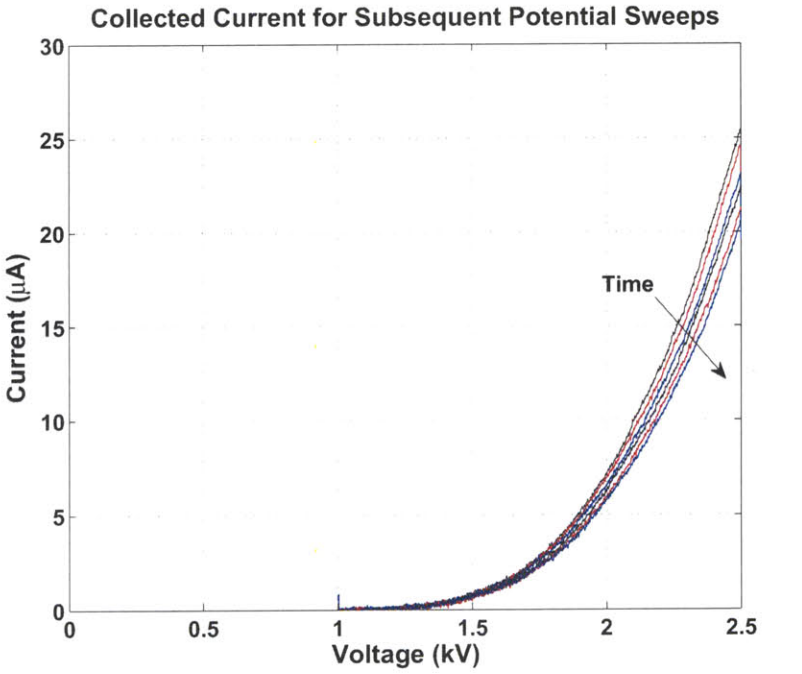

(b) The collected current was observed to decay over time. Here the data have been smoothed with a 10 point moving average to highlight the decay.

Figure 7-28: Sample data acquired with from an array without secondary etching and configured as in Fig. 7-25(a).

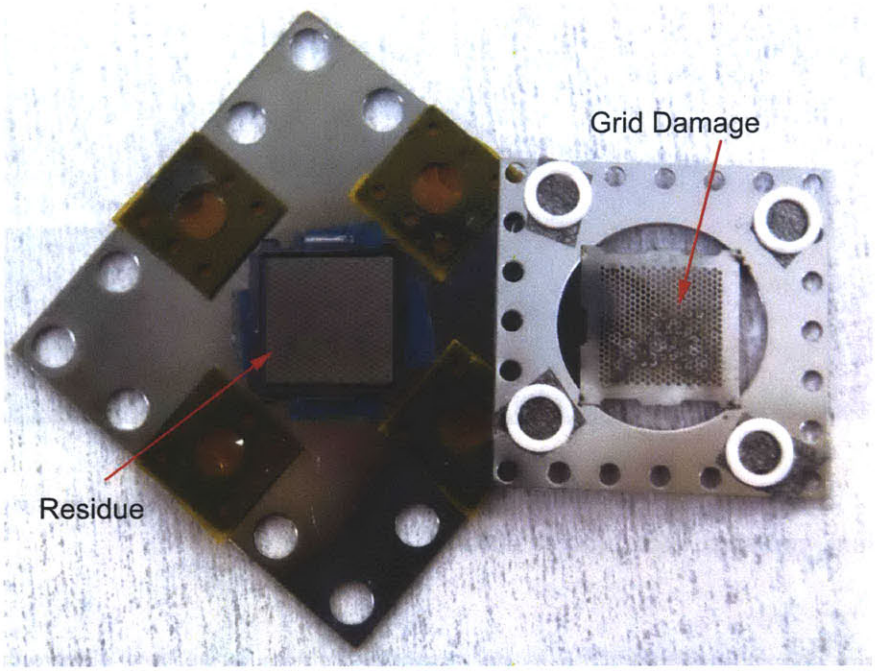

Figure 7-29: Photograph of the assembly after testing. Both the array and extractor grid were discolored in the vicinity of the relatively sharp emitters.

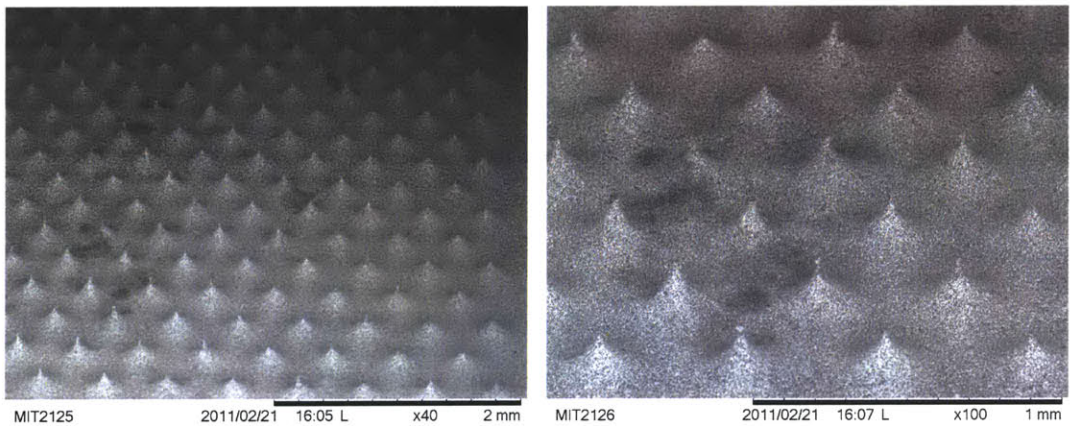

(a) SEM image at 40x

(b) SEM image at 100x

Figure 7-30: SEM image of the array tested in this section showing deposits largely between, rather than on, the emitters.

7.5.2 Sample Array 2 :

A Complete Porous Emitter Array with EMI-Im Propellant

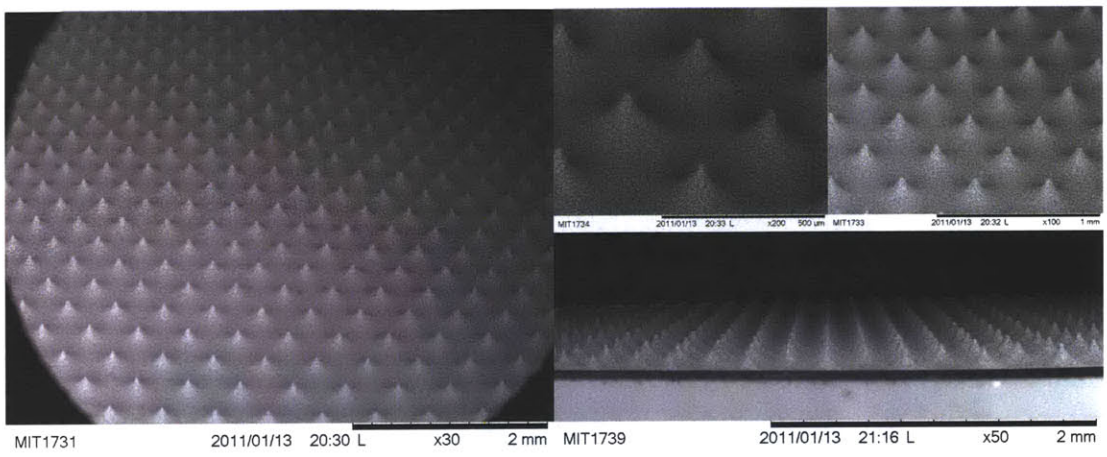

Figure 7-31: SEM images of the array tested here using EMI-Im. This array was fabricated using the final, two-step, etch process outlined in chapter 6.

The array shown in section 6.5 as an example for the secondary electrochemical etch using doped electrolytes was then mounted into the identical (including grid) structure as in the previous section. Figure 7-31 shows SEM images of this array before operation. The average tip to grid distance was measured, using an optical microscope, to be 120 μm with a large deviation of up to 25 μm between the edges and center the grid primarily due to the imperfectly flattened metal grid. This array was tested on two occasions without disassembly between test sessions. The sample was wetted with EMI-Im in the same manner as above and tested for emission. Subsequently the assembly was cleaned out (see below), more liquid added and tested again. The two test sessions are discussed in turn.

Test Session 1

Due to the apparent issues with negative emission found above, measurements from this array were first made at a single polarity (starting with positive) before proceeding to AC testing. In the context of electrochemical concerns the chronology of testing may play an important role and so the results will be presented in the order they were measured. At the beginning of this test the vacuum level was 7.4 x 10^{-6} Torr and continued to decrease throughout.

First a positive potential to the emitter was applied using a 0.75 to 1.5 kV ramp, in the

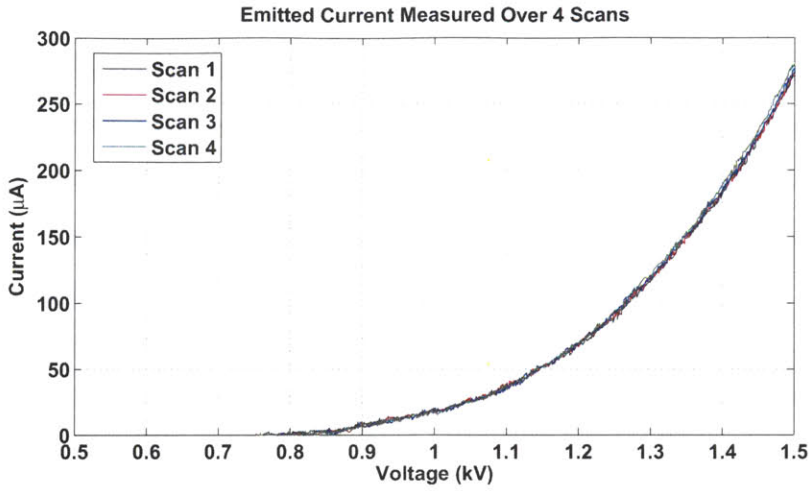

(a) Measured emitted currents at positive potentials over 4 consecutive scans.

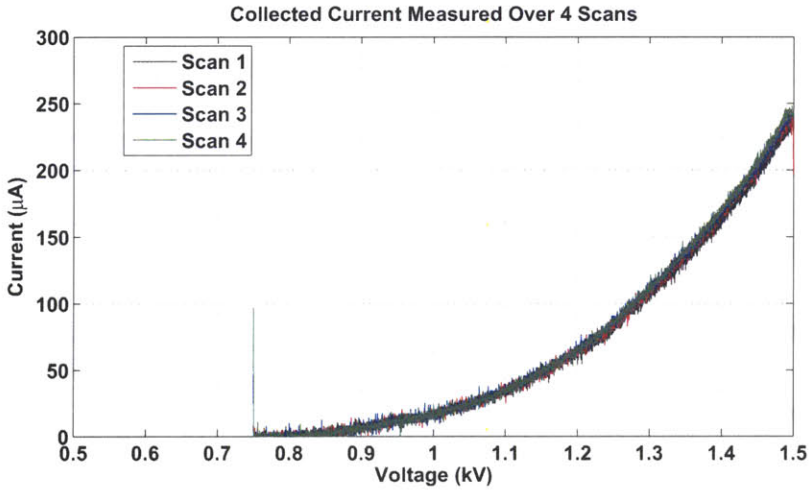

(b) Measured collected currents at positive potentials over 4 consecutive scans.

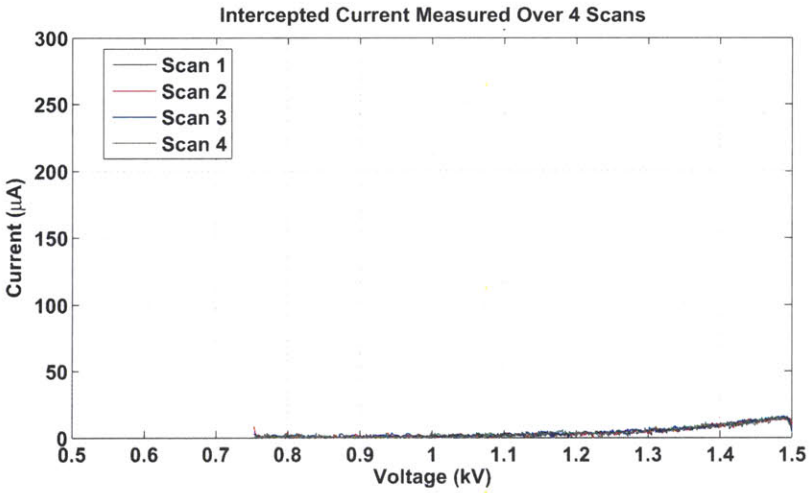

(c) Measured intercepted (at the grid) currents at positive potentials over 4 consecutive scans.

Figure 7-32: Positive emission data from test session 1.

same manner as in the previous section, with a 10 second period. Four scans were made in total. No spurious spikes on the measurement equipment were observed during these tests. The emitted and intercepted currents were measured with the same resistors and ScopeMeter as in the previous section. The measured emitted, collected and intercepted currents over four subsequent scans are plotted in Figure 7-32 without any smoothing. It should be noted that the measurement noise was influenced greatly by the high voltage supply. Specifically, if any common ground other than the primary ground point was established between the data logging oscilloscope and the high voltage supplies, the noise increased. Thus achieving no noise came with the tradeoff of removing the high voltage monitor signal meaning synchronizing the applied voltage and collected current had to be done manually. This has resulted in slight errors during the time to potential conversion, as can be observed on the the raw data (eg. the large current spike at 0.75 kV in Fig. 7-32(b)).

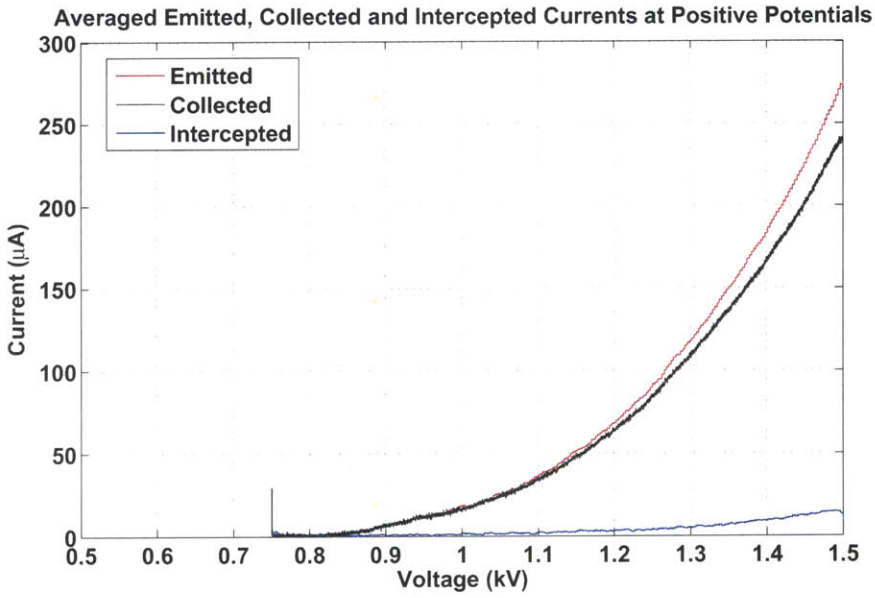

Figure 7-33: Smoothed emitted, collected and intercepted currents at positive potentials.

Given that the variations between scans were small (compared with the measurement noise), the data have been combined and smoothed with a 10 point moving average in Figure 7-33. The collected current was typically between 88 and 95 % of the emitted current with the majority of uncollected current observed at the extractor.

Similar scans were then performed at negative polarities. Here the potential was linearly swept from 0 to -1.25 kV over 10 second periods. All measurements (emitted, collected and

intercepted) contained high amplitude instabilities as the potential exceeded roughly -1.09 kV. The data are presented in Figures 7-34. Omitting these transients, the fractional collected current decreased from greater than 80 % at low voltages to (approximately) less than 70 % within the unstable region.

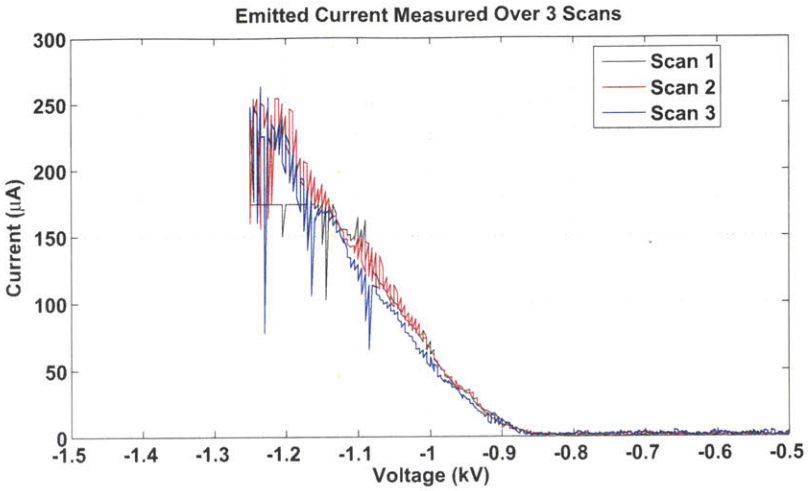

(a) Measured emitted currents at negative potentials over 4 consecutive scans.

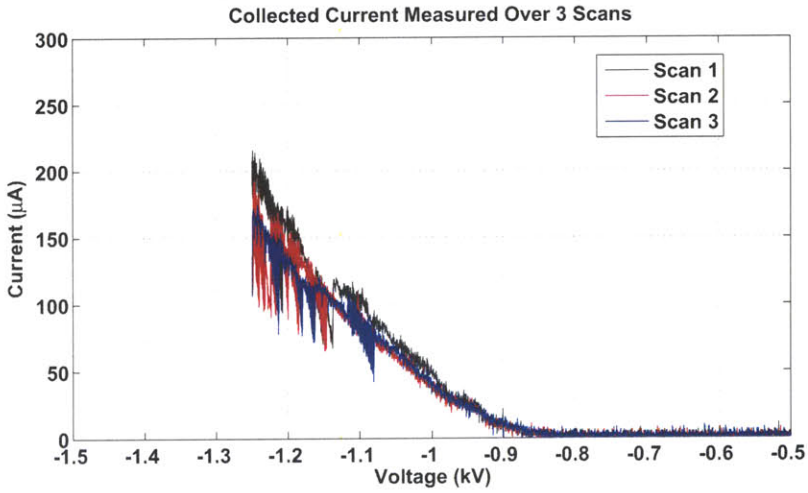

(b) Measured collected currents at negative potentials over 4 consecutive scans.

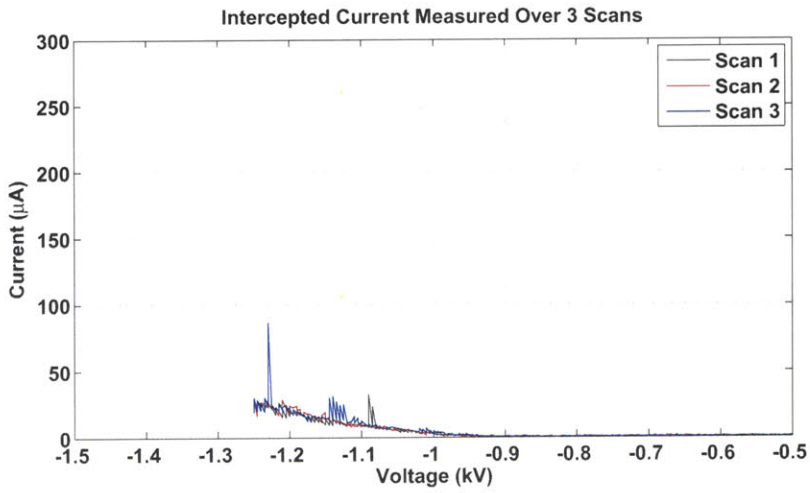

(c) Measured intercepted (at the grid) currents at negative potentials over 4 consecutive scans.

Figure 7-34: Negative emission data from test session 1.

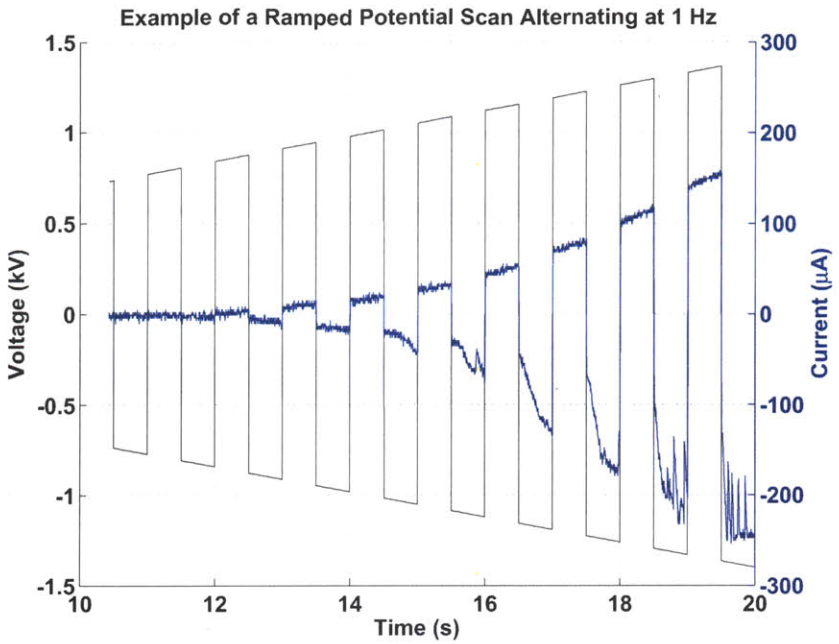

Figure 7-35: Example of the current collected while ramping the potential magnitude from 0 to 1.4 kV over a 20 second period and operating with an alternating polarity of 1 Hz.

The behavior under polarity alternation was then considered beginning with several scans using a ramped voltage magnitude with the polarity alternating at 1 Hz. Examples of the collected current and the applied potential as a function of time are given in Figure 7-35. During these tests the collected current was observed to begin decaying significantly with each subsequent measurement. In order to study this decay, the potential was set at $\pm$ 1.5 kV while the collected current was monitored over a period of roughly 17 minutes. The current, plotted in the upper two portions of Figure 7-36 quickly decayed over the first few minutes before setting into a more gradual decline. Note the change in scale between the upper and two lower figures. The device was operated continuously between scans 1 and 2 with only a few seconds lost restarting the data logging between the plots shown. After the second scan, the device was turned off for a period of 10 minutes and restarted under the same conditions. Another 8.5 minute run, the lower plot in the figure, was then performed but no significant deviations were observed and current continued to slowly decrease.

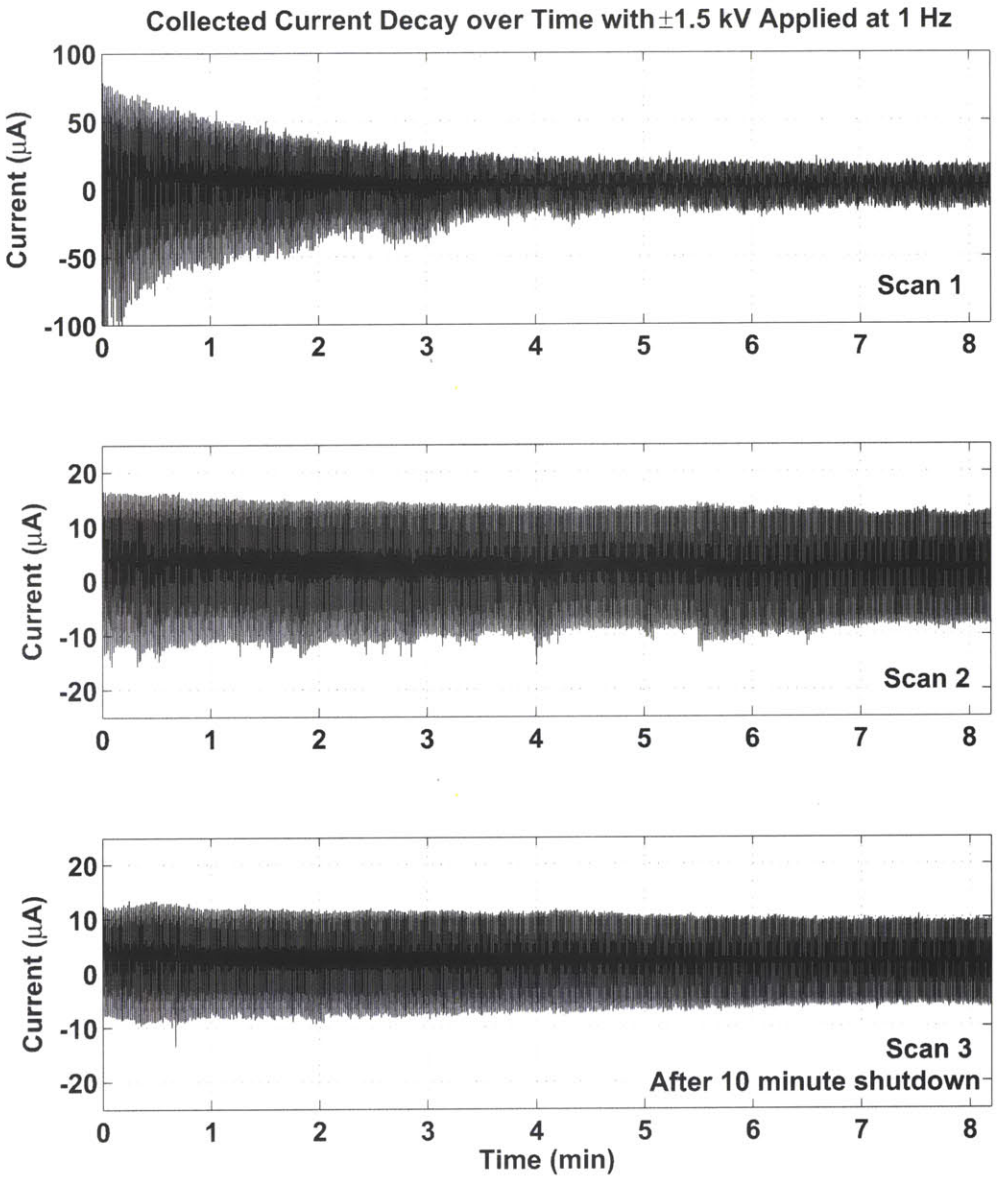

Figure 7-36: Measured current variation in time with $\pm$ 1.5 kV of applied potential alternating at 1 Hz.

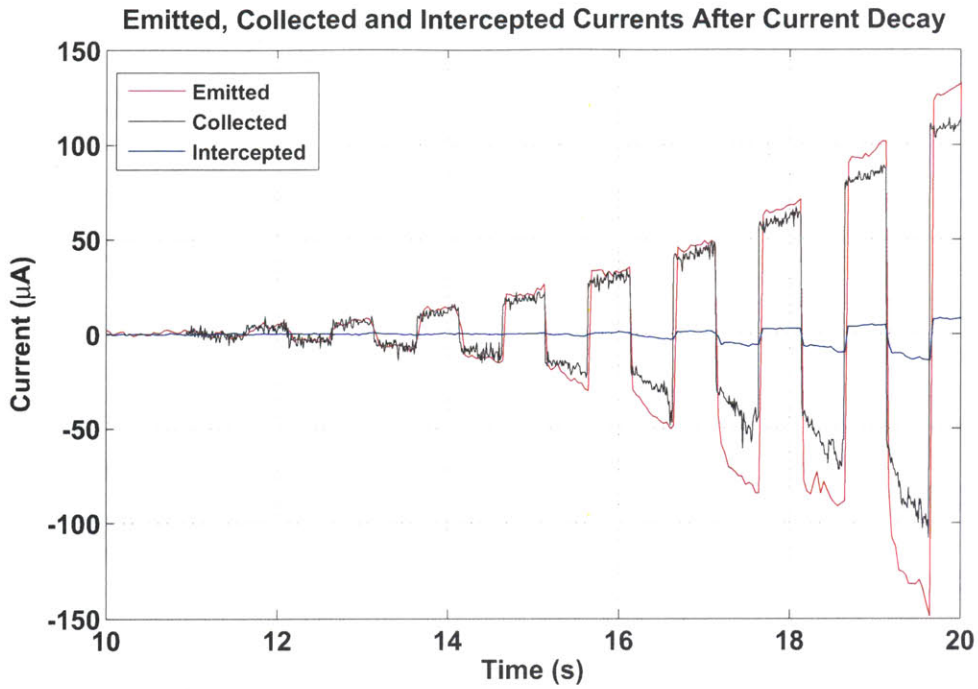

Figure 7-37: Emitted, collected and intercepted currents measured after the (relatively) long duration tests shown in Figure 7-36.

Immediately after these relatively long duration scans another potential magnitude sweep (with polarity alternation at 1 Hz), similar to that shown in Fig. 7-35 was performed. Here the potential magnitude was ramped from 0 up to 2 kV over a 20 second period. Figure 7-37 demonstrates that despite the observed decay, high currents and low interception fractions could still be achieved. However, as shown in Fig. 7-38, where the collected current of Figures 7-35 and 7-37 have been plotted as function of potential, much higher potentials were required to achieve the same currents observed before the decay.

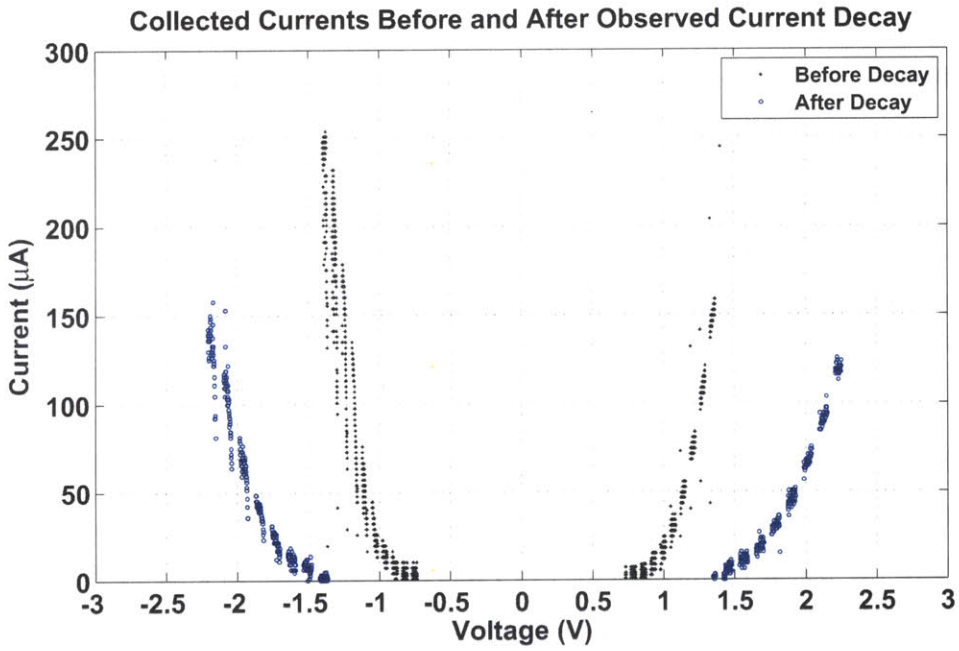

Figure 7-38: Collected current measured while alternating the emitter potential at 1 Hz and ramping the magnitude over a 20 s period before and after the, relatively, long duration testing of Fig. 7-36

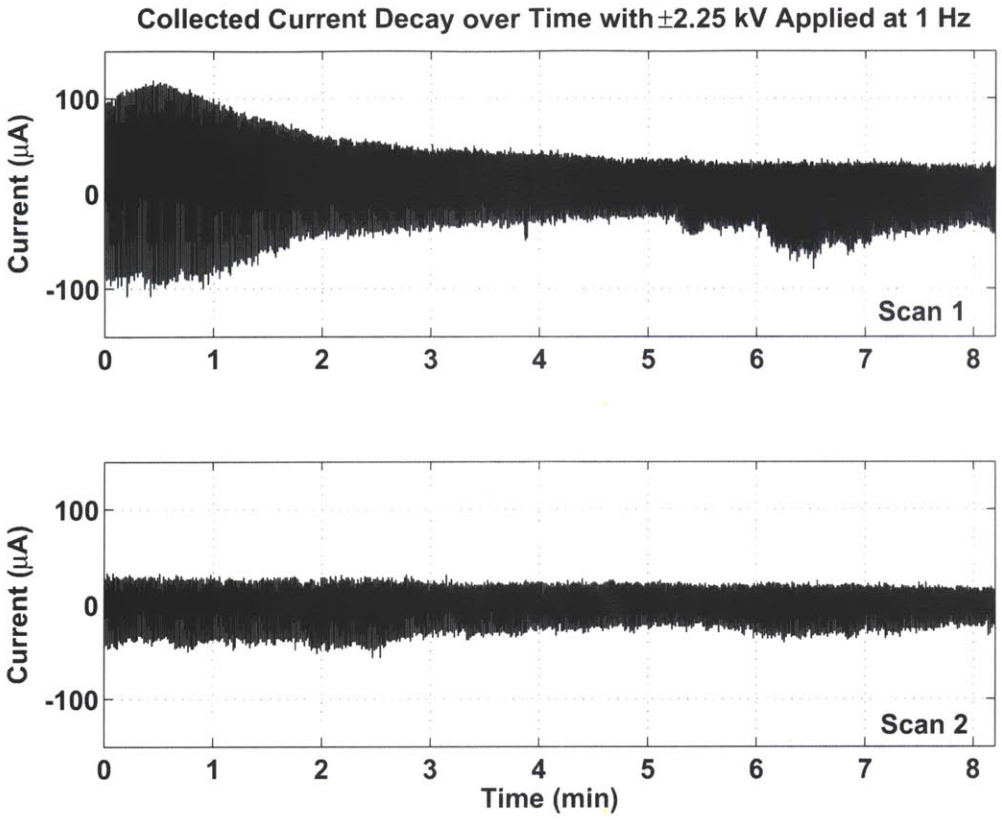

Figure 7-39: Observed current decay while alternating the polarity at 1 Hz with a 2.25 kV magnitude.

The time dependant behavior was then observed again, with the potential set to alternate again at 1 Hz but with $\pm$ 2.25 kV applied. These data are shown in Figure 7-39. Although the output initially rose, it soon decayed again after just over 1 minute. The decay continued over two consecutive scans totalling just under 17 minutes, at which point the average current had dropped by nearly an order of magnitude.

Test Session 2

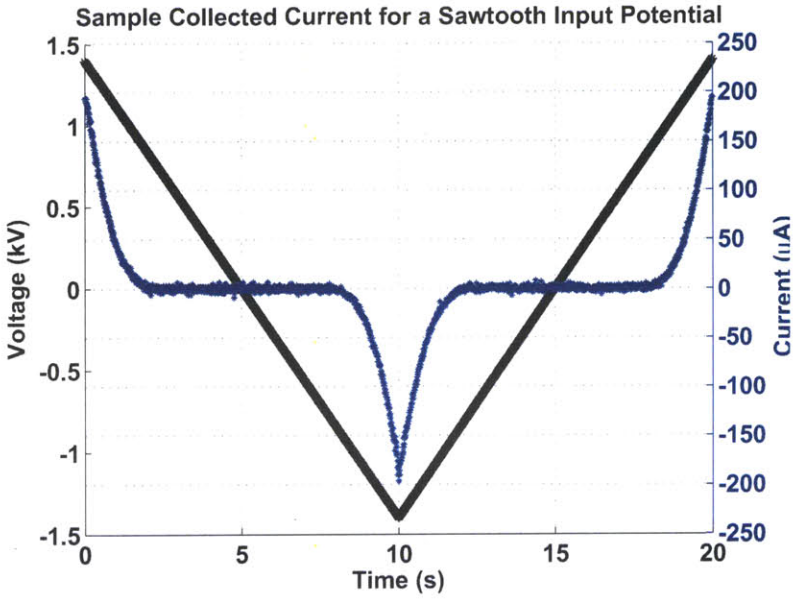

Figure 7-40: Input voltage and collected currents using a sawtooth wave from -1.4 to +1.4 kV over a 20 s period.

After firing and imaging the array, more ionic liquid was added in an effort to establish wether liquid depletion could have had an impact on the current decay over time. However; after exposure to vacuum at this stage an electrical short was detected and liquid appeared to have violently vacated the porous array. Without disassembling the source, filter paper was used to wick away excess liquid bridging between the extractor grid and the array. While EMI-Im is normally clear, the liquid removed in this manner was bright yellow in color. As much excess liquid as possible was removed in this manner, including from the rear feeding port. It was unclear to what degree the porous nickel was saturated at this point but, with the electrical short removed the device was loaded back into the test configuration and operated again.

At the beginning of these tests significant perturbations to the observed signals were present depending on wether the ScopeMeter was connected. It was therefore removed for the majority of tests leaving only the collected current measurements, but at greatly reduced noise levels, particulary in the negative operating polarity. Ramped measurements were then made using a sawtooth input to the potential. Figure 7-40 presents an example of the input signal and the unprocessed data collected in this manner.

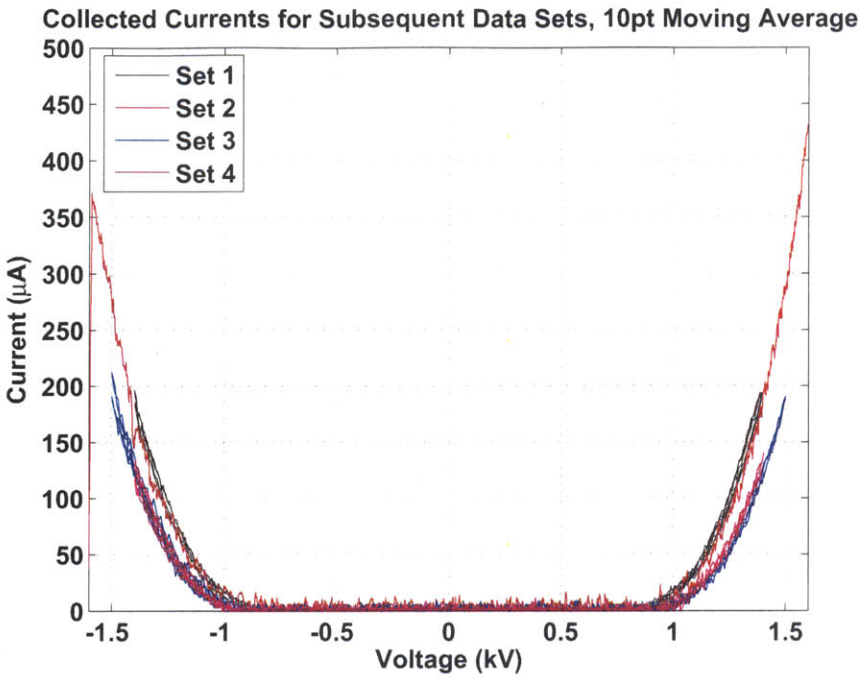

Figure 7-41: Magnitude of collected currents collected over subsequent data sets. After reaching peak emission in excess of 350 and 400 μA in the negative and positive modes respectively, the emission began to decay.

Figure 7-41 presents a set of subsequent scans acquired in this manner. In the plot each scan has been smoothed with a 10 point moving average to assist in highlighting the shift between sets 1-2 and sets 3-4. With the input potential set to reach $\pm$ 1.6 kV the collected current exceeded 350 and 400 μA in the negative and positive modes respectively. However; after acquiring these data, subsequent scans yielded lower currents at a given potential, or equivalently a shift higher potentials to maintain the same current.

After observing this shift the data shown in Figure 7-42 was collected during two subsequent scans with the ScopeMeter connected to the emitter line only. While these measurements demonstrated that transmission fractions comparable to those measured during the first test session, Figures 7-33 and 7-34, were maintained they also signalled the current was beginning to rapidly decay. The device was then shut down with the intention of acquiring beam spectroscopy using the time of flight apparatus. However; hardware problems with the time of flight apparatus prevented these measurements.

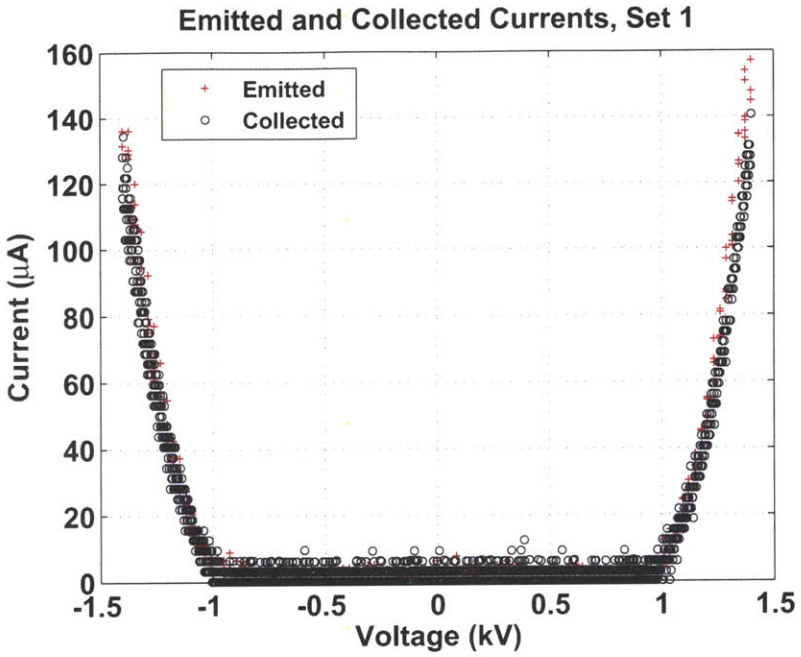

(a) Magnitudes of the emitted and collected currents.

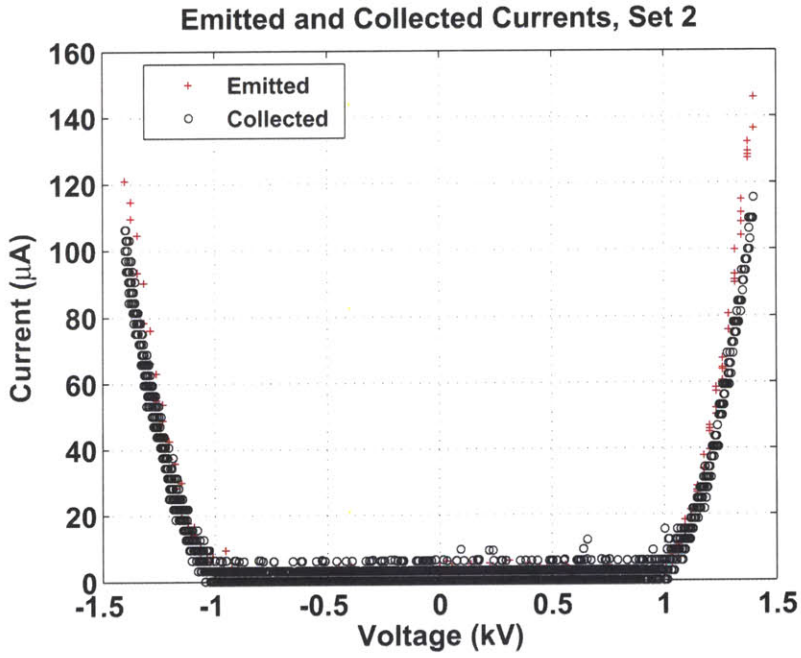

(b) Magnitudes of the emitted and collected currents measured immediately after the data plotted above.

Figure 7-42: Emitted and collected current during the second test run of this sample. The emission had begun to decay rapidly leading to difficulties synchronizing the Keithley and ScopeMeter measurements.

Comparing Test Sessions

The change in collected current between the two test session can be seen in Figure 7-43. The curves show data collected before any significant current decay had occurred. After removing the ScopeMeter, more stable current was collected in the negative operating mode, Figure 7-43(a). However; the curve has shifted to higher potential. In the positive mode, Figure 7-43(b), the onset potential and current magnitudes are comparable at low currents but begin to diverge with higher emission. Recall that between these test sessions the current decayed significantly during (relatively) long duration tests. The sample was cleared of a yellow colored liquid and more liquid was added. The reasonable agreement in Fig. 7-43(b) suggests that liquid contamination, rather than damage to the nickel surfaces may have been a primary cause for the observed decay. However; between these two tests the state of the propellant within the pores may be one of the greatest uncertainties contributing to the observed performance. A more sophisticated method for filling the arrays may assist in this regard.

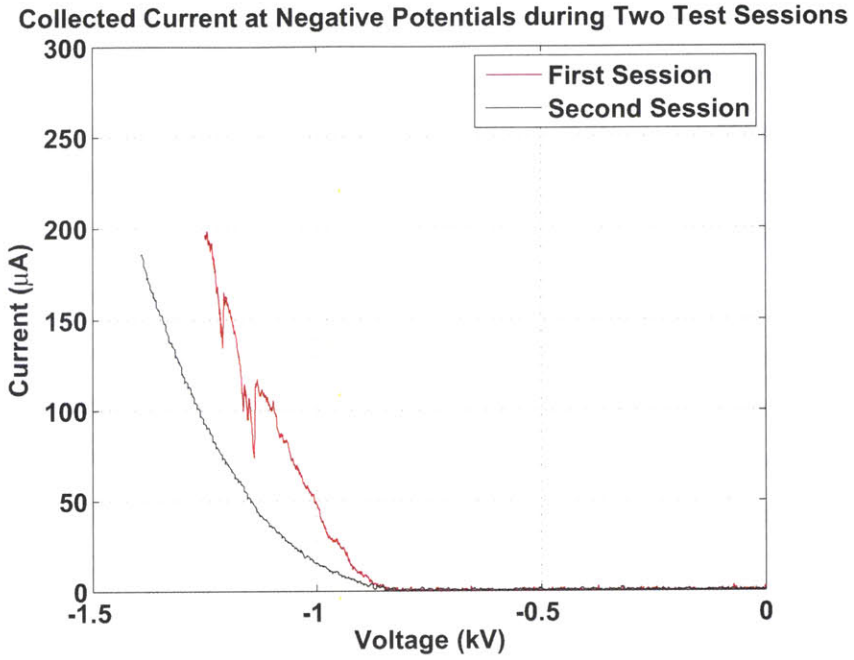

(a) Magnitude of collected currents at negative emitter potentials demonstrating a clear shift between test sessions.

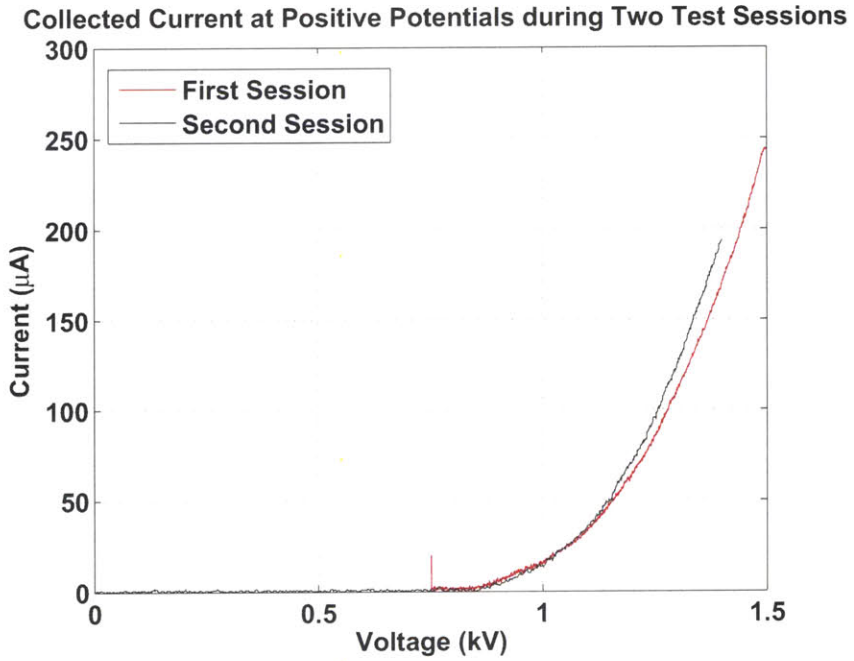

(b) Magnitude of collected currents at positive emitter potentials. Compared with the adjacent negative emission, these data are in better agreement.

Figure 7-43: Magnitude of the collected currents during both test sessions.

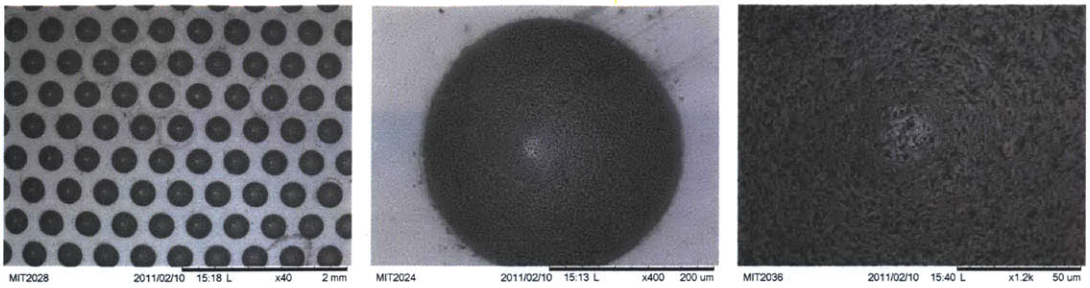

(a) Extractor grid after the first test session.

(b) A typical emitter and grid orifice after the first test session.

(c) Enhanced view of a typical emitter after the first test session showing no signs of residue.

Figure 7-44: SEM images of an array fired with EMI-Im between two test sessions.

Physical Observations after Testing an Array Emitting EMI-Im

After each test session described above, the array was imaged both photographically and using the SEM. Figure 7-44 presents SEM images of the extractor and emitters after the first test session. These images demonstrate that the alignment during this test was not ideal, the emitters were $\sim$ 20-40 μm from the center for the extractor orifices. Recall that this array was operated at 1 Hz for roughly 25 minutes, re-characterized and operated for another 16 minutes. However; no obvious residue could be seen on the emitters after this test.

After the second test session both the emitters and extractor grid appeared to be coated with residues when viewed with the SEM. In Figure 7-45 the dark, coated, emitters can be seen through the extractor in the upper left of the figure. With the extractor removed, the residues on the emitter array were observed to be concentrated around the emitter tips. Along one region, shown at low zoom in the upper left of the figure and enhanced zoom below, significantly more material was observed and appeared to bridge between emitters at some locations.

Photographs of the array, Figure 7-46(a), show the complete package after both test sessions. This package was not cleaned or altered between either these sessions or those presented in the previous section for a single etch step array. The material deposited on the source varied between a light blue to yellow color. This may have been caused by backsputtered material from the collector plate. The collector plates for sessions 1 and 2 are shown in Figures 7-46(b) and 7-46(c) respectively. New collector plates were used for each test. After the first session the emission caused a relatively dense, dark yellow buildup

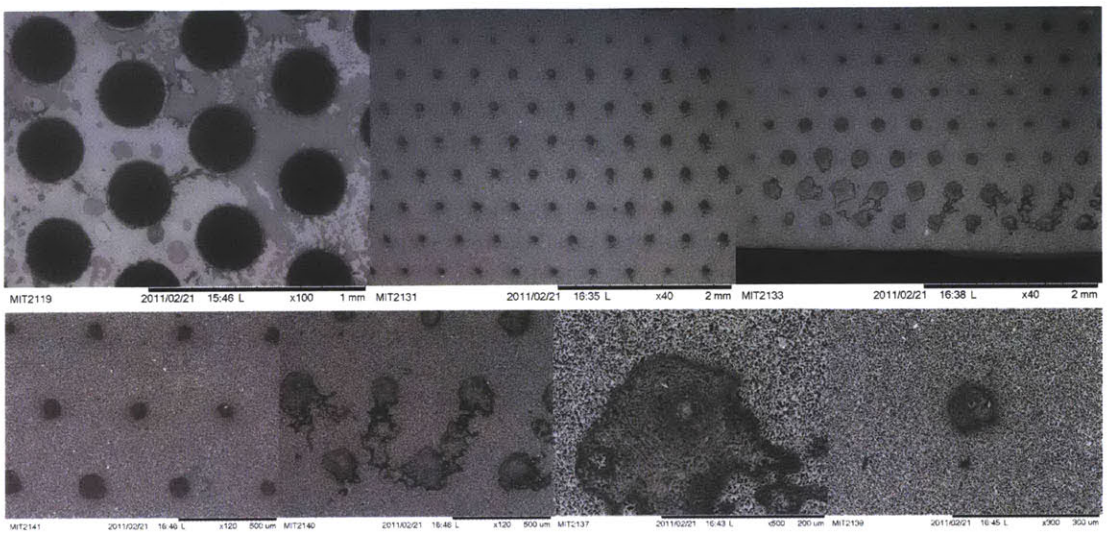

Figure 7-45: After a second test set, without relatively long term operation significant deposits were evident on the emitters. These were mostly concetrated near the emitter tip. The metal grid (upper left), showed evidence of a thin, uneven coating.

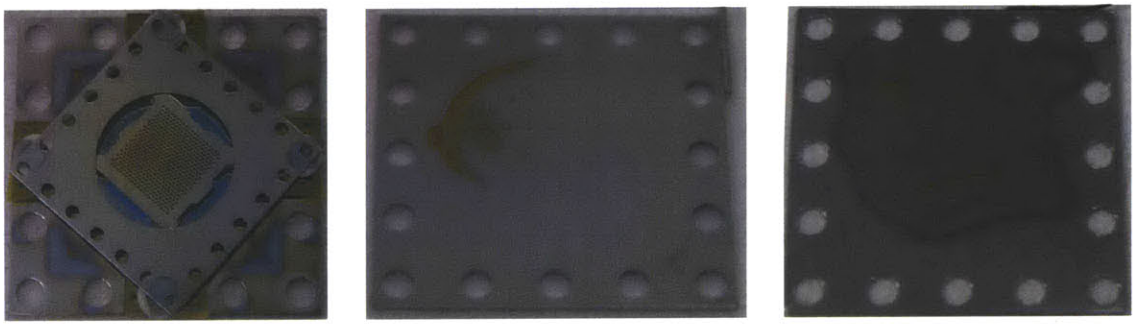

(a) Photograph of the source after both test sessions.

(b) Photograph of the collector plate used during the first test session.

(c) Photograph of the collector plate used during the second test session.

Figure 7-46: Photographs of the source and collector plates after two test sessions with an EMI-Im wetted array.

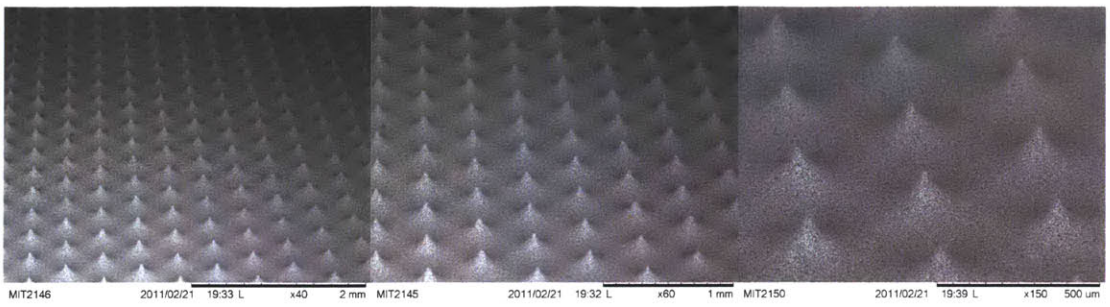

Figure 7-47: The array was tested with EMI-Im was removed from the source mount and cleaned using the solvent clean procedure described in section 6.2.2, the residues appears to have been removed.

in the upper left corner of the plate along with faint circular patterns around each of the corner support holes where mount spacers masked the plate. After the second test session, the new collector plate was again coated in a similar but more conformal material as can be seen in Fig. 7-46(c). As discussed at the end of this chapter, these observations suggest that, to some degree, the arrays may have been emitting charged droplets in lieu of, or in addition to, ions.

The array was cleaned using the solvent procedure outlined in section 6.2.2 after these tests. No lasting damage is visible in Figure 7-47 despite the significant deposits shown in Figure 7-45. No additional data was collected using this array after cleaning.

7.5.3 Sample Array 3 :

A Complete Porous Emitter Array with EMI-BF_4 Propellant

The second test of a fully processed nickel emitter array used EMI-BF_4 as propellant. Here the array shown in Figure 7-48 was mounted and aligned in the manner described in the previous section, however a new laser cut grid was used compared with the tests above. The average emitter to extractor distance was measured using an optical microscope to be 140 $\mu m \pm 25$ μm. The array was filled with EMI-BF_4 in the same manner as the tests above, however during this test the filling mass was measured to be 45.1 mg of propellant. Note that the EMI-BF_4, which is known to adsorb water vapor, was outgassed within the vacuum chamber just prior to filling the array. This array was again tested during two data sessions, however; unlike the EMI-Im case above the decision to break into two sets was caused by a physical short, presumably similar to those shown in Figure 7-18, and not a decay in current.

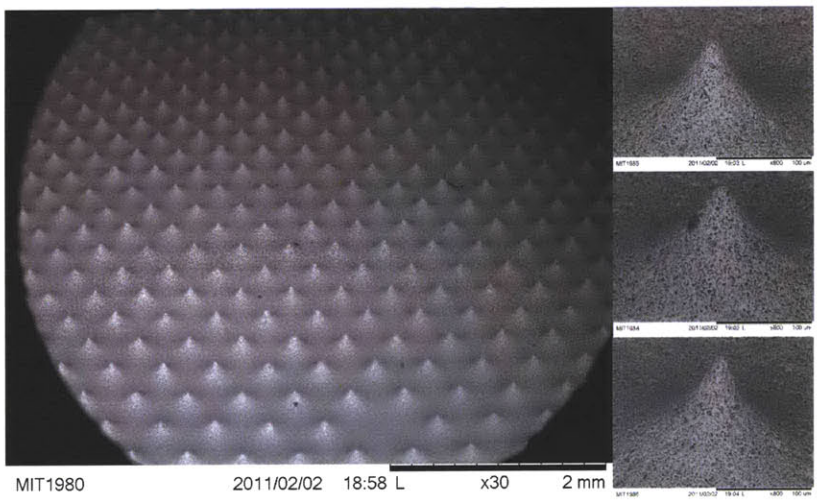

Figure 7-48: SEM images of the array used to test emission using EMI-BF_4. This was not the same array used with EMI-Im but was fabricated using the identical, complete, fabrication process.

Test Session 1 : IV Measurements

The initial pressure at the beginning of these tests was 6.5 x 10^{-6} Torr. As in the EMI-Im tests of the previous section, the ScopeMeter was detached from the setup throughout the majority of tests to reduce measurement errors. A sawtooth input was then used to drive

the emitting potential while observing the collected current. These scans were made over a 20 second period with symmetric peak voltages. In Figure 7-49 a sequence of tests has been plotted with increasing peak emitter voltages. In each curve a moving average over the number of consecutive scans at each condition (1 to 3) has been performed. As with the tests above, the array demonstrated strong currents could be achieved at relatively low extracting potentials. The emission current was held to the levels shown in an effort to prevent any current dependent decays occurring prior to the potential alternation testing below.

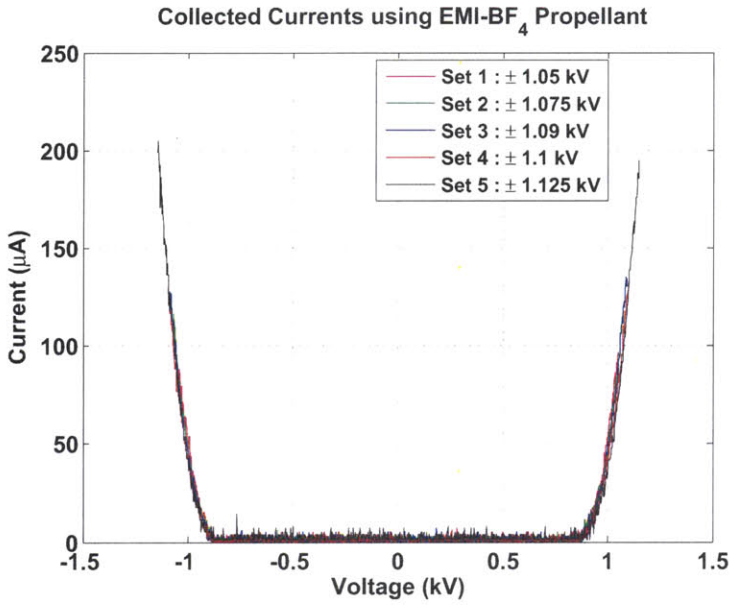

Figure 7-49: Magnitudes of the collected current measured using an array wetted with EMI-BF_4 over 5 scans. The applied potential was held low to minimize the net emission in advance of, relatively, long duration AC testing.

The ScopeMeter was then connected to the emitter array for three scans from -1.05 to 1.05 kV to measure the emitted and collected currents simultaneously. In Figure 7-50 the three scans have been combined and the currents averaged using a three point moving average. The emission was held to levels even lower than in Fig. 7-49 in an effort to prevent spurious measurements due to the ScopeMeter. The emitted and collected currents were in good agreement with little deviation visible within the measurement noise. Some brief (10's of seconds) testing at 1 Hz was then initiated with the array but a physical short arose. The device was shut down, removed from vacuum and checked out prior to further testing.

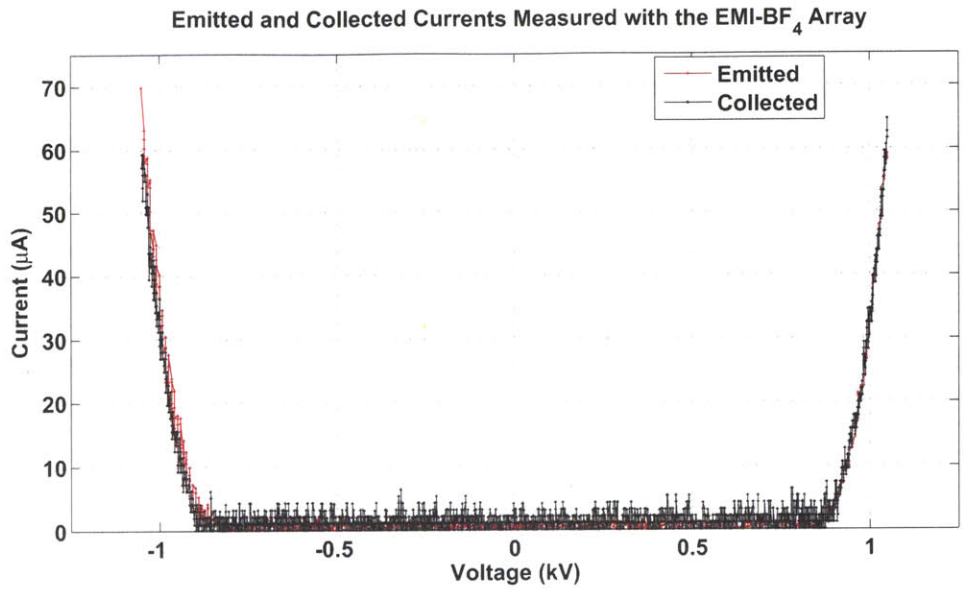

Figure 7-50: Emitted and collected currents using EMI-BF_4. The curves have been smoothed with a 3 point moving average.

Test Session 2 : Operation at Alternating Potentials

The short was removed with a gentle spray of clean nitrogen and the sample was reloaded into the chamber. The collected current behavior over time with alternating potentials applied was then measured. In order to increase accuracy during these long duration tests, the Keithley electrometer output was read by a data acquisition system (the same device used in the etch station described previously) capable of logging data continuously at a higher rate than the Agilent DSO5014A scope over long time periods. This acquisition system had a maximum input voltage of 10 V, and hence required the collector plate be reduced to 8 V in order to maintain full scale accuracy from the Keithley electrometer which outputs a $\pm$ 2 V proportional signal for monitoring the current.

Four consecutive scans have been made with both the alternation frequency and potential magnitudes varied between each scan. The measured currents during these tests are shown in Figure 7-51. In the figure, each test was made in succession with the source briefly turned off in between. During the first scan, Fig. 7-51(a), the polarity was alternated at 1 Hz with a magnitude of 1.11 kV. Although the current decayed slowly the fast decline observed with EMI-Im at 1 Hz, Fig. 7-36, was not observed. After 9 minutes of operation the voltage was increased to $\pm$ 1.14 kV to exceed 100 μA of collected current and the po-

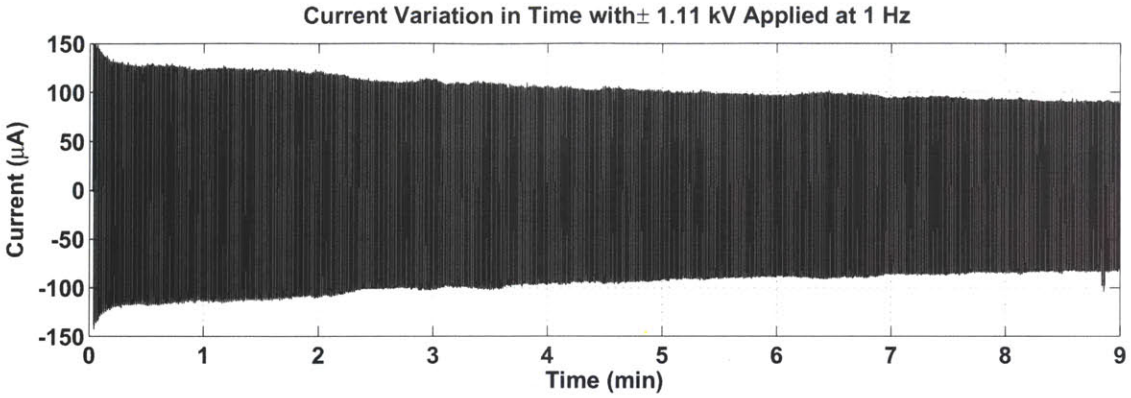

(a) Current evolution in time with a fixed, $\pm$ 1.11 kV at 1 Hz applied to the array.

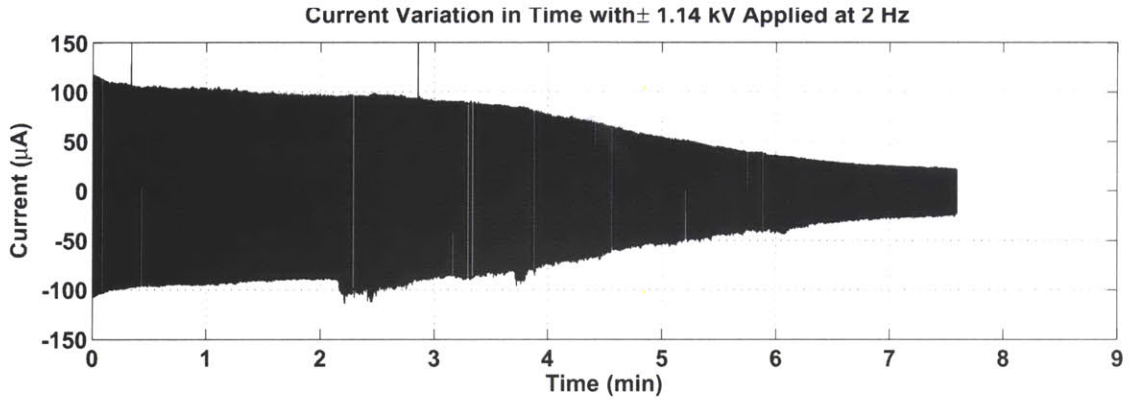

(b) Current evolution in time with a fixed, $\pm$ 1.14 kV at 2 Hz applied to the array.

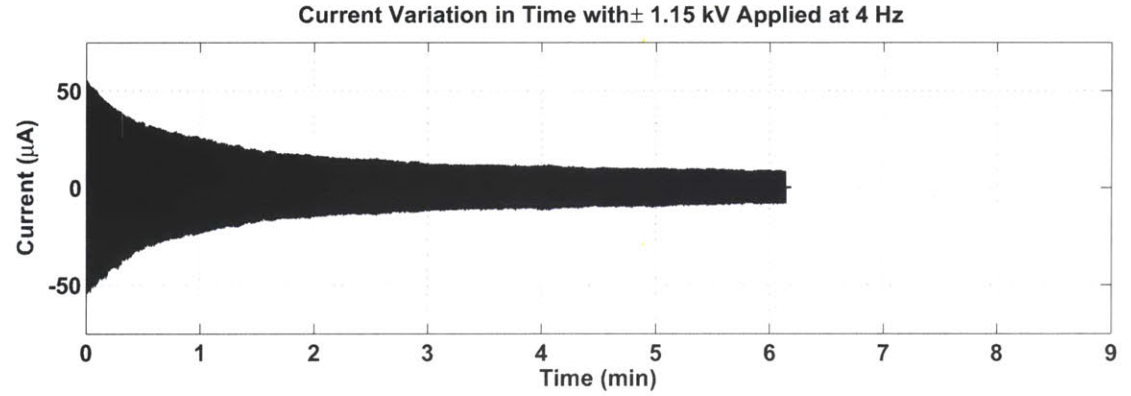

(c) Current evolution in time with a fixed, $\pm$ 1.15 kV at 4 Hz applied to the array.

Figure 7-51: Alternating potential scans made in succession with the device turned off between scans.

larity alternation frequency was increased to 2 Hz. Under these conditions, the collected current decayed slowly before quickly reducing by roughly a factor of 4 after 7.5 minutes. The test was stopped such that more testing could be attempted prior to further decay. The frequency was increased to 4 Hz and the potential increased to $\pm$ 1.15 kV. Here the collected current decayed rapidly over the first few minutes before settling at roughly $\pm$ 10 μA.

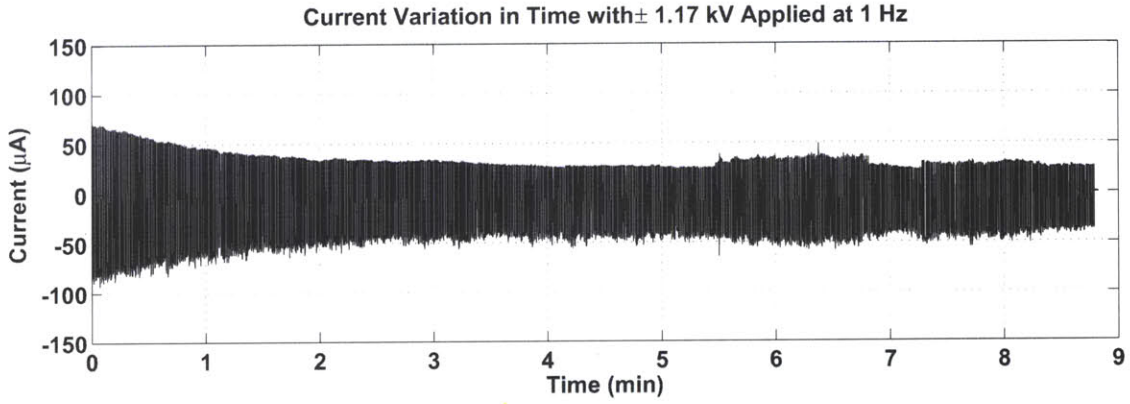

Figure 7-52: Alternating potential measurements made after the initial runs above. The potential was set to $\pm$ 1.17 kV at 1 Hz.

After these scans an additional test at 1 Hz polarity alternation was attempted to determine if the emission observed in Fig. 7-51(a) could be recovered to any degree. At 1 Hz again, significantly higher potentials were required to induce emission at the levels seen previously. Ramping the potential to $\pm$ 1.2 kV resulted in an electrical discharge causing the high voltage amplifiers to shut down. Somewhat stable emission was re-established at $\pm$ 1.17 kV but was generally unstable at negative polarities. Under these conditions a final 8.5 minute set of data was collected, see Figure 7-52. During this scan the collected current was highly non uniform, with more negative than positive currents measured throughout.

As in the EMI-Im test above, the chronology of the tests may have contributed to the results. Specifically, it is unclear to what degree increasing the potential alternation frequency contributed to the current decay in, for example, Fig. 7-51(b). Perturbations to the emitters or liquid leading to the decay may have been induced by the previous measurements and may or may not have any direct correlation to the potential alternation conditions.

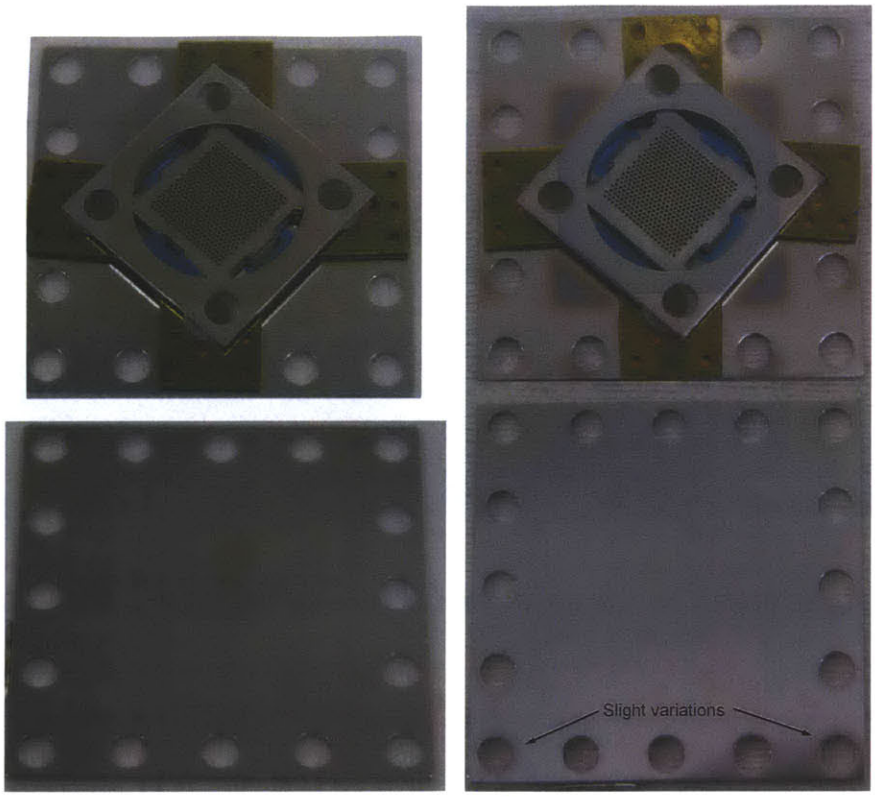

(a) Photographs of the source and collector plate after the initial IV characterization.

(b) Photographs of the source and a new collector plate after longer duration AC testing.

Figure 7-53: Photographs of the array and collector plates after each test set.

Physical Observations after Testing an Array Emitting EMI-BF_4

The array was photographed between the two test sessions and after the final alternating potential tests. Between tests some, presumably, back sputtered material could be seen on the array and support material, Figure 7-53(a) upper. The collector plate, the lower image, was mostly clean with a slight discoloration near the center. After the longer duration AC testing, the source was coated further, the coating had a blue tinge with yellow shadowing at the edges, Figure 7-53(b) upper. In the lower Figure, the collector plate was observed to be very clean. Some minor variations can be see at the corners where the ceramic spacers shielded the beam.

After the final test, the source was imaged using the SEM. Figure 7-54 gives some representative sample images. Similar to what was observed during the second set of EMI-Im testing, the emitters appear to be coated in material. The figure demonstrates examples

of both completely covered emitters and some with the tip exposed. The exact source and composition of this material is unknown but will be discussed further in section 7.7.7.

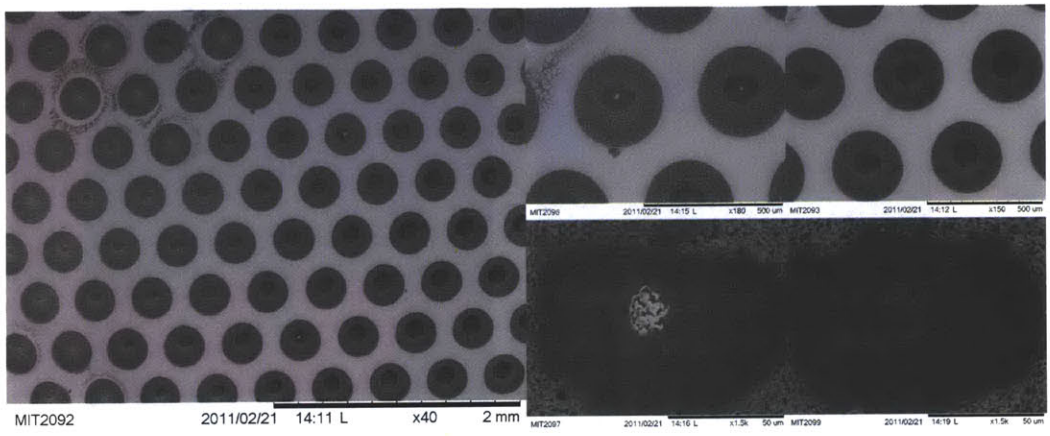

Figure 7-54: SEM images after firing an array wetted with EMI-BF_4.

This array was also cleaned after testing. However; a single run of the solvent clean did not remove all deposits, as shown in Figure 7-55.

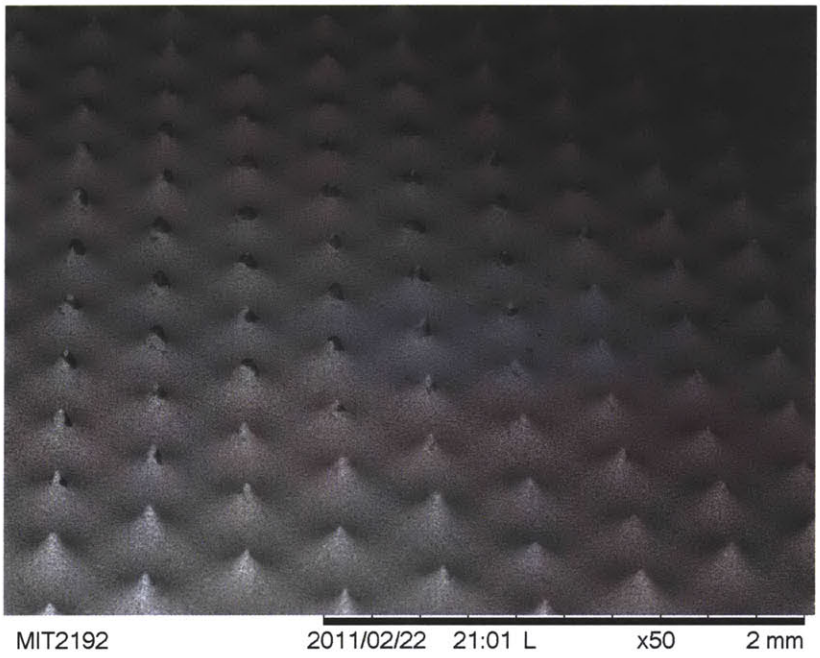

Figure 7-55: The array tested with EMI-BF_4 was removed from the source mount and cleaned using the solvent clean procedure described in section 6.2.2. In this case a region of coated emitters remained at the center of the sample.

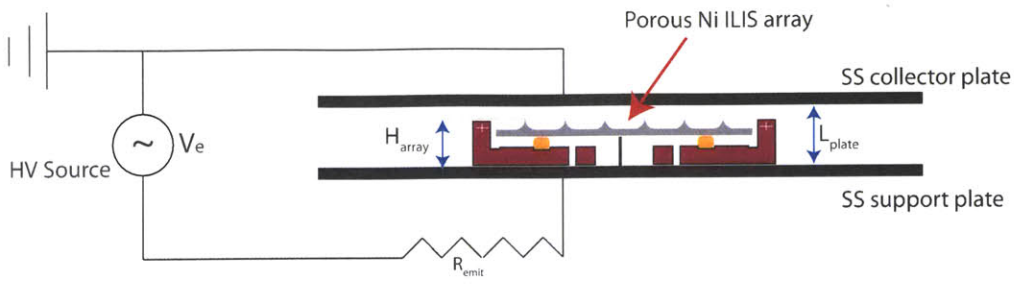

Figure 7-56: Schematic of the setup used to observe patterns induced on a stainless steel collector plate from porous nickel emitter arrays.

7.6 Ablation Testing

Two arrays have been isolated and configured, as in Figure 7-56, to fire against a stainless steel plate positioned just above the array. First an array fabricated using an early iteration of the fabrication process described in Chapter 6 was selected. This array was etched under constant voltage conditions, with no secondary etching, and hence was characteristically non uniform and featured emitters with sharply defined plateaus of varying diameter. Second, an array fabricated using the complete process, using pulsed etching and a secondary etch was tested in the same manner. These simple tests were intended to generate ablation profiles on the stainless steel plate which could provide some qualitative insight into the operating characteristics on a per emitter scale. In particular they were intended to verify if multiple emission sites can form on each porous emitter.

7.6.1 Array of Plateau Type Emitters

This array, shown in Figure 7-57(a) before the test, was configured with the support to collector spacing, L_{plate}, set to 1.91 mm and the support to emitter height, H_{array} was 1.7 $mm \pm 45\ \mu m$. The high degree of inaccuracy was due to the non uniform nature of this array. The corresponding distance from emitters to the collector was therefore 210 $\pm$ 45 μm. The array was wetted, from the rear feeding port, with EMI-BF_4 and operated with $\pm$ 1.6 kV applied at 1 Hz for roughly 40 minutes. The emission current began oscillating between roughly 200 and -150 μA and decayed significantly over the course of the tests. This current measurement was likely significantly influenced by secondary electron emission. These results were previously described at the 2010 Joint Propulsion Conference[61] as

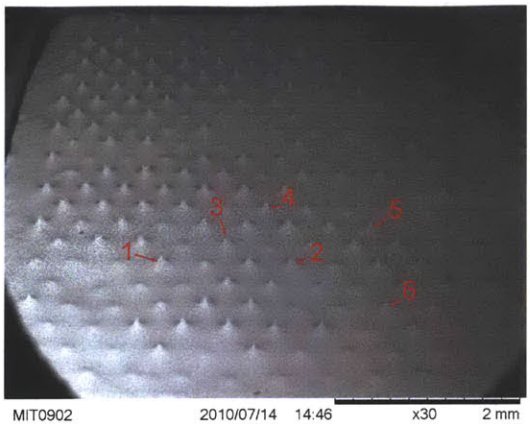

(a) Porous nickel array before ablation testing.

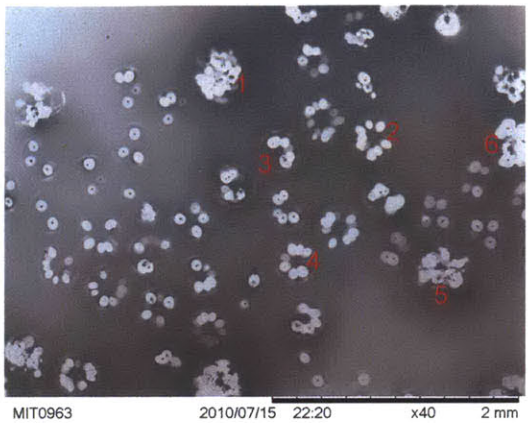

(b) Observed patterns on a stainless steel plate after collected current emitted from the adjacent array.

Figure 7-57: SEM images of an array of emitters etched using a constant voltage process, before firing, and a stainless steel plate after ablation testing with this array.

evidence for emission from porous nickel arrays.

In Figure 7-57(b), selected patterns observed on the stainless steel plate after firing are highlighted for comparison with the labeled emitters in the adjacent figure. The patterns are characterized by small bright circles bounded by larger halos roughly 320 μm in diameter.

7.6.2 Fully Processed Array

The metal to silicon epoxy bond on this array failed after the final cleaning stage but was bonded to the assembly again. Despite the reasonable uniformity and emitter shapes, the lack of alignment with the frame which resulted from bonding it back to the silicon after processing led to it being selected for this test. The sample was loaded as in Fig. 7-56, again with the collector to support plate distance at 1.91 mm. Due to the added epoxy, one region of emitters was raised higher than the others. Specifically, one corner of the array was positioned such that emitters there were roughly 60 μm closer to the collector plate than elsewhere. The plate to tip gap in this region, for a typical emitter, was as low as 50 μm. The array was fired against a plate such that 100 μA of net current was initially achieved while alternating the polarity at 1 Hz. The sample was saturated, from the rear, with EMI-BF_4 (42 mg was added).

After firing, the array and extractor were disassembled and imaged separately while noting the orientation of the ablation pattern. Figure 7-58 highlights two regions on the

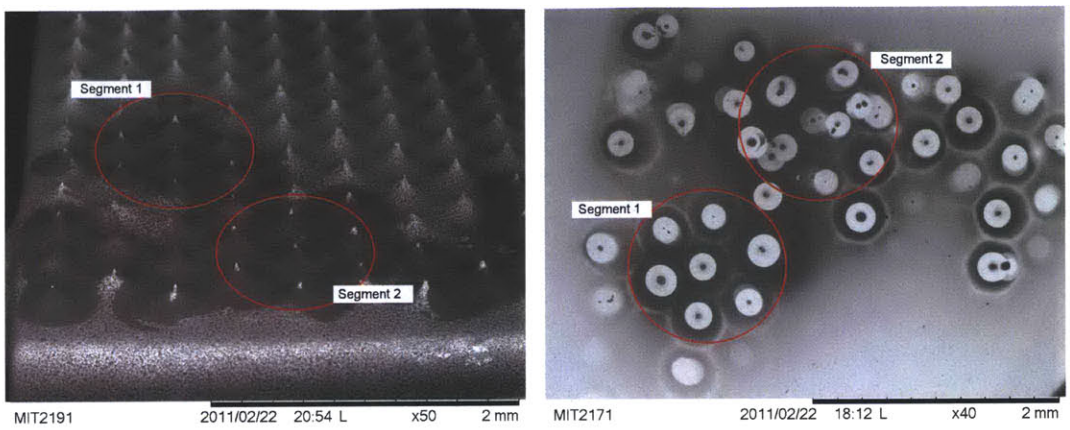

(a) An array of emitters, after firing, showing residue build up around a portion of the emitters. Due to an epoxy failure, this array was not seated flat within its silicon frame.

(b) Patterns observed on a stainless steel collector plate with the highlighted segments corresponding to the emitters in the adjacent figure.

Figure 7-58: SEM images of an array etched using the pulsed etching procedure, after firing, and the collector plate showing patterns from the corresponding segments of emitters.

array and the corresponding markings on the extractor grid positioned above. In segment 1 the emitters are relatively sharp, compared with segment 2 where an assortment of tip radii are present. In all cases, the collector plate shows two distinct types of feature from each emitter. A large, nearly circular, pattern with radius very close to the emitter spacing (450 μm) along with one, or more, bright circles of varying diameter. At the center of each bright circle a darker, possibly protruding, region can often be seen.

The two segments have been isolated and the collector patterns matched with specific emitters. In Figure 7-59, the relatively low tip radii emitters have resulted in mostly one or two bright circular patterns bounded within the larger perimeter pattern. The centers of the bright patterns do not inherently correspond with the centers of the larger circles.

In Figure 7-60, the second segment has been isolated. Here the emitter tips were typically larger than in segment 1. The collector plate patterns again feature larger bounding circles at most points; however, these emitters have typically produced several bright spots within each region. Note that in some cases, tips 1 and 2 for example, the larger bounding circle is much more faint, despite relatively intense bright patterns.

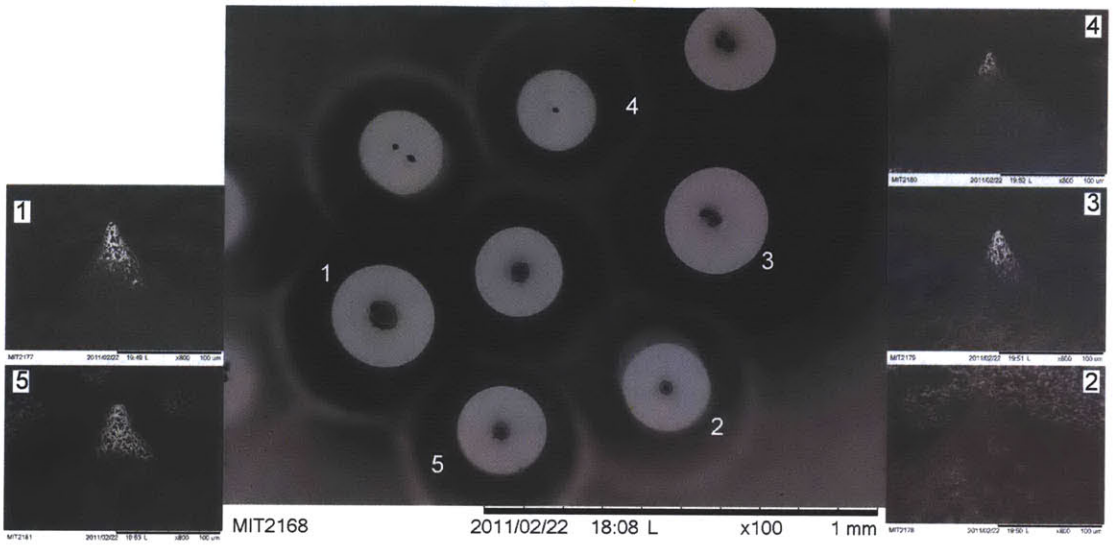

Figure 7-59: Correlations between emitters and observed patterns for relatively low radii emitters, segment 1 in Fig. 7-58(a).

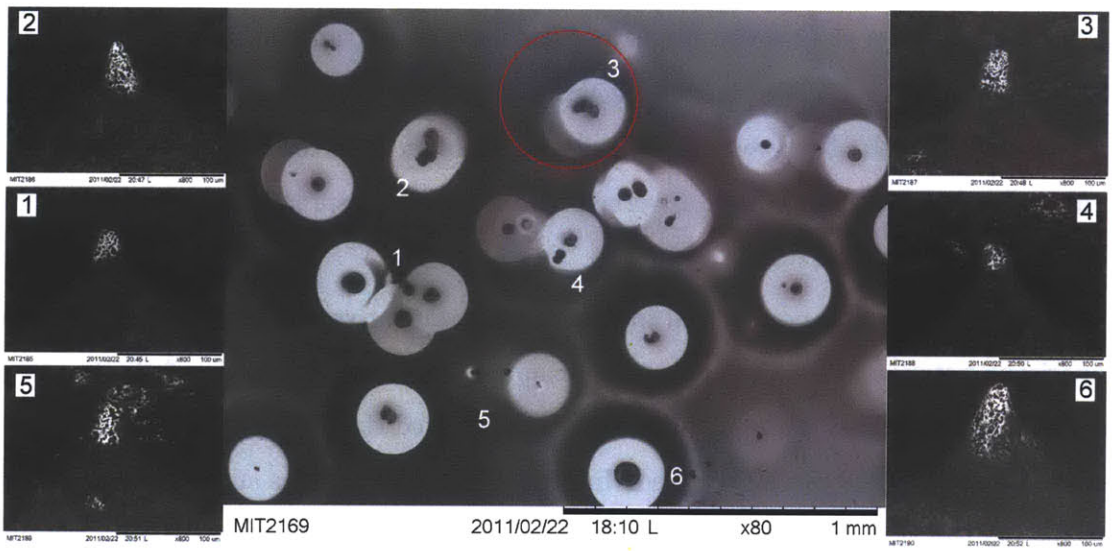

Figure 7-60: Correlations between emitters and observed patterns for relatively high radii emitters, segment 2 in Fig. 7-58(a).

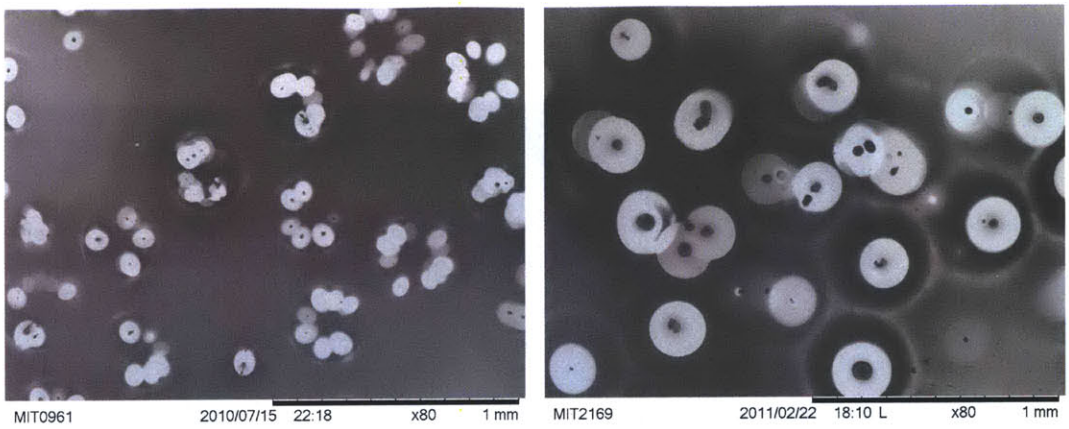

(a) A section of the observed profiles shown in Fig. 7-57(b) produced by a highly non uniform array etched with a single step.

(b) A section of the observed profiles shown in Fig. 7-58(b) produced by a relatively uniform, but poorly bonded, array etched using two steps.

Figure 7-61: Comparing the patterns observed using a single step etch (left) and a two step etch (right) after emission against stainless steel plates.

7.6.3 Interpretation of Observed Patterns

Samples of the plate patterns acquired from the two different arrays are shown in Figure 7-61. Here it is clear that during the first test the emission typically produced patterns of several bright circles within each larger bounding region, while using the fully processed emitters the patterns yield fewer bright regions with larger radii. The inaccuracies and differences in emitter to collector spacing measurements make comparing the sizes of the bright regions difficult. However; typically the emitters in the second test were closer than the first. If the pattern sizes were governed simply by beam spreading an opposite trend would be expected in this regard.

Further testing would be required to gain more quantitative, or simply more definitive, comparisons between these two cases. For example, direct visualization of the beam, as has been done previously with individual externally wetted ILIS[54], would be interesting if the individual beamlets can be resolved. In general these basic tests suggest that emission from the plateau type emitters may yield more emission sites, however these tests can not, accurately, establish if the emission was continuous from each site or if the patterns represent an unstable situation with emission occurring from only some points at any given time.

Gassend[50] performed a similar series of experiments using externally wetted silicon arrays. He observed that for low current operation, bright patterns very similar to Fig.

7-61(b) resulted. Those patterns included a central dark point, like that seen here, with typically one but sometimes two bright circles, presumably, formed from each emitter. As observed here, these bright inner circles were bound by a larger, faint boundary. At higher currents, Gassend observed more distributed patterns with many oblong features within very faint boundaries roughly corresponding to the spacing between emitters. Unlike the distributed bright patterns from plateau emitters tested here and shown in Fig. 7-61(a), the patterns Gassend observed at high currents were relatively diffuse. He postulated that at high currents, the sharp silicon emitters could be supporting field emission directly from the meniscus surface resulting in many, more spread out, beamlets.

Gassend proceeded to estimate beam divergence angles based on the size of the various patterns observed. This type of analysis has not been done here given the unexpected variation in spot sizes between Figs. 7-61(a) and 7-61(b) where the spot size increased for a decrease in emitter to target distance. This trend either suggests the correlation between spot and beam size is poor, or more simply, the target to tip distance measurements were not accurate. In either case, correlating to beam divergence would not be suitable.

7.7 Discussion

The majority of this discussion focuses on interpreting the results acquired using fully processed nickel arrays. However; the results of sections 7.2 and 7.3 are referenced to aid in the understanding.

7.7.1 Symmetry and Per Emitter Emission

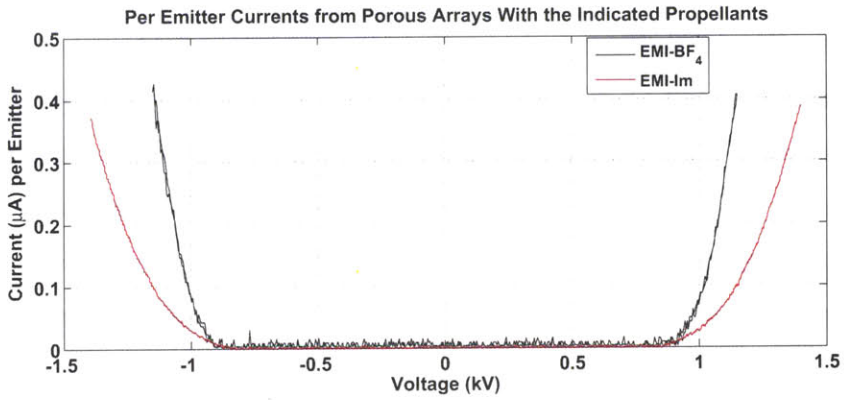

Figure 7-62: Samples of the collected current per emitter from the EMI-Im (second test session) and EMI-BF_4 arrays.

Both of the fully processed arrays, wetted with EMI-Im and EMI-BF_4, achieved high current levels at relatively low potentials. The typical currents, per emitter collected from both the EMI-Im and EMI-BF_4 devices prior to any significant current decay are plotted in Figure 7-62. Here the complete array of emitters (480 tips) has been assumed active, this is unlikely, making the plot an underestimate. Compared with the data collected from a single tungsten emitter, given in section 7.2, the current magnitudes are similar over the small range of potentials explored beyond the onset of measurable currents.

In Figure 7-63 typical collected current magnitudes are plotted against the magnitude of applied potential to demonstrate the emission symmetry for the two cases. In the case of EMI-Im, these data are not representative of negative emission during the first test session where interference due to the hardware was suspected. Both propellants demonstrate good agreement between polarities at low currents within the measurement noise.

Despite the apparent symmetry during ramped scans, the behavior under potential alternation was generally not symmetric. Figure 7-64 shows the collector current measured during the first 30 seconds of data collection with the EMI-BF_4 wetted array operating at

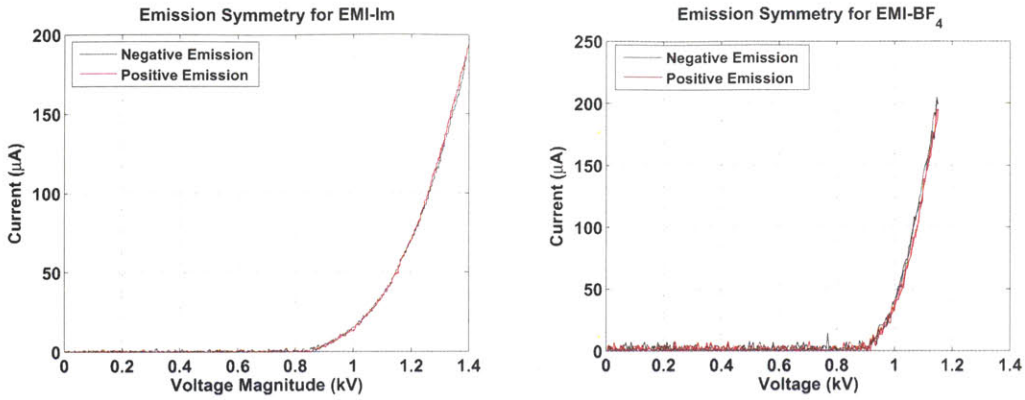

(a) Positive and negative collected currents using EMI-Im propellant.

(b) Positive and negative collected currents using $EMI\text{-}BF_4$ propellant.

Figure 7-63: Magnitude of currents collected at both positive and negative polarities, plotted together to highlight emission symmetry.

1 Hz (Fig. 7-51(a)). Although the amplitudes were similar, the positive measurement was $\sim$ 10 μA larger from the beginning of the test and onward. It is important to restate that during these relatively long duration measurements, the data acquisition system limited the secondary electron suppression potential to only 8 V, while in all other scans it was 20 V. As noted with the single tungsten emitter in section 7.2, poor secondary suppression could augment the apparent positive current collection.

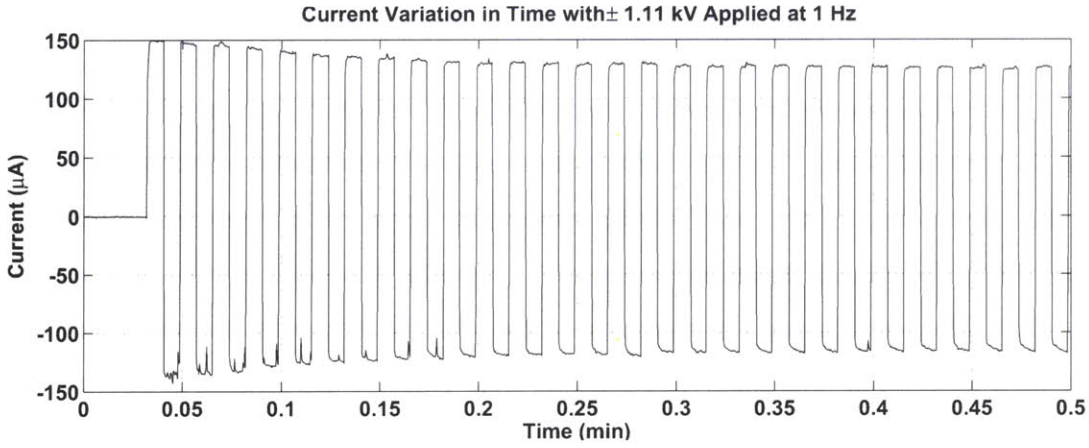

Figure 7-64: Despite the apparent symmetry of Fig. 7-63(b), the collected current with $\pm$ 1.11 kV applied at 1 Hz was not symmetric.

Figure 7-65 demonstrates the degree of excess current in the positive mode throughout the first two alternating potential scans made with $EMI\text{-}BF_4$. The excess current here is

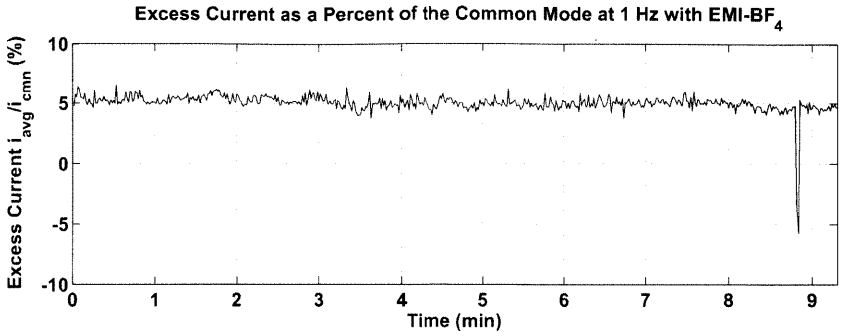

(a) At 1 Hz the excess current remained relatively steady around 5 % of the common signal.

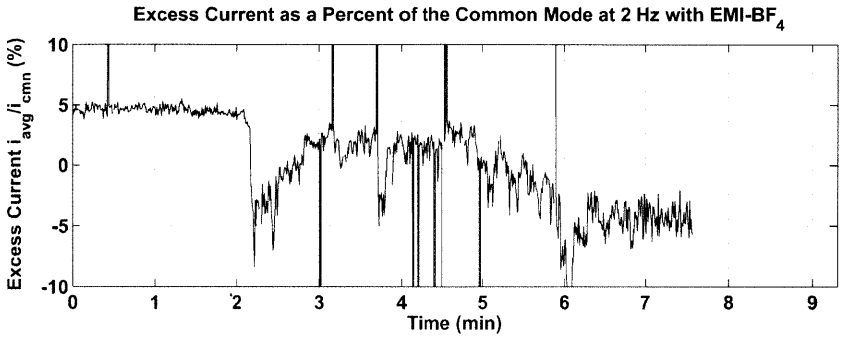

(b) At 2 Hz the excess current remained relatively steady around 5 % initially before a sudden transition to less stable operation accompanied by current decay shortly after.

Figure 7-65: Average current per cycle expressed as a percentage of the common mode amplitude using EMI-BF_4 and alternating the potentials.

the degree to which the average current exceeds the common mode signal at each period. For example, for emission oscillating between 110 μA and -100 μA at a 50 % duty cycle, $\pm$ 100 μA would be considered the common mode, while the average current would be 5 μA. Figs. 7-65(a) and 7-65(b) plot the ratio of the average current to common mode signal using the data from Figs. 7-51(a) and 7-51(b) respectively. It is interesting that during the first scan, where the current magnitudes decayed gradually, this metric is relatively constant at $\sim$ 5 %. However; during the second scan the behavior became much more erratic after roughly 2 minutes of operation. Referring to Fig. 7-51(b), more rapid decay was evident a few minutes after this point. A final scan was made with this array after increasing the applied potential to compensate for the decay in emission. Here the current again decayed quickly while slightly favoring negative emission.

The EMI-Im alternating potential measurements also demonstrated an un-symmetry but the spurious behavior at negative potentials, likely due to equipment errors, and low resolution data collection for those tests would discount an analysis as above. Finally, the

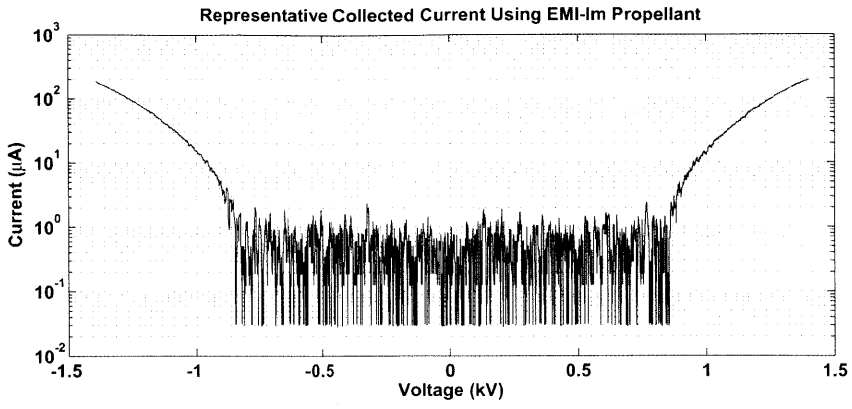

Figure 7-66: Representative data from an array wet with EMI-Im plotted on a logarithmic scale. Although the signal does begin within the noise, it rises quickly from roughly $\pm$ $\sim$0.85 kV. In this plot a 10 point moving average was used to smooth the data.

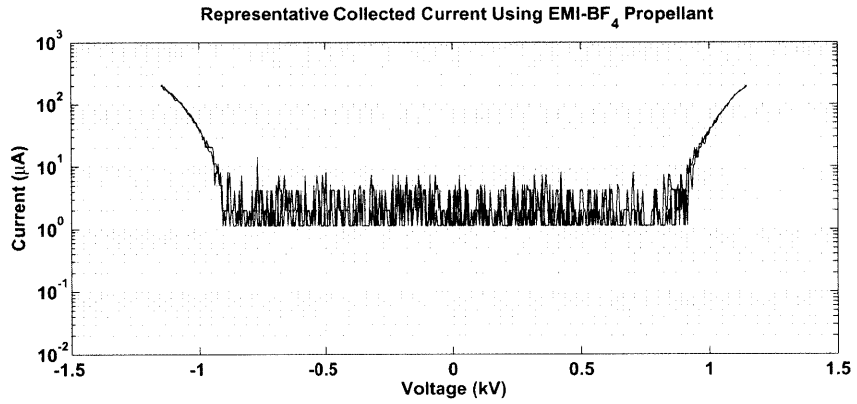

Figure 7-67: Representative data from an array wet with EMI-BF_4 plotted on a logarithmic scale. Although the signal again begins within the noise, it rises quickly from roughly $\pm$ $\sim$0.92 kV.

fully packaged device tested with EMI-Im was notable in that the collected current was generally not symmetric, favoring positive emission. This device was operated at 1 Hz at all times.

7.7.2 Starting Potentials

Accurately determining if a true startup potential exists, and if so its value, is difficult with the completed devices. As shown in Figures 7-66 and 7-67 the signal merges with the noise at low currents. However; if the unknown behavior within the noise is disregarded, it is possible to estimate a minimum potential where the current increased rapidly from the noise

level. For the EMI-Im sample this occurred at approximately $\pm$ 0.85 kV, while for EMI-BF_4 the signal emerges at approximately $\pm$ 0.92 kV. Comparisons with equation 2.7, motivated to be a modified relation for starting potentials on porous media in section 2.4.1, are perhaps unwise given that both the characteristic pore size and the typical radius of an emitting tip would need to be estimated. Nevertheless, equation 2.7 gives starting voltages around $\sim$ 1-2.5 kV for $\sim$ 10-30 μm tip radii and large 5 μm pore scales. Potentials higher than those observed during the testing presented here. Note that EMI-Im has a lower surface tension than EMI-BF_4 and hence lower starting potentials are expected. However, the array tested with EMI-Im had slightly larger tip radii on average, which would increase the starting potential. The single porous tungsten emitter presented in section 7.2 had relatively smaller pores and did require relatively large voltages to yield measurable currents, but the increase can partially be attributed to the large diameter wire loop extractor used for that test.

7.7.3 Wetting the Porous Arrays

The wetting technique has been rather arbitrary. This was, in part, due to the typical inaccuracies inherent in the two part epoxy scheme used to bond the porous nickel within the silicon mount. Specifically, the amount of type 377 epoxy allowed to clog some pores varied between samples leaving an unknown volume for propellant. However; the wetting method has been successful in that for all porous nickel array tests presented here the arrays were wetted from the rear. Capillarity alone supplied liquid to the tip of the emitters and emission was sustained.

Figure 7-68 shows two examples of emitters wetted in this way. Ionic liquid can be seen filling the pores near the emitter tips. It is important to note that in both cases shown here the arrays were tested prior to taking these images. The image on the left is an emitter, wetted with EMI-BF_4, on an array used for ablation testing. This emitter was at a location which did not create a pattern on the collector. Meanwhile the image of the right shows a tip on the fully processed array wetted with EMI-Im and could, therefore, be contaminated due to electrochemical reactions.

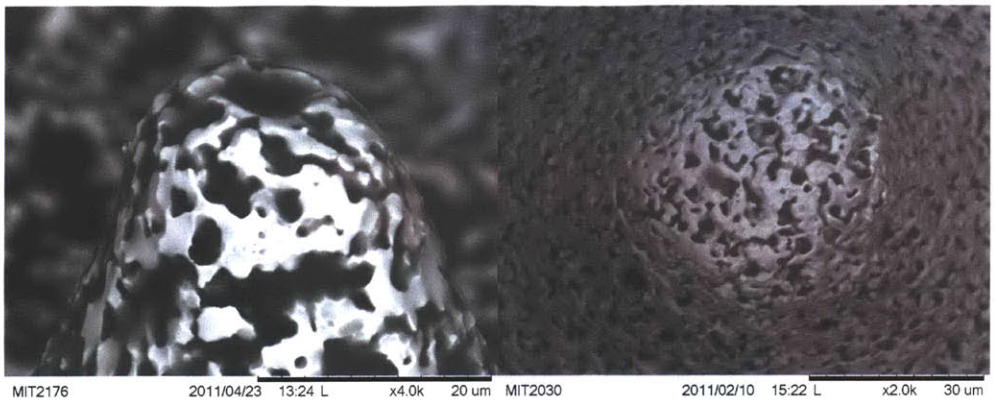

Figure 7-68: Examples of emitters wetted with EMI-BF_4 (left) and EMI-Im (right). In both cases these emitters were fired prior to imaging.

7.7.4 The Impact of Secondary Etching on Emission Characteristics

Although a limited number of arrays have been tested; the discrepancies in emission magnitude between the two cases of emission from arrays etched with a single step (sections 7.4.2 and 7.5.1) and those etched with the fully, two step, etch process are large. Consider the first two test samples presented in section 7.5. Both samples were wetted with EMI-Im and were tested within identical mounts, including the extractor grid. The largest discrepancy between cases, other than the etch procedure, was the region of over etched emitters along one edge of the single etch step case. Significantly higher currents at much lower operating potentials were achieved with the fully processed array. In addition, the fraction of emitted current intercepted by the extracting grid was reduced from $\sim$ 20-30 % to $\sim$ 5-12 % when using the two step process.

The emitter to extractor distances were similar in both cases ($\sim$ 140 μm) and the identical extractor grid was used. A reduction in current magnitude would be expected due to the number of over etched emitters on the single step array, however the large shift in operating potentials can not be explained by this alone.

Figure 7-70 provides SEM images of some typical emitters on each of the two arrays. These images show the actual arrays fired in the tests above. This type of image (perpendicular) only shows emitters near the edges of the arrays but some qualitative observations can be made. Some more general comparisons between arrays fabricated using the two different methods were provided in section 6.5. During the first test, with a single etch step allowed to continue until the resist mask had nearly fallen off, emitters resembling the

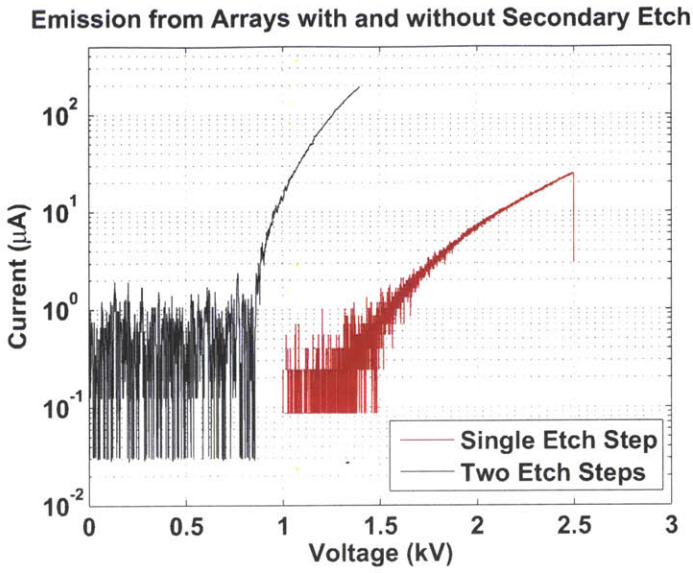

Figure 7-69: Samples of the overall collected current from an array etched with a single etch step and another with secondary sharpening. Both arrays used EMI-Im as propellant.

three predicted cases for small variations in the diffusion layer thickness in section 4.5 are present. These general cases have been identified in Figure 7-70(a). Meanwhile Figure 7-70(b) again demonstrates emitter to emitter variation but also the characteristic smoothing of the features achieved with the secondary etch step.

In section 4.5.7, it was argued that, electrostatically, the later case may favor more axially aligned beams and hence support the reduced beam interception. However; those arguments neglected the physical size of the pores, in essence assuming emission could occur from any point. If the hypothesis of section 2.2.3, that porous emitters sustain emission from emission sites localized to the physical pores, is valid then the situation with this particular, relatively high porosity, nickel may be much different. Consider the sketch in Figure 7-71, where exaggerated pores are drawn on the typical emitter shapes observed here. If the pores are significantly sized compared with the surface geometry, their spatial distribution may strongly dictate the emission properties. For example, although the sharp and plateau type emitters shown in the figure may yield strong fields at their sharp edges, high fields in the vicinity of a pore may be more difficult. However; the ablation tests presented in Figure 7.6 demonstrated emission from these type of emitters can occur. In addition, for a very sharp emitter, it may be possible that no clear fluid path can be made to the regions of strong electric field. Under these scenarios, higher voltages might be required

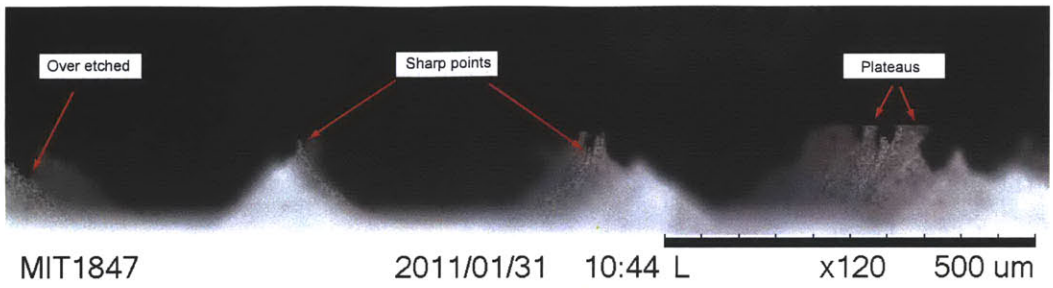

(a) SEM images of the array tested in section 7.5.1. Over-etched, sharp and plateau type emitters are all present on this array.

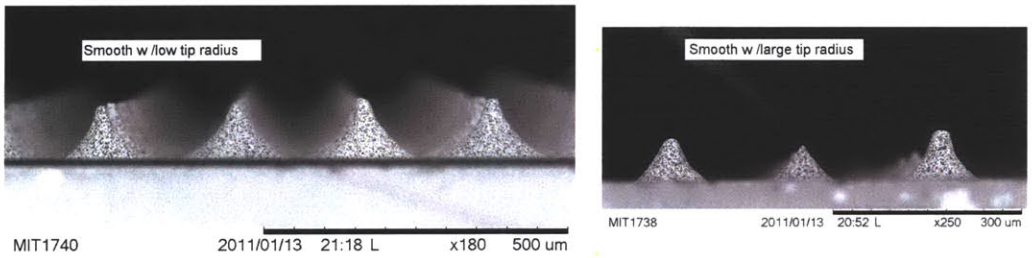

(b) SEM images of the array tested in section 7.5.2. This array was characterized by generally smooth emitters due to the secondary etch step.

Figure 7-70: SEM images of the arrays fired in section 7.5.1 and 7.5.2.

to obtain strong enough fields to form Taylor cones at the pores themselves. Further testing would be required to establish if this trend exists and, as discussed in chapter 2, an analysis approaching the complete behavior must also consider the hydraulic interactions between emission sites.

7.7.5 Ion Emission

The current versus voltage trends can be compared with those expected theoretically for field emission for a liquid surface. Equation 7.2 gives the current density, j, as developed

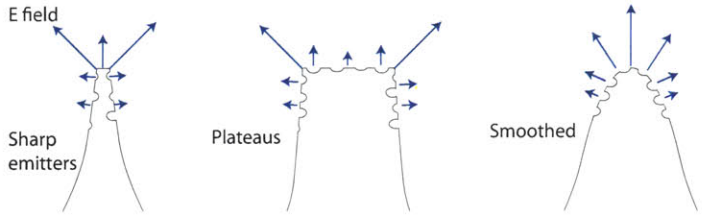

Figure 7-71: An exaggerated sketch of possible electric field and pore distributions. With such large pores, assuming that clear fluid path to the most, electrically, favored emission sites may not be valid.

using kinetic arguments by Iribarne and Thomson[27] and more rigorously derived elsewhere (see for example [22], [162]). Here the total energy barrier for ion evaporation is reduced from the energy of solvation, ΔG_0, by a quantity due to the applied field. In the equation, T is the liquid temperature, k is Boltzmann's constant, h is Planck's constant and σ is the surface charge density.

$$j = \sigma \frac{kT}{h} e^{-\frac{\Delta G_0 - \left(\frac{q^3 E}{4\pi\epsilon_0}\right)^{1/2}}{kT}} \tag{7.2}$$

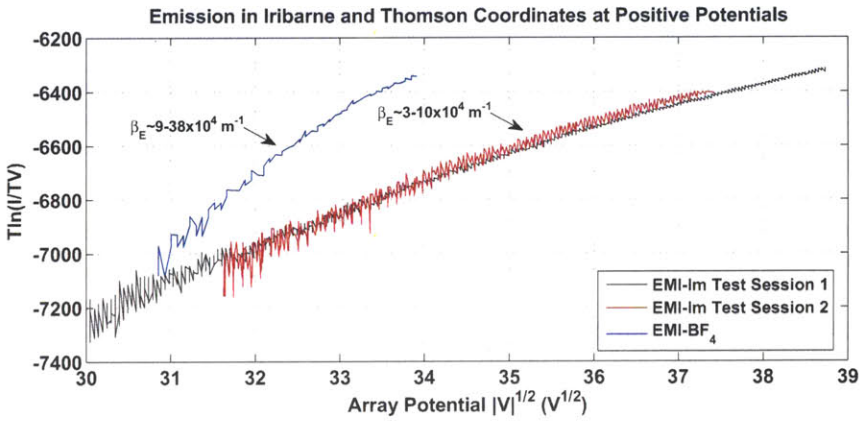

(a) Measured currents as a function of potential from both full porous nickel emitter array tests in the coordinates of 7.3 for positive species emission.

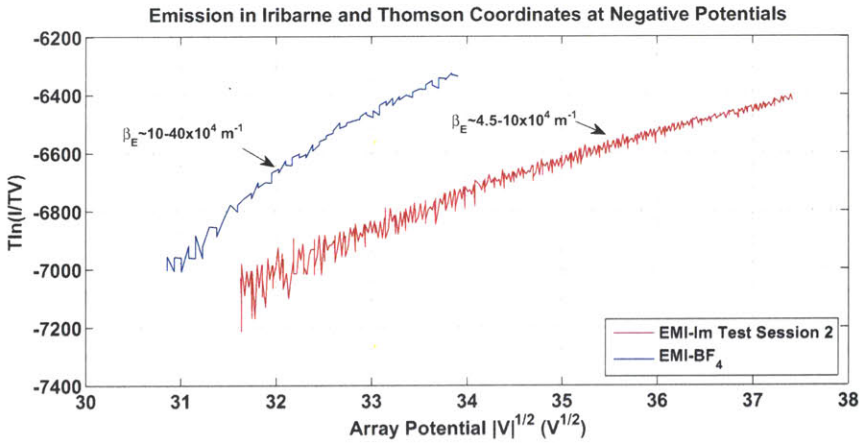

(b) Measured currents as a function of potential from both full porous nickel emitter array tests in the coordinates of 7.3 for negative species emission.

Figure 7-72: Current versus voltage measurements recast in the coordinates of equation 7.3. Complete agreement with equation 7.2 for field emission would yield straight lines in these coordinates.

Following the analysis of Gassend[50], a more tractable form of equation 7.2, using measured quantities, can be formulated by introducing some scaling parameters. Assuming

a perfectly conducting surface, $\sigma = \epsilon_0 E$. Let $E = \beta_E V$, such that β_E^{-1} is a length scale for the electric field at the point of emission and let $j = \alpha I_e$, where I_e is the current per emitter and $\alpha^{-1} \simeq \pi \beta_E^{-2}$ is a scale for the emitting area. The measured current is then $I = n_t I_e$, where n_t is the number of active emission sites. Using these factors, equation 7.3 results relating the measured current to the applied potential.

$$Tln\left(\frac{I}{TV}\right) = Tln\left(\frac{n_t \epsilon_0 \beta_E k}{\alpha h}\right) - \frac{\Delta G_0}{k} + \left(\frac{q^3 \beta_E}{4\pi\epsilon_0 k^2}\right)^{1/2} \sqrt{V} \tag{7.3}$$

Using measured currents from each of the full scale emission tests, the data has been recast in the form of equation 7.3 and plotted in Figure 7-72 assuming a temperature $T = 298^o K$. Note that for the EMI-Im cases the emitted current has been used, while in the case of EMI-BF_4 only limited emitted current data was acquired, hence the collected current is plotted here. However, for the latter case the intercepted current fraction was only a few percent. When plotted in this form, linear relationships do not result; however, this is not unexpected. As noted by Lozano[57] and Gassend[50], the active area (α^{-1}) at each emission site can not easily be defined and is not likely to be constant with increasing field strength. Similarly the number of active emission sites, n_t would likely vary with potential.

Referring to equation 7.3, the slope of the curves in Figs. 7-72 can give an approximation for β_E as it depends only on that parameter and other physical constants. Using linear fits over the initial and final regions of the curves, $\beta_E \sim$ 9-40x10^4 m^{-1} and $\beta_E \sim$ 3-10x10^4 m^{-1} result for the EMI-BF_4 and EMI-Im cases respectively. These values correspond to length scales from $\sim$ 2-10 μm and $\sim$ 10-30 μm for the two liquids respectively. Recall that the electric field here refers to that at the point of emission and should not be confused with the far field on an emitter discussed in section 2.4.1. Specifically, the field here is presumed to be that at the tip of a Taylor cone undergoing ion evaporation. In this respect, the length scales measured here are very large. Lozano and Higuera[65] motivated that for ion evaporation with typical solvation energies (a few eV), fields on the order of $\sim$ 1-2 V/nm are required. All data shown here was collected at around 1 kV. Hence for EMI-BF_4 the estimated field strength at the emission site was $\sim$ 0.1-0.6 V/nm (using $V \sim 1100$ V) while for EMI-Im it was much lower, $\sim$ 0.04-0.1 V/nm (for $V \sim 1200$ V).

The emission data from a single porous tungsten emitter, presented in section 7.2 can also be cast in terms of equation 7.3. In Figure 7-73 the collected current for both positive

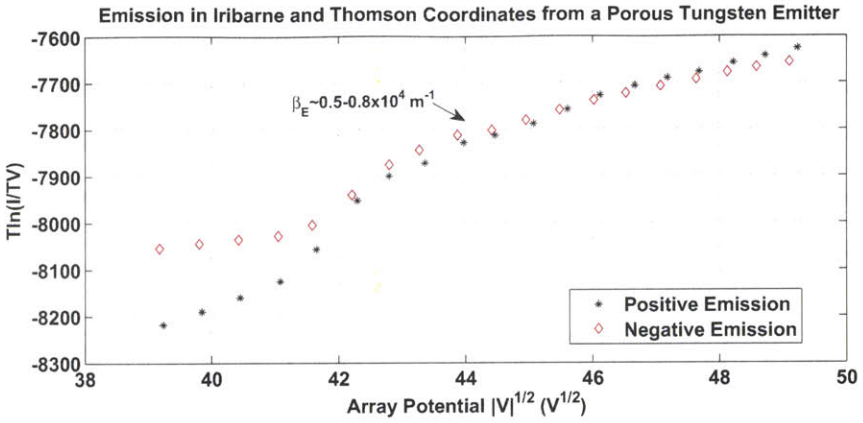

Figure 7-73: Measured currents as a function of potential from a single porous tungsten emitter in the coordinates of 7.3 for both positive and negative species emission.

and negative emission has been plotted in this form. The current measured with increasing potential was, in this case, characterized by an initial low current phase at a slightly lower slope prior to transition to a higher slope. This transition manifests as a step in Fig. 7-73. Beyond this step, the curves have typical slopes corresponding to $\beta_E \sim$ 0.5-0.8x10^4 m^{-1}, even lower than with the fully processed nickel arrays. The corresponding estimated electric field for these values is $\sim$ 0.005-0.02 V/nm for the range of operating potentials after the step (1.75-2.5 kV) and estimated the β_E values. Recall that for this emitter, pure ion emission was confirmed using time of flight spectroscopy.

The most significant differences between the porous tungsten and nickel emitters were the porosity and grid geometry. For emission from a Taylor cone, where extremely sharp surfaces result, the field after forming the Taylor cone should not depend greatly on geometrical factors. In section 2.4.3 it was argued that hydraulic effects should not limit emission, however; no accurate measurement of the porous media permeability and corresponding flow impedance has been made. The porous tungsten had both smaller particle sizes and reduced porosity, and hence a much lower permeability, compared with the nickel used in complete arrays. The reduced slope between the two cases, for the same ionic liquid (EMI-BF_4), could suggest hydraulics were a contributing current limiting mechanism but a more in-depth analysis of both the emission physics and hydraulic impedances would be required to draw any conclusions.

The shapes of the curves in Fig. 7-72 are also interesting. For all cases the slope decreases with increasing potential. A number of factors could induce this behavior as the

applied potential and net current both increase. As mentioned above, the number of active emission sites can not be assumed constant. For the arrays tested here significant variations in emitter geometries were present (see section 6.7.1). A reasonable assumption may be that the number of emission sites increases with potential. Referring to equation 7.3, we see that for n_t increasing slightly, the scaled current would also increase resulting in an enhanced slope of the curve. In this respect, the initially larger slope could be consistent with a rapid increase in active emitters at low potentials.

Another interesting consideration is the impact of the finite fluid electrical conductivity. The estimate for surface charge can be altered to include a finite electric field within the liquid, E_l, such that $\sigma = \epsilon_0(E - \epsilon E_l)$. Where if $E_l \sim j/K$[65], the current density divided by the ionic liquid electrical conductivity, we assume current is conducted normal to the surface at the liquid interface. With this modified estimate of the surface charge, a revised expression, equation 7.4, relating the current to potential ratio to applied potential results. The effects of conductivity constitute an additional term dependent on the ratio of the Ohmic length scale, $\frac{\epsilon\alpha I}{nKV}$, to that for field enhancement, β_E. For small currents at large potentials this term is negligible and equation 7.3 is recovered. Consider, the EMI-BF_4 examples in Fig. 7-72 where $\epsilon \sim 13$[163], and $K = 1.36\ S/m$. High currents, $I = 200\ \mu A$ were achieved at roughly 1.1 kV and $n_t \sim 500$ emission sites may be reasonable. If ion evaporation is assumed such that $E \sim 1.5\ V/nm$, then $\beta_E = 1.4\text{x}10^6\ m^{-1}$ and an emitting area factor for similar lengths scales would be $\alpha \sim \beta_E^2/\pi = 2\text{x}10^{12}\ m^{-2}$. With these parameters, the logarithmic term in equation 7.4 would be $\sim$ -1.5, a negligible contribution on the scale of Fig. 7-72. Repeating the calculation for the values of β_E found through fitting equation 7.3 to portions of the curves does not yield more significant effects.

$$Tln\left(\frac{I}{TV}\right) - Tln\left(1 - \frac{\epsilon\alpha I}{n_t KV\beta_E}\right) = Tln\left(\frac{n\epsilon_0\beta_E k}{\alpha h}\right) - \frac{\Delta G_0}{k} + \left(\frac{q^3\beta_E}{4\pi\epsilon_0 k^2}\right)^{1/2}\sqrt{V} \quad (7.4)$$

Temperature rise due to Joule heating would also impact the emission properties. In Figs. 7-72 and 7-73 a constant temperature was assumed in equation 7.3. Equation 7.5 includes a correction factor due to a temperature rise ΔT such that $T = T_0(1 + \Delta T/T_0)$ with an initial, or typical, temperature T_0. Here we assume a small temperature rise such that $ln(1+\Delta T/T_0) \sim 0$. The left hand side of this new expression is again the value plotted

in the figures, but we now see that increasing temperature with current (or voltage) would lead to a relative decrease in the plotted quantity.

$$T_0 ln\left(\frac{I}{TV}\right) = T_0 ln\left(\frac{n_t \epsilon_0 \beta_E k}{\alpha h}\right) + \frac{1}{1+\frac{\Delta T}{T_0}}\left[\frac{\Delta G_0}{k} + \left(\frac{q^3 \beta_E}{4\pi\epsilon_0 k^2}\right)^{1/2}\sqrt{V}\right] \tag{7.5}$$

Higuera[65] notes that for emission sites yielding hundreds, or thousands, of nA, significant Joule heating could take place. That author estimated a temperature rise assuming a thermal energy balance such that $\lambda \nabla^2 T + \vec{j} \cdot \vec{E_l} = 0$. Here λ is the thermal conductivity of the liquid, typically 0.1-0.2 W/mK for ionic liquids[164]. By assuming the length scales for the emitting area and that for temperature change are roughly equal we get a temperature rise of $\Delta T \sim IE_l/n_t\lambda$. Higuera proceeds to estimate that $E_l \sim E/\epsilon$ such that $\Delta T \sim IE/n_t\lambda\epsilon$. As noted by that author, estimates using this expression, for expected surface fields on the V/nm scale, suggest an alarming temperature rise, for example 120^o K for 200 μA from 500 emitters using EMI-BF_4. However; the assumed expression for E_l should be considered further and the expression, for Joule heating, lacks any dependence on electrical conductivity. Indeed, if the $E \sim \beta_E V$ as discussed above, we see that this expression is equivalent to $\Delta T \sim IV/n_t\epsilon \cdot \beta_E/\lambda$, which has the form of an input power divided by a characteristic thermal resistance. In this form, it is clear something is missing. For the large temperature differences predicted here the deposited power, $IV/n_t\epsilon$, is equivalent to $1/\epsilon$, or $\sim$ 5-10 % of the input power. It has been shown experimentally[36, 43] that the peak energy loss between measured beam energy and the input energy is typically a few volts out of thousands. Hence the beam power deficit is typically less than 1 % of the input power including other energy loss mechanisms, for example the $\sim$ 0.5-2 V potential drop across the electrochemical double layer (see section 7.2).

As an alternative, we can again approximate the internal field as that required for conducting the current through a characteristic area, $E_l \sim \alpha I/n_t K$. The expected temperature rise is then $\Delta T \sim \alpha I^2/n_t^2 K$. Here K is the liquid electrical conductivity. If $\alpha \sim \beta_E^2$ and again $\beta_E \sim 1\text{x}10^9/V$, this relation predicts a temperature increase of only $0.5^o K$ for the same EMI-BF_4 example used above. The power dissipated would then be $\sim \sqrt{\alpha} I^2/n_t^2 K$, equivalent to roughly 0.02 % of the input power for the EMI-BF_4 example. For a temperature drop of this magnitude, the correction factor in equation 7.5 would be small.

Finally, the possibility that a significant portion of the current is due to droplet emis-

sion should be considered. Typical electrospray droplet emission can be described by $I = \chi\sqrt{Q}$[22, 21], were Q is the flow rate and χ is a proportionality constant for the liquid (see the cited references for details on this relationship). The proportionality constant is roughly 1.1 EMI-Im and 1.6 for EMI-BF_4 in SI units. Hence for 200 μA of current from roughly 500 emitters, the flow rate per emitter would be 120 and 70 pL/s for EMI-Im and EMI-BF_4 respectively. The porous nickel used here had particle sizes in the order of $\sim$ 5 μm with a porosity of $\sim$ 45 %. The estimated permeability, using equation 2.12 for this material is roughly 4x10^{-14} m^2. In section 2.4.3, an expression for the pressure drop between a point within a bulk to a point near the emission site was developed for conical emitters as a function of permeability and geometry. Using that relation and approximating the emitters here as $\sim 20^o$ cones with 15 μm tip radii, 150 μm tall, the pressure drop would be $\sim$ 4x10^3 Pa and 7x10^3 Pa respectively for the two propellant cases. Meanwhile the electric stress for such an emitter spaced 150 μm from an extracting plate would be roughly 8x10^3 Pa using equation 2.6. That these two pressures are of comparable magnitude suggests that stable operation under a droplet only scenario is unlikely. However; this does not rule out a mixed ion droplet regime, and has assumed the porous array was not over filled with liquid.

In regard to confirming ion emission, this analysis is inconclusive. The approximate field strengths at the emission site estimated by fitting a kinetic model are somewhat lower than those expected. However; purely droplet emission of this magnitude would be unlikely using passive feeding through the porous media used here and a low estimated field strength was also found for emission from a tungsten source where pure ion emission was confirmed. An increasing number of emission sites, Joule dissipation and, to a lesser extent, electrical conductivity, could have contributed to the decreasing slopes in Figs. 7-72.

7.7.6 Performance Predictions

Accurate predictions of propulsive parameters (thrust, I_{sp}, efficiency...) would require more extensive diagnostics of the emission properties. Full beam time of flight spectroscopy, for example, would be imperative in determining the beam composition, including the contribution from solvated ions which break up within the acceleration region[58]. Once known, a reasonable estimate of the mass flow rate could be made. Similarly, beam energy measurements, again for the full beam, coupled with measurements of the spatial distribution (beam spreading) would be required to infer thrust with any degree of accuracy. Ultimately, accurate measurements of the propellant mass use along with direct thrust measurements, with a thrust balance, will be required to verify the performance.

Some rough estimates can nonetheless be made with this data to provide a taste for what *may* be achievable. During the full scale tests, typical grid to tip distances were $\sim$ 140 μm, while the laser cut grids were 300 μm in diameter and $\sim$ 90 μm thick. The transmitted beam must therefore have had, at most, a $\sim 30^o$ beam angle, θ_B. Typical, time of flight measurements for purely ionic emission, such as Fig. 7-9, show a significant contribution from both the monomer and dimer (singly solvated species). If a roughly even split is assumed, estimates for the mass flow can be made for a given current using equation 7.6. Similarly if the low energy deficits and peak widths typical of ILIS are neglected to a first approximation, the beam velocity for each species is estimated with equation 7.7. Here m_i is the species mass, from table 2.1, the monomer for $i = m$ and the dimer for $i = d$ and eV_e is the beam energy assumed to take the full value of the applied potential. The total thrust from the two species can then be estimated with equation 7.8.

$$\dot{m}_i \sim \frac{I}{2e} m_i \tag{7.6}$$

$$\bar{c}_i \sim \sqrt{\frac{2eV_e}{m_i}} cos(\theta_B) \tag{7.7}$$

$$T \sim \dot{m}_m \bar{c}_m + \dot{m}_d \bar{c}_d \tag{7.8}$$

Using these approximations, some peak thrust and specific impulse estimates are possible using the data, before decay, collected after emission from porous nickel arrays emitting

EMI-Im and EMI-BF_4. During the second EMI-Im test session, for one scan, relatively high currents were drawn, $\sim$ -380 and $\sim$ 425 μA for negative and positive emission respectively. The estimated total beam mass flow rate from both species, using equation 7.6, approached $\sim$ 1.9 $\mu g/s$ at -1.6 kV and 1.4 $\mu g/s$ at +1.6 kV. Using equations 7.6 through 7.8, these maxima correspond to $\sim$ 40 μN at -1.6 kV and $\sim$ 35 μN at +1.6 kV. The intercepted current fraction with that device varied from 5-12 %, increasing with potential. Taking this into account, the estimated specific impulses were roughly 1900 s and 2250 s for the negative and positive polarities. Recall that the Im^-, in EMI-Im is more than twice as massive as the EMI^+ ion, accounting for the range in peak specific impulse and thrust between polarities. At roughly 400 μA on average for 1.6 kV, this test had a maximum power consumption of $\sim$ 0.65 W.

For the EMI-BF_4 array, the maximum current was kept low to suppress emission decay before the alternating potential tests. At $\pm$ 1.125 kV the maximum current draws were -200 μA and +195 μA corresponding to roughly 0.4 $\mu g/s$ for both polarities. Again assuming a 30^o beam divergence angle, the maximum estimated thrust was $\sim$ 11 μN in each polarity. The beam interception fraction was within the measurement noise during this experiment. Assuming full transmission, the estimated specific impulses were 2850 s and 2560 s in the negative and positive polarities respectively. At the maximum measured current levels this device used $\sim$ 0.22 W of power.

It is interesting to note that the fast rising IV characteristics observed with the devices translates to a relatively small deviation in specific impulse, a few hundred s, between low (10's of μA) and high (100's of μA) current operation. Specifically, beyond a few 10's of μA, the EMI-Im and EMI-BF_4 IV curves had slopes of roughly 0.8 and 1.0 $\mu A/V$. Hence for EMI-BF_4 a 100 μA emission increase from say 10 to 110 μA would require only 100 V of additional potential resulting in roughly a 5 % increase in specific impulse. Therefore, to first approximation, these devices approach a constant specific impulse, variable thrust system.

7.7.7 Observed Current Decay from Fully Processed Emitters

The observed current decay during operation of fully processed arrays with both ionic liquids is extremely disconcerting. If these devices are to be used for spacecraft propulsion, consistent operation over 1000's of hours would be required. These decays are therefore a

significant stumbling block that must be overcome as part of future development approaching a practical thruster.

The problem was observed using both EMI-Im and EMI-BF_4 with fully processed emitters. This discussion primarily focusses on those tests due to the low beam interceptions. After all tests with each sample, significant residue was observed to have accumulated around the emitters. However; after the first session with the EMI-Im sample, the emitters appeared to be clean. For both propellants when relatively (minutes) long alternating potential testing was carried out, a period of strong decay lasting a few minutes was observed.

It is interesting to consider some general scenarios which may have, in whole or in part, contributed to the measured decays:

1. Beam composition : Without beam spectroscopy the relative composition of ions and droplets cannot be confirmed.

2. Physical effects : Although the cause of the residue is not clear, its impact could affect both the emitter electrostatics and fluid paths to the emission sites.

3. Propellant contamination : Any chemical or electrochemical reactions within the propellant could lead to a change in the emission characteristics.

Consider item 1 and the first test session made with EMI-Im. One explanation for the decay could be that the emission varied between an ion dominated and droplet dominated beam. Droplet emission at some point during the tests was likely with this ionic liquid given the residues observed on the collecting plates for both test sessions. Suppose the array was initially over saturated with liquid, such that the internal pressure of the liquid was relatively low and droplets could be extracted from Taylor cones spanning multiple pores. As the emission continued, this would lead to fluid depletion and therefore an increase in hydraulic impedance for emission. Gamero[26], showed that a mixed ion/droplet beam will transition from a droplet dominated to ion dominated beam as the flow rate is decreased. However; as the ionic contribution was increased, that work showed that the total emitted current will increase dramatically in approach to the purely ionic regime. In the experiments presented here, the current decreased with time. Hence for an initially droplet rich beam, the emission would have had to of been entirely droplet dominated, operating far from the ionic regime, all times when collecting this data. This may be unlikely given the high currents and flow

impedance discussion above but, without knowing the exact wetting conditions, should not be ruled out.

As an alternative, consider an initially ion dominated beam which transitions to include a substantial fraction of droplet emission. Droplets could explain the clean emitters observed with EMI-Im, as the increased fluid flow rate could remove residues, but this was not observed with EMI-BF_4. Similarly, the yellow residue on the collector plate for EMI-Im tests may be due to collected, contaminated, droplets. After this test session, attempts to add more liquid were plagued by overwetting. When the excess liquid was then removed using filter paper, it had a strong yellow colouration compared with pure EMI-Im. Hence, some decomposition of the liquid, the third item listed above, may also fit these observations. If, for example, the fluid conductivity decreased over time due to propellant decomposition, it could induce a transition from purely ionic to a mixed ion/droplet regime. Although again viscous loses would need to be overcome to sustain any reasonable amount of droplet emission.

The second item listed above is particularly applicable to the second test session with EMI-Im, and the EMI-BF_4 testing. Although the cause of residue build up may not have been consistent between the tests, its influence on beam emission fits the observations. Referring to Fig. 7-54, the relatively low conductivity (as indicated by the darker coloration compared with nickel in the SEM images) material appears to be relatively thick and often completely covers the emitters. Electrostatically, this would significantly alter the field distribution, possibly reducing the electric field to a level below that required to sustain emission. Furthermore, emitters that have been completely covered would not have a clear, uncontaminated, liquid path to suitable emission sites near the emitter tips. Both of these issues, reduced field strengths and blocked pores, are consistent with the requirement to increase the applied potential to maintain emission levels over time, as observed for both EMI-Im (see Fig. 7-41) and EMI-BF_4 (compare Figs. 7-51(a) and 7-52).

The relatively close separation between the array and the collector plate (24.7 mm) clearly resulted in significant back-sputtering of material from the collector. This can be seen in Figs. 7-46 and 7-53 for EMI-Im and EMI-BF_4 respectively. However, back-sputtered material would, and was observed to, coat all surfaces relatively uniformly. Hence the strong variation in material conductivity between the emitters and extracting grid revealed by SEM images, for example Fig. 7-54, are not consistent with this explanation. Furthermore, Fig.

7-45 shows that, with the extracting grid removed, some material has bridged between emitters after testing with EMI-Im. Clearly this region would have been blocked by the extracting grid and could not have been coated by sputtered material.

Propellant contamination, either through electrochemical or chemical reactions, remains as a likely underlying phenomenon leading to current decay. Whether inducing a transition between ion/droplet regimes, effecting physical changes to the emitters or simply altering the propellant properties the effects would be detrimental to operation. Purely chemical reactions on the time scales observed are an unlikely scenario since, in all porous nickel tests, the arrays were allowed to settle for several hours (typically overnight) after wetting.

7.7.8 Electrochemical Decomposition Discussion and Recommendations

Early experiments with ILIS quickly identified that prolonged operation at a single polarity can cause electrochemical degradation of the ionic liquid propellant[37]. As part of that work the authors estimated that for a symmetric (in terms of current) ion beam, voltage alternation at roughly 1 Hz should be sufficient to prevent charging of the interfacial double layer beyond the ionic liquid electrochemical window and hence avoid decomposition. No active current matching was performed during those tests[94].

Here the unbalanced average currents shown in section 7.7.1 and the relatively high emission currents from porous emitters compared with externally wetted may have led to relatively significant average charging. The most obvious action to be taken to confirm this would, at the laboratory level, be to include active feedback such that a zero net current, on average, is maintained from the emitter arrays. Operationally, the final configuration (see Chapters 1 and 2) would use two arrays simultaneously operating at opposite currents through a single power supply, which could prevent any unbalance intrinsically so long as both arrays yield similar emission properties. However; the dramatic and relatively quick effects of these reactions on operation with porous nickel emitters warrants future research into the details of electrochemical interactions on these devices.

Qualitative comparisons of probe measurements from tungsten and nickel externally wetted emitters showed the two metals yield similar results. This result was deemed sufficient to assume similar frequencies could be applied to nickel emitters as with tungsten. Figure 7-74 shows an additional probe example, measured while emitting EMI-BF_4 at 1 Hz from a nickel emitter, again similar to tungsten emitters. It is interesting to note that

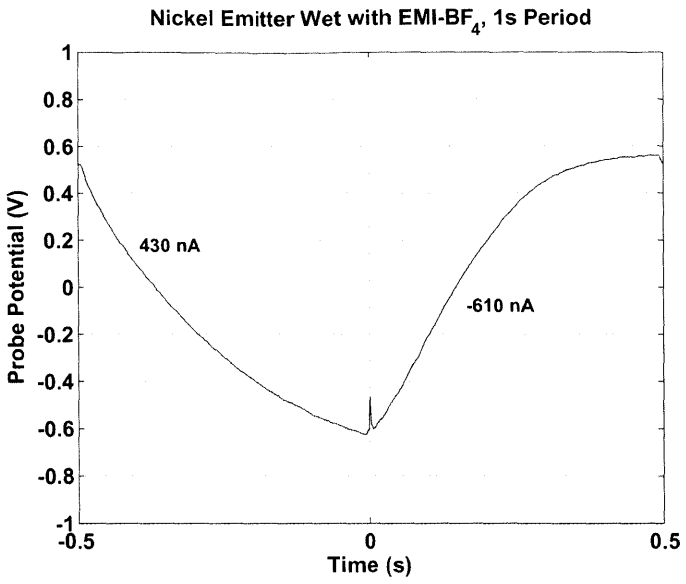

Figure 7-74: An example of probing data acuquired at 1 Hz using a nickel externally wetted emitter wet with EMI-BF_4.

despite the increase in frequency over the measurements in section 7.3.4, the shape of the curve has generally scaled with time. That is, even at this frequency, the stronger currents at the negative polarity result in a probe measurement which appears to approach saturation. If this relative saturation, for both materials, can be interpreted as an indication that reactions are occurring, the underlying issue may be the different products or reactions between materials. Lozano noted that during long alternating potential tests the current slightly favored negative emission on average and that during fixed polarity operation at negative potentials the reaction products were observed to take the form of a gas. An evaporated gas would still represent a loss of propellant but may not damage the emitter surface. Hence, even if the kinetics of the reactions have not changed significantly between metals the products formed by excess positive emission from porous nickel arrays may simply be relatively detrimental. In section 7.3.4 no residues were observed after testing, however those tests tended to favor negative ion emission over positive ions.

The externally wetted probing experiments were relatively simple to perform and are generally a much more controlled experiment compared with porous emitter arrays. For this reason they are a good candidate for further experimental investigation of electrochemical effects. In general, a quantitative interpretation of these curves is not very well understood. The following notes outline some recommended topics and techniques which could be useful

for future work in this regard. The goals of such a study could be to 1) obtain a correlation between onset of Faradaic currents (reactions) and probe measurements, 2) use such a correlation to confirm that at predicted alternation conditions (frequency and current balance) reactions are suppressed and 3) seek applications of the model to porous emitters.

Properties of the Electrochemical Double Layer

The electrochemical double layer between a conducting electrode and an electrolyte is often[119] modeled as a parallel capacitance, C_{dl} and resistance r_{dl} per unit of surface area.

The electrochemical window refers to a region where $r_{dl} \approx \infty$, described by $|\Delta V_{dl}| < |V_w|$, where $|V_w|$ is the approximate electrochemical window and ΔV_{dl} is the difference between the midpoint of the window and the current double layer potential. Within this region, Faradaic current (current crossing the double layer) is deemed negligible. This definition alone should draw concern for ILIS application. Electrochemical breakdowns are a kinetic process and, as a result, definition of a window must be accompanied by a selected cut off limit to the current. Ohno[165] discusses this limit and notes that for most reports using ionic liquids it is typically around 0.1 to 1.0 mA/cm^2. For example, Moganty[166], used cut off currents in the range of 0.1 to 0.4 mA/cm^2 in establishing electrochemical windows for BMI-BF_4. Applied to an externally wetted emitter with 5 mm of exposed length along a 0.5 mm diameter wire, this corresponds to $\sim$ 15-60 μA of current, orders of magnitude more than the typical emitted current as an ILIS. Those authors note that for applications at relatively lower currents, significantly lower effective windows should be used. Furthermore, the window for decomposition is known to depend on the electrode material[167, 168, 166]. Galiński[169], for example, notes that compared with glassy-carbon or platinum electrodes, the electrochemical window measured against a tungsten electrode may increase by several volts. Conversely, anodic dissolution of nickel may effectively reduce the electrochemical window[170]. Finally, the effect of impurities should not be ignored. At the low currents used in ILIS, ensuring high purities may be extremely important as any impurities could significantly reduce the apparent limit of capacitive behavior, see for example Galiński and Barrose-Antle[167] for discussions of impurity effects.

Furthermore under certain conditions using ionic liquids, the effective capacitance, C_{dl}, can depend strongly on potential. The relationship takes the form of a bell shape centered

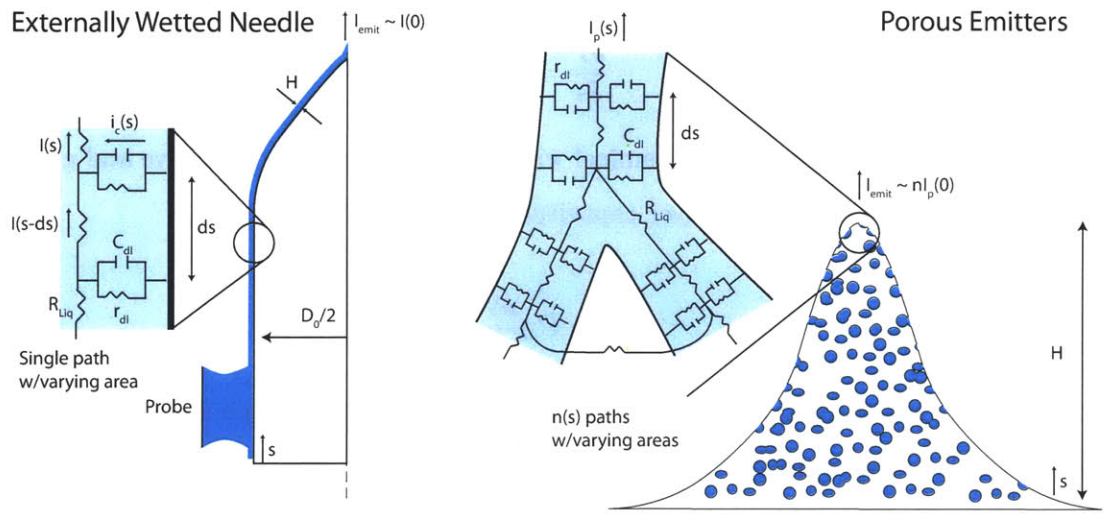

Figure 7-75: Modeling ion emission as a current source, the substrate to liquid double layer will depend on the geometry and physical properties of the double layer. For an externally wetted emitter, the behavior can be described by equation 7.12, voltage diffusion modified by the variable path area. For porous emitters the interconnected network of pores complicates the analysis.

near the potential for zero charge[171, 172, 173] with up to an order of magnitude increase over the baseline value. However; Nanjundiah[171] notes that this behavior was accompanied by Faradaic currents and that measurements outside of this region are relatively stable. Lozano and Martínez-Sánchez used those results for EMI-BF_4 and showed that to first approximation $C_{dl} \sim \epsilon_0 \epsilon / \delta_a$ in the region far from Faradaic currents. Here δ_a is the diameter of a single anion . Operating well within the electrochemical window may be accompanied by relatively constant capacitance per unit area but an analysis of the behavior approaching the window limit should consider this variability.

Ohmic Contributions, Voltage Diffusion

The discussion above concerned an element of area along the interface. In order to interpret experimental data, as acquired in section 7.3.4 for an operating emitter, a model for the distribution of potential over the entire surface would be required. The left side of Figure 7-75 shows an approach to modeling this behavior on externally wetted emitters. Here the current within a thin liquid layer, of thickness H is assumed to be parallel to the surface and increases by an amount $i_c wds$ between points s-ds and s, leading to equation 7.9. Here $i_c(s)$ and $w(s)$ are the capacitive current density and surface perimeter at s respectively.

$$\frac{\delta I}{\delta s} = i_c w \tag{7.9}$$

For operation below the electrochemical window, $i_c(s)$ is purely capacitive and given by equation 7.10, where the double layer capacitance per unit area is C_{dl}.

$$i_c = C_{dl}\frac{\delta V}{\delta t} \tag{7.10}$$

Meanwhile, the current at s, where conduction is assumed to dominate over convection, is proportional to the potential gradient as in equation 7.11. Here $A(s)$ is the fluid cross-sectional area ($\sim Hw(s)$ for an externally wetted emitter) and K is the liquid conductivity.

$$I = -AK\frac{\delta V}{\delta s} \tag{7.11}$$

Substituting equation 7.10 and the derivative of equation 7.11 into equation 7.9 yields an expression for the fluid potential, equation 7.12.

$$-\frac{\delta}{\delta s}\left(AK\frac{\delta V}{\delta s}\right) = C_{dl} w \frac{\delta V}{\delta t} \tag{7.12}$$

Under conditions where $dA/ds \sim 0$, equation 7.12 can be reduced to equation 7.13. This relation is equivalent to a diffusion of voltage along the interface, with diffusivity $AK/C_{dl}w$. Recall that C_{dl} is the characteristic capacitance per unit area for the ionic liquid/metal interface in question and may be strongly dependent on potential.

$$\frac{AK}{C_{dl}w}\frac{\delta^2 V}{\delta s^2} + \frac{\delta V}{\delta t} = 0 \tag{7.13}$$

Applied to probed externally wetted emitters, like those tested in this research, solutions to equation 7.13, or 7.12, could provide information concerning both the time required to reach the electrochemical window limit near the emitter tip and the corresponding behavior at a probe far from the emission site.

This analysis is fundamentally equivalent to that of Lozano and Martínez-Sánchez[37], where 1 Hz frequencies were deemed suitable, but only goes so far as to pose the problem rather than estimate a solution for the time scale for a specific geometry. In that paper, C_{dl} was approximated to be $\sim \epsilon\epsilon_0/\delta_i$, where δ_i was the diameter of an ion. The authors focused

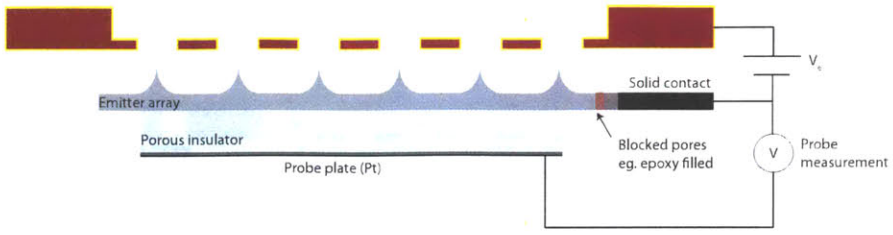

Figure 7-76: A suggested approach to probing electrochemical behaviour of porous emitter arrays, if deemed feasible/useful following theoretical considerations. The wetted porous insulator couples the ionic liquid to a probe plate, while a region of blocked pores allows for contact to the nickel substrate without ionic liquid contact.

on the maximum potential, near the tip, and estimated the time scale for it to reach the electrochemical window. Full solutions to equation 7.12, possibly calculated numerically, could provide a more complete, time dependent description.

Applicability to Porous Emitters

Porous emitters are characterized by both long (conducting) fluid paths and high liquid to metal interface areas. The right side of Fig. 7-75 demonstrates the complexity of these emitters. One approach could be to use a derivation as above but with estimates for the net capacitative and resistive areas as a function of emitter height, this has not been attempted here. Porous emitters could be probed using a coupling like that shown in Figure 7-76 to isolate the ionic liquid from within the porous bulk using an non conducting porous intermediate. However, the degree to which useful measurements could be discerned from these measurements, far from the emission site, would need to be considered analytically before proceeding.

7.8 Future Recommendations

These arrays function in the sense that they can produce a beam of charged particles. However; a tremendous amount of work remains before they can be ready for application as a thruster. In the previous chapter some recommendations were made for improving and/or modifying the electrochemical etching scheme. In the context of producing the desired fully microfabricated arrays, some more pressing issues are apparent. The following

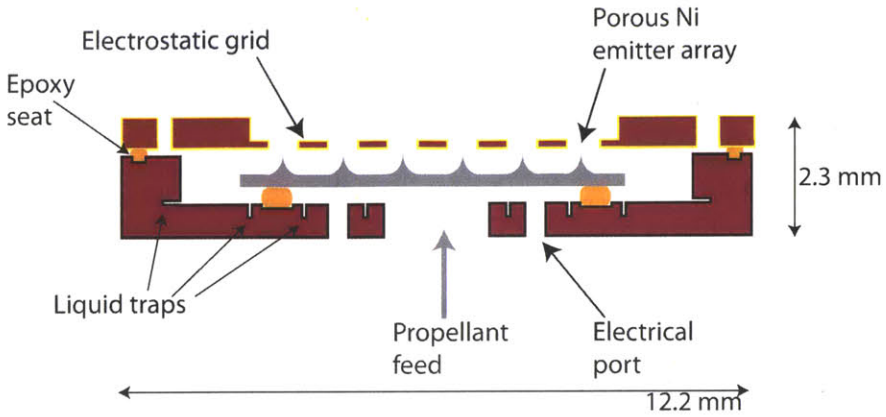

Figure 7-77: A modified packaging scheme including more liquid traps, a seat (or pocket) to localize the grid epoxy and an increased gap between the emitter array and the package sidewall. Thrust density (per unit area) could be maintained by increasing the emitter density.

list discusses some recommended topics to considered for further development of the devices, in no particular order.

- **Operating Practices :** The rather arbitrary wetting procedure used here undoubtedly contributed to the electrical failures observed using fully processed devices. A much more regimental and repeatable approach to wetting would be crucial in both ensuring the thrusters are operated in a consistent manner and preventing these problems. Similarly, simple physical contamination was unfortunately a major issue. The testing and preparation process should be carried out in a clean environment in the future if possible.

- **Packaging and Electrical Isolation :** Operation of the fully microfabricated devices was extremely limited. The close spacing between the support structure and array may have contributed to overwetting problems. Relaxing this spacing could be achieved without loss of performance per unit area by simultaneously increasing the emitter density. As evidenced by the partially etched 952 emitter array shown in section 6.7, a moderate increase in density should be well within the capabilities of the current etch process. A package similar to that shown in Figure 7-77, including liquid traps and a seat for the epoxy, could be a good first approach. The grid to tip alignment method is inherently sound, but suffered in complete packages due to the

tendency for the grids to shift during epoxy curing. As the final process step, this failure was particularly inefficient and a more robust procedure should be developed as soon as possible.

- **Suppressing Electrochemical Reactions :** In the short term, this problem may be dealt with by ensuring the thrusters are always operated at appropriate frequencies and under conditions of zero net charge transfer. In a thruster application, bipolar operation of two devices may achieve the later requirement inherently. Alternative metals and ionic liquids could be more resilient to detrimental reactions, as tungsten appears to be with the liquids tested here. However; the details of the problem are complicated and could only benefit from a greater level of understanding.

- **Measuring Beam Composition :** The title of the this thesis may be somewhat optimistic. Evidence, with EMI-Im at least, suggests that in their current form these devices may emit a combination of both ions and charged droplets. This may not be terrible. If, for example, the conditions required to vary the relative contributions of the two modes could be controlled, it would be useful in modulating the device specific impulse. However; understanding the performance capabilities of these devices relies heavily on confirming if and when purely ionic emission can in fact be achieved.

- **Single Emitter Experiments :** On a per emitter level, much work remains to be done in understanding the operation of porous electrospray emitters. For example, the ultimate limiting mechanism which determines the IV characteristics of these devices has not been established. Meanwhile, the simultaneous existence and stability of multiple emission sites on each emitter has not been conclusively confirmed. Studies of the downstream beam spatial and energy distributions from a single emitter as a function of operating conditions (voltage, geometry, emitter material) could offer some clues in this regard.

- **Propellant Supply Tank :** The current thruster modules have a propellant capacity of roughly 40 μL. For useful thrusters a propellant tank will be required. Confirmation that such a tank, with a useful amount of propellant, can be passively coupled to a device would be a major milestone in verifying the overall thruster concept. A high porosity and relatively benign material, for example one of the aerogels discussed in

Chapter 3, could be ideal in this regard.

- **Direct Thrust and I_{sp} Measurements :** Direct measurements of the total device thrust, coupled with measurements of the total mass loss during testing would be required before any definitive statements of performance can be made.

Chapter 8

Conclusions

Many decades after their discovery electrospray thrusters are gaining a new life, largely because they are intrinsically small. The challenge of applying these devices to small satellites remains a scaling problem but instead of scaling down, we try to scale up these efficient devices to achieve useful thrust levels, through multiplexing.

The underlying motivation for performing this research has been to aid in developing useful propulsion systems for these satellites. The porous ionic liquid ion source concept is particularly exciting in that, if properly packaged and combined with a simple power processing unit, the resulting thrusters could yield performance levels which meet, or exceed, state of the art propulsion systems available for much larger satellites. However; excitement alone can not propel a satellite. In this research, arrays of emitters capable of emitting high current beams have been fabricated from bulk porous materials in an effort to support making these thrusters a reality. Specifically, as discussed in Chapter 3, a fabrication scheme for the emitter arrays, electrochemical etching on porous nickel, was selected not only because it was promising for fabricating emitters, but because it offered the opportunity to do so in a manner conducive for packaging the array in a complete thruster.

This decision was not made lightly. To be applied to porous materials, a particular characteristic of electrochemical etching had to be exploited. Specifically, its ability to induce etch rates fast enough for mass transport properties to become the rate limiting mechanism. This regime, described in section 4.1, is well understood in the context of etching on solid materials, but its applicability to bulk porous materials had not be considered in detail. As a result, choosing this technique in lieu of other more established microfabrication tech-

nologies required the majority of this thesis to be focused, not on space propulsion, but on developing both an understanding of electrochemical etching on porous materials and a tool capable of exploiting that knowledge at μm scales.

Electrochemical etching, in general, can be very complex and challenging to predict in practice. However; we have shown in this research that for uniform hydraulic conditions and high etch rates, the situation improves greatly, particularly for forming arrays of porous ILIS. First, material removed within the pores of a given metal must diffuse over a greater distance to reach the bulk electrolyte. As the overall etch rate increases, the removal rate at the surface of pores will far exceed that for material removed within them, the result is an effective shielding such that (virtually) no etching occurs within the pores. This concept was described in section 4.3. Second, under these conditions generally complex etching theories reduce to a relatively simple diffusion problem. Combined, these traits allow for a process which is well suited for porous materials and can also be considered, to a relatively reasonable degree of accuracy, using analytical and numerical models. Specifically, in section 4.4, we have treated the transient transport behavior analytically and applied the results to etching porous materials under both constant and pulsed voltage conditions. Similarly, in section 4.5, a numerical model was described and employed to simulate feature profiles with varied hydraulics and masking conditions. This model offered insight into the challenges to be expected when attempting to achieve emitters which are both suitable for operation as ILIS and uniformly distributed across a planar array.

In Chapter 6 we have applied this technique to the specific case of fabricating emitter arrays on porous nickel. Once a general electrochemical cell was established, at the experimental level, a tool which parameterizes the necessary electrical and hydraulic conditions was matured in tandem with developing an understanding for the most sensitive conditions. The components and features comprising this tool were described in section 6.1. In section 6.3 we demonstrated that porous nickel, in a hydrochloric acid solution, can be etched in a transport limited regime whereby limited etching occurs in the porous structure. Furthermore, using the processes outlined in section 6.2.1, and applied throughout Chapter 6, we have demonstrated that dry film photoresists, as opposed to spin on resists, are well suited for masking porous materials and are compatible with acid based electrolytes often used in electrochemical etching. In section 6.4 we discussed how, primarily through variations to the hydraulic conditions, the process approached a point where moderately

uniform structures could be fabricated on porous nickel samples which were packaged and patterned within a silicon frame. As the technique matured the analytical investigations became more relevant. Specifically, the applicability of pulsed voltage etching to porous substrates was discussed in section 4.4 where we found that smooth surface etching may be maintained at relatively high duty cycles and low frequencies. In section 6.4.4 we applied this technique to forming porous emitter arrays and observed a significant increase in both array and batch level uniformity compared with samples etched using a constant voltage. Similarly, in section 4.5 we postulated that transient effects could be detrimental to the ability for this tool to etch porous materials over short time periods. This concern was validated in section 6.5 where a relatively short duration etch lead to in pore etching when attempting to tailor plateau shaped emitters. However, as described in that section, this problem was suppressed by adding salts to the etch solution such that the transport limited reaction rate and the amount of etched material required to saturate the substrate surface were both reduced. This result was then integrated into a complete, two step, etching process previously motivated using numerical simulations. First a long duration pulsed voltage etch was stopped well before completely undercutting circular masks, leaving a uniform array of plateaus. The masks were then removed chemically such that the plateaus could be rounded into useful electrospray emitters using a short etch within a doped electrolyte. This final process was summarized in section 6.6.

Ultimately, these efforts led to a process for producing arrays of emitters, within a silicon package, ready for testing as ILIS. By aligning the emitters to the silicon frame, we found that an electrostatic grid, either bonded to (section 7.4) or held just above (section 7.5) the silicon frame, could be aligned to the same markings. This form of alignment produced good tip to grid orifice alignment as shown during a discussion of the complete thruster fabrication process in Chapter 5. When applied as an electrospray source, in Chapter 7, this configuration yielded very promising emission levels. Specifically, referring to the cases presented in section 7.5, many hundreds of μA were sustained from two different devices, using two different ionic liquids, after adding drops of liquid to the rear of the device. Hence we achieved a passively fed emission source using bulk porous media. The emission was remarkable in that collected currents were observed to rise at rates approaching 1 $\mu A/V$ and began at potentials as low as 850 V. Only a small fraction of the beam was intercepted by the extracting grids, a value which, possibly, could be reduced further if future iterations

are focused on enhancing ion optics. To be applied as useful propulsion systems these devices would require significantly more development and some recommended topics for investigation in this regard were summarized in section 7.8. However, this preliminary study suggests thrusts on the order of a few 10's of μN can be sustained by these small, 1.2 x 1.2 x 0.2 cm devices at power levels around 0.5 W. These performance levels would be ideal for small satellites as was discussed for, as an example, a CubeSat in Chapter 1.

However; the story is not entirely a happy ending. All arrays tested for longer than a few minutes, in section 7.5, experienced a significant current decay which was often accompanied by a thick residue coating the emitters. As discussed in section 7.7.8, this issue was likely due to electrochemistry, but it is not clear if the problem can be attributed to current imbalance, a reduced electrochemical window when using nickel with these ionic liquids, or another unforseen issue. This must, of course, be investigated further and some promise remains given the good success when using tungsten emitters for relatively long emission times. Furthermore, while the majority of results presented here used porous nickel substrates, transport limited conditions suitable for machining porous media can be enforced on a variety of materials, as demonstrated with titanium in section 6.3. The findings of these research could therefore be applicable even as an understanding of ionic liquid ion source electrochemistry evolves, possibly towards an ideal metal and ionic liquid combination.

Bibliography

[1] "The Radio Amateur Satellite Corporation : CubeSat Launch History," www.amsat.org/amsat-new/satellites/cubesats.php, 2010.

[2] Waydo, S., Henry, D., and Campbell, M., "CubeSat Design for LEO-Based Earth Science Missions," *IEEE Aerospace Conference Proceedings*, Vol. 1, 2002, pp. 435.

[3] Mueller, J., Hofer, R., and Ziemer, J., "Survey of propulsion technologies applicable to cubesats," *NASA Technical Report*, 2010.

[4] Toorian, A., Diax, K., and Lee, S., "The CubeSat Approach to Space Access," *IEEE Aerospace Conference*, Big Sky, MT, March 2008.

[5] Ladner, L. E. and Ragsdale, G. C., "Earth Orbital Satellite Lifetime," *NASA Technical Note*, 1964, TN-D-1995.

[6] Larson, W. J. and Wertz, J. R., *Space Mission Analysis and Design*, Microcosm Press and Kluwer Academic Publishers, 2005.

[7] Jahn, R. G., *Physics of Electric Propulsion*, Dover Publications, Inc., Menieola, New York, 1968.

[8] Martínez-Sánchez, M., "MIT Course 16.522, Space Propulsion Notes," MIT Open Coursware, http://ocw.mit.edu.

[9] Goebel, D. M. and Katz, I., *Fundamentals of Electric Propulsion: Ion and Hall Thrusters*, John Wiley and Sons, Inc., Hoboken, New Jersey, 2008.

[10] Martínez-Sánchez, M. and Pollard, J. E., "Spacecraft Electric Propulsion - An Overview," *Journal of Propulsion and Power*, Vol. 14, No. 5, 1998, pp. 688–699.

[11] Soulas, G. C., Domonkos, M. T., and Patterson, M. J., "Performance Evaluation of the NEXT Ion Engine," NASA Memorandum.

[12] Newton, I., *The Mathematical Principles of Natural Philosophy, Volume 1*, London, 1729, English edition translated by Andrew Motte.

[13] Goebel, D. M., Jameson, K. K., Watkins, R. M., Katz, I., and Mikellides, I. G., "Hollow Cathode Theory and Experiment. I. Plasma Characterization Using Fast Miniature Scanning Probes," *Journal of Applied Physics*, Vol. 98, No. 113302, 2005.

[14] Ketsdever, A. D. and Mueller, J., "Systems Considerations and Design Options for Microspacecraft Propulsion Systems," 35^{th} *Joint Propulsion Conference and Exhibit*, Los Angeles, CA, June 1999.

[15] "EMCO High Voltage," www.emcohighvoltage.com.

[16] Zeleny, J., "The Electrical Discharge from Liquid Points, and a Hydrostatic Method of Measuring the Electric Intensity at their Surfaces," *The Physical Review*, Vol. 3, No. 2, 1914.

[17] Zeleny, J., "Instability of Electrified Liquid Surfaces," *The Physical Review*, Vol. 10, No. 1, 1917.

[18] Taylor, G. I., "Disintegration of Water Drops in an Electric Field," *Proceedings of the Royal Society of London A*, Vol. 280, No. 1382, 1964, pp. 383–397.

[19] de la Mora, J. F., "The Fluid Dynamics of Taylor Cones," *The Annual Review of Fluid Mechanics*, Vol. 39, 2007, pp. 217–243.

[20] Hendricks, C. D. and Pfeifer, R. J., "Parametric Studies of Electrohydrodynamic Spraying," 5^{th} *Electric Propulsion Conference*, San Diego, CA, March 1966, also AIAA–66–252.

[21] Khayms, V., "Advanced Propulsion for Microsatellites," Ph.D Thesis, Massachusetts Institute of Technology, Cambridge, MA, 2000.

[22] Lozano, P. and Martínez-Sánchez, M., "Studies on the Ion-Droplet Mixed Regime in Colloid Thrusters," Ph.D Thesis, Massachusetts Institute of Technology, Cambridge, MA, 2003.

[23] de la Mora, J. F. and Loscertales, I. G., "The current emitted by highly conducting Taylor cones," *Journal of Fluid Mechanics*, Vol. 260, 1994, pp. 155–184.

[24] Perel, J., Mahoney, J. F., Moore, R. D., and Yahiku, A. Y., "Research and Development of a Charged-Particle Bipolar Thruster," *AIAA Journal*, Vol. 7, No. 3, 1969, pp. 507–511.

[25] Loscertales, I. G. and de la Mora, J. F., "Experiments on the kinetics of field evaporation of small ions from droplets," *Journal of Chemical Physics*, Vol. 103, No. 12, 1995.

[26] Gamero-Castano, M. and de la Mora, J. F., "Direct measurement of ion evaporation kinetics from electrified liquid surfaces," *Journal of Chemical Physics*, Vol. 113, No. 2, 2000.

[27] Iribarne, J. V. and Thomson, B. A., "On the Evaporation of Small Ions from Charged Droplets," *The Journal of Chemical Physics*, Vol. 64, No. 6, 1976, pp. 2287–2294.

[28] Bartoli, C., von Rohden, H., Thompson, S. P., and Blommers, J., "A liquid caesium field ion source for space propulsion," *Journal of Applied Physics D*, Vol. 17, 1984, pp. 2473–2483.

[29] Swatik, D. S., "Production of High Current Density Ion Beams by Electrohydro Dynamic Spraying Techniques," *Technical Report, Air Force Office of Scientific Research*, 1969.

[30] Tajmar, M., Vasiljevich, I., Plesescu, F., Grienauer, W., Buldrini, N., Betto, M., and del Amo, J. G., "Development of a Porous Tungsten mN-FEEP Thruster," *Space Propulsion 2010*, San Sebastian, Spain, May 2010.

[31] Cook, K. D., "Electrohydrodynamic mass spectrometry," *Mass Spectrometry Reviews*, Vol. 5, 1986, pp. 467–519.

[32] Higuera, F. J., "Liquid flow induced by ion evaporation in an electrified meniscus," *Physics Review E*, Vol. 69, No. 066301, 2004.

[33] Scharlemann, C. and Tajmar, M., "Development of Propulsion Means for Microsatellites," 43^{rd} *Joint Propulsion Conference & Exhibit*, Cincinnati, OH, July 2007.

[34] Romero-Sanz, I., nd M. Gamero-Castano, R. B., de la Mora, J. F., and Lozano, P., "Source of heavy molecular ions based on Taylor cones of ionic liquids operatin in the pure ion evaporation regime," *Journal of Applied Physics*, Vol. 94, No. 5, 2003.

[35] Welton, T., "Room-Temperature Ionic Liquids. Solvents for Synthesis and Catalysis," *Chemical Reviews*, Vol. 99, 1999, pp. 2071.

[36] Lozano, P. and Martínez-Sánchez, M., "Ionic liquid ion sources: characterization of externally wetted emitters," *Journal of Colloid and Interface Sciences*, 2005.

[37] Lozano, P. and Martínez-Sánchez, M., "Ionic liquid ion sources: suppression of electrochemical reactions using voltage alternation," *Journal of Colloid and Interface Sciences*, Vol. 280, 2004, pp. 149–154.

[38] Castro, S. and de la Mora, J. F., "Effect of tip curvature on ionic emission from Taylor cones of ionic liquids from externally wetted tungsten tips," *Journal of Applied Physics*, Vol. 105, 2009.

[39] Castro, S., Larriba, C., Sumer, S., Saito, G., Yoshida, Y., Lozano, P., and de la Mora, J. F., "Effect of liquid properties on electsprays from externally wetted ionic liquid ion sources," *Journal of Applied Physics*, Vol. 102, 2007.

[40] Larriba, C., Garoz, D., Bueno, C., Romero-Sanz, I., Castro, S., and de la Mora, J. F., "Taylor Cones of Ionic Liquids as Ion Sources: The Role of Electrical Conductivity and Surface Tension," *Ionic Liquids: Not Just Solvents Anymore*, edited by J. F. Brennecke, R. D. Rogers, and K. R. Seddon, Oxford University Press, New York, 2007.

[41] Yoshida, Y., Fujii, J., Muroi, K., Otsuka, A., Saito, G., Takahashi, M., and Yoko, T., "High conducting ionic liquids based on 1-ethyl-3methylimidazolium cation," *Synthetic Metals*, Vol. 153, 2005, pp. 421–424.

[42] Martino, W., de la Mora, J. F., Yoshida, Y., Saito, G., and Wilkes, J., "Surface tension measurements of highly conducting ionic liquids," *Green Chemistry*, Vol. 8, 2006, pp. 390–397.

[43] Lozano, P., "Energy Properties of an EMI-Im ionic liquid ion source," *Journal of Physics D: Applied Physics*, Vol. 39, 2006, pp. 126–134.

[44] Larriba, C., Castro, S., de la Mora, J. F., and Lozano, P., "Monoenergetic source of kilodalton ions from Taylor cones of ionic liquids," *Journal of Applied Physics*, Vol. 101, 2007.

[45] Takahashi, N., Zorzos, A., and Lozano, P., "Emission of Ions from Electrically Stressed Ionic Liquid Menisci in Vacuum," *Symposium on Molten Salts*, Kobe, Japan, October 2008.

[46] Hagiwara, R., Hirashige, T., Tsuda, T., and Ito, Y., "A Highly Conductive Room Temperature Molten Fluoride: EMIF2.3HF," *Journal of The Electrochemical Society*, Vol. 149, No. 1, 2002, pp. D1–D6.

[47] Yoshida, Y. and Saito, G., "Influence of structural variations in 1-alkyl-3-methylimidazolium cation and tetrahalogenoferrate(III) anion on the physical properties of paramagnetic ionic liquids," *Journal of Materials Chemistry*, Vol. 16, 2006, pp. 1254–1262.

[48] Fedkiw, T. P. and Lozano, P. C., "Development and characterization of an iodine field emission ion source for focused ion beam applications," *Journal of Vacuum Science and Technology B*, Vol. 27, No. 6, 2009, pp. 2648–2653.

[49] Fenn, J. B., Mann, M., Meng, C. K., Wong, S. F., and Whitehouse, C. M., "Electrospray Ionization for Mass Spectrometry of Large Biomolecules," *Science*, Vol. 246, No. 4926, 1989, pp. 64–71.

[50] Gassend, B., "A Fully Microfabricated Two-Dimensional Electrospray Array with Applications to Space Propulsion," PhD Thesis, Massachusetts Institute of Technology, Cambridge, MA, 2007.

[51] Brennecke, J. F. and Maginn, E. J., "Ionic Liquids: Innovative Fluids for Chemical Processing," *American Institute of Chemical Engineers Journal*, Vol. 47, No. 11, 2001, pp. 2384–2389.

[52] Buzzeo, M. C., Evans, R. G., and Compton, R. G., "Non-Haloaluminate Room-Temperature Ionic Liquids in Electrochemistry-A Review," *A European Journal of Chemical Physics and Physical Chemistry*, Vol. 5, 2004, pp. 1106–1120.

[53] Zorzos, A. N. and Lozano, P., "The use of ionic liquid ion sources in focused ion beam applications," *Journal of Vacuum Science and Technology B*, Vol. 26, No. 6, 2008, pp. 2097–2102.

[54] Perez-Martinez, C., Guilet, S., Gogneau, N., Jegou, P., Gierak, J., and Lozano, P., "Development of ion sources from ionic liquids for microfabrication," *Journal of Vacuum Science and Technology B*, Vol. 28, No. 3, 2010, pp. L25–L27.

[55] Ziemer, J. K., Randolph, T. M., Franklin, G. W., Hruby, V., Spence, D., Demmons, N., Roy, T., Ehrbar, E., Zwahlen, J., Martin, R., and Connolly, W., "Colloid nicronewton thrusters for the space technology 7 mission," *IEEE Aerospace Conference 2010*, Big Sky, MT, March 2010, also AERO–2010–5446760.

[56] Stark, J., Stevens, B., Alexander, M., and Kent, B., "Fabrication and Operation of Microfabricated Emitters as Components for a Colloid Thruster," *Journcal of Spacecraft and Rockets*, Vol. 42, No. 4, 2005, pp. 628–639.

[57] Lozano. P. and Martínez-Sánchez. M., "Efficiency Estimation of $EMI - BF_4$ Ionic Liquid Electrospray Thrusters," 41^{st} *Joint Propulsion Conference & Exhibit*, Tuscon, Arizona, 2005.

[58] Fedkiw, T. P., "Characterization of an Iodine-Based Ionic Liquid Ion Source and Studies on Ion Fragmentation," S.M. Thesis, Massachusetts Institute of Technology, Cambridge, MA, 2010.

[59] Mueller, J., "Thruster Options for Microspacecraft: A Review and Evaluation of State-of-the-Art and Emerging Technologies," *Micropropulsion for Small Spacecraft*, edited by M. M. Micci and A. D. Ketsdever, American Institute of Aeronautics and Astronautics Inc., 2000.

[60] Ziemer, J. K. and Merkowitz, S. M., "Microthrust Propulsion for the LISA Mission," 40^{th} *Joint Propulsion Conference*, Fort Lauderdale, FL, July 2004, also AIAA–2004–3439.

[61] Courtney, D. G., Li, H., Macqueo, P. D. G., Fedkiw, T. P., and Lozano, P., "On the Validation of Porous Nickel as Substrate Material for Electrospray Ion Propulsion,"

46^{th} *Joint Propulsion Conference & Exhibit*, Nashville, TN, July 2010, AIAA–2010–7020.

[62] Tajmar, M., Genovese, A., and Steiger, W., "Indium Field Emission Electric Propulsion Microthruster Experimental Characterization," *Journal of Propulsion of Power*, Vol. 20, No. 2, 2004, pp. 211–218.

[63] Merkowitz, S., Castellucci, K. E., Depalo, S. V., Generie, J. A., Maghami, P. G., and Peabody, H. L., "Current LISA Spacecraft Design," *Journal of Physics*, Vol. 154, No. 012021, 2009.

[64] Cohen, E. and Huberman, M. H., "Research on charged particle electrostatic thrustors," *Technical Report, Air Force Aero Propulsion Lab.*, 1966, AFAPL-TR-66-94.

[65] Higuera, F. J., "Model of the meniscus of an ionic-liquid ion source," *Physics Review E*, Vol. 77, No. 026308, 2008.

[66] Courtney, D. G. and Lozano, P., "Porous Ionic Liquid Ion Source Thrusters for Small Satellite Propulsion," 15^{th} *CASI Astronautics Conference*, Toronto, Canada, May 2010.

[67] Velásquez-García, L. F., Akinwande, A. I., and Martínez-Sánchez, M., "A Planar Array of Micro-Fabricated Electrospray Emitters for Thruster Applications," *Journal of Microelectromechanical Systems*, Vol. 15, No. 5, 2006, pp. 1272–1280.

[68] Washburn, E. W., "The Dynamics of Capillary Flow," *The Physical Review*, Vol. 17, No. 3, 1921, pp. 273.

[69] Legge, R., Lozano, P., and Martínez-Sánchez, M., "Fabrication and Characterization of Porous Metal Emitters for Electrospray Thrusters," 30^{th} *International Electric Propulsion Conference*, Florence, Italy, September 2007, also IEPC–07–145.

[70] Legge, R. and Lozano, P., "Fabrication and Characterization of Porous Metal Emitters for Electrospray Applications," S. M. Thesis, Massachusetts Institute of Technology, Cambridge, MA, 2008.

[71] Courtney, D. G. and Lozano, P., "Porous Ionic Liquid Ion Source Fabrication Refinements and Variable Beam Energy Experiments," 45^{th} *Joint Propulsion Conference & Exhibit*, Denver, CO, August 2009, also AIAA–2009–5087.

[72] Legge, R. and Lozano, P., "Performance of Heavy Ionic Liquids with Porous Metal Electropsray Emitters," 44^{th} *Joint Propulsion Conference & Exhibit*, Hartford, CT, July 2008, also AIAA–2008–5002.

[73] Courtney, D. G. and Lozano, P., "Development of Ionic Liquid Electrospray Thrusters Using Porous Substrates," 27^{th} *International Symposium on Space Technology and Science*, Tsukuba, Japan, July 2009.

[74] Clark, K. E., "Survey of Electric Propulsion Capability," 10^{th} *AIAA/SAE Propulsion Conference*, San Diego, CA, Oct. 1974, also AIAA–74–1082.

[75] Rosen, S. G., "Colloid and Pulsed Plasma Thrusters for Spacecraft Propulsion," 9^{th} *AIAA/SAE Propulsion Conference*, Las Vegas, NV, November 1973, also AIAA-73-1254.

[76] Perel, J., Mahoney, J. F., and Daley, H. L., "Duration Test of an Annular Colloid Thruster," 9^{th} *AIAA Electric Propulsion Conference*, Bethesda, MD, April 1972, also AIAA–72–483.

[77] Bailey, A. G., Bracher, J. E., and von Rohden, H. J., "A capillary-fed annular colloid thruster," *Journal of Spacecraft and Rockets*, Vol. 9, No. 7, 1972, pp. 518–521.

[78] Gamero-Castano, M., "Characterization of a Six-Emitter Colloid Thruster Using a Torsional Balance," *Journal of Propulsion and Power*, Vol. 20, No. 4, 2004, pp. 736–741.

[79] Krpoun, R. and Shea, H. R., "Integrated out-of-plane nanoelectrospray thruster arrays for spacecraft propulsion," *Journal of Micromechanics and Microengineering*, Vol. 19, 2009.

[80] Lenguito, G., de la Mora, J. F., and Gomez, A., "Multiplexed Electrospray for Space Propulsion Applications," 46^{th} *Joint Propulsion Conference & Exhibit*, Nashville, TN, July 2010, also AIAA–2010–6521.

[81] Deng, W., Klemic, J. F., Li, X., Reed, M. A., and Gomez, A., "Increase of electrospray througput using multiplexed microfabricated sources for the scalable generation of monodisperise droplets," *Aerosol Science*, Vol. 37, 2006, pp. 696–714.

[82] Velásquez-García, L. F., "A Microfabricated Colloid Thruster Array," S.M. Thesis, Massachusetts Institute of Technology, Cambridge, MA, June 2001.

[83] Velásquez-García, L. F., "The Design, Fabrication and Testing of Micro-fabricated Linear and Planar Colloid Thruster Arrays," Ph.D. Thesis, Massachusetts Institute of Technology, Cambridge, MA, June 2004.

[84] Gassend, B., Velásquez-García, L. F., Akinwande, A. I., and Martínez-Sánchez, M., "A Fully-Integrated microfabricated externally-wetted electrospray thruster," 30^{nd} *International Electric Propulsion Conference*, Florence, Italy, September 2007, also IEPC–2007–233.

[85] Tajmar, M., Genovese, A., Buldrini, N., and Steiger, W., "Miniaturized Indium-FEEP Multiemitter Design and Performance," *NanoTech 2002*, Houston, TX, September 2002.

[86] Biagioni, L., Ceccanti, F., Saverdi, M., Saviozzi, M., and Andrenucci, M., "Qualification Status of the FEEP-150 Electric Micropropulsion Subsystem," 41^{st} *Joint Propulsion Conference and Exhibit*, Tucson, AZ, March 2005, also AIAA–2005–4261.

[87] Mason, G. and Morrow, N. R., "Effect of Contact Angle on Capillary Displacement Curvatures in Pore Throats Formed by Spheres," *Journal of Colloid and Interface Science*, Vol. 168, 1994, pp. 130–141.

[88] Lago, M. and Araujo, M., "Capillary Rise in Porous Media," *Physica A*, Vol. 289, 2001, pp. 1–17.

[89] Perry, R. H. and Green, D. W., *Perry's Chemical Engineers' Handbook, 7^{th} Edition*, McGraw-Hill, 1997.

[90] III, W. D. C., "Goodbye, Hazen; Hello, Kozeny-Carman," *Journal of Geotechnical and Geoenvironmental Engineering*, Vol. 129, No. 11, 2003, pp. 1054–1056.

[91] Dullien, F. A. L., "Capillary and Viscous Effects in Porous Media," *Handbook of Porous Media*, edited by K. Vafai and H. A. Hadim, Marcel Dekker, Inc., New York, 2000.

[92] Glover, P. W. J. and Walker, E., "Grain-size to Effective Pore-size Transformation Derived from Electrokinetic Theory," *Geophyics*, Vol. 74, No. 1, 2009, pp. E17–E29.

[93] Mair, G. L. R., "Theoretical Determination of Current-Voltage Curves for Liquid Metal Ion Sources," *Journal of Physics D: Applied Physics*, Vol. 17, 1984, pp. 2323–2330.

[94] Lozano, P., "Personal Communications," 2010.

[95] Garza, T. C., "Optimizing Wettability of Externally Wetted Microfabricated Silicon Electrospay Thrusters," S.M. Thesis, Massachusetts Institute of Technology, Cambridge, MA, 2007.

[96] Senturia, S., *Microsystem Design*, Springer Science + Business Media, LLC, 2001.

[97] Herino, R., Bomchil, G., Barla, K., Bertrand, C., and Ginoux, J. L., "Porosity and Pore Size Distributions of Porous Silicon Layers," *Journal of The Electrochemical Society*, Vol. 134, No. 8, 1987, pp. 1994–2000.

[98] Steiner, P. and Lang, W., "Micromachining applications of porous silicon," *Thin Solid Films*, Vol. 255, 1995, pp. 52–58.

[99] Feyh, A., Laermer, F., Kronmüller, S., and Mokwa, W., "A novel process for the preparation of thick porous silicon layers with very high porosity," *Phys. Stat. Sol.*, Vol. 202, No. 8, 2005, pp. 1597–1601.

[100] Smith, R. L. and collins, S. D., "Porous silicon formation mechanisms," *Journal of Applied Physics*, Vol. 71, No. 8, 1992.

[101] Yue, W. K., Parker, D. L., and Weichold, M. H., "Porous silicon electron-emitting source," *Electron Devices Meeting, 1990*, San Francisco, CA, Dec. 1990, also IEDM–1990–237201.

[102] Tang, C. C. and Hess, D. W., "Tungsten Etching in CF_4 and SF_6 Discharges," *Journal fo the Electrochemical Society: Solid-State Science and Technology*, Vol. 131, No. 1, 1984, pp. 115–120.

[103] Williams, K. R., Gupta, K., and Wasilik, M., "Etch Rates for Micromachining Processes- Part II," *Journal of Microelectromechanical Systems*, Vol. 12, No. 6, 2003, pp. 761.

[104] Liu, L., Loh, N. H., Tay, B. Y., Tor, S. B., Murakoshi, Y., and Maeda, R., "Micro powder injection molding: Sintering kintects of microstructured components," *Scripta Materialia*, Vol. 55, 2006, pp. 1103–1106.

[105] Fu, G., Loh, N. H., Tor, S. B., Murakoshi, Y., and Maeda, R., "Effects of Injection Molding Parameters on the Production of Microstructures by Micropowder Injection Molding," *Materials and Manufacturing Processes*, Vol. 20, 2005, pp. 977–985.

[106] Yeo, S. H., Choo, J. H., and Sim, K. H. A., "On the Effects of ultrasonic vibrations on localized electrochemical deposition," *Journal of Micromechanics and Microengineering*, Vol. 12, 2002, pp. 271–279.

[107] Jansson, A., Thornell, G., and Johansson, S., "High Resolution 3D Microstructures Made by Lozalized Electrodeposition of Nickel," *Journal of the Electrochemical Society*, Vol. 147, No. 5, 2000, pp. 1810–1817.

[108] Spindt, C. A., Brodie, I., Humphrey, L., and Westerberg, E. R., "Physical properties of thin-film field emission cathodes with molybdenum cones," *Journal of Applied Physics*, Vol. 57, No. 12, 1976, pp. 5248–5263.

[109] Hart, A. J. and Slocum, A. H., "Rapid Growth and Flow-Mediated Nucleation of Millimeter-Scale Aligned Carbon Nanotube Structures from a Thin-Film Catalyst," *Journal of Physical Chemistry B*, Vol. 110, 2006, pp. 8250–8257.

[110] García, E. J., Hart, A. J., Wardle, B. L., and Slocum, A. H., "Fabrication of composite microstructures by capillarity-driven wetting of aligned carbon nanotubes with polymers," *Nanotechnology*, Vol. 18, No. 165602, 2007.

[111] de Heer, W. A., Chatelain, A., and Ugarte, D., "A Carbon Nanotube Field-Emission Electron Source," *Science*, Vol. 270, No. 5239, 1995, pp. 1179–1180.

[112] Fan, S., Chapline, M. G., Franklin, N. R., Tombler, T. W., Cassell, A. M., and Dai, H., "Self-Oriented Regular Arrays of Carbon Nanotubes and Their Field Emission Properties," *Science*, Vol. 283, 1999, pp. 512–514.

[113] Maqueo, P. D. G., "Personal Communications," 2010.

[114] Akimov, Y. K., "Field of Application of Aerogels (Review)," *Instruments and Experimental Techniques*, Vol. 46, No. 3, 2003, pp. 5–19.

[115] Yokokawa, R., Paik, J., Dunn, B., Kitazawa, N., Kotera, H., and Kim, C., "Mechanical properties of aerogel-like thin films used for MEMS," *Journal of Micromechanics and Microengineering*, Vol. 14, 2004, pp. 681–686.

[116] Tappan, B. C., Huynh, M. H., Hiskey, M. A., Chavez, D. E., Luther, E. P., Mang, J. T., and Son, S. F., "Ultralow-Density Nanostructured Metal Foams: Combustion Synthesis, Morphology and Composition," *Journal of the American Chemical Society*, Vol. 128, No. 20, 2006, pp. 6589–6594.

[117] Erlebacher, J., Aziz, M. J., Karma, A., Dimitrov, N., and Sieradzki, K., "Evolution of nanoporosity in dealloying," *Nature*, Vol. 410, 2001, pp. 450–453.

[118] Sun, L., Chien, C.-L., and Searson, P. C., "Fabrication of Nanoporous Nickel by Electrochemical Dealloying," *Chemistry of Materials*, Vol. 16, 2004, pp. 3125–3129.

[119] Bockris, J. O., Reddy, A. K. N., and Gamboa-Aldeco, M., *Modern electrochemistry 2A: Fundamentals of Electrodics, Second Edition*, Kluwer Academic/Plenum Publishers, New York, 2000.

[120] Dandolt, D., Chauvy, P.-F., and Zinger, O., "Electrochemical Micromachining, Polishing and Surface Structuring of Metals: Fundamental Aspects and New Developments," *Electrochimica Acta*, Vol. 48, 2003, pp. 3185–3201.

[121] Datta, M., "Anodic Dissolution of Metals at High Rates," *IBM Journal of Research and Development*, Vol. 37, No. 2, 1993, pp. 207.

[122] Datta, M. and Landolt, D., "Fundamental Aspects and Applications of Electrochemical Microfabrication," *Electrochimica Acta*, Vol. 45, 2000, pp. 2535–2558.

[123] Grimm, R. D., West, A. C., and Landolt, D., "AC Impedance Study of Anodically Formed Salt Films on Iron in Chloride Solution," *Journal of the Electrochemical Society*, Vol. 139, No. 6, 1992, pp. 1622–1629.

[124] Russell, P. and Newman, J., "Anodic Dissoultion of Iron in Acidic Sulfate Electrolytes," *Journal of the Electrochemical Society: Electrochemical Science and Technology*, Vol. 133, No. 1, 1986, pp. 59–69.

[125] Madore, C., Piotrowski, O., and Landolt, D., "Through-Mask Electrochemical Micromachining of Titanium," *Journal of The Electrochemical Society*, Vol. 146, No. 7, 1999, pp. 2526–2532.

[126] Selman, J. R. and Tobias, C. W., "Mass-Transfer Measurements by the Limiting-Current Technique," *Advances in Chemical Engineering*, edited by T. B. Drew, G. R. Cokelet, J. W. Hoopes, and T. Vermeulen, Academic Press, New York, 1978.

[127] Isaacson, M. S. and Sonin, A. A., "Sherwood Number and Friction Factor Correlations for Electrodialysis Systems, with Application to Process Optimization," *Industrial and Engineering Chemistry Process Design and Development*, Vol. 15, No. 2, 1976, pp. 313–321.

[128] Speight, J. G., *Lange's Handbook of Chemistry, 16^{th} Edition*, McGraw-Hill, 2005.

[129] Datta, M. and Landolt, D., "Surface Brightening During High Rate Nickel Dissolution in Nitrate Electrolytes," *Journal of the Electrochemical Society : Electorchemical Science and Technology*, Vol. 122, No. 11, 1975, pp. 1466–1472.

[130] Strehblow, H.-H. and Wenners, J., "Investigation of the Processes on Iron and Nickel Electrodes at High Corrosion Curreent Densities in Solutions of High Chloride Content," *Electrochimica Acta*, Vol. 22, 1977, pp. 421–427.

[131] Madore, C. and Landolt, D., "Electrochenmical Micromachining of Controlled Topographies on Titanium for Bilogical Applications," *Journal of Micromechanics and Microengineering*, Vol. 7, 1997, pp. 270–275.

[132] Datta, M. and Landolt, D., "Electrochemical Saw Using Pulsating Voltage," *Journal of Applied Electrochemistry*, Vol. 13, 1983, pp. 795–802.

[133] Kern, P., Veh, J., and Michler, J., "New developments in through-mask electrochemical micromachining of titanium," *Journal of Micromechanics and Microengineering*, Vol. 17, 2007, pp. 1168–1177.

[134] Lescuras, V., Andre, J. C., Lapicque, F., and Zouari, I., "Jet electrochemical etching of nickel in a sodium chloride medium assisted by a pulsed laser beam," *Journal of Applied Electrochemistry*, Vol. 25, 1995, pp. 933–939.

[135] Datta, M. and Harris, D., "Electrochemical Micromachining: An Environmentally Friendly, High Speed Processing Technology," *Electrochimica Acta*, Vol. 42, No. 20-22, 1997, pp. 3007–3013.

[136] Kozak, J., Rajurkar, K. P., and Makkar, Y., "Selected problems of micro-electrochemical machining," *Journal of Materials Processing Technology*, Vol. 149, 2004, pp. 426–431.

[137] Bhattacharyya, B., Mitra, S., and Boro, A., "Electrochemical machining: new possbilities for micromachining," *Robotics and Computer Integrated Manufacturing*, Vol. 18, 2002, pp. 283–289.

[138] Rosier, R. C. A. D. B. and Sani, R. L., "Effect of Fluid Flow on Removal of Dissolution Products from Small Cavities," *Journal of the Electrochemical Society : Electrochemical Science and Technology*, Vol. 131, No. 12, 1984, pp. 2785–2800.

[139] Hampson, N. A. and McNeil, A. J. S., "The Electrochemistry of Porous Electrodes: Flooded, Static (Natural) Electrodes," *Electrochemistry Volume 8*, edited by D. Pletcher, The Royal Society of Chemistry, 1983.

[140] Newman, J. S. and Tobias, C. W., "Theoretical Analysis of Current Distribution in Porous Electrodes," *Journal of the Electrochemical Society*, Vol. 109, No. 12, 1962, pp. 1183–1191.

[141] Alkire, R. C., Grens-II, E. A., and Tobias, C. W., "A Theory for Porous Electrodes Undergoing Structural Change by Anodic Dissolution," *Journal of the Electrochemical Society : Electrochemical Science*, Vol. 116, No. 10, 1969, pp. 1328–1333.

[142] Bockris, J. O. and Reddy, A. K. N., *Modern electrochemistry 1: Ionics, Second Edition*, Plenum Press, New York, 1998.

[143] Chin, D.-T., "Mass Transfer and Current-Potential Relation in Pulse Electrolysis," *Journal of the Electrochemical Society : Electrochemical Science and Technology*, Vol. 130, No. 8, 1983, pp. 1657–1667.

[144] Ibl, N., "Some Theoretical Aspects of Pulse Electrolysis," *Surface Technology*, Vol. 10, 1980, pp. 81–104.

[145] Cheh, H. Y., "Electrodeposition of Gold by Pulsed Current," *Journal of the Electrochemical Society: Electrochemical Science*, Vol. 118, No. 4, 1971, pp. 551–557.

[146] Datta, M. and Landolt, D., "Experimental Investigation of Mass Transport in Pulse Plating," *Surface Technology*, Vol. 25, 1985, pp. 97–110.

[147] Tang, C. C. and Wan, C. C., "Effect of Pulsating Current on the Limiting Current and Deposit Structure of a Silver Plating System," *Materials Chemistry and Physics*, Vol. 24, 1990, pp. 503–509.

[148] Dukovic, J. O., "Computation of current disbritubtion in electrodeposition, a review," *EBM Journal of Research and Development*, Vol. 34, 1990.

[149] Datta, M. and Landolt, D., "Eletrochemical machining under pulsed current conditions," *Electrochimica Acta*, Vol. 26, No. 7, 1981, pp. 899–907.

[150] Clerc, C. and Landolt, D., "Anodic Levelling of Model Profiles with Pulsating Current," *Journal of Applied Electrochemistry*, Vol. 17, 1987, pp. 1144–1149.

[151] Chin, D.-T. and Venkatesh, S., "A-C Modulation of a Rotating Zinc Electrode in an Acid Zinc-Chloride Solution," *Journal of the Electrochemical Society : Electrochemical Science and Technology*, Vol. 128, No. 7, 1981, pp. 1439–1442.

[152] Chin, D.-T., Sethi, R., and McBreen, J., "Zinc Electrode Morphology in Alkaline Solutions," *Journal of the Electrochemical Society : Electrochemical Science and Technology*, Vol. 129, No. 12, 1982, pp. 2677–2685.

[153] Alkire, R. and Deligianni, H., "The Role of Mass Transport on Anisotropic Electrochemical Pattern Etching," *Journal of the Electrochemical Society : Electrochemical Science and Technology*, Vol. 135, No. 5, 1988, pp. 1093–1099.

[154] West, A. C., Madore, C., Matlosz, M., and Landolt, D., "Shape Changes during Through-Mask Electrochemical Micromachining of Thin Metal Films," *Journal of the Electrochemical Society*, Vol. 139, No. 2, 1992, pp. 499–506.

[155] Datta, M. and Romankiw, L. T., "Electrochemical Micromachining Tool and Process for Through-Mask Patterning of Thin Metallic Films Supported by Non-Conducting or Poorly Conducting Surfaces," United States Patent 5,284,554, 1994.

[156] Li, H. Q., Courtney, D. G., Maqueo, P. D. G., and Lozano, P., "Fabrication and Testing of an Ionic Electrospray Propulsion System with a Porous Metal Tip Array," *Transducers 2011*, Beijing, China, June 2011.

[157] NASA, "Outgassing Data for Selecting Spacecraft Materials," http://outgassing.nasa.gov/.

[158] Timoshenko, S. P. and Woinowsky-Krieger, S., *Theory of Plates and Shells*, McGraw-Hill, 1959.

[159] Ericson, F. and Schweitz, J.-A., "Micromechanical Fracture Strength of Silicon," *Journal of Applied Physics*, Vol. 68, No. 11, 1990.

[160] Piotrowski, O., Maore, C., and Landolt, D., "The Mechanism of Electropolishing of Titanium in Methanol-Sulfuric Acid Electrolytes," *Journal of Electrochemical Society*, Vol. 145, No. 7, 1998, pp. 2362–2369.

[161] Cavallini, M. and Biscarini, F., "Electrochemically etched nickel tips for spin polarized scanning tunneling microscopy," *Review of Scientific Instruments*, Vol. 71, 2000, pp. 4457.

[162] Takahashi, N., "Molecular Dynamics Modeling of Ionic Liquids in Electrospray Propulsion," S.M. Thesis, Massachusetts Institute of Technology, Cambridge, MA, 2010.

[163] Wakai, C., Oleinikova, A., Ott, M., and Weingärtner, H., "How Polar Are Ionic Liquids? Determination of the Static Dielectric Constant of an Imidazolium-based Ionic Liquid by Microwave Dielectric Spectroscopy," *The Journal of Physiacl Chemistry B: Letters*, Vol. 109, 2005, pp. 17028–17030.

[164] Valkenburg, M. E. V., Vaughn, R. L., Williams, M., and Wilkes, J. S., "Ionic Liquid Heat Transfer Fluids," 15^{th} *Symposium on Thermophysical Properties*, Boulder, CO, June 2003.

[165] Ohno, H., *Electrochemical Aspects of Ionic Liquids*, John Wiley and Sons, Hoboken, New Jersey, 2005.

[166] Moganty, S. S., Baltus, R. E., and Roy, D., "Electrochemical Windows and Impedance Characteristics of $[Bmim^+][BF_4^-]$ and $[Bdmim^+][BF_4^-]$ Ionic Liquids at the Surfaces of Au, Pt, Ta and Glassy Carbon Electrodes," *Chemical Physics Letters*, Vol. 483, 2009, pp. 90–94.

[167] Barrose-Antle, L. E., Bond, A. M., Compton, R. G., O'Mahony, A. M., Rogers, E. I., and Silvester, D. S., "Voltammetry in Room Temperature Ionic Liquids: Comparisions and Contrasts with Conventional Electrochemical Solvents," *Chemistry - An Asian Journal*, Vol. 5, 2010, pp. 202–230.

[168] Chen, P.-Y. and Sun, I.-W., "Electrochemical Study of Copper in a Basic 1-ethyl-3-methylimidazolium tetrafluoroborate Room Temperature Molten Salt," *Electrochemica Acta*, Vol. 45, 1999, pp. 441–450.

[169] Galiński, M., Lewandowski, A., and Stępniak, I., "Ionic Liquids as Electrolytes," *Electrochimica Acta*, Vol. 51, 2006, pp. 5567–5580.

[170] Aurbach, D., *Nonaqueous Electrochemistry*, CRC Press, 1999.

[171] Nanjundiah, C., McDevitt, S. F., and Koch, V. R., "Differential Capacitance Measurements in Solvent-Free Ionic Liquids at Hg and C Interfaces," *Journal of the Electrochemical Society*, Vol. 144, No. 10, 1997, pp. 3392–3397.

[172] Fedorov, M. and Kornyshev, A. A., "Ionic Liquid Near a Charged Wall: Structure and Capaciatance of Electrical Double Layer," *The Journal of Physical Chemistry B: Letters*, Vol. 112, 2008, pp. 11868–11872.

[173] Kornyshev, A. A., "Double-Layer Ionic Liquids: Paradigm Change?" *Journal of Physical Chemistry B*, Vol. 111, 2007, pp. 5545–5557.

Appendix A

Low Density Porous Tungsten Arrays with Two Microfabricated Grids

This experiment was a direct extension of previous work by Legge[70] using flat/linear arrays of porous tungsten emitters.

These experiments had two goals, first, to demonstrate the capability to control both emitted current and beam energy using two electrostatic grids, as was briefly mentioned in section 2.1.2, and second, to test if available silicon wafers could be used as electrostatic grids for porous electrospray thrusters.

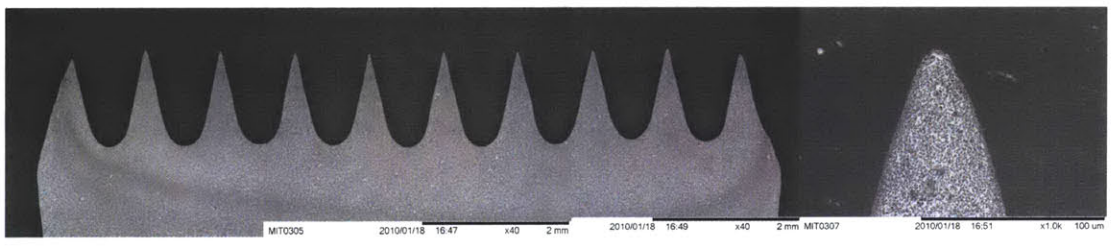

Figure A-1: SEM composite image and emitter from a sample linear array representative of those used in these tests.

A.1 Source Design

This design used grids fabricated from standard (n-test, ~1-10 $\Omega - cm$) silicon wafers available from the MIT Micro Technologies Laboratory. The grids were fabricated by etching 750 μm wide, 15 mm long trenches through 650 μm thick silicon wafers using reactive ion etching, details of this etch are provided below. The emitter strips used here were etched electrochemically in a simple NaOH cell, before development of the etch station described in this thesis. The process used to fabricate the emitters was altered slightly from that developed by Legge, particularly through using a dry film mask adding secondary etching to round the emitters. Further details concerning the etching scheme can be found in a paper presented at the 2009 Joint Propulsion Conference[71]. A sample array is shown in Figure A-1.

The arrays were mounted in a 3D printed ABS plastic base as shown in Figure A-2(a). The equipment listed in section 7.1.1 was used during these tests. An additional Matsusada AMS-5B6 power supply was added to the standard configuration (Fig. 7-2). With this additional supply the extracting potential, $V_{extract}$, defined here as the difference between the emitter and extracting grid potentials was held constant while the overall potential drop, V_{emit} was altered. In the absence of field penetration from the second downstream grid, this setup would ideally allow for independent control of the current, through $V_{extract}$, and the net energy, through V_{emit}.

In the variable beam experiments below, the two Matsusada supplies were driven by a single Agilent signal generator with the desired emitting current applied through a manual bias to one of these supplies. The input signal was set to step the total emitter potential from over a desired range while maintaining the extracting potential constant over 13 steps, repeated every 10 seconds. Figure A-3 provides an example of the inputs used to vary the beam potential from 0.5 to 2.5 kV while maintaining a 1.5 kV extracting potential. The ScopeMeter was used to monitor the emitting and extractor plate currents while the accelerating grid and collector plate currents were measured with the 6514 and 6517 Keithley electrometers respectively.

Initial tests used an array consisting of 2 strips of 10 emitters with variable tip and grid spacings. This setup was used to select appropriate spacings between the extractors and the emitter, as shown in Figure A-2(b). The final device used 8 new strips of 10 emitters

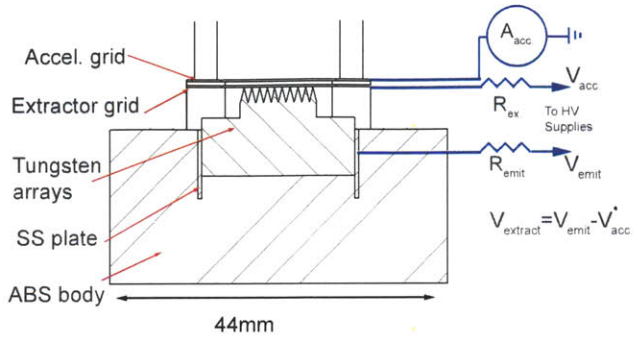

(a) Schematic cross section of the mount used to house porous tungsten linear arrays, with 10 emitters per array.

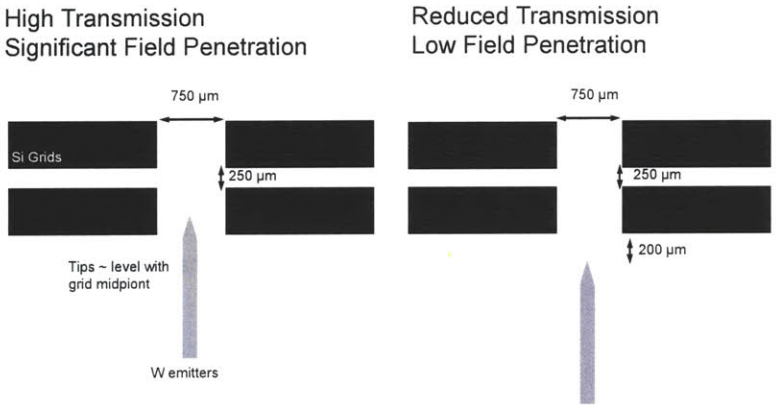

(b) The positions of the thick electrostatic grids relative to themselves and the array tips impacted performance.

Figure A-2: Overview of the dual grid tungsten emitter array mount and key geometrical parameters.

per array for 80 emitters total. Images of the final device are shown in Figure A-4. Along each strip, the emitters were spaced 1 *mm* apart, as shown in Figure A-1. The strips were spaced 2.5 *mm* apart within the ABS mount.

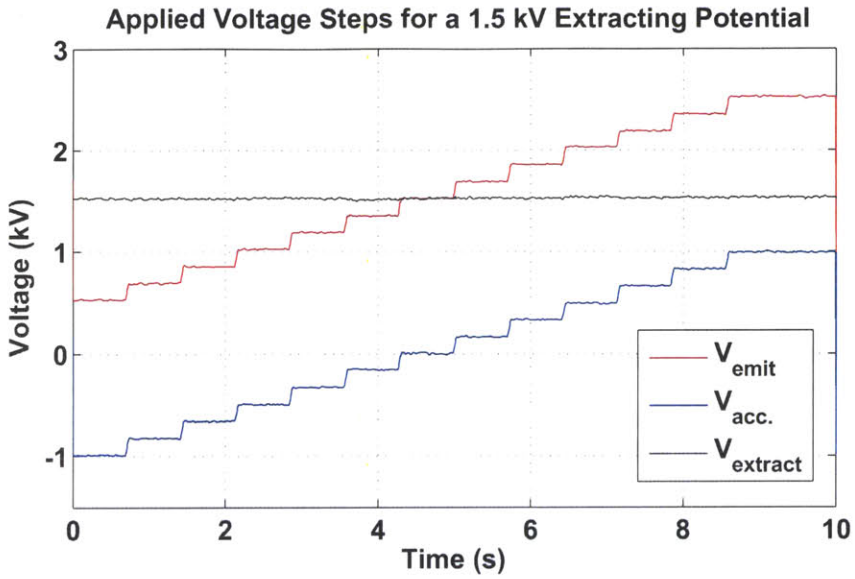

Figure A-3: Measurements at variable beam energy with constant extracting potential were performed by stepping V_{emit} and $V_{acc.}$ together while maintaining a constant differential.

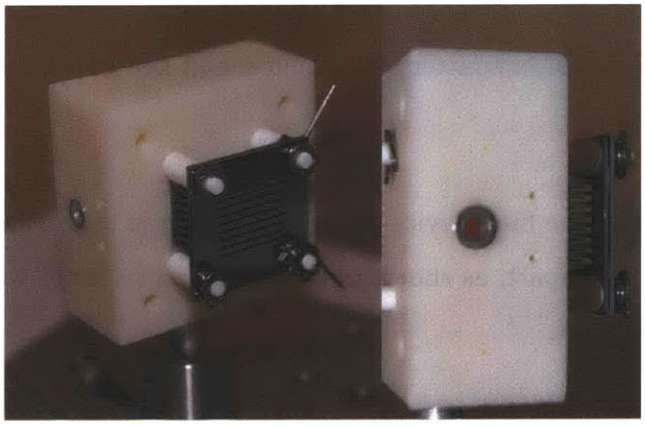

(a) Photographs of the assembled emitter thruster with two silicon electrostatic grids.

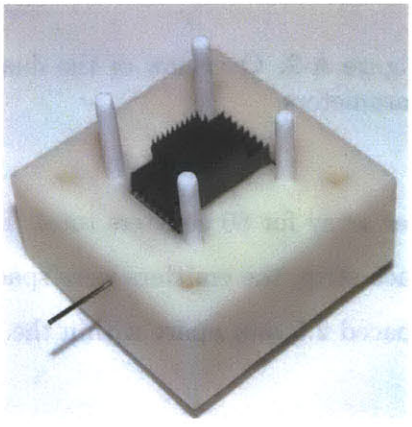

(b) Photograph of the linear 8 arrays of 10 porous tungsten emitters assembled into the ABS mount.

Figure A-4: Photographs of the 80 emitter porous tungsten, dual grid, test thruster.

A.1.1 Grid Fabrication Process

Grids were fabricated within the Technology Research Laboratory (TRL) portion of MTL beginning with $6''$ wafers. The process was recommended by Anthony Zorzos and Dennis Ward of MIT and is outlined in table A.1.

Table A.1: Fabrication Process for Silicon Slit Grids

Process Stage	**Equipment**	**Wafers**	**Notes**
Resist coating	spin coater	Silicon	8 μm of AZP4620 resist
	$95°C$ furnace	Silicon	30 minute bake
	spin coater	Silicon	8 μm of AZP4620 resist
	$95°C$ furnace	Silicon	60 minute bake
Photolithography	aligner	Silicon	7 intervals, $15s$ exposure, $15s$ relaxation time
		Silicon	Develop in AZ 440 MIF
Wafer mounting	spin coater	Quartz	AZP4620 target pattern
		Silicon/Quartz	Mount silicon wafer onto dummy quartz wafer
	$95°C$ furnace	Silicon/Quartz	30 minute bake
Through wafer etch	SF_6/C_4F_8 plasma	Silicon/Quartz	DRIE etch through silicon wafer ($\sim$ 12 hours)

A.2 Variable Beam Energy Demonstrations

Data acquired using the 20 emitter array configured as on the left side of Fig. A-2(b) are presented in Figure A-5. In this case the array was configured for maximum transmission through the first electrostatic grid. Here the extracting potential has been held constant at $\pm$ 2.0 kV while the overall potential V_{emit} was varied from 0 to 4.0 kV. The data are plotted against the ratio of the overall emitter potential to the extracting potential. The data has been averaged over each step in emitter potential with the indicated errorbars giving the standard deviation during that step. The plots show that while low interception on the grid was maintained, the emitted current varies significantly throughout the test. Recall that ideally the emitted and transmitted currents would remain fixed throughout this scan as the beam is electrostatically slowed or accelerated downstream.

The second configuration shown in Fig. A-2(b) was identified, using the 20 emitter array, to have less potential penetration and was selected when assembling the larger 80 emitter array thruster shown in Fig. A-4. Before testing for variable energy, an IV sweep was taken with both electrostatic grids grounded (no downstream acceleration). As shown in Figure A-2(b), high emission currents were obtained with this device but the beam current was greatly reduced due to high levels of interception on both electrostatic grids.

The thruster was then used for variable beam energy measurements as in the example above. In this case the total emitter potential was varied from 0.5 to 2.5 kV (as in Fig. A-3) in both positive and negative polarities. Samples of the collected data are provided in Figure A-7. The collected data suffered from high levels of noise, particularly in the positive polarity case. However; despite the noise, the results indicate that, compared with the transmission targeted example above, this configuration can sustain emission more favorably during deceleration. Although the emitted current is clearly influenced by the net beam potential, the dependence has been reduced at the expense of significant beam interception.

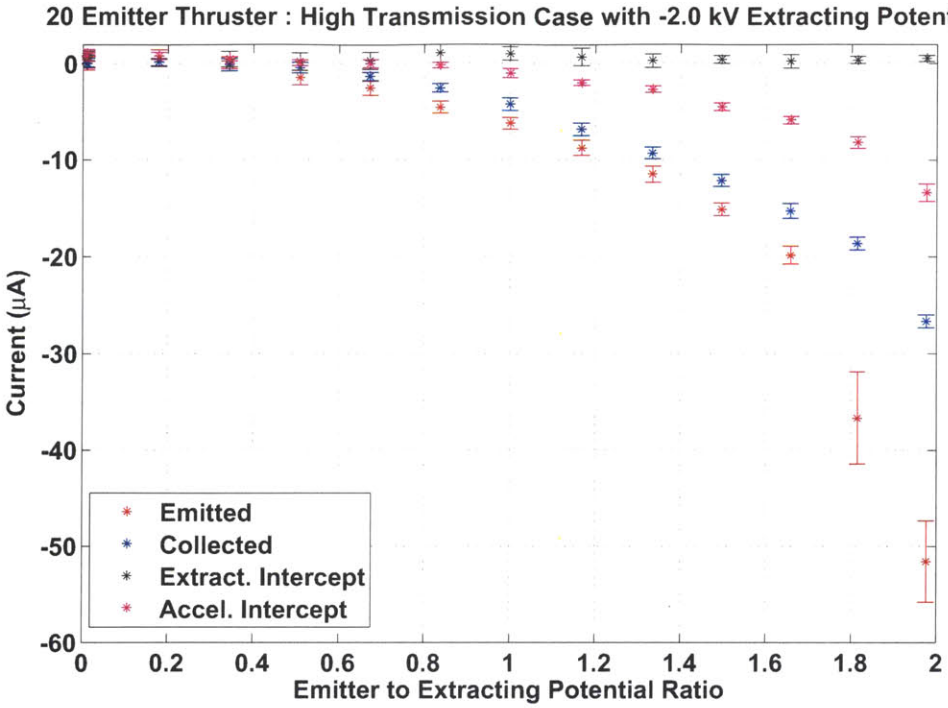

(a) Current measurements made while ramping the net emitter potential while holding the extracting potential constant at -2.0 kV.

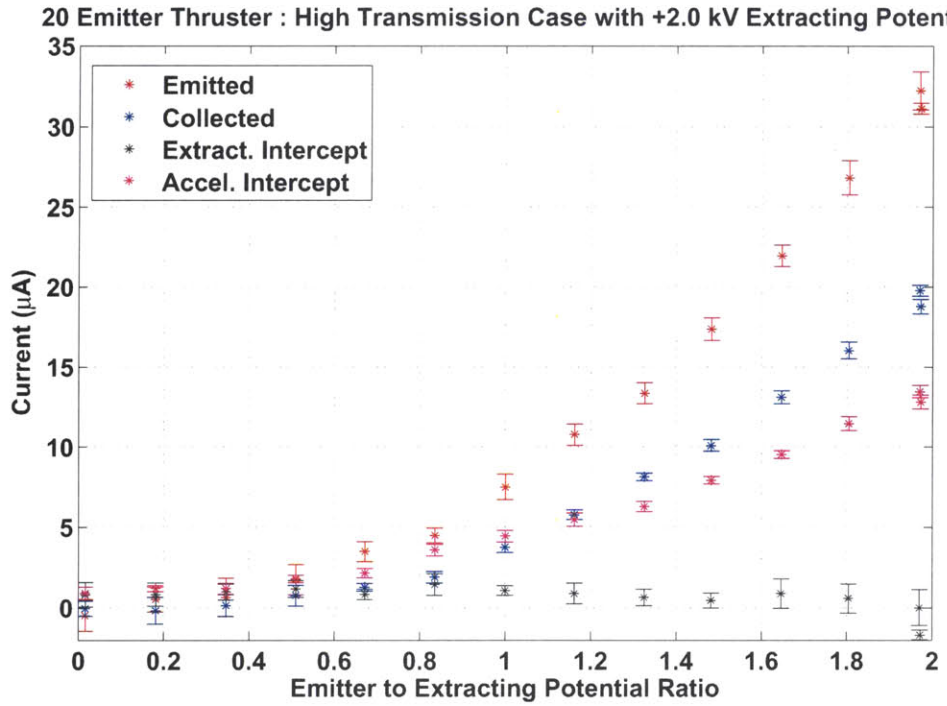

(b) Current measurements made while ramping the net emitter potential while holding the extracting potential constant at +2.0 kV.

Figure A-5: Variable beam energy tests for an extracting potential of $\pm$ 2.0 kV for the low beam interception case of Fig. A-2(b)

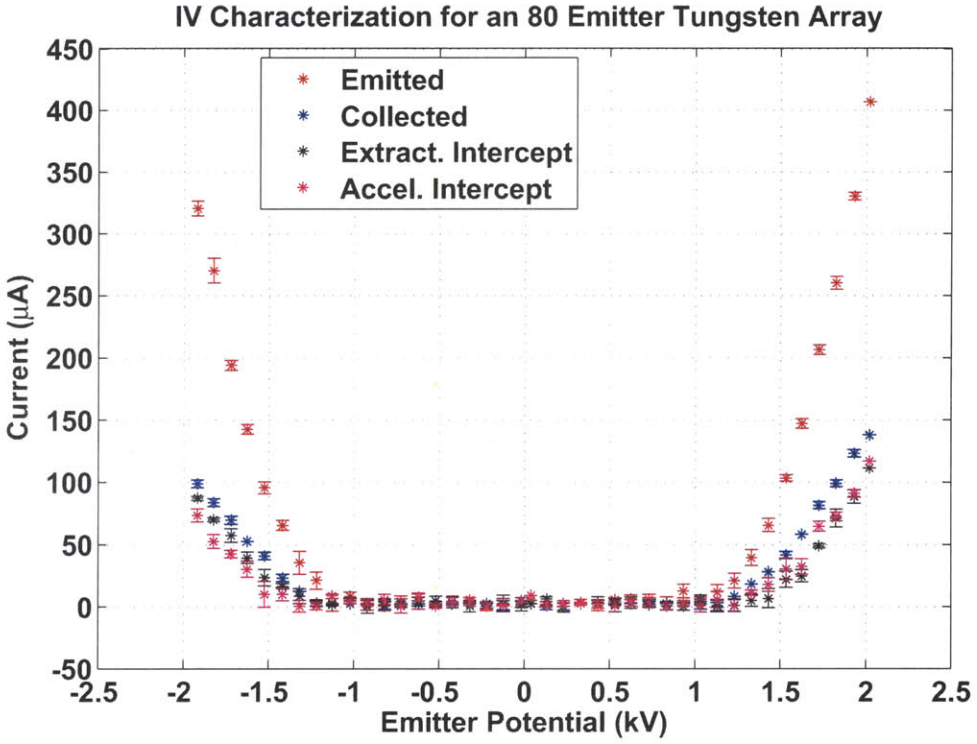

Figure A-6: Initial IV characterization of an 80 emitter, porous tungsten array configured using the low field penetration grid and emitter spacings shown in Fig. A-2(b).

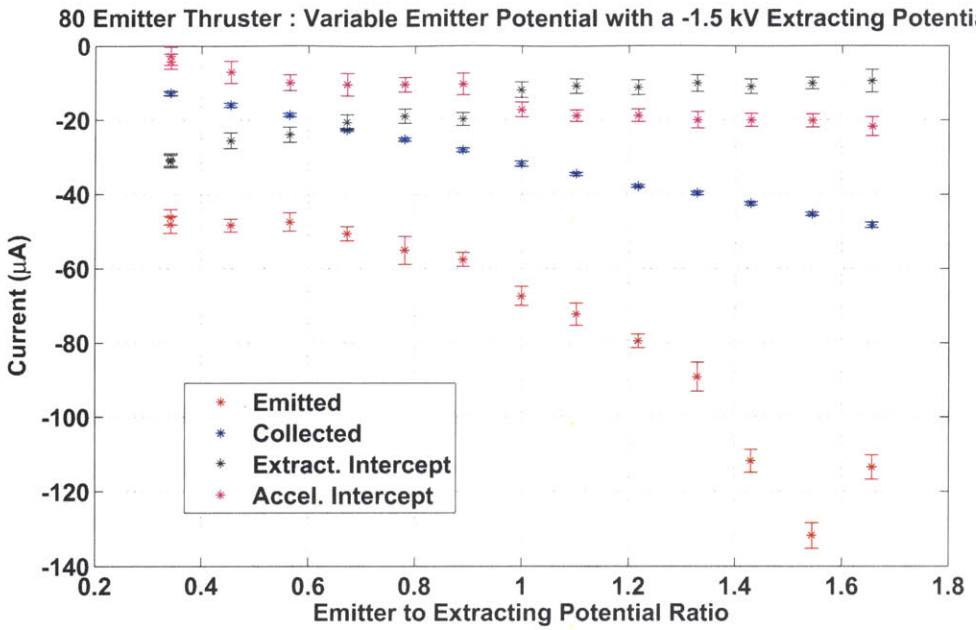

(a) Current measurements made while ramping the net emitter potential while holding the extracting potential constant at -1.5 kV.

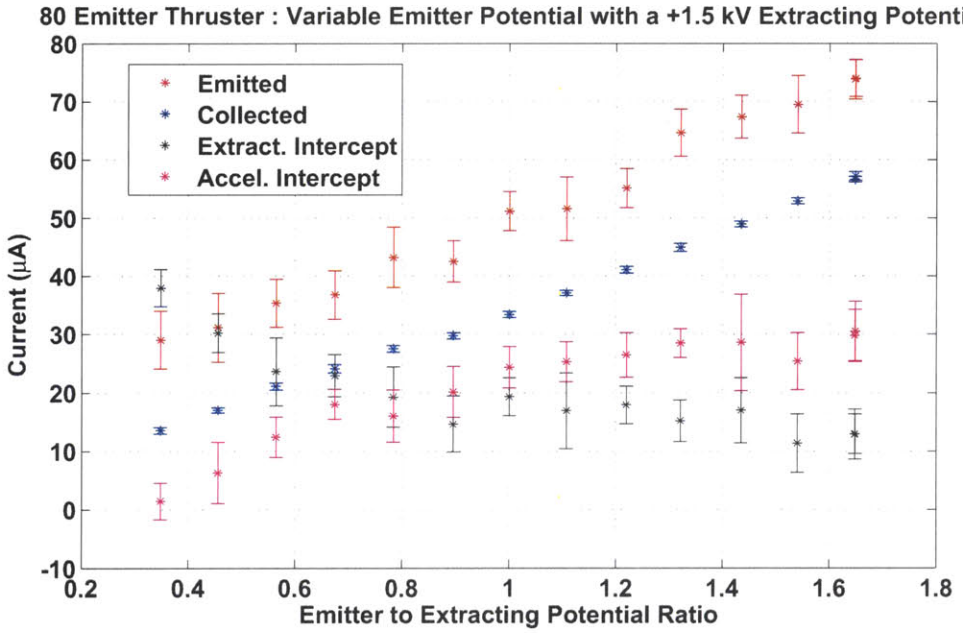

(b) Current measurements made while ramping the net emitter potential while holding the extracting potential constant at +1.5 kV.

Figure A-7: Variable beam energy tests for an extracting potential of $\pm$ 1.5 kV for the low field penetration case of Fig. A-2(b) using the 80 emitter array.

A.2.1 Discussion and Applicability to Microfabricated Thruster Arrays

The results suggested that silicon grids, without metal coatings, may be suitable for porous emitter arrays. However; these grids are nearly 10 times thicker and much more dense than those used in the microfabricated porous nickels thrusters developed here (see Chapter 5 for details of those grids). Thin, un-coated grids were initially tested with nickel emitter arrays but strong discharges and inconsistent behavior resulted, leading to the gold coated grids used in the final package.

Emission from this device was held to a minimum to prevent any damage or decay prior to future work to be done by other researchers. Nevertheless, the limited data offers support for variable beam energy operation if proper beam optics can be developed. From a microfabrication standpoint, adding a second, aligned, grid to the design shown in Chapter 5 would be feasible. A primary challenge in that case would lie with ensuring sufficient electrical insulation between grids. A first step towards achieving this would logically be an improvement in the characterization of typical beam divergence profiles from planar porous emitters. Subsequently a design to maximize beam optics while maintaining axial potential gradients could be attempted.

Although some degree of field penetration from the second, downstream, grid may never be eliminated, this influence could be actively adjusted for by a simple controller on a spacecraft. Alternatively open loop control may be possible by fully characterizing the device over a larger range of operating conditions. In either case, this would allow for the desired independent control of both emitted current and beam potential. In terms of propulsive applications, this would equate to independent control of beam power and specific impulse.